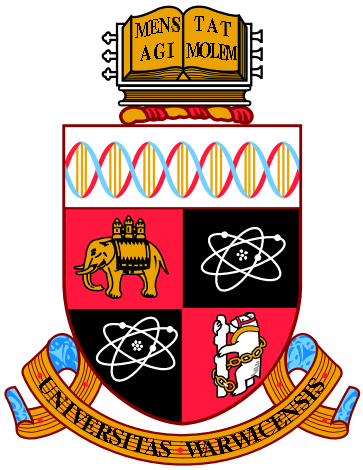


# Metaphase Chromosome Dynamics Investigated by High Resolution Tracking and Data-Driven Modelling.

by

**Edward Harry**

**Thesis**

Submitted to the University of Warwick

for the degree of

**Doctor of Philosophy**

**Warwick Medical School**

July 2014

THE UNIVERSITY OF WARWICK

# Contents

# List of Figures

Graphs and images were created using MATLAB. 3D images were rendered with IMARIS using the IMARIS-XT interface to MATLAB. Diagrams and figure edits were produced with Adobe Illustrator.

# List of Tables

# List of Acronyms

**SAC** spindle assembly checkpoint

**MAP** microtubule associated protein

**PSF** point spread function

**MHT** multiple hypothesis tracking

**RMS** root mean square

**CCAN** constitutive centromere-associated network

**PCM** pericentriolar material

**MSD** mean squared displacement

**DMEM** Dulbecco's modified Eagle's medium

**FCS** foetal calf serum

**PBS** phosphate buffered saline solution

**siRNA** short interfering RNA

**MEM** minimum essential media

**CMLE** classic maximum likelihood estimation

**eGFP** enhanced green fluorescent protein

**GMM** Gaussian mixture-model

**LAP** linear assignment problem

**OLS** ordinary least-squares

**WLS** weighted least-squares

**LMS** least-median squares

**MCMC** Markov chain Monte Carlo

**hMC** hidden Markov Chain

**PEF** polar ejection force

# Declarations

This thesis is submitted to the University of Warwick in support of my application for the degree of Doctor of Philosophy. It has been composed by myself and has not been submitted in any previous application for any degree.

The work presented (including data generated and data analysis) was carried out by the author except in the cases outlined below:

**List of data provided and/or analysis carried out by collaborators.**

- Chapter 4: The model and statistical framework presented here were conceived and originally implemented by Nigel Burroughs. Model-fitting software was originally written by Nigel Burroughs with modifications by the author.
- Chapters 5 and 6: Model-fitting software was originally written by Nigel Burroughs with modifications by the author. Data interpretation was carried out in collaboration with Nigel Burroughs and Andrew McAinsh.

**Parts of this thesis have been published by the author:**

- Chapter 1: Parts of this chapter have been published in the following review:
  E. Vladimirou et al. "Springs, clutches and motors: driving forward kinetochore mechanism by modelling". In: *Chromosome Res.* 19.3 (Apr. 2011), pp. 409–421.
- Chapter 3, Section 3.12: The algorithm described in this section was used in the following publication:
  Liam P Cheeseman et al. "Specific removal of TACC3-ch-TOG-clathrin at metaphase deregulates kinetochore fiber tension." In: *Journal of Cell Science* 126.Pt 9 (May 2013), pp. 2102–2113.

**List of publications including submitted papers.**

- E. Vladimirou et al. “Springs, clutches and motors: driving forward kinetochore mechanism by modelling”. In: *Chromosome Res.* 19.3 (Apr. 2011), pp. 409–421.

- Liam P Cheeseman et al. “Specific removal of TACC3-ch-TOG-clathrin at metaphase deregulates kinetochore fiber tension.” In: *Journal of Cell Science* 126.Pt 9 (May 2013), pp. 2102–2113.

# Abstract

Kinetochores are multi-protein machines that control chromosome movements by regulating the dynamics of attached microtubules. In human cells chromosome movements are orchestrated by the leading kinetochore tracking a shrinking microtubule whilst its sister tracks a growing microtubule. Directional switches occur when (both) kinetochore-attached microtubules flip between these two states, adaptive and coordinated switching then giving rise to the oscillations observed during metaphase. However the mechanisms (and rules) controlling directional switching are poorly understood. This work demonstrates that by tracking kinetochores with sub-pixel resolution in HeLa cells and fitting stochastic mathematical models that a sensor on the leading sister triggers switching when the tension across the centromeric spring connecting the sisters builds up sufficiently rapidly. Further it is shown that the trailing sisters polymerisation state is stabilised by high spring tension. These mechanisms pre-empt trail-first switching that would otherwise impose abnormal pulling forces between sister chromatids. As a consequence sister-switching is biased towards lead-first switching, switching of the trailing sister rapidly following as the spring tension falls, this removing the force dependent stabilisation of the trailing sisters K-fibre (kinetochore bound microtubules). This model explains how switching events are initiated and resolved, the centromeric spring tension providing a means for inter-sister communication and cross regulation that results in coordinated oscillations within a context of low spring tension. This study demonstrates that high throughput analysis and modelling pipelines can provide novel mechanistic insight into mechanochemical systems.

**Thesis Supervisors:** Andrew McAinsh[1] and Nigel Burroughs[2]

[1] Biomedical Cell Biology Division, Warwick Medical School, University of Warwick

[2] Warwick Systems Biology Centre, University of Warwick

# Chapter 1

# Introduction

## 1.1 Overview of Mitosis

Once per cell cycle eukaryotic cells go through mitosis, the process of nuclear division [1]. M-phase (mitosis combined with cytokinesis) occurs at the end of the cell cycle [2]. Cell division is the basis for growth, development and damage repair for all multi-cellular organisms [2]. Proper cell division results in two new cells, known as daughter cells, that are genetically identical to the parent. Inaccurate cell division is the precursor to many downstream genetic disorders and cancers [3–7]. DNA replication takes place during interphase (specifically S-phase). Complete DNA replication, along with many other factors will satisfy the cell's G2 checkpoint and the cell will enter mitosis [8]. A successful mitosis (*i.e.* assuming no errors occur) results in the accurate segregation of identical genetic material into the new daughter cells. A successful M-phase will result in two new daughter cells both starting the cycle again at the G1 (or G0) phase (Figure 1.1). Mitosis is a relatively short cycle period [2] but is where the most dramatic physical changes to the internal cell structure occur [9] (Figure 1.2). Mitosis itself can be divided into five distinct phases:

- **Prophase**, where duplicated strands of DNA (duplicated during the preceding S-phase) condense into distinct chromosomes. Each one consisting of two identical sister-chromatids joined along their length by condensin complexes and cohesin rings, and at their midpoint known as the centromere. Outside the nucleus the centrosomes begin to separate.

- **Prometaphase**, begins with the breakdown of the nuclear envelope separating the chromosomes from the rest of the cell. The chromosomes diffuse out into the cytoplasm and bind to mitotic spindle microtubules via the kinetochore complex assembled on each sister-chromatid. Sister-kinetochores continually capture and release microtubules until they achieve a bi-orientated state (each sister-kinetochore attached to an unique spindle-pole) while chromosomes congress to the spindle equator.

- **Metaphase**, when captured chromosomes are all aligned to the middle of the spindle. Aligned chromosomes form an effective two-dimensional plane normal to the axis between the spindle-poles. Chromosomes remain in a stably bi-orientated state while oscillating towards and away from each spindle-pole.

- **Anaphase**, the beginning of physical sister-chromatid segregation. The cohesin rings joining the sister-chromatids are cleaved and each chromatid is pulled towards its respective spindle-pole. Anaphase can be divided into two distinct phases; anaphase A where kinetochore-engaged microtubule depolymerisation pulls chromatids poleward followed by anaphase B where the two halves of the spindle slide apart by the action of molecular motors, microtubule dynamics and cell cortex interactions.

- **Telophase**, the forming of two new nuclei. Once genetic material has been segregated to each spindle-pole a new nuclear envelope forms around each set of chromatids. DNA begins to de-condense and eventually two new genetically-identical nuclei are formed.

After telophase is complete the cell completes cytokinesis (not considered part of mitosis) where the cell physically separates its cytoplasm and pinches close its cell membrane forming two new cells.

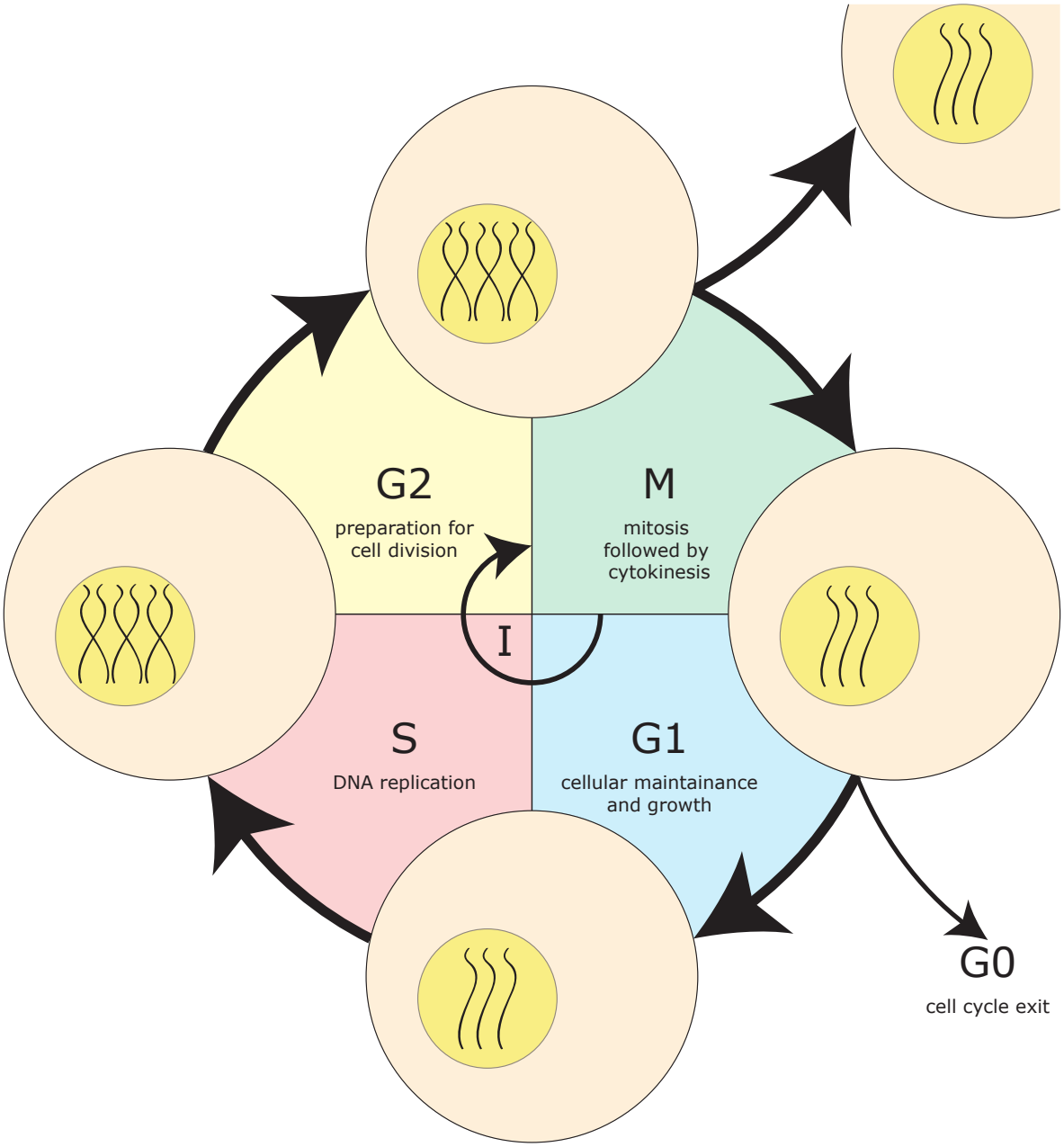


**Figure 1.1:** Overview of the cell cycle. **G1:** Main phase of cellular growth. G1/S checkpoint controls the transition to S-phase. **S:** Phase of DNA replication. **G2:** Additional phase of growth and protein synthesis in preparation for cell division. G2/M checkpoint controls the transition to M-phase. **M:** Mitosis followed by cytokinesis, two genetically identical daughter cells formed. G1 plus S plus G2 are known as interphase (**I**). **G0:** Cell cycle exit, a resting phase where no growth or division takes place.

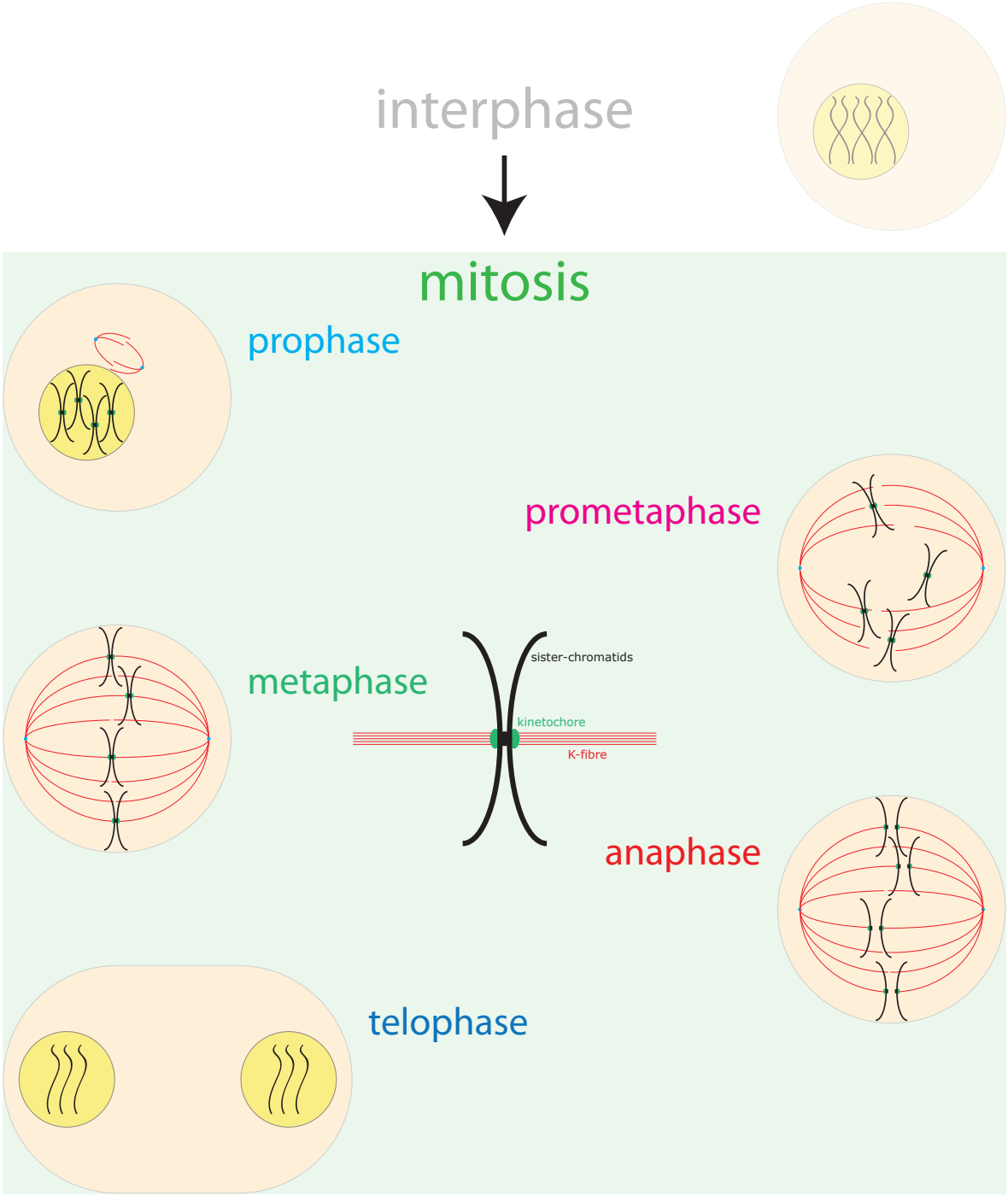


**Figure 1.2:** Overview of mitosis. **Prophase:** DNA condensation and beginning of centrosome separation. **Prometaphase:** Spindle establishes across the cell body, chromosomes begin to engage spindle microtubules via their kinetochores. **Metaphase:** Bi-orientated chromosomes have all congressed to form the metaphase plate. **Anaphase:** Sister-chromatids separate and start to move towards their respective spindle-poles. **Telophase:** DNA decondensation and nuclear reformation.

## 1.2 Mitotic Machinery

### 1.2.1 Mitotic Spindle Assembly

The mitotic spindle self-assembles around the chromosomes during prometaphase. The mitotic spindle is an active polymer structure made of dynamic microtubules, motors and microtubule associated proteins (MAPs) [10–12]. Microtubules are formed by the polymerisation of tubulin hetero-dimers consisting of alpha- and beta-tubulin sub-units [2]. Tubulin hetero-dimers polymerise end-on-end between alpha-tubulin and beta-tubulin creating a microtubule protofilament [13]. A microtubule is typically formed by 13 protofilaments arranged laterally in a cylindrical structure [14]. Because of the sub-unit structure of the protofilaments microtubules have a distinct polarisation with exposed alpha-subunits at one end and beta-subunits at the other. The beta-tubulin end is referred to as the plus-end with the other referred to as the minus-end. Polymerisation typically takes place at the plus-end [15]. A free tubulin hetero-dimer binds two molecules of GTP, one bound to alpha-tubulin and one to beta-tubulin. Alpha-tubulin bound GTP is stable while beta-tubulin bound GTP has the ability to hydrolyse to GDP [13]. Only a hetero-dimer with GTP-bound beta-tubulin can be incorporated into a microtubule polymer, whereupon hydrolysation of the GTP is promoted [16]. A hetero-dimer at the plus-end of a microtubule that becomes GDP-bound will rapidly disassociate from the polymer. Therefore if the rate of hetero-dimer addition to a microtubule becomes smaller than the rate of GTP-to-GDP hydrolysation the 'cap' of GTP at the plus-end will start to disappear. Once the hydrolysation catches-up with the last hetero-dimer the microtubule will start to rapidly depolymerise (known as 'catastrophe') [17]. Incorporation of new GTP-bound tubulin at the plus-end can halt disassembly or 'rescue' the microtubule. Microtubules therefore have the ability to switch between periods of polymerisation and depolymerisation. The microtubules of the spindle emanate from two spindle-poles that are located at opposite sides of the cell. The structure that becomes a spindle-pole is a microtubule organising centre known as a centrosome [18]. During interphase the cell contains a single centrosome serving as the main microtubule organising centre of the cell that sits on the surface of the nucleus. The centrosome contains a pair of embedded cylindrical structures known as centrioles [2, 11]. One centriole is known as the mother centriole and the other as the

daughter (the daughter having been nucleated from the mother). The centrioles serve as the organising centres of the pericentriolar material (PCM) that makes up the body of the centrosome [19]. The PCM contains gamma-tubulin ring complexes which serve as nucleation sites for microtubules that nucleate from their minus-ends outward [20]. Before the onset of mitosis (during S-phase) the centrosome is duplicated [18]. Mother and daughter centrioles separate and nucleate two new daughters [18]. Once both new centrioles are formed the centrosome is duplicated. During prophase the two centrosomes move to opposite sides of the nucleus and then begin to move to opposite sides of the cell via microtubule sliding [18]. Microtubules from each pole engage the chromosomes via the two kinetochores sitting either side of each centromere by a search and capture mechanism. Through detection of their attachment state the kinetochores selectively turn over microtubules [21] until they are bi-orientated (each kinetochore attached to microtubules emanating from opposite spindle-poles) while the chromosomes congress to the spindle equator [22]. The microtubules of the spindle can be roughly divided into three populations: inter-polar microtubules that span the spindle structure, making anti-parallel overlaps with microtubules from the opposite spindle-pole. Inter-polar microtubules are thought to give structure to the rest of the spindle and provide an initial formation pathway as the spindle first forms [23], sliding against each other moving the two spindle-poles to opposite ends of the cell by the action of the motor proteins that provide some of the crosslinking [24]. Kinetochore microtubules are the microtubules that directly engage with the kinetochores; as mentioned previously their dynamic turnover is modified by the kinetochore thus forming a more stable attachment. Bundles of kinetochore microtubules are called K-fibres, ranging from 1 microtubule in yeast to $\sim$ 25 in humans [25]. Astral microtubules emanate from the spindle-pole radially and make physical contact with the cell cortex. Through coupling to dynein motors at the cortex astral microtubules are responsible for maintaining the global positioning of the spindle [26]. The microtubules of the spindle also provide a transport network for other proteins, molecular motors and proteins that bind directly to the growing plus-tips of microtubules providing a means to both transport and localise cargo [27]. Figure 1.3 shows a schematic of the kinetochore - K-fibre - spindle-pole system.

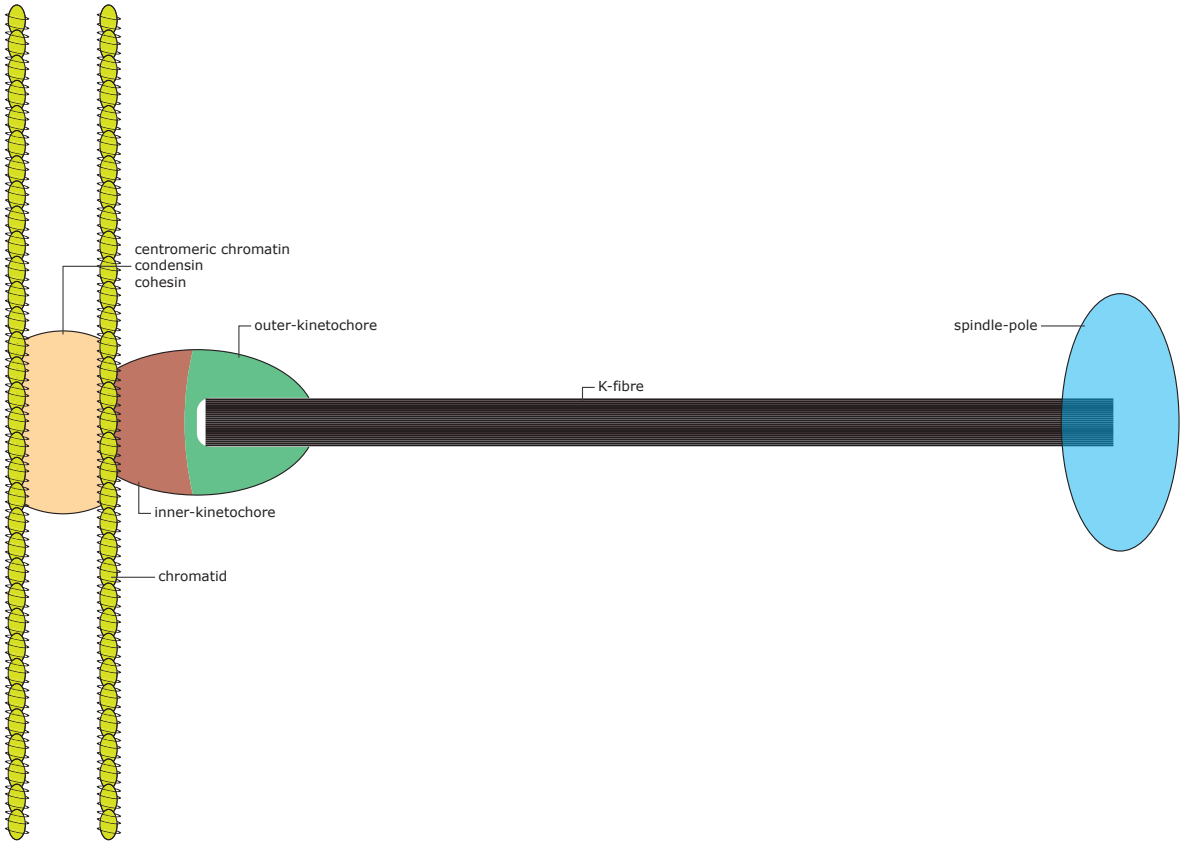


**Figure 1.3:** Schematic of the kinetochore - K-fibre - spindle-pole system.

## 1.2.2 Kinetochores

### 1.2.2.1 Kinetochore Assembly

A large multi-protein super-complex called the kinetochore assembles on each duplicated sister-chromatid at the centromere [28–30]. Kinetochore assembly starts with an epigenetic marker for the kinetochore's location. The histone H3 variant CENP-A serves as this marker [31, 32]. CENP-A remains stably incorporated into centromeres over several cell cycles [31, 33] and thus is the stable base upon which the rest of the kinetochore forms. The inner kinetochore, also known as the constitutive centromere-associated network (CCAN) complex, directly binds to centromeric DNA / nucleosomes [34, 35]. A main structural component of the CCAN is the CENP-T-W-S-X nucleosome-like complex [36–39]. CENP-T-W-S-X binds directly to DNA and thus forms a second structural basis for the kinetochore along with CENP-A. In-fact both CENP-A and the CENP-T-W-S-X complex each offer a different structural pathway for kinetochore assembly. CENP-A directly binds CENP-C [40] which in-turn binds to the other kinetochore component Mis-12 [41]. Meanwhile the CENP-T subunit of the CENP-T-W-S-X complex directly binds the Ndc80 complex of the outer kinetochore,

which itself also binds to Mis-12 [42]. See Figure 1.4 for a structural schematic of a kinetochore.

#### 1.2.2.2 Kinetochore Control of Microtubule Dynamics

Outer kinetochore components directly bind microtubules and are thought to form the bulk of kinetochore-microtubule attachments [30, 43]. The microtubule engagement site of the kinetochore outer-plate is the KMN network. A single engagement site forms multiple bonds along a microtubule lattice [44]. The KMN network is a multi-protein complex consisting of KNL-1, Mis12 and Ndc80. KNL-1 and Ndc80 directly bind to microtubules [44, 45]. The lifetime of attachment of semi-purified kinetochore particles to microtubules has been shown to depend on the level of tension applied *in vitro* [46] and this tension across the kinetochore has been shown to correlate with the state of the spindle assembly checkpoint (SAC) [47, 48]. Molecular motors and MAPs associate with kinetochore-bound microtubules. The Ska complex for example directly binds to the KMN network and affects microtubule stability [22, 49]. The human Ska complex is comprised of three proteins: SKA1, SKA2 and SKA3. SKA1 and SKA2 are recruited by Ndc80 to kinetochore-microtubule attachment sites [50]. SKA3 is recruited to kinetochores where all three subunits are required for the formation of the Ska complex [51–55]. The Ska complex has been shown to directly bind and stabilise kinetochore-bound microtubules, remaining bound to the plus end of depolymerising microtubules [55, 56]. Ska has also been shown to play a role in chromosome congression, the kinetochore interface with the SAC and segregation during anaphase [50–54]. Molecular motors such as the plus-end directed motor CENP-E and the minus-end directed motor dynein associate with the kinetochore and provide ATP fuelled sliding of microtubules [22]. Other molecular motors that affect microtubule growth and shrinkage rates such as Kinesin-8 [57] and Kinesin-13 [58] are also found associated with the kinetochore, offering further regulation of microtubule dynamics. Subunits of the inner-kinetochore CCAN complex have been shown to affect microtubule plus-end turnover rates, change abundance on sister kinetochores during oscillations (preferring the trailing sister) and even bind microtubules directly [59, 60].

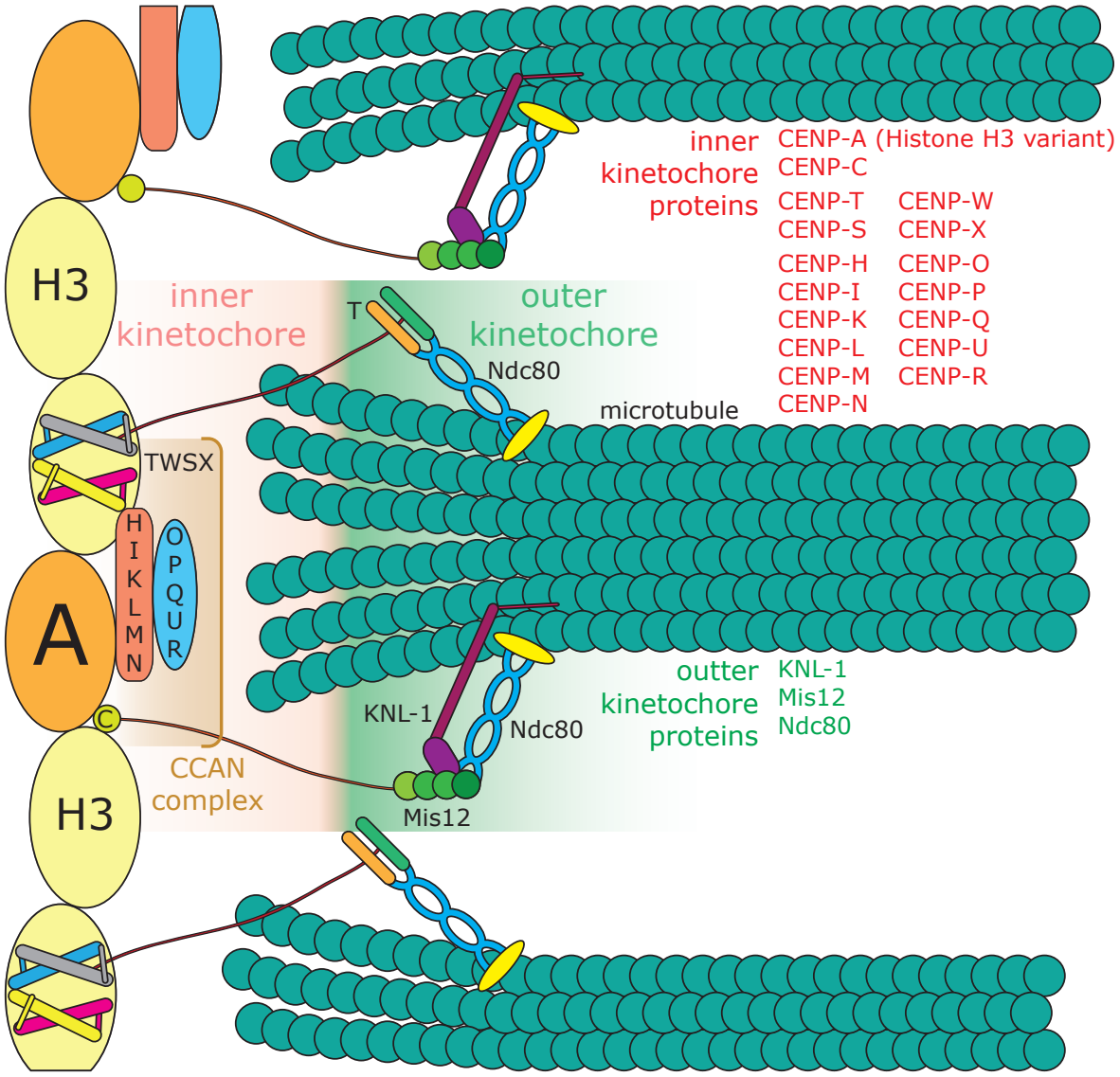


**Figure 1.4:** Structural schematic of a kinetochore. The inner-kinetochore (CCAN complex) includes the CENP- proteins: A; C; H; I; K; L; M; N; O; P; Q; U; R; T; W; S and X. CENP-TWSX and CENP-C provide a structural linkage between the inner- and outer-kinetochore. The outer-kinetochore includes the KMN network consisting of: KNL-1, Mis12 and Ndc80. Components of the outer-kinetochore bind directly to microtubules.

### 1.2.3 Structural Integrity of the Sister-Chromatid Linkage by Condensins and Cohesins

Condensation of duplicated genetic material into chromosomes during prophase requires the action of condensin proteins [61]. Condensins are enzymes than use the energy derived from ATP hydrolysis to induce coiling in DNA fragments [61]. Two versions of condensins are found in mammalian cells: condensin I and condensin II. Both condensin I and II are structurally similar. Both consist of two long subunits SMC2 and SMC4 (also known as CAP-E and CAP-C respectively) hinged at one end [62]. The other end of SMC2 and SMC4 are the ATPase heads and bind to the third subunit, a kleisin complex [62]. In the case of condensin I the kleisin subunit is known as CAP-H and in the case of condensin II as CAP-H2 [62]. The kleisin binds a fourth and a fifth subunit, a pair of HEAT repeats, CAP-D2 and CAP-G in the case of condensin I and CAP-D3 and CAP-G2 in the case of condensin II [62]. Condensins as well as being necessary for mitotic chromosome formation also play a key role in maintaining structural integrity of the sister-chromatid linkage throughout mitosis pre-anaphase [63, 64]. Condensin I binds to chromosomes via the CAP-D2 HEAT repeat subunit to histones H1 and H3 [62, 65]. Condensin II binds to histone H4 via both its HEAT repeats CAP-D3 and CAP-G2 [62, 66]. Condensin is thought to bind chromosomal regions together topologically by encircling DNA strands in their ring-like structure, with the ATP hydrolysis of the SMC2 and SMC4 heads affecting the binding with the kleisin subunit thereby closing/releasing the lock [62, 67]. Another key structural component of mitotic sister-chromatids is the cohesin complex. Cohesin complexes are distributed along the chromosome arms and like condensin is thought to topologically bind sister-chromatids by forming ring-like structures [68]. Cohesins have a very similar structure to condensins, cohesins consist of two long subunits SMC1 and SMC3 hinged and one end. The other ends of SMC1 and SMC3 bind to a kleisin complex RAD21 which itself bind to a fourth subunit, either STAG1 or STAG2 [69, 70].

### 1.2.4 The Spindle Assembly Checkpoint

Only when all the chromosomes are properly positioned at the spindle equator and are properly attached to the spindle does the spindle assembly checkpoint (SAC) deactivate, causing each chromosome to separate and each sister chromatid to be pulled towards its corresponding spindle-pole. The main target of the SAC is the anaphase promoting complex APC/C. Active APC/C triggers the onset of anaphase [71, 72]. APC/C activation requires the binding of CDC20. The SAC delays the transition to anaphase by promoting the formation of the mitotic checkpoint complex MCC [72, 73]. MCC sequesters CDC20 thereby preventing the activation of APC/C [72]. An incorrectly attached kinetochore phosphorylates the outer kinetochore protein KNL1 via the protein kinase MPS1 [72, 74]. The current working model is that phosphorylated KNL1 binds the protein BUB3 which then recruits BUB1 which in turn recruit the BUBR1/MAD3 complex [72]. BUB1, BUB3 and BUBR1/MAD3 then recruit MAD1 and MAD2 [75]. MAD1 catalyses MAD2 from an 'open' to a 'closed' formation. Closed MAD2 then is able to bind CDC20. MAD2-CDC20 then binds BUBR1/MAD3 and BUB3 to form MCC [72, 73]. Upon forming stabilised microtubule attachments the MAD2 recruitment scaffold established at the kinetochore is removed by the action of dynein motors bound to Rod-Zw10-Zwilch (RZZ) complexes [76]. This interaction offers an effective checkpoint silencing pathway for kinetochores that establish correct attachments. MCC is continually degraded by Cdc20 auto-ubiquitylation [76, 77] therefore the eventual depletion of the pool of 'closed' MAD2 at kinetochores upon achieving a correct attachment state eventually results in the loss of MCC and therefore activate APC/C which in turn can start the transition to anaphase. The exact kinetics and control mechanisms that make the SAC both robust and sensitive enough to delay the anaphase transition until all chromosomes have become bi-orientated are still active areas of research. Studies have began to reveal the minimum level of MCC required to block APC/C and the minimum amount of time required to establish the checkpoint [77, 78]. There is evidence that under certain circumstances the SAC can deactivate before all chromosomes have become bi-orientated leading to potential aneuploidy [77].

## 1.3 Mitotic Chromosome Dynamics

### 1.3.1 Phase Contrast and DIC Microscopy Reveal Coordinated Chromosome Dynamics

Studies on the internal dynamics of eukaryotic cells during mitosis, with particular emphasis on the dynamics of the chromosomes, have been conducted for over 70 years. As distinct chromosomes formed by DNA condensation during prophase they became macroscopically distinct from the rest of the nuclear material and cytoplasm. Phase contrast microscopy, invented in the 1930s [79], allowed mitotic chromosomes to be visualised *in vivo* [80, 81]. Phase contrast converts differences in the phase of incident light to brightness variations. Phase differences between beams of light arise when the light rays move through media with differing refractive indexes. Chromosomes for example have a higher refractive index than the background cytoplasm due to the higher density of the chromosomes. These observations led to the conclusion that chromosome movements during mitosis, particularly during anaphase, were driven by the direct interaction of fibres of the mitotic spindle with the chromosomes [81]. Refinements to phase contrast techniques in the 1960s yielded Nomarski or Differential Interference-Contrast (DIC) microscopy [82]. The improved image quality along with the advent of digital image capture and storage technologies allowed mitotic chromosomes to be visualised in greater spatio-temporal detail [83–91]. In parallel to the greater resolving power available for live-cell imaging advances in fixed sample imaging such as electron microscopy revealed the fine-structure of the mitotic machinery [85, 92]. Electron microscopy images of chromosomes and their associated sister-kinetochore complexes indicated that the kinetochore was the site of microtubule interaction between the chromosome and the mitotic spindle [92]. Later *in vitro* experiments confirmed that kinetochore mobility was driven by microtubule depolymerisation [93]. Observations of chromosomes during prometaphase and metaphase up to the initialisation of anaphase uncovered the fact that chromosomes undergo periodic-like movements towards and away from the centrosomes on either side of the spindle, both in mitosis and meiosis [83–85]. The amplitude and frequency of these oscillations varied between species but was observed in all model eukaryotic cell lines. Chromosome oscillations were first

assumed to be sinusoidal in nature [86, 87, 89] but more detailed analysis revealed that oscillating chromosomes exhibit a saw-tooth-like motion, termed directional instability *i.e.* periods of relatively constant velocity travelling towards each spindle-pole separated by relatively rapid reversals of direction [90]. Both bi-orientated and mono-orientated (one kinetochore attached to one spindle-pole) chromosomes were found to oscillate indicating that single kinetochores can cause both poleward and anti-poleward movements [90]. Phase synchronisation between sister-kinetochores during chromosome oscillations were assumed to be controlled by the tension between the kinetochores *i.e.* across the chromosome. Laser-microsurgery experiments confirmed this hypothesis by cutting the connection between sister-kinetochores leading to two de-synchronised oscillating kinetochores [91]. The mechanisms by which this works however are still unknown.

### 1.3.2 Fluorescent Markers Allow Direct Measurements of Mitotic Machinery

The advent of fluorescent markers as a tool in live-cell imaging allowed kinetochores and various other mitotic proteins to be tagged and their dynamics ascertained directly. These kinds of measurements offered new insights into chromosome dynamics and allowed hypotheses to be tested in greater detail. For example the coupled asymmetry between sister-kinetochores in terms of microtubule attachment *i.e.* a poleward moving kinetochore is attached to depolymerising microtubules while an anti-poleward moving kinetochore is attached to polymerising microtubules was shown by the injection of fluorescently marked anti-bodies against the plus-end tracking protein EB1 [27]; plus-end tracking proteins are proteins that bind-to and follow the growing ends of microtubules [94]. Combined phase contrast and fluorescent imaging showed that EB1 is enriched at the trailing kinetochore during a bi-orientated oscillation *i.e.* the anti-poleward moving kinetochore, indicating that the kinetochore in question is attached to polymerising microtubules [27]. After a directional switch EB1 no longer associates with the now leading / poleward moving kinetochore, indicating that the kinetochore is now attached to depolymerising microtubules. Advances in high volume data processing and computer vision technologies alongside continuing refinements in

light-microscopy techniques allowed kinetochore dynamics to be studied in an increasingly high-throughput manner [95–100]. Three-dimensional imaging of kinetochores throughout mitosis and meiosis for example has revealed the mechanisms and pathways chromosomes take to form the metaphase plate [95, 97, 98]. Studies on mouse oocytes tracking kinetochores through meiosis have shown that chromosomes and the mitotic spindle initially form a ball-like structure after nuclear-envelope-breakdown [95, 97]. The structure evolves into a belt or ring-like formation as prometaphase continues before morphing into the metaphase plate at the onset of metaphase. Chromosomes were observed to undergo multiple rounds of error-correction during prometaphase *i.e.* correcting merotelic (one kinetochore attached to two spindle-poles) and syntelic (both kinetochores attached to a single spindle-pole) attachments. This ring-like structure of chromosomes has also been observed in studies on RPE1 cells [98]. Here the authors hypothesised that the ring-like structure optimised the search-and-capture mechanism of kinetochore-microtubule interaction. Automatic object detection and tracking techniques allow for a large range of kinetochore dynamics to be sampled and their statistical distributions to be analysed. Such techniques have been implemented in high-throughput assays allowing for a relatively quick pipeline to take image data and determine kinetochore coordinate data with minimal human-bias [96, 99, 100]. The oscillation period of chromosomes was shown to depend on both molecular motors at the kinetochores and on the mechanical linkage between the kinetochores [96]. Poleward and anti-poleward moving kinetochores were shown to behave with different dynamics *e.g.* they move with different speeds [99, 100]. The inter-kinetochore displacement was shown to oscillate with approximately twice the frequency of the chromosome oscillation, with the maximal inter-kinetochore stretch occurring before a directional switch [96, 100].

### 1.3.3 Tracking Kinetochores with Sub-Pixel Accuracy

Fluorescent tags that are small relative to the resolving power of an optical microscope appear as diffraction-limited intensity distributions. The locations of these tagged features can be resolved with an uncertainty smaller than classical optical theory would suggest, using an appropriate model of the intensity distribution. Various spot-fitting

algorithms have been applied to the study of kinetochore dynamics [99–106]. Sub-pixel resolution becomes important in measuring kinetochore dynamics when trying to capture relatively rapid events such as directional switches. The cost of spot fitting is an increased computational time and complexity, generally scaling non-linearly with the number of features to fit. Super-resolution spot fitting has been used to resolve inner- and outer-kinetochore components (tagged in different colours) sufficient to measure intra-kinetochore stretch during oscillations [47, 48, 100]. Kinetochore stretch was found to be smaller on poleward moving kinetochores. Individual kinetochore components have been resolved using super-resolution spot-fitting in fixed-cells (again using different coloured tags) where longer exposure times and higher light intensities can be used to collect higher quality images compared with live-cell imaging [106]. Major conformational changes in the sub-unit architecture of the kinetochore were observed under taxol treatment, a microtubule stabilisation agent; specifically in the separation between the outer-kinetochore component Ncd80 and the inner-kinetochore CCAN. Taxol treatment has been shown to activate the SAC [107, 108]. The authors therefore concluded that the spatial organisation of kinetochore sub-units is sensitive to active microtubule tension and generates a SAC activation signal. Parallel measurements of individual kinetochore components have been used to show the correlation between intra-kinetochore stretch and SAC activation [47, 48]. Similar analysis on proteins integral to SAC signalling revealed close associations between SAC proteins and the KMN network [109].

## 1.4 Modelling Chromosome Dynamics During Mitosis

### 1.4.1 The Kinetochore as a Molecular-Clutch

The kinetochore can be thought of as a ‘molecular-clutch’ transforming stochastic GTP hydrolysis based microtubule forces into useful work in transporting chromosomes [110]. The high regularity of chromosome oscillations when compare to the highly stochastic nature of microtubule growth and shrinkage suggest that kinetochores impose a great deal of control over K-fibre dynamics. Centromeric chromatin that forms the physical

linkage across sister-kinetochores is generally modelled as a linear elastic spring [88]. This elasticity can be inferred by the observed inter-sister displacements oscillating in phase (with double the frequency) of kinetochore oscillations [96, 100] and the high but not perfect synchronisation of the motion of sister-kinetochores [96]. Studies have found that centromeric chromatin may diverge from a linear spring model by displaying a kind of plastic deformity *i.e.* a hysteresis that could correlate with the kinetochore attachment state [111]. Non-linear spring-like behaviour could also be contributed to by conformation changes within the internal multi-layered structure of the kinetochore [106]. Other components to consider that could influence chromosome dynamics are molecular motors. Both plus- and minus-end directed motors are found associated with kinetochores and exert force on kinetochore-bound microtubules [112]. External forces to the kinetochore include the polar ejection force (PEF) pushing chromosomes away from the ends of the spindle and poleward microtubule flux *i.e.* depolymerisation of kinetochore-bound microtubules at their minus- *i.e.* spindle-pole bound end. The PEF is thought of as a repulsive force field that acts on the chromosomes emanating from either spindle-pole and is believed to be the average action of microtubules on the chromosome arms, either directly by the steric interactions of polymerising microtubules or by chromosome-bound chromokinesin motors [113]. The whole mitotic spindle itself can generate forces that may need to be considered as well *e.g.* though the dynamics of the spindle-poles themselves [114].

### 1.4.2 Dynamic Forces at Chromosomes

A model needs at least two elements to reproduce oscillations: a spatial force gradient to bias chromosomes to the centre of the cell *i.e.* to the metaphase plate and a force-based feedback process to regulate the resultant polymerisation and depolymerisation of kinetochore-bound microtubules. The PEF is usually a reliable candidate for the force gradient, it being a relatively well studied phenomena that acts towards the cell centre. Force-feedback is necessary in order to endow the system with oscillatory dynamics. The nature of kinetochore-bound microtubules is highly model-dependent and can range from simple binary-state polymerisation / depolymerisation models up to the incorporation of a full microtubule regulatory process at the kinetochore. Almost all

models impose force-balance whilst iterating forward through time to generate dynamic trajectories of the system. These kinds of force-balance models have well developed principles [115] and have been used extensively throughout theoretical biology *e.g.* modelling the action of actin filaments [116] and a model of Drosophila embryo spindle morphogenesis [117].

### 1.4.3 The Kinetochore-Microtubule Interface

#### 1.4.3.1 Passive Binding - Microtubule Sleeves

There have been many proposed models of chromosome oscillations that feature intricate models of the kinetochore-microtubule interface as a primary component. For example the model of Joglekar and Hunt [118, 119] is a one-dimensional chromosome dynamic model. The model consists of force-balance between microtubule-based forces and a PEF. Numerical simulation of a set of equations is used where microtubules and kinetochores update their states by moving to a state of lowest free energy. Model parameters are either taken from experiments on PtK1 or Newt lung cells or are estimated [118]. For the kinetochore-microtubule interface the Joglekar and Hunt model incorporates the Hill-sleeve model [120]. A Hill-sleeve is a theorised binding site that is able to bind multiple tubulin heterodimers of a single microtubule. A single sleeve is modelled as being 40nm in length as this is the inferred depth of the outer-kinetochore plate based on electron micrograph measurements [121]. A tubulin heterodimer is 8nm in length therefore 40nm/8nm = 5 heterodimers can enter the sleeve simultaneously lengthwise. A single microtubule is made of 13 cylindrically arranged protofilaments therefore $13 \times 5 = 65$ heterodimers can enter the sleeve simultaneously in total, therefore it is assumed that there are 65 tubulin binding sites per sleeve. A microtubule interacting with a Hill-sleeve is modelled as follows: as a microtubule enters a sleeve more and more binding sites become occupied, an occupied binding site has a lower free-energy than a non-occupied one therefore the state of lowest energy is where the microtubule has completely penetrated the sleeve. The microtubule will therefore be biased to enter the sleeve. However to actually penetrate further into the sleeve a microtubule must break all its current bonds, there is therefore an increasingly large energy barrier for the microtubule to overcome. Once

the tip of a microtubule has entered a sleeve it is assumed that it cannot interact with any free tubulin dimers therefore it cannot polymerise. Therefore a microtubule can move relative to a sleeve by either depolymerising or by diffusion of the sleeve over the microtubule lattice. In the Joglekar and Hunt model each kinetochore has multiple sleeves connected by linear elastic springs. A microtubule tip position inside a sleeve is therefore affected by the polymerisation state of the microtubule and the restoring force on the sleeve, a higher restoring force moving the tip further out of the sleeve. A sleeve will therefore move on a microtubule lattice to its equilibrium position in response to its restoring force and its free binding energy. Assuming that a microtubule tip moves relative to a sleeve much more rapidly than the overall velocity of the tip, sleeves will tend to follow a microtubule tip at a constant rate until they detach from the microtubule lattice. This endows the system with the property that kinetochores move at a constant velocity *i.e.* a key property of directional instability. Experimental evidence for a sleeve-like structure of the kinetochore-microtubule interface does exist. The KMN network of the outer-plate of a vertebrate kinetochore has been shown to have the ability to form multiple bonds to a microtubule lattice [44]. The KMN network consists of KNL-1, Mis12 and Ndc80; both the Ndc80 complex and KNL-1 have been shown to bind microtubules [44, 45]. Specifically Ndc80 has been shown to bind inter- and intra-tubulin dimer interfaces forming oligomeric arrays along the microtubule lattice [43]. This gives Ndc80 the ability to form multiple interactions along a single microtubule. *In vivo* studies have shown that kinetochore-bound microtubules are bound to at least 10 copies of the Ndc80 complex [122]. Additional *in vitro* experiments have shown that the kinetochore-associated Ska complex also binds microtubules by oligomerising into ring-like structures [55, 56]. These complexes provide experimental justification for the binding sites required by the Hill-sleeve model in the correct order-of-magnitude. The Ndc80 and Ska complexes have been shown to be able to form load-bearing attachments to depolymerising microtubules via optical trapping experiments [55, 123]. There are also many molecular motors and MAPs that could provide microtubule interaction sites for the kinetochore [124]. However quantitative comparison between these binding complexes and the properties of a Hill-sleeve model has basically failed to proceed beyond an initial conception since there are a vast multitude of parameters *e.g.* elasticity, binding-energy that are still unknown. To account for

the dynamic instability of microtubules the Joglekar and Hunt model uses a modified Hill-sleeve, microtubules are assumed to depolymerise much faster than the kinetochore velocities therefore only a polymerising microtubule can enter an empty sleeve. Kinetochore- *i.e.* sleeve-bound microtubules are assumed to be stabilised compared to free-microtubules, an assumption justified by *in vivo* experiments [125, 126] (although the Joglekar and Hunt model does not propose any mechanism for microtubule stabilisation). Within the model stabilised microtubules are modelled by switching to a depolymerising state with a different (lower) rate than non sleeve-bound microtubules. Finally sister-kinetochores are connected by a linear elastic spring, a feature of most models of chromosome dynamics [90, 91, 99, 127]. During a chromosome-oscillation the leading kinetochore follows its sleeve-bound depolymerising microtubules at a constant rate. The lead kinetochore's sleeves are subjected to a greater and greater restoring force. On the trailing kinetochore the sleeves are under a relatively low load, any microtubules that undergo catastrophe *i.e.* switch to a depolymerising state are lost relatively quickly as the whole kinetochore is moving in the opposite direction. Therefore in the Joglekar and Hunt model the chromosome is 'pulled' entirely by the lead kinetochore. Laser microsurgery experiments have supported this assumption by cutting the microtubules of the trailing kinetochore which did not affect the poleward velocity of the chromosome. However cutting the microtubules of the leading kinetochore completely aborted all poleward movement [128]. However it should be noted that other studies have concluded that kinetochores can produce pushing forces, though poleward-flux [129] and though measurement of centromere deformation during anti-poleward movements [90]. A directional switch occurs within the Joglekar and Hunt model when the restoring force on the lead kinetochore overcomes the binding bias of the sleeves and all the microtubules detach. This causes the chromosome to stall causing the other kinetochore to accumulate a majority of depolymerising microtubules and then the chromosome will start to follow the new lead kinetochore. This behaviour is consistent with experiments on purified kinetochore particles that showed that kinetochore particle-microtubule attachment lifetimes decrease with the application of a threshold force [46]. However this study did show that a smaller applied force stabilises attachments, consistent with results from *in vivo* experiments [88]. The other component in the model is the PEF which is vital in order to bias the chromosome

to the middle of the cell. The PEF is assumed to be proportional to the density of microtubules from the spindle so is assumed to follow an inverse-square distribution ($\propto x^{-2}$) although the oscillatory dynamics have been shown to be robust to the exact form of the distribution. Microsurgery experiments have tested the effects of the PEF on chromosome oscillations [130]. Chromosome arms were severed during oscillations; the main characteristics of directional instability such as constant speed remained unaltered while the average amplitude of oscillations increased indicating a dependence on the magnitude of the PEF acting on the whole chromosome. These observations support the force-field model of the PEF where the magnitude of the resultant force being dependent on the microtubule density on the surface area of the chromosome arms, thus also providing support for the Joglekar and Hunt model. This study did however infer a PEF distribution quite different than an inverse-square dependence; the estimated distribution went approximately as the square-root of the distance from the cell centre ($\propto x^{0.57}$). It still remains to be tested how such a distribution would affect the results of the Joglekar and Hunt model. Autocorrelation time-series analysis of Joglekar and Hunt model simulated trajectories suggests that the trajectories exhibit regular oscillation-type behaviour with a period of around 300s [110] which is not dissimilar from experimental observations [128]. Autocorrelation curves also qualitatively appear similar to those calculated from human kinetochore trajectories [96, 110] (Figure 3.25b). The Joglekar and Hunt model is therefore capable of producing qualitatively similar kinetochore trajectories to experimental measurements. However as a mechanistic model of chromosome dynamics the Joglekar and Hunt model lacks many important features. As previously discussed the model lacks molecular detail on the nature of the microtubule binding sites and on the mechanisms of microtubule stabilisation. The turnover rate of kinetochore-bound microtubules have been shown to be on the order of 10 times smaller than of free microtubules [126]. Many kinetochore-associated proteins have been shown to affect bound microtubule catastrophe rates such as aurora-B whose inhibition further reduces the turnover rate [131]; depletion of the CCAN complex on the other hand results in microtubule catastrophe rates identical to free microtubules [59]. The CENP-H and -I subunits of this complex have been shown to be asymmetrically localised to the trailing kinetochore during oscillations with their depletion causing more frequent directional switches and stochastic

oscillations [59]. Integrated protein-based feedback-control mechanisms of microtubule dynamics are obviously crucial to chromosome-oscillations and will need to be incorporated into any mechanistic model. On the mesoscopic scale the model does not consider three-dimensional dynamics of sister-kinetochores *i.e.* torques and rotations of the system; it also does not consider the possibility of any steric interactions between neighbouring chromosomes. It has been shown that kinetochores undergo internal deformations during oscillations [47, 48, 100]; this could be considered consistent with the model as microtubule-bound sleeves become stretched away from their parent kinetochore during poleward-movement. However live-cell measurements have reported that intra-kinetochore displacements decrease on poleward-moving kinetochores compared to anti-poleward ones [100], directly in contradiction with the Joglekar and Hunt model. Lastly the model does not consider many additional sources of external force generation such as molecular motors and microtubule flux.

#### 1.4.3.2 Active Binding - Molecular Motors

Models that base chromosome-dynamics on the action of molecular motors have been proposed such as the Civelekoglu-Scholey et al model [132]. This model's components are well-characterised and thus it is relatively well constrained. Again the model employs force-balance-based numerical simulation with parameters estimated from experimental observations of Drosophila syncytial blastoderm embryos. Multiple sources of force generation are considered, sources present on the kinetochore and from kinetochore-bound microtubules. Kinetochore based forces are: the viscous drag of the kinetochore moving in the cytoplasm; molecular motor based forces from the plus-end directed motor CENP-E and the minus-end directed motor dynein; the steric force of a polymerising microtubule pushing against the kinetochore; the PEF pushing the kinetochore away from the spindle-poles and lastly a force due to a linear spring that connects sister-kinetochores. The antagonistic action of plus- and minus-end directed motors generate relatively stable kinetochore-microtubule connections consisting of multiple individual binding sites, thus is similar to a Hill-sleeve except that motor-based movement requires ATP hydrolysis. Both motor species have been well characterised previously and thus properties such as maximum motor speed, force-speed dependences and stall forces are well known. Therefore a kinetochore-microtubule

binding sleeve is parameterised only by the number of each motor per unit microtubule length. Kinetochore-based force-balance takes into account the net action of motors at the kinetochore-microtubule interface, poleward microtubule flux and microtubule depolymerisation. Microtubule depolymerisation is modelled to be due to the action of the depolymerase motor kinesin-13 (KLP59C). Kinetochore-bound microtubules switch between polymerising and depolymerising states stochastically. The model incorporates feedback-based control of microtubule dynamics by modifying the rates of microtubule state-switching based on the level of tension acting on the kinetochore. Tension-based feedback control has been used in other models such as a model of chromosome congression in budding yeast [133]. Under low tension the rate of switching to a depolymerising state is high and vice versa. Thus within the model a poleward moving kinetochore which is under relatively high tension becomes increasingly more likely to have its microtubules switch to a polymerising state. This property allows kinetochores to remain attached to its microtubules while under tension, consistent with the observations that kinetochore-microtubule attachment improves up to a point with increasing load [46, 88]. Tension-based regulation of kinetochore components is supported by experiment [134]. Human kinesin-13 (MCAK) however has been shown to be activated rather than deactivated under tension [135]. It is unknown whether other depolymerases play a role at the kinetochore, for instance there is some evidence that human kinesin-8 (Kif18a) is a kinetochore-associated microtubule depolymerase although this is still not conclusive [136, 137]. Simulations of the Civelekoglu-Scholey model can qualitatively reproduce chromosome behaviour of Drosophila embryonic spindles during metaphase (where oscillations are rapid with a low amplitude) and anaphase by simply removing the sister-kinetochore connection. Oscillations can be produced with a high kinetochore-bound microtubule turnover rate and a low poleward flux rate, similar to conditions found in budding yeast. However human chromosome dynamics cannot be produced where the kinetochore-bound microtubule turnover rate is relatively low. More critically the role of molecular motors within the model raises serious questions on the model's generality. Experiments on human cells have shown no significant effect on directional switching by the depletion of either CENP-E or MCAK [96]. Experiments have shown however that motors MCAK and Kif18a influence the speed of chromosome oscillations [57, 58, 96]. A modified version of this

model was proposed [138] to describe the observation that in many species, including PtK1 and human cells, during metaphase chromosomes found near the middle of the metaphase plate display oscillatory-type dynamics while those found nearer the edges of the plate show more suppressed oscillations and generally more stochastic dynamics [57, 99]. The model was modified by replacing the molecular motors used as microtubule binding sites with non-motor outer-kinetochore components. Microtubule-binding components are tethered to the kinetochore not by simple elastic springs but by viscoelastic connections *i.e.* a spring in parallel with a dampener. A viscoelastic connection is also used for the sister-kinetochore connection. Molecular motors take on the reduced role of microtubule sliding at the kinetochore. Another necessary feature of the model was a different non-linear PEF acting on central and peripheral chromosomes. The justification for this was that peripheral chromosomes in PtK1 cells are observed to be larger in size compared to central ones [138] therefore present a larger surface area for interaction with microtubules. This model more closely resembles the Joglekar and Hunt model due to the multiple passive microtubule binding sites per microtubule engagement site. The model was able to qualitatively reproduce the spatially dependent range of oscillations observed at the metaphase plate. The model also has the slight advantage over the previous model in that kinetochore-microtubule interactions are not strictly motor-dependent, although the model has not been tested under full depletion of CENP-E or MCAK which as previously stated should only affect oscillation speeds. A radially varying non-linear PEF has not been experimentally observed. The viscoelastic nature of intra- and inter-kinetochore bonds has also not been experimentally tested, the physical properties of which were estimated for the model. The affect on simulated trajectories of taking the limit of the viscoelastic bonds to either full spring-like or dampener-like connections has not been explored. The model could produce inter-kinetochore stretching but could not produce inter-kinetochore oscillations with twice the frequency of chromosome oscillations [96, 100]. The model could also not produce the observed intra-kinetochore stretches observed in PtK1 cells [100]. A reasonable future direction for mechanistic modelling of chromosome-oscillations would be to combine sleeve-like binding sites with molecular motors. Both kinds of models are able to produce oscillations suggesting that merely being able to qualitatively produce directional instability is not sufficient to justify a 'correct' modelling framework.

Models will need to be closely developed in conjunction with experimental data with emphasis on careful perturbation experiments. Model outputs will need to be tested for their dependence on all model parameters. Models that can produce oscillations in different species will need to include conserved components with differing functional dependency.

### 1.4.4 Mechanochemical Feedback Mechanisms

Mechanochemical feedback refers to model components that regulate dynamic properties (such as microtubule (de)polymerisation rates for example) in response to mechanical influences, like the tension across a kinetochore. Experimental evidence suggests that kinetochores contain force-sensitive complexes that regulate microtubule dynamics [139]. Models have been proposed that incorporate feedback mechanisms into models of kinetochore-oscillations [132, 138, 140, 141]. Some models focus solely on chemical feedback [140] *i.e.* ignoring multi-part sources of force at kinetochores. In this model kinetochores engage microtubules and move either poleward or anti-poleward depending on the state of the bound microtubules. Tension sensors at the kinetochore control the rate of microtubule catastrophe. Oscillations produced by this model are highly periodic *i.e.* do not exhibit sawtooth-like motion and do not closely resemble experimental data. More sophisticated models incorporate both chemical feedback and mechanical force-balance such as the two versions of the Civelekoglu-Scholey et al model previously discussed [132, 138]; a more complex feedback system was used in the model by Shtylla and Keener [141]. This model can be thought of as the Joglekar and Hunt [118] model modified with an additional multi-part tension-sensitive chemical feedback mechanism that affects kinetochore-bound microtubule dynamics. The justification for including such tension-sensitive components is that the model attempted to explain kinetochore-oscillations for both bi-orientated and mono-orientated chromosomes; tension-sensors allowed the dynamics to be more robust to transitions between the attachment states [141]. Tension-sensing at kinetochores remains a controversial issue and is a matter of current debate [142]; the main thrust of which is focused however on the question of whether the state of the SAC is regulated by kinetochore tension or by kinetochore-microtubule attachment. Evidence however suggests that kinetochore-

microtubule attachment affinity does respond to tension since *in vitro* kinetochore particles bound to single microtubules have binding lifetimes that vary according to the applied pulling force [46]. Further experimental investigation into tension-sensitive kinetochore components is clearly important to improve the realisation of kinetochore dynamics models.

### 1.4.5 Data-Driven Modelling as a Future Direction for Studying Chromosome Dynamics

Reasonable models of chromosome-oscillations have demonstrated that, as previously stated, two elements are crucial for establishing directional instability: a spatial force gradient biased towards the middle of the cell and a feedback mechanism at the kinetochore. Mechanical load-dependent microtubule-binding feedback as in the model of Joglekar and Hunt [118] and/or mechanochemical feedback as in the models of Civelekoglu-Scholey et al [132, 138] or Shtylla and Keener [141] demonstrate a range of reasonable principle configurations for feedback mechanisms that endow the system with qualitatively realistic characteristic dynamics. Establishing which components of the kinetochore that are essential for oscillatory dynamics requires continued high-throughput experimentation. Given the range of different model systems that can produce qualitatively reasonable oscillations indicates that simply establishing oscillatory dynamics is not sufficient to uniquely identify mechanisms. Given the number of kinetochore proteins that can be depleted without destroying oscillatory dynamics, as previously stated, the system is not minimal. A key question is what are the key characteristics of the dynamics beyond simply directional instability during oscillations and how are these behaviours produced. Most of the experimental work in measuring chromosome dynamics has taken place in marsupial epithelial, newt lung and grasshopper spermatocytes cells that are typically large flat cells and so are ideal for imaging. Measuring chromosome dynamics in human cells is more challenging because of the larger number of kinetochore pairs, their higher density and smaller amplitudes. Given these challenges mathematical models and quantification are required to determine the mechanistic and regulatory processes governing oscillatory dynamics. Models are able to identify concepts whilst a statistical framework to fit models can determine the

level of support for specific mechanisms from experimental data. Model predictions can then be confirmed by perturbation experiments. Here this iterative experiment-modelling programme is implemented using data driven model analysis to extract information from individual trajectories. Given the high stochasticity and inter-trajectory variability large sample sizes of trajectories are essential to both determine levels of heterogeneity in the data and also confidence in the conclusions.

# References


[1] N. Paweletz and W. Flemming. "Walther Flemming: pioneer of mitosis research". In: *Nat. Rev. Mol. Cell Biol.* 2.1 (Jan. 2001), pp. 72–75.

[2] B. Alberts et al. *Molecular Biology of the Cell, Fourth Edition*. New York: Garland Science, 2002.

[3] L. N. Geller and H. Potter. "Chromosome missegregation and trisomy 21 mosaicism in Alzheimer's disease". In: *Neurobiol. Dis.* 6.3 (June 1999), pp. 167–179.

[4] M. Rachidi and C. Lopes. "Molecular and cellular mechanisms elucidating neurocognitive basis of functional impairments associated with intellectual disability in Down syndrome". In: *Am J Intellect Dev Disabil* 115.2 (Mar. 2010), pp. 83–112.

[5] J. M. Schvartzman, R. Sotillo, and R. Benezra. "Mitotic chromosomal instability and cancer: mouse modelling of the human disease". In: *Nat. Rev. Cancer* 10.2 (Feb. 2010), pp. 102–115.

[6] A. Janssen et al. "Chromosome segregation errors as a cause of DNA damage and structural chromosome aberrations". In: *Science* 333.6051 (Sept. 2011), pp. 1895–1898.

[7] A. D. Silk et al. "Chromosome missegregation rate predicts whether aneuploidy will promote or suppress tumors". In: *Proc. Natl. Acad. Sci. U.S.A.* 110.44 (Oct. 2013), E4134–4141.

[8] G. R. Stark and W. R. Taylor. "Analyzing the G2/M checkpoint". In: *Methods Mol. Biol.* 280 (2004), pp. 51–82.

[9] J. Richard McIntosh, Maxim I. Molodtsov, and Fazly I. Ataullakhanov. "Biophysics of mitosis". In: *Quarterly Reviews of Biophysics* 45 (02 May 2012), pp. 147–207.

[10] S Gadde and R Heald. "Mechanisms and molecules of the mitotic spindle". In: *Curr Biol* 14.18 (Sept. 2004). 0960-9822 (Print) Journal Article Review, R797–805.

[11] S. Meunier and I. Vernos. "Microtubule assembly during mitosis - from distinct origins to distinct functions?" In: *J. Cell. Sci.* 125.Pt 12 (June 2012), pp. 2805–2814.

[12] K. J. Helmke, R. Heald, and J. D. Wilbur. "Interplay between spindle architecture and function". In:

*Int Rev Cell Mol Biol* 306 (2013), pp. 83–125.

[13] R. C. Weisenberg. "Microtubule formation in vitro in solutions containing low calcium concentrations". In: *Science* 177.4054 (Sept. 1972), pp. 1104–1105.

[14] D. Chretien et al. "Lattice defects in microtubules: protofilament numbers vary within individual microtubules". In: *J. Cell Biol.* 117.5 (June 1992), pp. 1031–1040.

[15] R. A. Walker et al. "Dynamic instability of individual microtubules analyzed by video light microscopy: rate constants and transition frequencies". In: *J. Cell Biol.* 107.4 (Oct. 1988), pp. 1437–1448.

[16] R. C. Weisenberg, W. J. Deery, and P. J. Dickinson. "Tubulin-nucleotide interactions during the polymerization and depolymerization of microtubules". In: *Biochemistry* 15.19 (Sept. 1976), pp. 4248–4254.

[17] Tim Mitchison and Marc Kirschner. "Dynamic instability of microtubule growth". In: *Nature* 312.5991 (Nov. 15, 1984), pp. 237–242.

[18] M. Bettencourt-Dias and D. M. Glover. "Centrosome biogenesis and function: centrosomics brings new understanding". In: *Nat. Rev. Mol. Cell Biol.* 8.6 (June 2007), pp. 451–463.

[19] I A Vorobjev and Chentsov YuS. "Centrioles in the cell cycle. I. Epithelial cells." In: *The Journal of Cell Biology* 93.3 (1982), pp. 938–949.

[20] A. Khodjakov and C. L. Rieder. "The sudden recruitment of gamma-tubulin to the centrosome at the onset of mitosis and its dynamic exchange throughout the cell cycle, do not require microtubules". In: *J. Cell Biol.* 146.3 (Aug. 1999), pp. 585–596.

[21] K. K. Sarangapani and C. L. Asbury. "Catch and release: how do kinetochores hook the right microtubules during mitosis?" In: *Trends Genet.* 30.4 (Apr. 2014), pp. 150–159.

[22] Ajit P Joglekar, Kerry S Bloom, and Ed Salmon. "Mechanisms of force generation by end-on kinetochore-microtubule attachments". In: *Curr Opin Cell Biol* (Jan. 2010).

[23] M. Winey and K. Bloom. "Mitotic spindle form and function". In: *Ge-*

*netics* 190.4 (Apr. 2012), pp. 1197–1224.

[24] Kuniyoshi Kaseda, Andrew D McAinsh, and Robert A Cross. "Walking, hopping, diffusing and braking modes of kinesin-5". In: *Biochem Soc Trans* 37.Pt 5 (Oct. 2009), pp. 1045–9.

[25] C. L. Rieder. "The formation, structure, and composition of the mammalian kinetochore and kinetochore fiber". In: *Int. Rev. Cytol.* 79 (1982), pp. 1–58.

[26] Stella M. Hurtley. "Spindle Positioning". In: *Science* 299.5615 (2003), p. 1949.

[27] J Tirnauer et al. "EB1 targets to kinetochores with attached, polymerizing microtubules". In: *Mol Biol Cell* 13.12 (Dec. 2002). 1059-1524 (Print) Journal Article, pp. 4308–16.

[28] D Cleveland, Y Mao, and K Sullivan. "Centromeres and kinetochores: from epigenetics to mitotic checkpoint signaling". In: *Cell* 112.4 (Feb. 2003). 0092-8674 (Print) Journal Article Review, pp. 407–21.

[29] Andrew D McAinsh, Jessica D Tytell, and Peter K Sorger. "Structure, function, and regulation of budding yeast kinetochores". In: *Annu Rev Cell Dev Biol* 19 (Jan. 2003), pp. 519–39.

[30] S Santaguida and A Musacchio. "The life and miracles of kinetochores". In: *Embo J* (July 2009).

[31] Jonas F Dorn and Paul S Maddox. "Kinetochore dynamics: how protein dynamics affect chromosome segregation". In: *Current Opinion in Cell Biology* 24.1 (Feb. 2012), pp. 57–63.

[32] Gary H Karpen and Robin C Allshire. "The case for epigenetic effects on centromere identity and function". In: *Trends in genetics : TIG*. Elsevier Trends Journals, Dec. 1997, pp. 489–496.

[33] P Hemmerich et al. "Dynamics of inner kinetochore assembly and maintenance in living cells". In: *The Journal of Cell Biology* 180.6 (Mar. 2008), pp. 1101–1114.

[34] Tetsuya Hori et al. "CCAN makes multiple contacts with centromeric DNA to provide distinct pathways to the outer kinetochore". In: *Cell* 135.6 (Dec. 2008), pp. 1039–52.

[35] Christopher W Carroll, Kirstin J Milks, and Aaron F Straight. "Dual recognition of CENP-A nucleosomes is required for centromere as-

sembly". In: *J Cell Biol* 189.7 (June 2010), pp. 1143–55.

[36] K. E. Gascoigne and I. M. Cheeseman. "T time for point centromeres". In: *Nat. Cell Biol.* 14.6 (June 2012), pp. 559–561.

[37] Tatsuya Nishino et al. "CENP-T-W-S-X forms a unique centromeric chromatin structure with a histone-like fold." In: *Cell* 148.3 (Feb. 2012), pp. 487–501.

[38] Tetsuya Hori et al. "CCAN Makes Multiple Contacts with Centromeric DNA to Provide Distinct Pathways to the Outer Kinetochore ". In: *Cell* 135.6 (Dec. 2008), pp. 1039–1052.

[39] Karen E Gascoigne et al. "Induced ectopic kinetochore assembly bypasses the requirement for CENP-A nucleosomes." In: *Cell* 145.3 (Apr. 2011), pp. 410–422.

[40] D. Fachinetti et al. "A two-step mechanism for epigenetic specification of centromere identity and function". In: *Nat. Cell Biol.* 15.9 (Sept. 2013), pp. 1056–1066.

[41] Emanuela Screpanti et al. "Direct Binding of Cenp-C to the Mis12 Complex Joins the Inner and Outer Kinetochore". In: *Current Biology* 21.5 (Mar. 2011), pp. 391–398.

[42] Tatsuya Nishino et al. "CENP-T provides a structural platform for outer kinetochore assembly." In: *The EMBO Journal* 32.3 (Feb. 2013), pp. 424–436.

[43] Gregory M Alushin et al. "The Ndc80 kinetochore complex forms oligomeric arrays along microtubules". In: *Nature* 467.7317 (Oct. 2010), pp. 805–10.

[44] Iain M Cheeseman et al. "The Conserved KMN Network Constitutes the Core Microtubule-Binding Site of the Kinetochore". In: *Cell* 127.5 (Dec. 2006). 0092-8674 (Print) Journal Article, pp. 983–97.

[45] Ronnie R Wei et al. "Structure of a central component of the yeast kinetochore: the Spc24p/Spc25p globular domain". In: *Structure* 14.6 (June 2006), pp. 1003–9.

[46] Bungo Akiyoshi et al. "Tension directly stabilizes reconstituted kinetochore-microtubule attachments". In: *Nature* 468.7323 (Nov. 2010), pp. 576–9.

[47] Thomas J Maresca and Edward D Salmon. "Intrakinetochore stretch is associated with changes in kinetochore phosphorylation and spindle assembly checkpoint activity".

In: *J Cell Biol* 184.3 (Feb. 2009), pp. 373–81.

[48] K Uchida et al. "Kinetochore stretching inactivates the spindle assembly checkpoint". In: *J Cell Biol* 184.3 (Feb. 2009), pp. 383–390.

[49] D. Varma and E. D. Salmon. "The KMN protein network–chief conductors of the kinetochore orchestra". In: *J. Cell. Sci.* 125.Pt 24 (Dec. 2012), pp. 5927–5936.

[50] A. Hanisch, H. H. Sillje, and E. A. Nigg. "Timely anaphase onset requires a novel spindle and kinetochore complex comprising Ska1 and Ska2". In: *EMBO J.* 25.23 (Nov. 2006), pp. 5504–5515.

[51] T. N. Gaitanos et al. "Stable kinetochore-microtubule interactions depend on the Ska complex and its new component Ska3/C13Orf3". In: *EMBO J.* 28.10 (May 2009), pp. 1442–1452.

[52] J. R. Daum et al. "Ska3 is required for spindle checkpoint silencing and the maintenance of chromosome cohesion in mitosis". In: *Curr. Biol.* 19.17 (Sept. 2009), pp. 1467–1472.

[53] J. A. Raaijmakers et al. "RAMA1 is a novel kinetochore protein involved in kinetochore-microtubule attachment". In: *J. Cell. Sci.* 122.Pt 14 (July 2009), pp. 2436–2445.

[54] M. Theis et al. "Comparative profiling identifies C13orf3 as a component of the Ska complex required for mammalian cell division". In: *EMBO J.* 28.10 (May 2009), pp. 1453–1465.

[55] Julie P I Welburn et al. "The human kinetochore Ska1 complex facilitates microtubule depolymerization-coupled motility". In: *Dev Cell* 16.3 (Mar. 2009), pp. 374–85.

[56] M. A. Abad et al. "Structural basis for microtubule recognition by the human kinetochore Ska complex". In: *Nat Commun* 5 (Jan. 2014), p. 2964.

[57] Jason Stumpff et al. "The Kinesin-8 Motor Kif18A Suppresses Kinetochore Movements to Control Mitotic Chromosome Alignment". In: *Dev Cell* 14.2 (Feb. 2008), pp. 252–62.

[58] L. Wordeman, M. Wagenbach, and G. von Dassow. "MCAK facilitates chromosome movement by promoting kinetochore microtubule turnover". In: *J. Cell Biol.* 179.5 (Dec. 2007), pp. 869–879.

[59] Ana C Amaro et al. "Molecular control of kinetochore-microtubule dynamics and chromosome oscillations". In: *Nat Cell Biol* (Mar. 2010).

[60] Nunu McHedlishvili et al. "Kinetochores accelerate centrosome separation to ensure faithful chromosome segregation." In: *Journal of Cell Science* (Mar. 2012).

[61] R. Thadani, F. Uhlmann, and S. Heeger. "Condensin, chromatin crossbarring and chromosome condensation". In: *Curr. Biol.* 22.23 (Dec. 2012), R1012–1021.

[62] Ilaria Piazza, Christian H Haering, and Anna Rutkowska. "Condensin: crafting the chromosome landscape". In: *Chromosoma* 122.3 (Apr. 2013), pp. 175–190.

[63] D. F. Hudson et al. "Condensin is required for nonhistone protein assembly and structural integrity of vertebrate mitotic chromosomes". In: *Dev. Cell* 5.2 (Aug. 2003), pp. 323–336.

[64] A. D. Stephens et al. "Cohesin, condensin, and the intramolecular centromere loop together generate the mitotic chromatin spring". In: *J. Cell Biol.* 193.7 (June 2011), pp. 1167–1180.

[65] A. R. Ball et al. "Identification of a chromosome-targeting domain in the human condensin subunit CNAP1/hCAP-D2/Eg7". In: *Mol. Cell. Biol.* 22.16 (Aug. 2002), pp. 5769–5781.

[66] Wen Liu et al. "PHF8 mediates histone H4 lysine 20 demethylation events involved in cell cycle progression". In: *Nature* 466.7305 (July 2010), pp. 508–512.

[67] Sara Cuylen, Jutta Metz, and Christian H Haering. "Condensin structures chromosomal DNA through topological links". In: *Nature Structural & Molecular Biology* 18.8 (July 2011), pp. 894–901.

[68] Yasuto Murayama and Frank Uhlmann. "Biochemical reconstitution of topological DNA binding by the cohesin ring". In: *Nature* (Dec. 2013), pages.

[69] Andrew J Wood, Aaron F Severson, and Barbara J Meyer. "Condensin and cohesin complexity: the expanding repertoire of functions." In: *Nature Reviews Genetics* 11.6 (June 2010), pp. 391–404.

[70] Jan-Michael Peters, Antonio Tedeschi, and Julia Schmitz. "The cohesin complex and its roles in chromosome biology." In: *Genes*

*& Development* 22.22 (Nov. 2008), pp. 3089–3114.

[71] C. Acquaviva and J. Pines. "The anaphase-promoting complex/cyclosome: APC/C". In: *J. Cell. Sci.* 119.Pt 12 (June 2006), pp. 2401–2404.

[72] Emily A Foley and Tarun M Kapoor. "Microtubule attachment and spindle assembly checkpoint signalling at the kinetochore". In: *Nature Reviews Molecular Cell Biology* 14.1 (Dec. 2012), pp. 25–37.

[73] W. C. Chao et al. "Structure of the mitotic checkpoint complex". In: *Nature* 484.7393 (Apr. 2012), pp. 208–213.

[74] Y. Yamagishi et al. "MPS1/Mph1 phosphorylates the kinetochore protein KNL1/Spc7 to recruit SAC components". In: *Nat. Cell Biol.* 14.7 (July 2012), pp. 746–752.

[75] M. W. Moyle et al. "A Bub1-Mad1 interaction targets the Mad1-Mad2 complex to unattached kinetochores to initiate the spindle checkpoint". In: *J. Cell Biol.* 204.5 (Mar. 2014), pp. 647–657.

[76] A. Ciliberto and J. V. Shah. "A quantitative systems view of the spindle assembly checkpoint". In: *EMBO J.* 28.15 (Aug. 2009), pp. 2162–2173.

[77] A. E. Dick and D. W. Gerlich. "Kinetic framework of spindle assembly checkpoint signalling". In: *Nat. Cell Biol.* 15.11 (Nov. 2013), pp. 1370–1377.

[78] P. Collin et al. "The spindle assembly checkpoint works like a rheostat rather than a toggle switch". In: *Nat. Cell Biol.* 15.11 (Nov. 2013), pp. 1378–1385.

[79] F. Zernike. "How I Discovered Phase Contrast". In: *Science* 121.3141 (1955), pp. 345–349.

[80] WH Lewis. "Changes of viscosity and cell activity". In: *Science* (1939).

[81] A Hughes and MM Swann. "Anaphase movements in the living cell". In: *Journal of Experimental Biology* (Jan. 1948).

[82] Jacques Padawer. "The Nomarski interference-contrast microscope. An experimental basis for image interpretation*". In: *Journal of the Royal Microscopical Society* 88.3 (1968), pp. 305–349.

[83] T. Seto, J. Kezer, and C. M. Pomerat. "A cinematographic study of meiosis in salamander spermatocytes in vitro". In: *Z Zell-*

*forsch Mikrosk Anat* 94.3 (1969), pp. 407–424.

[84] A. Bajer and J. Mole-Bajer. "Lateral movements in the spindle and the mechanism of mitosis". In: *Soc. Gen. Physiol. Ser.* 30 (1975), pp. 77–98.

[85] U. P. Roos. "Light and electron microscopy of rat kangaroo cells in mitosis. III. Patterns of chromosome behavior during prometaphase". In: *Chromosoma* 54.4 (Mar. 1976), pp. 363–385.

[86] A. S. Bajer. "Functional autonomy of monopolar spindle and evidence for oscillatory movement in mitosis". In: *J. Cell Biol.* 93.1 (Apr. 1982), pp. 33–48.

[87] H Fuge. "Oscillatory movements of bipolar-oriented bivalent kinetochores and spindle forces in male meiosis of Mesostoma ehrenbergii". In: *European Journal of Cell Biology* (1987).

[88] R. B. Nicklas. "The forces that move chromosomes in mitosis". In: *Annu Rev Biophys Biophys Chem* 17 (1988), pp. 431–449.

[89] H Fuge. "Rapid kinetochore movements in Mesostoma ehrenbergii spermatocytes: Action of antagonistic chromosome fibres". In: *Cell Motility and the Cytoskeleton* 13.3 (1989), pp. 212–220.

[90] R. V. Skibbens, V. P. Skeen, and E. D. Salmon. "Directional instability of kinetochore motility during chromosome congression and segregation in mitotic newt lung cells: a push-pull mechanism". In: *J Cell Biol* 122.4 (Aug. 1993), pp. 859–75.

[91] R.V. Skibbens, C.L. Rieder, and E.D. Salmon. "Kinetochore motility after severing between sister centromeres using laser microsurgery: evidence that kinetochore directional instability and position is regulated by tension". In: *Journal of Cell Science* 108.7 (1995), pp. 2537–2548.

[92] B. R. Brinkley and E. Stubblefield. "The fine structure of the kinetochore of a mammalian cell in vitro". In: *Chromosoma* 19.1 (1966), pp. 28–43.

[93] D. E. Koshland, T. J. Mitchison, and M. W. Kirschner. "Polewards chromosome movement driven by microtubule depolymerization in vitro". In: *Nature* 331.6156 (Feb. 1988), pp. 499–504.

[94] A. Akhmanova and C. C. Hoogenraad. "Microtubule plus-end-tracking proteins: mechanisms and

functions". In: *Curr. Opin. Cell Biol.* 17.1 (Feb. 2005), pp. 47–54.

[95] M. Schuh and J. Ellenberg. "Self-organization of MTOCs replaces centrosome function during acentrosomal spindle assembly in live mouse oocytes". In: *Cell* 130.3 (Aug. 2007), pp. 484–498.

[96] Khuloud Jaqaman et al. "Kinetochore alignment within the metaphase plate is regulated by centromere stiffness and microtubule depolymerases". In: *J Cell Biol* 188.5 (Mar. 2010), pp. 665–79.

[97] T. S. Kitajima, M. Ohsugi, and J. Ellenberg. "Complete kinetochore tracking reveals error-prone homologous chromosome biorientation in mammalian oocytes". In: *Cell* 146.4 (Aug. 2011), pp. 568–581.

[98] V. Magidson et al. "The spatial arrangement of chromosomes during prometaphase facilitates spindle assembly". In: *Cell* 146.4 (Aug. 2011), pp. 555–567.

[99] Xiaohu Wan et al. "The coupling between sister kinetochore directional instability and oscillations in centromere stretch in metaphase PtK1 cells." In: *Molecular biology of the cell* (Feb. 2012).

[100] S. Dumont, E. D. Salmon, and T. J. Mitchison. "Deformations within moving kinetochores reveal different sites of active and passive force generation". In: *Science* 337.6092 (July 2012), pp. 355–358.

[101] D Thomann et al. "Automatic fluorescent tag detection in 3D with super-resolution: application to the analysis of chromosome movement." In: *Journal of microscopy* 208.Pt 1 (Oct. 2002), pp. 49–64.

[102] D. Thomann et al. "Automatic fluorescent tag localization II: Improvement in super-resolution by relative tracking". In: *J Microsc* 211.Pt 3 (Sept. 2003), pp. 230–248.

[103] J. F. Dorn et al. "Yeast kinetochore microtubule dynamics analyzed by high-resolution three-dimensional microscopy". In: *Biophys. J.* 89.4 (Oct. 2005), pp. 2835–2854.

[104] K. Jaqaman et al. "Comparative autoregressive moving average analysis of kinetochore microtubule dynamics in yeast". In: *Biophys. J.* 91.6 (Sept. 2006), pp. 2312–2325.

[105] K. Jaqaman et al. "Phenotypic clustering of yeast mutants based on kinetochore microtubule dynam-

ics". In: *Bioinformatics* 23.13 (July 2007), pp. 1666–1673.

[106] X. Wan et al. "Protein architecture of the human kinetochore microtubule attachment site". In: *Cell* 137.4 (May 2009), pp. 672–684.

[107] J. C. Waters et al. "Localization of Mad2 to kinetochores depends on microtubule attachment, not tension". In: *J. Cell Biol.* 141.5 (June 1998), pp. 1181–1191.

[108] P. Clute and J. Pines. "Temporal and spatial control of cyclin B1 destruction in metaphase". In: *Nat. Cell Biol.* 1.2 (June 1999), pp. 82–87.

[109] D. Varma et al. "Spindle assembly checkpoint proteins are positioned close to core microtubule attachment sites at kinetochores". In: *J. Cell Biol.* 202.5 (Sept. 2013), pp. 735–746.

[110] E. Vladimirou et al. "Springs, clutches and motors: driving forward kinetochore mechanism by modelling". In: *Chromosome Res.* 19.3 (Apr. 2011), pp. 409–421.

[111] J. Loncarek et al. "The centromere geometry essential for keeping mitosis error free is controlled by spindle forces". In: *Nature* 450.7170 (Nov. 2007), pp. 745–749.

[112] D. J. Sharp, G. C. Rogers, and J. M. Scholey. "Microtubule motors in mitosis". In: *Nature* 407.6800 (Sept. 2000), pp. 41–47.

[113] T. M. Kapoor and D. A. Compton. "Searching for the middle ground: mechanisms of chromosome alignment during mitosis". In: *J. Cell Biol.* 157.4 (May 2002), pp. 551–556.

[114] S. Dumont and T. J. Mitchison. "Force and length in the mitotic spindle". In: *Curr. Biol.* 19.17 (Sept. 2009), R749–761.

[115] J. Howard. "Elastic and damping forces generated by confined arrays of dynamic microtubules". In: *Phys Biol* 3.1 (Mar. 2006), pp. 54–66.

[116] A. Mogilner and G. Oster. "Force generation by actin polymerization II: the elastic ratchet and tethered filaments". In: *Biophys. J.* 84.3 (Mar. 2003), pp. 1591–1605.

[117] E. N. Cytrynbaum, J. M. Scholey, and A. Mogilner. "A force balance model of early spindle pole separation in Drosophila embryos". In: *Biophys. J.* 84.2 Pt 1 (Feb. 2003), pp. 757–769.

[118] Ajit P Joglekar and Alan J Hunt. "A simple, mechanistic model for directional instability during mi-

totic chromosome movements". In: *Biophysical Journal* 83.1 (July 2002), pp. 42–58.

[119] M. K. Gardner and D. J. Odde. "Modeling of chromosome motility during mitosis". In: *Curr. Opin. Cell Biol.* 18.6 (Dec. 2006), pp. 639–647.

[120] T L Hill. "Theoretical problems related to the attachment of microtubules to kinetochores". In: *Proc Natl Acad Sci USA* 82.13 (July 1985), pp. 4404–8.

[121] B. R. Brinkley, I. Ouspenski, and R. P. Zinkowski. "Structure and molecular organization of the centromere-kinetochore complex". In: *Trends Cell Biol.* 2.1 (Jan. 1992), pp. 15–21.

[122] K. Johnston et al. "Vertebrate kinetochore protein architecture: protein copy number". In: *J. Cell Biol.* 189.6 (June 2010), pp. 937–943.

[123] A. F. Powers et al. "The Ndc80 kinetochore complex forms load-bearing attachments to dynamic microtubule tips via biased diffusion". In: *Cell* 136.5 (Mar. 2009), pp. 865–875.

[124] H. Maiato et al. "The dynamic kinetochore-microtubule interface". In: *J. Cell. Sci.* 117.Pt 23 (Nov. 2004), pp. 5461–5477.

[125] E. D. Salmon and D. A. Begg. "Functional implications of cold-stable microtubules in kinetochore fibers of insect spermatocytes during anaphase". In: *J. Cell Biol.* 85.3 (June 1980), pp. 853–865.

[126] Y. Zhai, P. J. Kronebusch, and G. G. Borisy. "Kinetochore microtubule dynamics and the metaphase-anaphase transition". In: *J. Cell Biol.* 131.3 (Nov. 1995), pp. 721–734.

[127] CL Rieder and ED Salmon. "Motile kinetochores and polar ejection forces dictate chromosome position on the vertebrate mitotic spindle". In: *The Journal of Cell Biology* 124.3 (1994), pp. 223–233.

[128] A Khodjakov and C L Rieder. "Kinetochores moving away from their associated pole do not exert a significant pushing force on the chromosome." In: *The Journal of Cell Biology* 135.2 (1996), pp. 315–327.

[129] A. Toso et al. "Kinetochore-generated pushing forces separate centrosomes during bipolar spindle assembly". In: *J. Cell Biol.* 184.3 (Feb. 2009), pp. 365–372.

[130] K. Ke, J. Cheng, and A. J. Hunt. "The distribution of polar ejection forces determines the amplitude of chromosome directional instability". In: *Curr. Biol.* 19.10 (May 2009), pp. 807–815.

[131] D. Cimini et al. "Aurora kinase promotes turnover of kinetochore microtubules to reduce chromosome segregation errors". In: *Curr. Biol.* 16.17 (Sept. 2006), pp. 1711–1718.

[132] G Civelekoglu-Scholey et al. "Model of chromosome motility in Drosophila embryos: adaptation of a general mechanism for rapid mitosis". In: *Biophysical Journal* 90.11 (June 2006), pp. 3966–3982.

[133] M. K. Gardner et al. "Tension-dependent regulation of microtubule dynamics at kinetochores can explain metaphase congression in yeast". In: *Mol. Biol. Cell* 16.8 (Aug. 2005), pp. 3764–3775.

[134] M. A. Lampson and I. M. Cheeseman. "Sensing centromere tension: Aurora B and the regulation of kinetochore function". In: *Trends Cell Biol.* 21.3 (Mar. 2011), pp. 133–140.

[135] G. J. Gorbsky. "Mitosis: MCAK under the aura of Aurora B". In: *Curr. Biol.* 14.9 (May 2004), R346–348.

[136] M. I. Mayr et al. "The human kinesin Kif18A is a motile microtubule depolymerase essential for chromosome congression". In: *Curr. Biol.* 17.6 (Mar. 2007), pp. 488–498.

[137] Y. Du, C. A. English, and R. Ohi. "The kinesin-8 Kif18A dampens microtubule plus-end dynamics". In: *Curr. Biol.* 20.4 (Feb. 2010), pp. 374–380.

[138] G. Civelekoglu-Scholey et al. "Dynamic bonds and polar ejection force distribution explain kinetochore oscillations in PtK1 cells". In: *J. Cell Biol.* 201.4 (May 2013), pp. 577–593.

[139] P. D. Andrews et al. "Aurora B regulates MCAK at the mitotic centromere". In: *Dev. Cell* 6.2 (Feb. 2004), pp. 253–268.

[140] Jian Liu et al. "An integrated mechanobiochemical feedback mechanism describes chromosome motility from prometaphase to anaphase in mitosis". In: *Proceedings of the National Academy of Sciences of the United States of America* 105.37 (Sept. 2008), pp. 13752–13757.

[141] Blerta Shtylla and James P Keener. "A mechanomolecular model for the movement of chromosomes during mitosis driven by a minimal kinetochore bicyclic cascade". In: *Journal of theoretical biology* 263.4 (Apr. 2010), pp. 455–470.

[142] A. Khodjakov and J. Pines. "Centromere tension: a divisive issue". In: *Nat. Cell Biol.* 12.10 (Oct. 2010), pp. 919–923.

# Chapter 2

# Experimental Methods

## 2.1 Cell Culture

A human cell line, HeLa-K was used as a model system expressing enhanced green fluorescent protein (eGFP) fused to kinetochores and/or centrioles as a fluorescent marker. HeLa-K cells stably expressing eGFP - CENP-A and eGFP - Centrin1 (a gift from Patrick Meraldi, University of Geneva) [60] or eGFP - CENP-A [96] (its parental cell line) were grown in Dulbecco's modified Eagle's medium (DMEM) (Fisher) containing 10% foetal calf serum (FCS) (Fisher) and 1% Penicillin-Streptomycin solution (Fisher) maintained in atmospheric conditions of 10% $CO_2$ at 37 °C. eGFP - CENP-A over-expression was maintained by a supplement of 0.1$\mu$g/ml Puromycin (Fisher) added to the cell media. eGFP-Centrin1 over-expression was maintained by a supplement of 500$\mu$g/ml Geneticin (Fisher) added to the cell media. Cells were grown in 10ml of DMEM in 10cm dishes (Fisher). When at or near 100% confluency cells were split from their dish and seeded into another 10cm dish (maintaining an active cell line) and also seeded into 35mm glass bottom dishes (MatTek Corporation) for imaging experiments if required. Cells were split by first removing their current media then washing the cells twice with 10ml sterile phosphate buffered saline solution (PBS). The cells were then incubated with 3ml of trypsin (Invitrogen) at 37 °C for 5 min in order to detach the cells from the dish surface. 7ml of DMEM was then added to the dish and the trypsin/DMEM mixture was washed over the dish surface several times to ensure as many cells as possible were detached and mixed into the media at a uniform

density. This mixture was used to seed a new 10cm dish at an appropriate ratio with fresh media for a desired confluency (*e.g.* 1ml of cells plus 9ml of new media would give a new dish at approximately 10% confluency). The desired confluency of the new dish was selected to control the time at which the cells could next be split (controlling the time when cells dishes would be ready for experiments for example). The cell mixture was also used to seed imaging dishes at an appropriate confluency depending on how long after seeding imaging was to take place and/or on further experimental protocols (see below); *e.g.* for imaging untreated cells 0.5ml of cells would be seeded along with 1ml fresh media to be imaged 48 hours later.

## 2.2 Short Interfering RNA Transfection and Drug Treatments

For short interfering RNA (siRNA) transfection experiments 80$\mu$l of 100% confluent cells were seeded in imaging dishes along with 1.5ml of fresh DMEM. 24 hours later media was changed to 1ml minimum essential media (MEM) (Fisher) containing 10% FCS. Each dish was treated with a siRNA mixture consisting of 124$\mu$l Optimem (Fisher), 6$\mu$l Oligofectamine (Fisher) and 3$\mu$l RNA solution at 20$\mu$M. The siRNA mixture was created by first mixing 100$\mu$l of Optimem with the RNA solution while separately mixing 24$\mu$l of Optimem with the Oligofectamine. After 8 min at room temperature the two mixtures were combined and left to incubate for a further 25 min at room temperature. Dishes were incubated with the siRNA mixture for 24 hours after which the media was changed back to DMEM. 24 hours later the cells were either ready for imaging or further drug treatment (see below). The siRNA oligonucleotides used were the 'scramble' custom RNA sequence for siRNA control [143], a siRNA against Nuf2 [144] and a siRNA against CAPD2 [96] (Qiagen). For microtubule depolymerisation experiments cells were treated with 2$\mu$g/ml Nocodazole (Fisher) (Methyl (5-[2-thienylcarbonyl]-1H-benzimidazol-2-yl) [145] and incubated for between 16 and 24 hours before imaging.

## 2.3 Live Cell Imaging

Before imaging cell media was changed to 1ml $CO_2$ independent Leibovitz L-15 (Fisher) supplemented with 10% FCS and 1% Penicillin-Streptomycin solution. Cells were imaged using a 100X 1.4 NA objective on a confocal spinning-disk microscope (VOX Ultraview; Perkin and Elmer) fitted with an environmental chamber maintained at 37 °C controlled by Volocity 6.0 (Perkin and Elmer) running on a Windows 7 64bit (Microsoft) PC (IBM). Cells were located by brightfield. For time-series collection laser power (488nm) was set to 15% and the camera (ORCA-R2; Hamamatsu) was set to 2x2 pixel binning (138nm x 138nm), a 16 bits per pixel imaging depth and an exposure time of 50ms. The time-lapse was set to 2 sec per frame with a total experiment time of 5 min. For imaging cells with metaphase plates the Z range was set to 12$\mu$m with a step size of 0.5$\mu$m. For imaging cells without metaphase plates (Nocodazole treated and Nuf2 siRNA treated cells) the Z range was set to 6$\mu$m with a step size of 0.2$\mu$m. Imaging conditions were chosen by adjusting parameters (exposure time, laser power, total imaging time) until it was found that over 90% of imaged cells went on to complete anaphase either during or within approximately 30 minutes after imaging (see Figure 2.1).

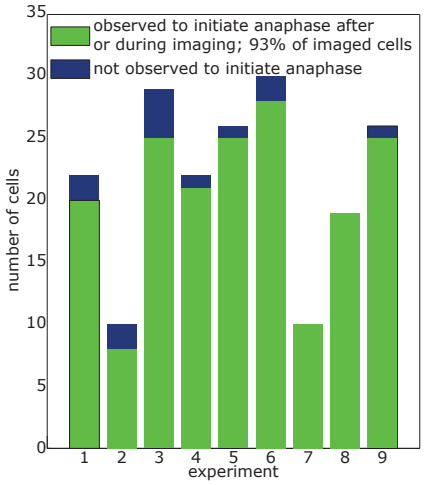


**Figure 2.1:** Cell anaphase progression. Number of cells that were and were not observed to successfully complete anaphase.

## 2.4 Image Pre-Processing

All image pre-processing of confocal images was performed on an OSX 10.6 Power-Mac (Apple). First images were exported from their native Volocity format to .OME.TIFFs (The Open Microscopy Environment) using Volocity 6.0 before further processing. Images were next deconvolved with Huygens 4.1 (SVI) using the 'classic maximum likelihood estimation (CMLE)' algorithm using a point spread function (PSF) measured from micro-bead images (see below). Processed images were exported from Huygens to a .r3d format (Applied Precision) and then read into MATLAB (The Mathworks) using the loci-tools Java library (The Open Microscopy Environment). Images were then stored in a native MATLAB format.

### 2.4.1 System Point Spread Function Measurements

Microscope point spread functions were measured for the Ultraview microscope using images of 200nm diameter micro-beads (Fisher). A bead slide was imaged by setting the camera to 1x1 binning (69nm x 69nm) and a 16 bits per pixel imaging depth. Exposure times and laser powers (488nm laser) were set manually for maximum observed image quality. Z step size was set to 69nm. The Z-range was set as to capture as many beads as possible. Point spread functions were measured for the 488nm channel using the Huygens 'PSF distiller' averaging over $> 20$ beads. The PSF templates were then saved in Huygens (.h5) format to be used for image deconvolution.

### 2.4.2 Live Cell Image Processing

All images collected from single imaging sessions were processed in batch using the Huygens batch processor along with MATLAB and Python scripting. A generic deconvolution template was created with the Huygens batch processor for a single image using the measured PSF. For batch processing a selection of .OME.TIFFs was made using MATLAB, a MATLAB program would read the metadata from each image using the loci-tools Java plugin and save the pixel sizes. MATLAB would then pass this information to a Python program that would create a custom batch deconvolution script based on the generic template, with the correct pixel sizes set for each image. The

Huygens batch processor would then be automatically launched, reading in the custom batch script and starting the deconvolution jobs. When all the jobs were complete the MATLAB program would continue, reading in the processed image data again using the loci-tools Java plugin. Figure 2.2 shows an example of a live cell movie frame before and after deconvolution.

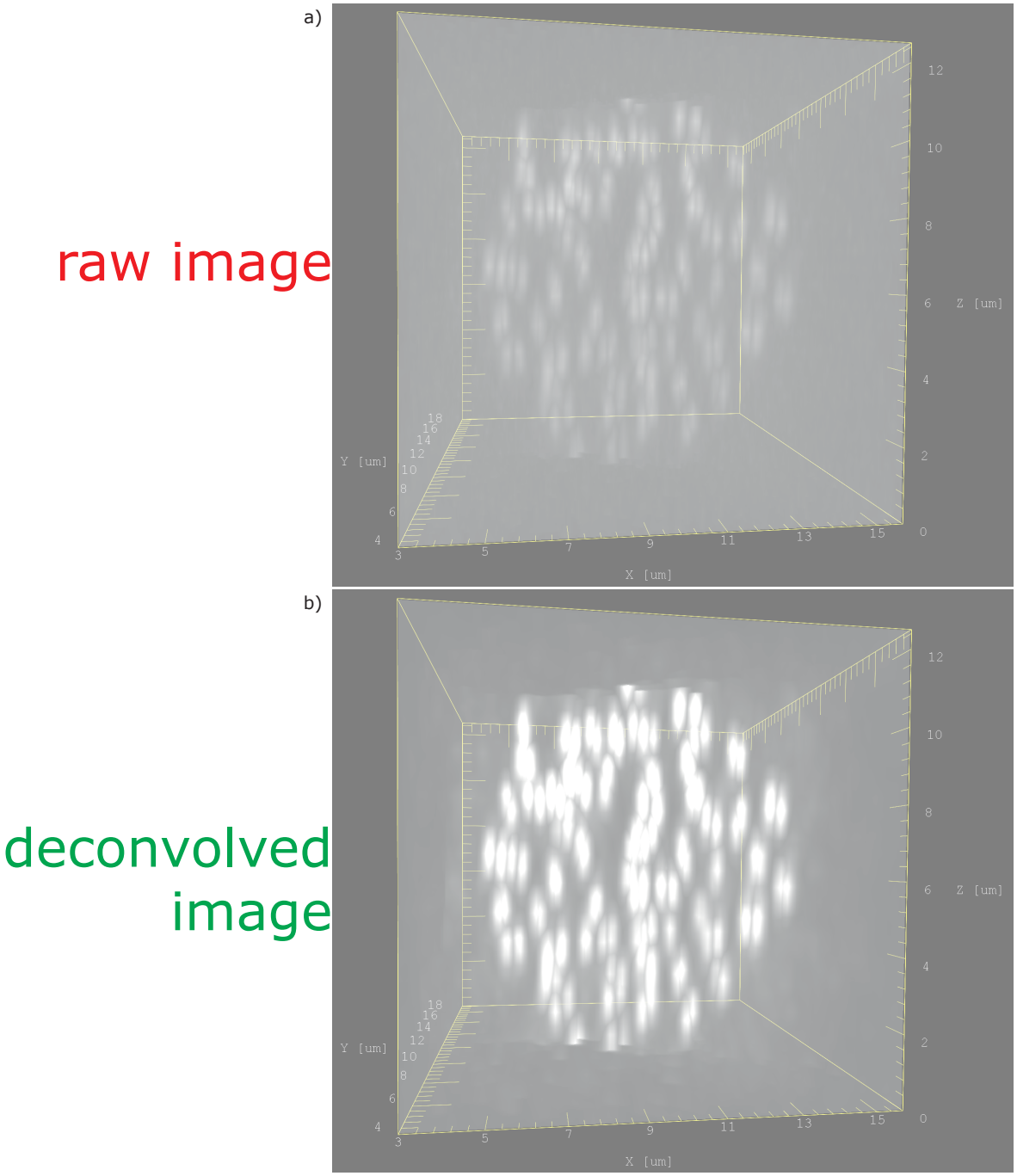


**Figure 2.2:** Deconvolution of confocal spinning-disk images. **a)** Confocal spinning-disk raw image frame (rendered in 3D) of a HeLa-K eGFP - CENP-A eGFP - Centrin1 cell. Image consists of $130 \times 160 \times 25$ voxels in X, Y, Z respectively. Voxel dimensions = $\{0.138, 0.500\}$ $\mu$m in $\{\mathrm{X/Y, Z}\}$ respectively. **b)** Deconvolved image (rendered in 3D). Deconvolution performed as described in Section 2.4.

# References

[60] Nunu McHedlishvili et al. "Kinetochores accelerate centrosome separation to ensure faithful chromosome segregation." In: *Journal of Cell Science* (Mar. 2012).

[96] Khuloud Jaqaman et al. "Kinetochore alignment within the metaphase plate is regulated by centromere stiffness and microtubule depolymerases". In: *J Cell Biol* 188.5 (Mar. 2010), pp. 665–79.

[143] Samora CP et al. "MAP4 and CLASP1 operate as a safety mechanism to maintain a stable spindle position in mitosis". In: *Nature Cell Biology* (2011).

[144] Patrick Meraldi, Viji M Draviam, and Peter K Sorger. "Timing and Checkpoints in the Regulation of Mitotic Progression". In: *Developmental Cell* 7.1 (2004), pp. 45–60.

[145] Richard F Luduena and Mary C Roach. "Tubulin sulfhydryl groups as probes and targets for antimitotic and antimicrotubule agents". In: *Pharmacology & Therapeutics* 49.1-2 (Jan. 1991), pp. 133–152.

# Chapter 3

# Development of High Spatio-Temporal Resolution Kinetochore and Spindle-Pole Tracking Assay

## 3.1 High-Throughput Measurement of Human Kinetochore Dynamics

This chapter describes the development of a computational assay designed to track sister-kinetochore pairs and (optionally) spindle-pole dynamics during metaphase in HeLa cells. Fully automated analysis is performed on four-dimensional (three spatial dimensions plus time) image series of cells expressing fluorescently tagged kinetochores and (optionally) spindle-poles (Figure 3.1). Live cell images were captured on a spinning disk confocal microscope using a cell line stably expressing eGFP - CENP-A as a kinetochore marker and eGFP - Centrin1 as a spindle-pole marker, see Chapter 2 for details on all experimental conditions. Computational methods employed here are based on a previous kinetochore tracking assay [96] with minor or major improvements introduced at almost every computational stage. Details of each computational step, from a pre-processed image series to generation of a set of kinetochore and spindle-pole trajectory coordinates, are described in the following sections. Changes and improve-

ments on the original work [96] are described where relevant. A significant feature implemented here is the use of Gaussian mixture-model (GMM) intensity fitting, allowing kinetochore and spindle-pole positions to be determined with super-resolution accuracy. GMM intensity fitting has been applied in live cell tracking of kinetochores in previous studies *e.g.* on 2 dimensional image projections of PtK1 cells [99] and on full 3 dimensional images of GFP-labelled chromosomes in budding yeast [101]. However to the best of knowledge, no published study has used GMM intensity fitting for obtaining super-resolution positions of kinetochores from live-cell images of human cells. Using GMM intensity fitting for kinetochore localisation in human cells represents a significant technical challenge, the structure of the metaphase plate requires a large number of kinetochore locations to be jointly fit (in 3D) per image frame (nearly complete imaging of the metaphase plate is required for metaphase plate fits, see Section 3.5). The number of spots required to be jointly fit per frame is on the order of $\sim 100$ (an order of magnitude more than present in PtK1 cells). A combination of new computational techniques that significantly improve performance (see Section 3.4) combined with a dedicated computational cluster allowed analysis to be completed in a reasonable amount of time. Combined with a spinning-disk confocal microscope with a piezoelectric stage as an image source, capable of capturing a full metaphase plate image stack in 2 seconds, this work represents a database of human kinetochore dynamics during metaphase at the highest spatio-temporal resolution ever recorded. Figure 3.2 gives an overview of the assay pipeline.

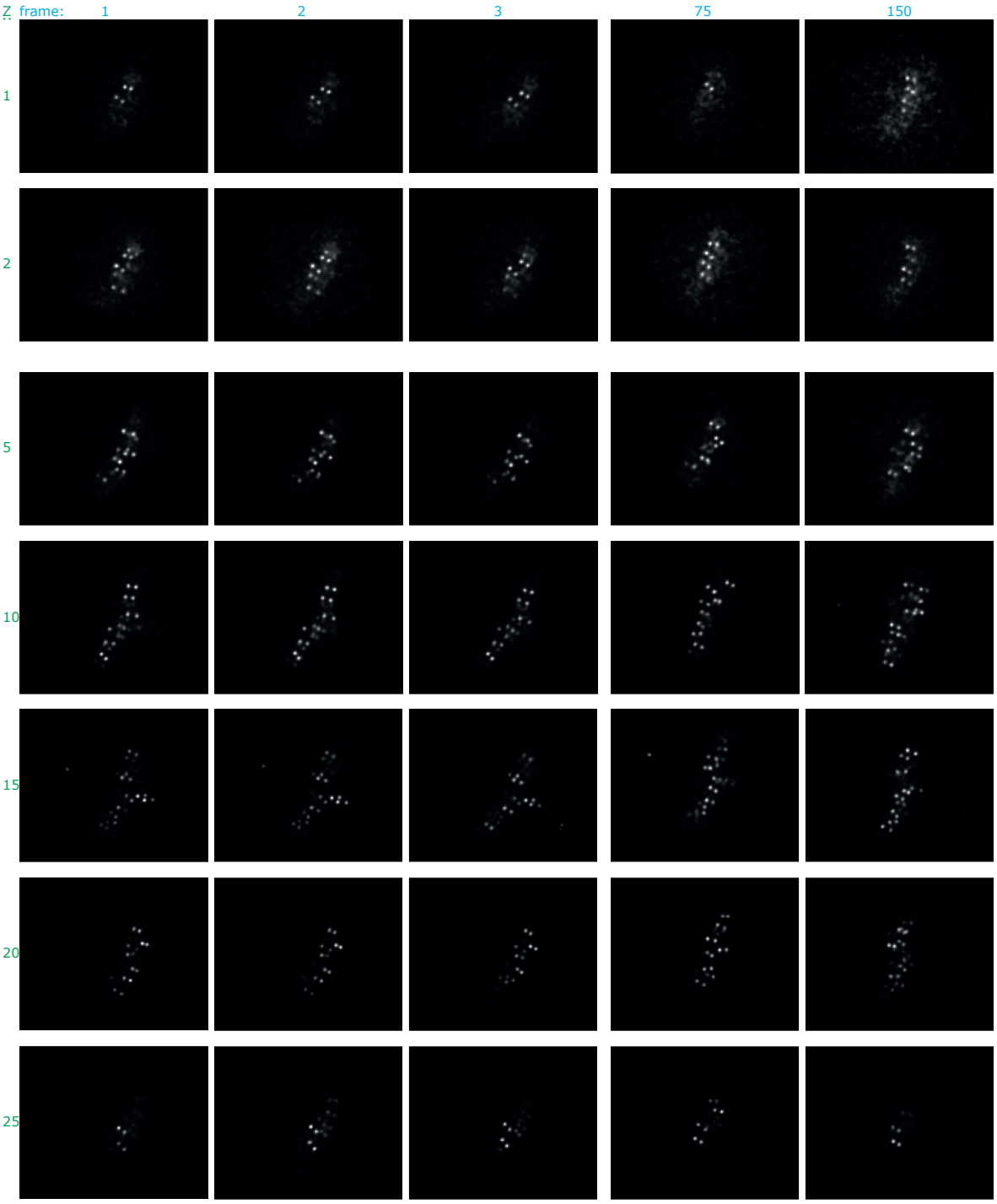


**Figure 3.1:** Example of a tagged-kinetochore image series. Individual 2D image planes (various Z sections and time-points). Pixel size: 0.138$\mu$m, Z spacing: 0.5$\mu$m, time-lapse: 2s per frame.

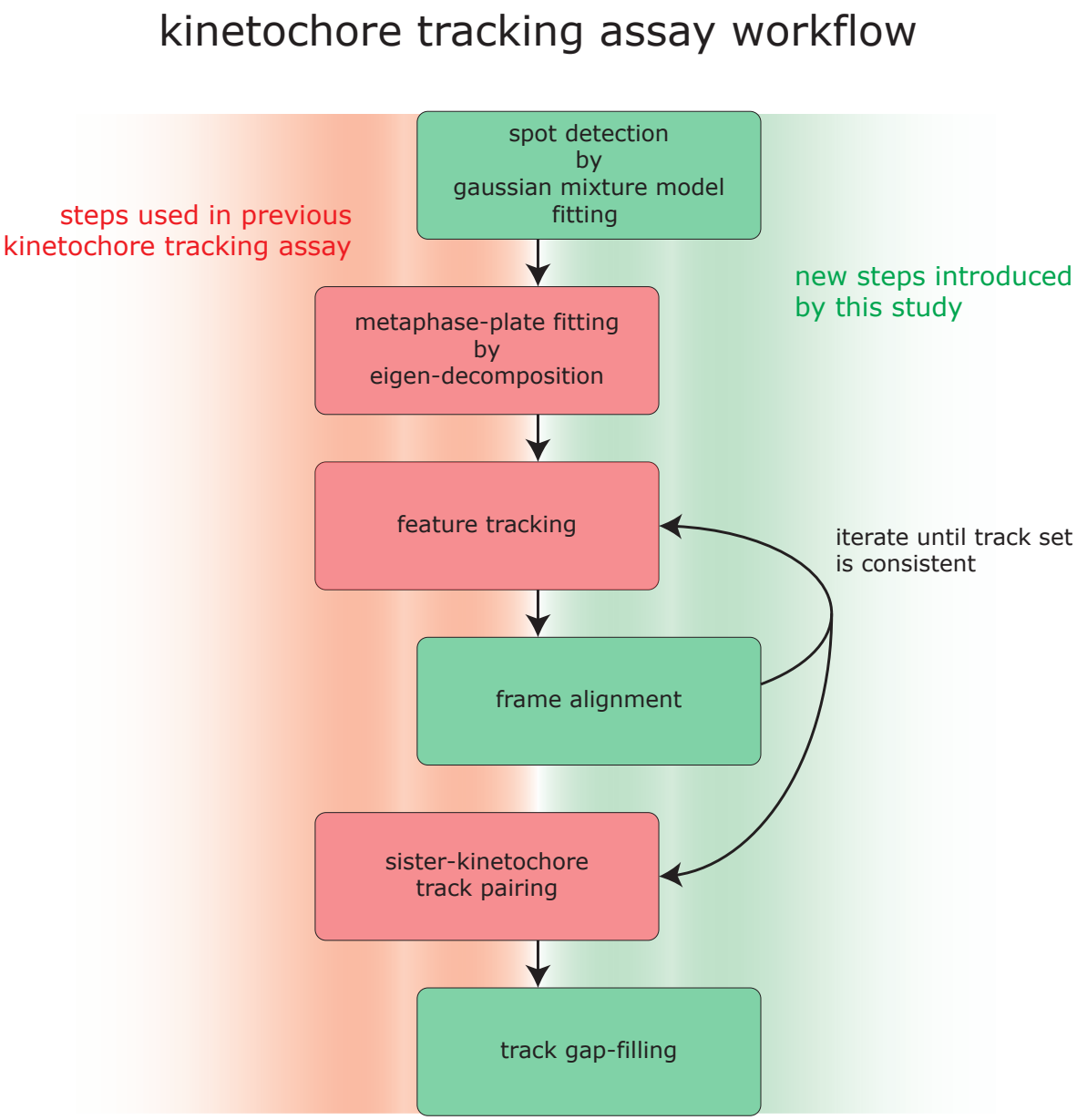


**Figure 3.2:** Overview of the kinetochore tracking assay pipeline. The workflow is based on the assay described in [96] where the main steps were as follows: kinetochore localisation; metaphase plate fitting; feature tracking and sister-kinetochore track pairing. For this work the pipeline was updated with additional steps: kinetochore localisation was performed by using 3D Gaussian mixture-model-fitting; an additional step of frame alignment was introduced after feature tracking and finally an algorithm was introduced that attempted to resolve any gaps in sister-kinetochore tracks. Algorithms for metaphase plate fitting, feature tracking and sister-kinetochore track pairing were taken from [96] with some modification.

## 3.2 Robust Outlier Detection

Many of the techniques and methods discussed in this chapter made use of a robust statistical method for detecting and removing outlying data points from sets of data. Outlying data points are those that do not follow the statistical distribution followed by the majority of the set for a given data model. The method implemented here is that of least-median squares (LMS) [146, 147]. In brief LMS first attempts to find a solution to the minimisation problem

$$\min_x \text{median}\left[(Ax - B) \cdot C \cdot (Ax - B)\right] \tag{3.1}$$

where $B$ is a vector of data points, assuming Gaussian distributed residuals. This is in contrast to ordinary least-squares (OLS) (where $C = 1$) or weighted least-squares (WLS) that attempt to find the minimum sum of squares. LMS is insensitive to data outliers in finding a solution. In the simplest case for estimating the mean of an outlier contaminated data set $B$ consisting of $n$ data points $A_{1\ldots n} = 1$ , $C = 1$, the problem reduces to finding the value $x$ that minimises the median of the squared residuals

$$\min_x \underset{i=1\ldots n}{\text{median}} \left[(x - B_i)^2\right] \tag{3.2}$$

The solution $x^*$ and the associated squared residuals $R$ allow the set of outliers in the data to be estimated. A data point is considered an outlier if its squared residual $R_i > (k\sigma_R)^2$ where $\sigma_R$ is the robust standard deviation estimate and $k$ is the sensitivity of the outlier detection. Unless otherwise stated $k$ is usually set equal to 3, with $\sigma_R = 1.4826\sqrt{M}$ where $M = \text{median}\,(R)$ (see [146] for derivation of $\sigma_R$). No general method exists for solving (3.1) (and 3.2) so in practice the solution is estimated using the *fminsearch* function in MATLAB, which uses a Nelder-Mead simplex search through parameter space. Once outliers have been detected and removed from the data set other least-squares techniques can then be used on the inlier set *e.g.* OLS or WLS to find a final solution. In the case of estimating the mean of a data set with outliers the final estimate is the arithmetic mean of the inlier points. Figure 3.3 shows LMS fitting of the mean for a random synthetic data set consisting of 1000

normally distributed data-points $N(0,1)$ plus 500 uniformly distributed data-points $U(4,8)$. The data-sets were combined and (3.2) was fitted to the joint data (Figure 3.3a,b) producing a solution $x^*$. The squared residuals around $x^*$ were used to calculate test values for each point ($= \frac{R_i}{1.4826^2 M}$). Test values above $k^2$ were considered outliers (Figure 3.3c,d). Inlier/outlier partitioning effectively recovered the two original populations ($N(0,1)/U(4,8)$ respectively) with a small proportional error (0.7% false negatives) (Figure 3.3e).

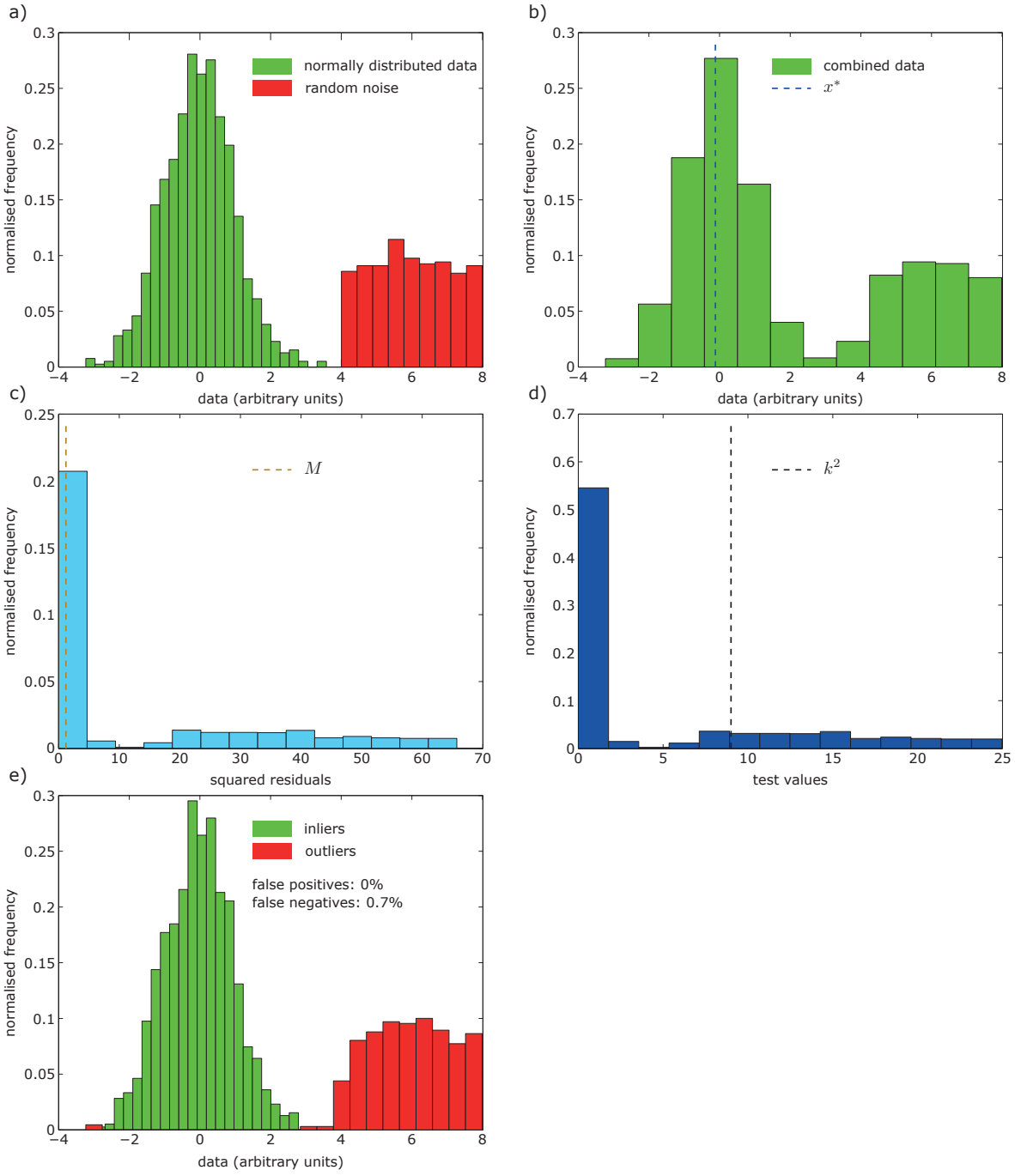


**Figure 3.3:** Least-median squares for robust outlier detection. **a)** Histograms of random synthetic data drawn from two populations: $N(0,1)$ (green; 1000 samples) and $U(4,8)$ (red; 500 samples). **b)** Histogram of combined data-set. Dashed blue line shows the solution to (3.2) $x^*$ for the data-set. **c)** Histogram of squared residuals for the data-set around $x^*$. Dashed orange line shows the median squared residual $M$. **d)** Histogram of data-set test values (= squared residuals/$(1.4826^2 M)$). Black dashed line shows inlier/outlier cut-off $k^2$ (with $k = 3$). **e)** Histograms of inlier data (green) and outlier data (red). Proportion of false positives (incorrectly labelled inlier data) and false negatives (incorrectly labelled outlier data) shown in legend.

## 3.3 Initial Spot Location Estimates

Initial estimates of spot positions are needed before super-resolution spot fitting. Voxels (single 3D image units) that are local intensity maxima are selected as initial estimates of spot locations [96]. A local intensity maxima is any voxel that has an intensity greater than any of its 26 surrounding voxels. Before selecting local intensity maxima the image is convolved with a Gaussian kernel which reduces the background intensity of the image while having a smaller effect on features *i.e.* it increases the intensity difference between spots and the image background (Figure 3.4). The Gaussian kernel is an approximation to the PSF of the optical system which is a $1st$ order *Bessel* function [101]. The standard deviations describing the profile of the Gaussian, $\sigma_x$ and $\sigma_z$ ($\sigma_x = \sigma_y$ due to axis symmetry of the light path) are estimated by a theoretical Gaussian fit to the point spread function [101].

$$\sigma_x = \frac{0.21\frac{\text{wvl}}{\text{NA}}}{\text{vox}_{xy}} \quad \sigma_z = \frac{0.66n\frac{\text{wvl}}{\text{NA}^2}}{\text{vox}_z}$$

where

$$\text{wvl} \rightarrow \text{emission wavelength of imaging channel}$$

$$\text{NA} \rightarrow \text{numerical aperture of microscope lens}$$

$$\text{vox}_{xy} \rightarrow \text{voxel size in X and Y}$$

$$\text{vox}_z \rightarrow \text{voxel size in Z}$$

$$\text{n} \rightarrow \text{refractive index of imaging media}$$

Even after suppression of background effects by using a Gaussian filter, local maxima still results in many false-positives. To separate true local maxima from false positives histogram unimodal thresholding on the filtered voxel intensity was used [96, 148]. The method separates the two populations of voxels based on their filtered intensity; it is a conservative method since it gets rid of almost all background local maxima but also some of the true local maxima *i.e.* it gets rid of almost all false positives but generates some false negatives. Figure 3.5 shows an example image and its local maxima divided

into two sets based on unimodal thresholding.

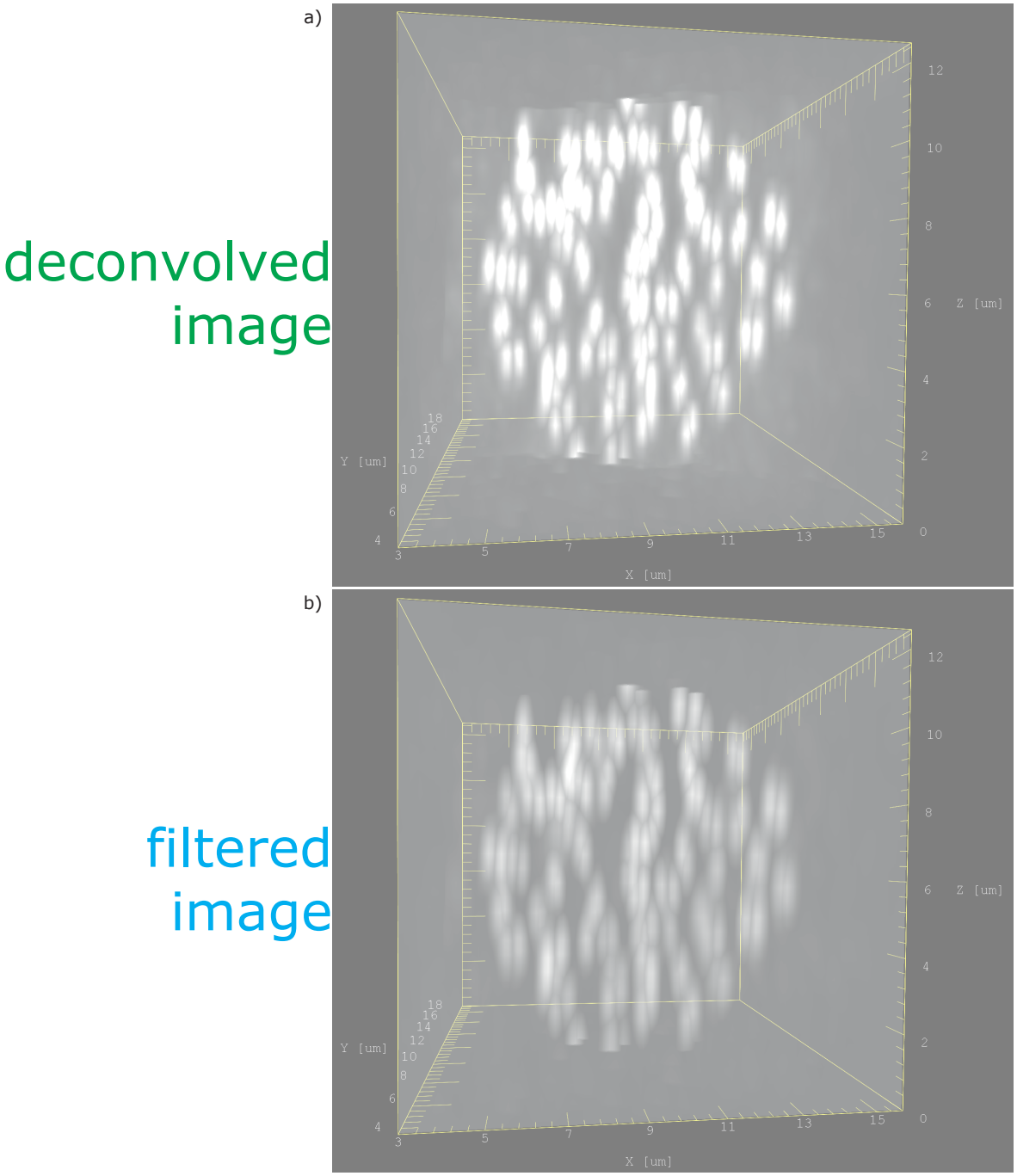


**Figure 3.4:** Image filtering with a Gaussian kernel. **a)** Deconvolved image frame (from Figure 2.2b). **b)** Image after filtering with a Gaussian kernel (see Section 3.3).

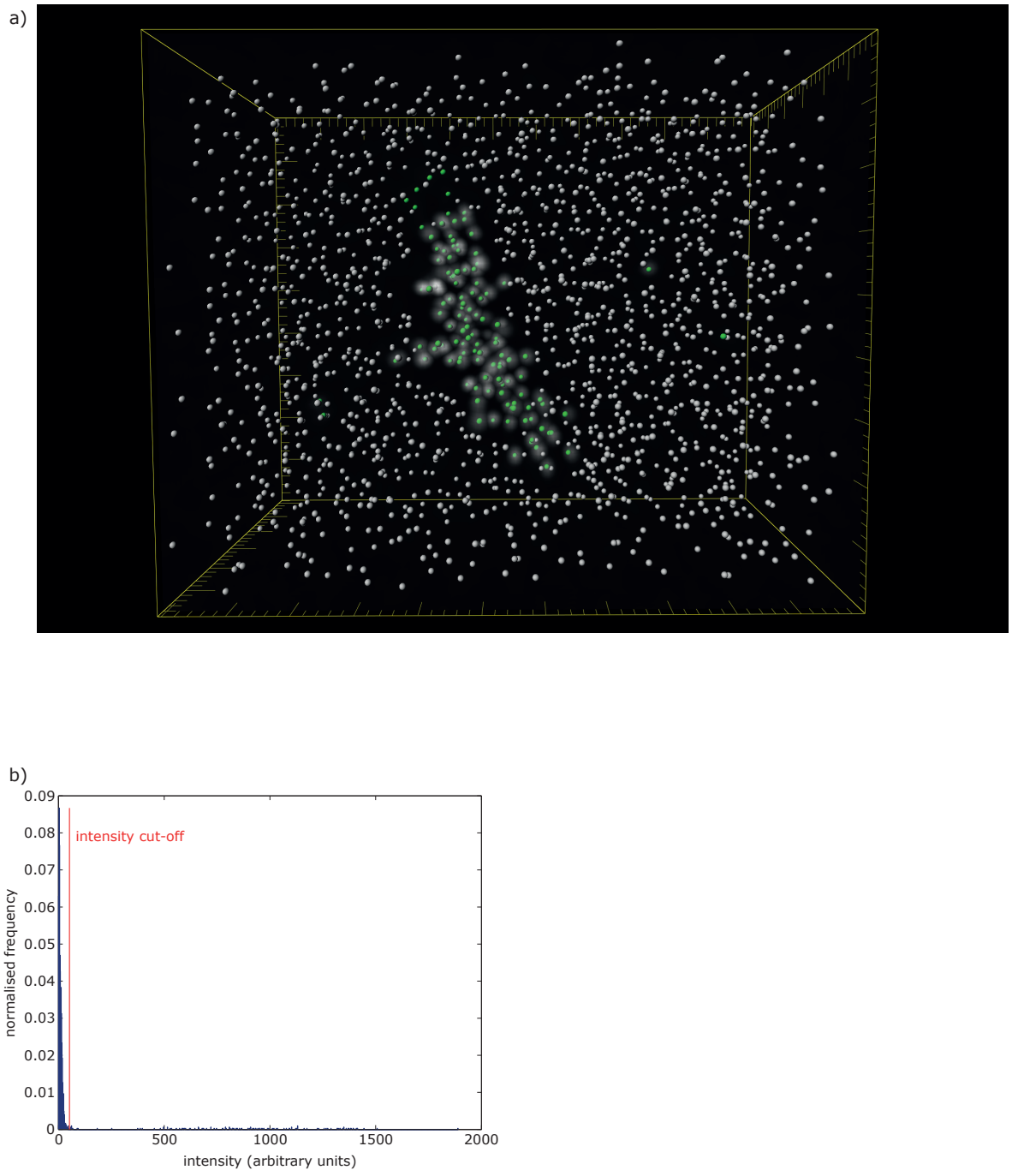


**Figure 3.5:** Local voxel maxima. **a)** Filtered image frame (see Section 3.3). Local voxel maxima above/below intensity cut-off marked with green/silver spheres respectively. **b)** Histogram of local maxima intensity with intensity cut-off marked (red line). Cut-off determined by unimodal thresholding (Section 3.3).

## 3.4 Super-Resolution Spot Localisation by Gaussian Mixture-Model-Fitting

This section describes how to locate spots in fluorescent images by Gaussian mixture-model-fitting, a highly accurate method of sub-pixel resolution spot localisation. Many of the methods detailed in this section are based on ideas described in [101], which used 3D Gaussian mixture-models to locate kinetochores and spindle poles in movies of yeast cells during mitosis. Specifically the method consists of using a mixture of Gaussian kernels to model the intensity distribution in an image of overlapping diffraction-limited fluorescent objects. This study [101] also introduced the method described in Section 3.4.3.2 where additional kernels are added iteratively depending on the significance of the (relative) fits. Computational methods were based on parts of the 'U-track' package, computer code published at *lccb.hms.harvard.edu/software.html*. This software was originally written to perform Gaussian mixture-model-fitting on 2D images, which was re-written here to work on 3D images. Partitioned Least Squares Fitting, Section 3.4.1.2, was based on work originally by Jonas Dorn and Jacques Boisvert of the Université de Montréal; again, originally designed to work in 2D and re-written in this study to work in 3D.

Fluorescently labelled structures smaller than the imaging sampling volume (voxel size) appear as diffraction limited intensity distributions. As mentioned in Section 3.3 this distribution can be approximated by a Gaussian distribution. This model of the intensity distribution around a spot allows spot positions (and uncertainties) to be inferred directly by least squares fitting. Figure 3.6 shows 2D image planes (single Z-sections) taken from three example frames from a live-cell movie of labelled kinetochores. Overlaid on the images are: the local maxima voxels *i.e.* the initial location estimates, the sub-pixel location inferred by Gaussian fitting and for comparison the sub-pixel location inferred by centroid fitting. Centroid fitting estimates the sub-pixel location by calculating the intensity centre of mass of a target volume ($5 \times 5 \times 5$) of the image centred on the object's initial location estimate. Centroid fitting is a comparatively quick method (compared to Gaussian mixture-model-fitting) for estimating an object's sub-voxel location. Centroid fitting was the method used in [96]. Visual inspection shows that the Gaussian fit appears to be more accurate than the centroid fit.

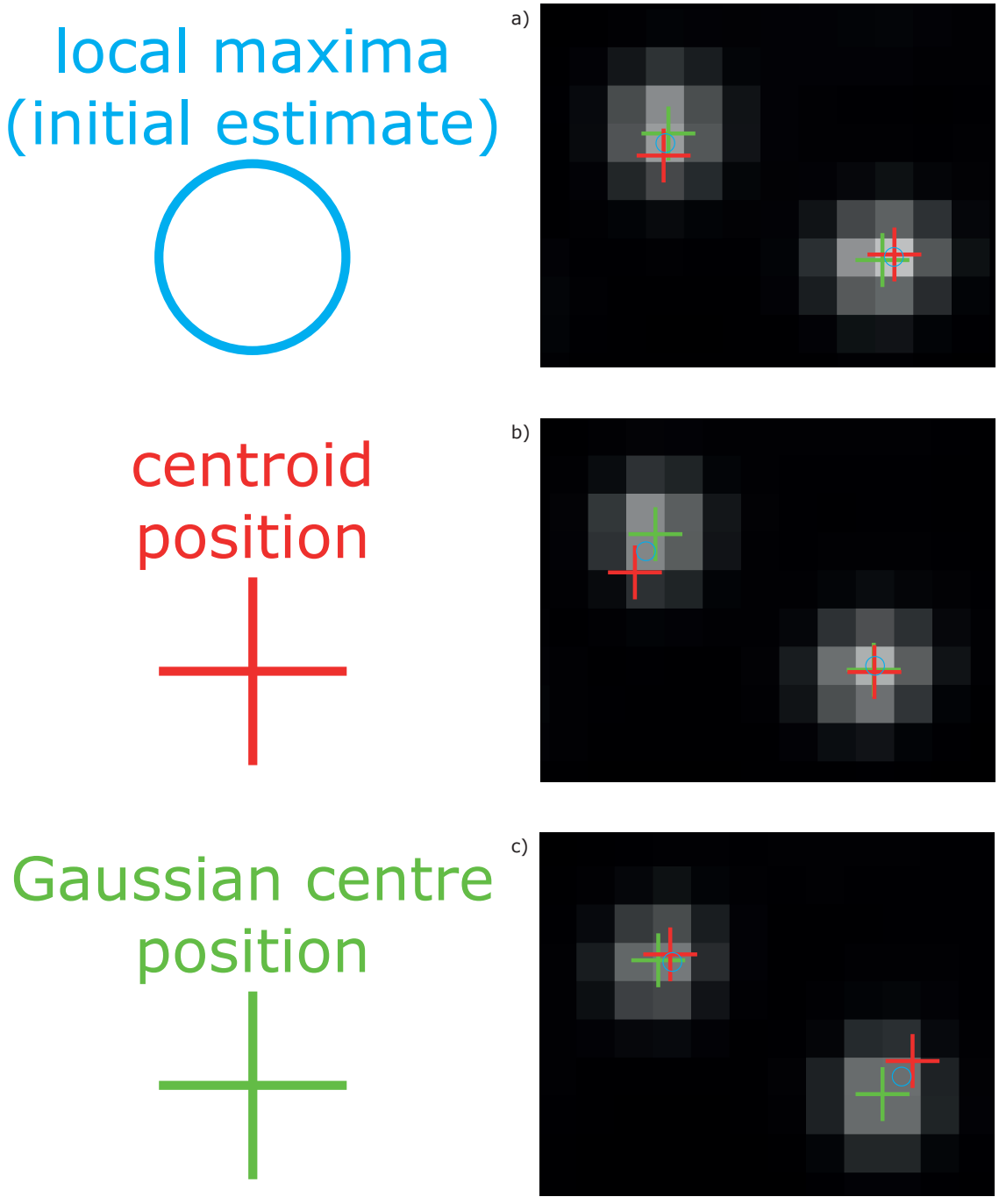


**Figure 3.6:** Gaussian model and centroid spot fitting examples. **a)**, **b)** and **c)** show example centroid (red) and Gaussian (green) spot fitting results overlaid on a single 2D image plane. Initial position estimate *i.e.* local maxima marked in blue.

### 3.4.1 Least Squares Gaussian Fitting

Gaussian models of intensity distributions are fitted to image data using a large-scale least-squares optimisation strategy. Here the technical details of this optimisation are laid out. The aim is to minimise the sum of squares of the parameters of the length $m$ vector $F$ ($m$ voxel intensities)

$$\min_{v} \| F(v) \|_2^2 \tag{3.3}$$

where $v$ is a vector of parameters of length $4n+1$ comprising model spot positions and amplitudes plus a global background value as follows,

$$v = \begin{pmatrix} x_1 \\ y_1 \\ z_1 \\ A_1 \\ x_2 \\ \vdots \\ x_n \\ y_n \\ z_n \\ A_n \\ b \end{pmatrix} \tag{3.4}$$

where

$n \rightarrow$ number of spots

$x_i \rightarrow$ x coordinate of spot $i$

$y_i \rightarrow$ y coordinate of spot $i$

$z_i \rightarrow$ z coordinate of spot $i$

$A_i \rightarrow$ amplitude of spot $i$

$$b \rightarrow \text{background amplitude}$$

$F(v)$ is the difference between the Gaussian mixture-model for the image and the real image

$$F(v) = M(v) - I \tag{3.5}$$

$M(v) \rightarrow$ Gaussian mixture-model representation of the image intensity based on the parameters of $v$

$$I \rightarrow \text{real image voxel intensities}$$

where both $M(v)$ and $I$ are length $m$ vectors

$$M(v) = \begin{pmatrix} p_1^\zeta \\ p_2^\zeta \\ \vdots \\ p_m^\zeta \end{pmatrix} \tag{3.6}$$

$$I = \begin{pmatrix} p_1 \\ p_2 \\ \vdots \\ p_m \end{pmatrix} \tag{3.7}$$

where $p_j^\zeta$ is the intensity of voxel $j$ from the model and $p_j$ is the intensity of voxel $j$ from the real image.

#### 3.4.1.1 Full Least Squares Fitting

The problem of finding the $v$ that minimises $\|F(v)\|_2^2$ can be implemented as a full non-linear least-squares optimisation. In calculating $M(v)$, the intensity in each voxel ($p^\zeta$) is calculated as the contribution from each spot through the PSF *i.e.* the integral of the Gaussian distribution over the voxel space from each spot.

$$p_j^{\zeta} = \left( \sum_{i=1}^{n} \int_{x_{\min}^j}^{x_{\max}^j} \int_{y_{\min}^j}^{y_{\max}^j} \int_{z_{\min}^j}^{z_{\max}^j} g\left(\chi, \gamma, \xi, x_i, y_i, z_i, A_i\right) \, \mathrm{d}\chi \, \mathrm{d}\gamma \, \mathrm{d}\xi \right) + b \tag{3.8}$$

where

$$g\left(\chi, \gamma, \xi, x_i, y_i, z_i, A_i\right) = A_i \exp\left( - \left( \frac{\left(\chi - x_i\right)^2}{2\sigma_x^2} + \frac{\left(\gamma - y_i\right)^2}{2\sigma_x^2} + \frac{\left(\xi - z_i\right)^2}{2\sigma_z^2} \right) \right) \tag{3.9}$$

$x_{\min}^j \rightarrow$ minimum $x$ value in image coordinates of voxel $j$

$x_{\max}^j \rightarrow$ maximum $x$ value in image coordinates of voxel $j$

$y_{\min}^j \rightarrow$ minimum $y$ value in image coordinates of voxel $j$

$y_{\max}^j \rightarrow$ maximum $y$ value in image coordinates of voxel $j$

$z_{\min}^j \rightarrow$ minimum $z$ value in image coordinates of voxel $j$

$z_{\max}^j \rightarrow$ maximum $z$ value in image coordinates of voxel $j$

$\sigma_x \rightarrow$ PSF standard deviation in XY

$\sigma_z \rightarrow$ PSF standard deviation in Z

The integral of a Gaussian distribution is calculated numerically using the error function, implemented here using the *erfc* function in MATLAB. So the intensity of voxel $j$ at position $\{C_x^j, C_y^j, C_z^j\}$ due to a spot at position $\{x_i, y_i, z_i\}$ (coordinates in image space) with amplitude $A_i$ is calculated by

$$p_{ji}^{\zeta} = A_i \Gamma\left(C_x^j, x_i, \sigma_x\right) \Gamma\left(C_y^j, y_i, \sigma_x\right) \Gamma\left(C_z^j, z_i, \sigma_z\right) \tag{3.10}$$

where

$$\Gamma\left(C,x,\sigma\right)=\sigma\sqrt{\frac{\pi}{2}}\left(erfc\left(\frac{-\frac{1}{2}-C+x}{\sqrt{2}\sigma}\right)-erfc\left(\frac{\frac{1}{2}-C+x}{\sqrt{2}\sigma}\right)\right)$$

Also required for least-squares minimisation is the Jacobian of $F\left(v\right)$, denoted $J\left(v\right)$. The Jacobian is the $\left(4n+1\right)\times m$ matrix of partial derivatives of the values of $F$ with respect to the parameters $v$. Note that because $F\left(v\right)=M\left(v\right)-I$, and $I$ is a constant, the Jacobian of $F$ is the Jacobian of $M$

$$J\left(v\right)=\begin{bmatrix}\frac{\partial p_1^\zeta}{\partial x_1} & \frac{\partial p_1^\zeta}{\partial y_1} & \frac{\partial p_1^\zeta}{\partial z_1} & \frac{\partial p_1^\zeta}{\partial A_1} & \cdots & \frac{\partial p_1^\zeta}{\partial A_n} & \frac{\partial p_1^\zeta}{\partial b}\\ \frac{\partial p_2^\zeta}{\partial x_1} & \frac{\partial p_2^\zeta}{\partial y_1} & \frac{\partial p_2^\zeta}{\partial z_1} & \frac{\partial p_2^\zeta}{\partial A_1} & \cdots & \frac{\partial p_2^\zeta}{\partial A_n} & \frac{\partial p_2^\zeta}{\partial b}\\ \vdots & & & \ddots & & & \vdots\\ \frac{\partial p_m^\zeta}{\partial x_1} & \frac{\partial p_m^\zeta}{\partial y_1} & \frac{\partial p_m^\zeta}{\partial z_1} & \frac{\partial p_m^\zeta}{\partial A_1} & \cdots & \frac{\partial p_m^\zeta}{\partial A_n} & \frac{\partial p_m^\zeta}{\partial b}\end{bmatrix} \tag{3.11}$$

where

$$\begin{aligned}\frac{\partial p_j^\zeta}{\partial x_i}&=A_i\Lambda\left(C_x^j,x_i,\sigma_x\right)\Gamma\left(C_y^j,y_i,\sigma_x\right)\Gamma\left(C_z^j,z_i,\sigma_z\right)\\ \frac{\partial p_j^\zeta}{\partial y_i}&=A_i\Lambda\left(C_y^j,y_i,\sigma_x\right)\Gamma\left(C_x^j,x_i,\sigma_x\right)\Gamma\left(C_z^j,z_i,\sigma_z\right)\\ \frac{\partial p_j^\zeta}{\partial z_i}&=A_i\Lambda\left(C_z^j,z_i,\sigma_z\right)\Gamma\left(C_x^j,x_i,\sigma_x\right)\Gamma\left(C_y^j,y_i,\sigma_x\right)\\ \frac{\partial p_j^\zeta}{\partial A_i}&=\Gamma\left(C_x^j,x_i,\sigma_x\right)\Gamma\left(C_y^j,y_i,\sigma_x\right)\Gamma\left(C_z^j,z_i,\sigma_z\right)\\ \frac{\partial p_j^\zeta}{\partial b}&=1\end{aligned} \tag{3.12}$$

where

$$\Lambda\left(C,x,\sigma\right)=\exp\left(-\left(\frac{\left(C-x-\frac{1}{2}\right)^2}{2\sigma^2}\right)\right)-\exp\left(-\left(\frac{\left(C-x+\frac{1}{2}\right)^2}{2\sigma^2}\right)\right)$$

#### 3.4.1.2 Partitioned Least Squares Fitting

Minimising $||F\left(v\right)||_2^2$ can be partitioned between two optimisation procedures. Equation (3.9) can be re-written as

$$g\left(\chi,\gamma,\xi,x_i,y_i,z_i,A_i\right)=A_iG\left(\chi,\gamma,\xi,x_i,y_i,z_i\right) \tag{3.13}$$

where

$$G\left(\chi,\gamma,\xi,x_i,y_i,z_i\right)=\exp\left(-\left(\frac{\left(\chi-x_i\right)^2}{2\sigma_x^2}+\frac{\left(\gamma-y_i\right)^2}{2\sigma_x^2}+\frac{\left(\xi-z_i\right)^2}{2\sigma_z^2}\right)\right) \tag{3.14}$$

separating the contributions of amplitude ($A_i$) and position ($x_i, y_i$ and $z_i$). Applying this idea to the construction of the image model, (3.6) and (3.8) can be combined and written in a matrix form

$$M\left(v\right)=N\left(v\right)\times a\left(v\right) \tag{3.15}$$

where

$$N\left(v\right)=\begin{bmatrix} q\left(1,1,v\right) & \dots & q\left(n,1,v\right) & 1 \\ & \ddots & & \vdots \\ q\left(1,m,v\right) & \dots & q\left(n,m,v\right) & 1 \end{bmatrix} \tag{3.16}$$

with

$$q\left(i,j,v\right)=\int_{x_{\min}^j}^{x_{\max}^j}\int_{y_{\min}^j}^{y_{\max}^j}\int_{z_{\min}^j}^{z_{\max}^j}G\left(\chi,\gamma,\xi,x_i,y_i,z_i\right)\,\mathrm{d}\chi\,\mathrm{d}\gamma\,\mathrm{d}\xi$$

and

$$a\left(v\right)=\begin{pmatrix} A_1 \\ \vdots \\ A_n \\ b \end{pmatrix} \tag{3.17}$$

Combining (3.5) and (3.15)

$$F=Na-I \tag{3.18}$$

For a given set of spot positions, *i.e.* the matrix $N$, minimising $\|F\|_2^2$ constitutes minimising $\|Na-I\|_2^2$ over $a$. This is an ordinary least-squares (OLS) optimisation problem. This effectively removes the need to have the spot amplitudes and background as input to $F$, the calculation of optimal amplitudes now being an intermediary step. Instead finding

$$\min_{v^\tau} \|F\left(v^\tau\right)\|_2^2 \tag{3.19}$$

where $v^\tau$ is a $3n$ length vector of model spot positions.

$$v^\tau = \begin{pmatrix} x_1 \\ y_1 \\ z_1 \\ \vdots \\ x_n \\ y_n \\ z_n \end{pmatrix} \tag{3.20}$$

the amplitudes $a'$ are found using the 'left matrix divide' or \ operator in MATLAB *i.e.* $a' = N\backslash I$, which performs an OLS optimisation for an under- or over-determined system of equations. $F$ is then calculated from (3.18), $F = Na' - I$.

The Jacobian of $F\left(v^\tau\right)$, $J^\tau\left(v^\tau\right)$ is calculated in the same manner as (3.11) using (3.12).

$$J^\tau\left(v^\tau\right) = \begin{bmatrix} \frac{\partial p_1^\zeta}{\partial x_1} & \frac{\partial p_1^\zeta}{\partial y_1} & \frac{\partial p_1^\zeta}{\partial z_1} & \cdots & \frac{\partial p_1^\zeta}{\partial z_n} \\ & & \ddots & & \\ \frac{\partial p_m^\zeta}{\partial x_1} & \frac{\partial p_m^\zeta}{\partial y_1} & \frac{\partial p_m^\zeta}{\partial z_1} & \cdots & \frac{\partial p_m^\zeta}{\partial z_n} \end{bmatrix} \tag{3.21}$$

note this is a reduced Jacobian of the system, matching the reduced input vector $v^\tau$. Nevertheless a full Jacobian can be calculated using (3.12) since spot and background amplitudes are available from $a'$. The full Jacobian is used to calculate the parameter covariance matrix (see Section 3.4.1.5).

#### 3.4.1.3 Sparse Jacobian Structuring

To increase the computational speed of least-squares fitting an additional processing step was introduced. In practice not all the terms of $J$ need to be used during the minimisation. Only the local gradients around each spot are needed. For any given spot only the voxels both within a $4 \times \sigma_x$ in XY and a $4 \times \sigma_z$ in Z range were chosen to have their gradients retained for the minimisation routines. By exploiting this high level of sparsity in $J$ the computational time needed for minimisation was significantly reduced. That is, for example given 2 spots $c_1$ and $c_2$ the voxels of the image both within a $4\times\sigma_x$ in XY and a $4\times\sigma_z$ in Z of each spot were determined *e.g.* voxels $j = m_1^1$ to $m_1^2$ for spot 1 and voxels $j = m_2^1$ to $m_2^2$ for spot 2. Then in calculating $J$ only the relevant terms are kept.

For the full model (Section 3.4.1.1) the sparsity pattern has the form

$$
\begin{array}{cccccccccc}
\vdots & & & & & & & & & \\
 & & & & & & & & & \\
0 & & & & & & & & & \\
\frac{\partial p_{m_1^1}^{\zeta}}{\partial x_1} & \frac{\partial p_{m_1^1}^{\zeta}}{\partial y_1} & \frac{\partial p_{m_1^1}^{\zeta}}{\partial z_1} & \frac{\partial p_{m_1^1}^{\zeta}}{\partial A_1} & 0 & \cdots & & & & \\
\vdots & \vdots & \vdots & \vdots & \frac{\partial p_{m_2^1}^{\zeta}}{\partial x_2} & \frac{\partial p_{m_2^1}^{\zeta}}{\partial y_2} & \frac{\partial p_{m_2^1}^{\zeta}}{\partial z_2} & \frac{\partial p_{m_2^1}^{\zeta}}{\partial A_2} & 0 & \cdots \\
\frac{\partial p_{m_1^2}^{\zeta}}{\partial x_1} & \frac{\partial p_{m_1^2}^{\zeta}}{\partial y_1} & \frac{\partial p_{m_1^2}^{\zeta}}{\partial z_1} & \frac{\partial p_{m_1^2}^{\zeta}}{\partial A_1} & \vdots & \vdots & \vdots & \vdots & & \\
 & & \cdots & 0 & \frac{\partial p_{m_2^2}^{\zeta}}{\partial x_2} & \frac{\partial p_{m_2^2}^{\zeta}}{\partial y_2} & \frac{\partial p_{m_2^2}^{\zeta}}{\partial z_2} & \frac{\partial p_{m_2^2}^{\zeta}}{\partial A_2} & 0 & \cdots \\
 & & & & & & & 0 & & \\
 & & & & & & & \vdots & &
\end{array}
$$

Note that the last column of $J$ has $\frac{\partial p_j^{\zeta}}{\partial b} = 1$.

For the partial model (Section 3.4.1.2) the sparsity pattern has the form

$$
\begin{array}{cccccccc}
\vdots & & & & & & & \\
 & & & & & & & \\
0 & & & & & & & \\
\frac{\partial p^{\zeta}_{m_1^1}}{\partial x_1} & \frac{\partial p^{\zeta}_{m_1^1}}{\partial y_1} & \frac{\partial p^{\zeta}_{m_1^1}}{\partial z_1} & 0 & \cdots & & & \\
\vdots & \vdots & \vdots & \frac{\partial p^{\zeta}_{m_2^1}}{\partial x_2} & \frac{\partial p^{\zeta}_{m_2^1}}{\partial y_2} & \frac{\partial p^{\zeta}_{m_2^1}}{\partial z_2} & 0 & \cdots \\
\frac{\partial p^{\zeta}_{m_1^2}}{\partial x_1} & \frac{\partial p^{\zeta}_{m_1^2}}{\partial y_1} & \frac{\partial p^{\zeta}_{m_1^2}}{\partial z_1} & \vdots & \vdots & \vdots & & \\
 & \cdots & 0 & \frac{\partial p^{\zeta}_{m_2^2}}{\partial x_2} & \frac{\partial p^{\zeta}_{m_2^2}}{\partial y_2} & \frac{\partial p^{\zeta}_{m_2^2}}{\partial z_2} & 0 & \cdots \\
 & & & & & 0 & & \\
 & & & & & \vdots & &
\end{array}
$$

Figure 3.7 compares the fitting times for the frames of a movie using both full and partitioned least-squares with and without a sparse Jacobian structure. Figure 3.7a shows that by using partitioned least squares over full least-squares the fitting times are reduced by approximately 73%. Figure 3.7b shows that by using a sparse Jacobian structure when using full least-squares fitting the fitting times are reduced by approximately 74%. Figure 3.7c shows that by using a sparse Jacobian structure when using partitioned least-squares fitting the fitting times are reduced by approximately 65%. Finally Figure 3.7d shows that by using a partitioned least-squares fitting with a sparse Jacobian structure over full least-squares without a sparse Jacobian structure the fitting times are reduced by approximately 91%.

#### 3.4.1.4 Non-Linear Least Squares Minimisation

Minimisation is performed using the *lsqnonlin* function in MATLAB using a trust-region reflective algorithm [149, 150] with a tolerance of $10^{-6}$ set for changes in the input parameters and for changes in $\|F\|_2^2$. Briefly, the algorithm constructs a quadratic approximation to the objective function within a small region of parameter space (the trust-region). A Newton-Raphson method is then used to compute a minimisation step to the approximated function. If a minimisation step crosses pre-set constraints in the values of the parameters it is reflected back along the appropriate direction(s), *i.e.* if a computed minimisation step $s = (s_1 \dots s_n)$ causes parameter $i$ to cross a constraint then $s_i = -s_i$. The parameters of $v$ (for the full model, Section 3.4.1.1) or $v^{\tau}$ (for

the partial model, Section 3.4.1.2) were constrained between realistic upper and lower bounds (using the box constraint option of *lsqnonlin*), positions ($(x, y, z)$ parameters of $v$ or $v^\tau$) were constrained between $\pm 2 \times \sigma_x$ in XY and $\pm 2 \times \sigma_z$ in Z relative to the initial location estimates. For the full model, amplitudes and the background were constrained between 0 and 1. These amplitude constraints were implemented by first normalising the entire image by the maximum possible voxel intensity for the image bit-depth (dividing all intensities by $B$ where $B = 2^{\text{bit-depth}} - 1$).

$$v_{\text{ lower bound}} = \begin{pmatrix} x_1^{lm} - 2\sigma_{xy} \\ y_1^{lm} - 2\sigma_{xy} \\ z_1^{lm} - 2\sigma_z \\ 0 \\ \vdots \\ x_n^{lm} - 2\sigma_{xy} \\ y_n^{lm} - 2\sigma_{xy} \\ z_n^{lm} - 2\sigma_z \\ 0 \\ 0 \end{pmatrix} \qquad v_{\text{ upper bound}} = \begin{pmatrix} x_1^{lm} + 2\sigma_{xy} \\ y_1^{lm} + 2\sigma_{xy} \\ z_1^{lm} + 2\sigma_z \\ 1 \\ \vdots \\ x_n^{lm} + 2\sigma_{xy} \\ y_n^{lm} + 2\sigma_{xy} \\ z_n^{lm} + 2\sigma_z \\ 1 \\ 1 \end{pmatrix}$$

$$v^\tau_{\text{lower bound}} = \begin{pmatrix} x_1^{lm} - 2\sigma_{xy} \\ y_1^{lm} - 2\sigma_{xy} \\ z_1^{lm} - 2\sigma_z \\ \vdots \\ x_n^{lm} - 2\sigma_{xy} \\ y_n^{lm} - 2\sigma_{xy} \\ z_n^{lm} - 2\sigma_z \end{pmatrix} \qquad v^\tau_{\text{upper bound}} = \begin{pmatrix} x_1^{lm} + 2\sigma_{xy} \\ y_1^{lm} + 2\sigma_{xy} \\ z_1^{lm} + 2\sigma_z \\ \vdots \\ x_n^{lm} + 2\sigma_{xy} \\ y_n^{lm} + 2\sigma_{xy} \\ z_n^{lm} + 2\sigma_z \end{pmatrix}$$

where $\left\{x_i^{lm}, y_i^{lm}, z_i^{lm}\right\}$ is the initial local maxima location estimate for spot $i$.

Figure 3.8 gives a breakdown of the fitting times detailed in Figure 3.7 into the time taken by each algorithm to calculate its respective objective function ($F$ from (3.5)) and Jacobian ($J$ from (3.11) or (3.21)) (including the time taken to calculate Jacobian sparsity patterns) and the time taken by the *lsqnonlin* algorithm to calculate each subsequent minimisation step. Figure 3.8a shows the number of iterations taken by

*lsqnonlin* when using each algorithm to converge to an answer (within defined bounds). The use of partitioned least-squares and a sparse Jacobian structure both have the effect of reducing the number of iterations taken to converge. Figure 3.8b shows the time taken by *lsqnonlin* to calculate each subsequent minimisation step *i.e.* the time to calculate each new input vector ($v$ from (3.4) or $v^{\tau}$ from (3.20)) when using each algorithm. Again, using partitioned least-squares and a sparse Jacobian both have the (compounded) effect of reducing the time taken to calculate each subsequent minimisation step. Figure 3.8c shows the time taken by each algorithm to calculate its objective function and Jacobian. Using sparse Jacobians increases the time taken since the sparsity patterns also need to be calculated. Using partitioned least-squares also increases the time taken since the intensity values need to be calculated by OLS each iteration. Figure 3.8d shows the sparsity fraction of each algorithm using sparse Jacobians *i.e.* the fraction of the Jacobian that is non-zero. For both algorithms the sparsity fraction is less than 2% with the value decreasing to less than 0.5% for the case of partitioned least-squares.

#### 3.4.1.5 Parameter Uncertainties

Uncertainties of the parameters of $v$ can also be inferred [151]. Upon minimisation the minimised parameter vector $v^*$ is obtained and the values of $\|F(v^*)\|_2^2$ and the Jacobian $J^*$ at that point can be determined. The covariance matrix for the parameters of $v^*$ is then given by

$$\mathrm{c} = \frac{\|F(v^*)\|_2^2}{\mathrm{dof}} \times \left(J^{*T} \times J^*\right)^{-1} \tag{3.22}$$

where

$$\mathrm{dof} = m - (4n + 1)$$

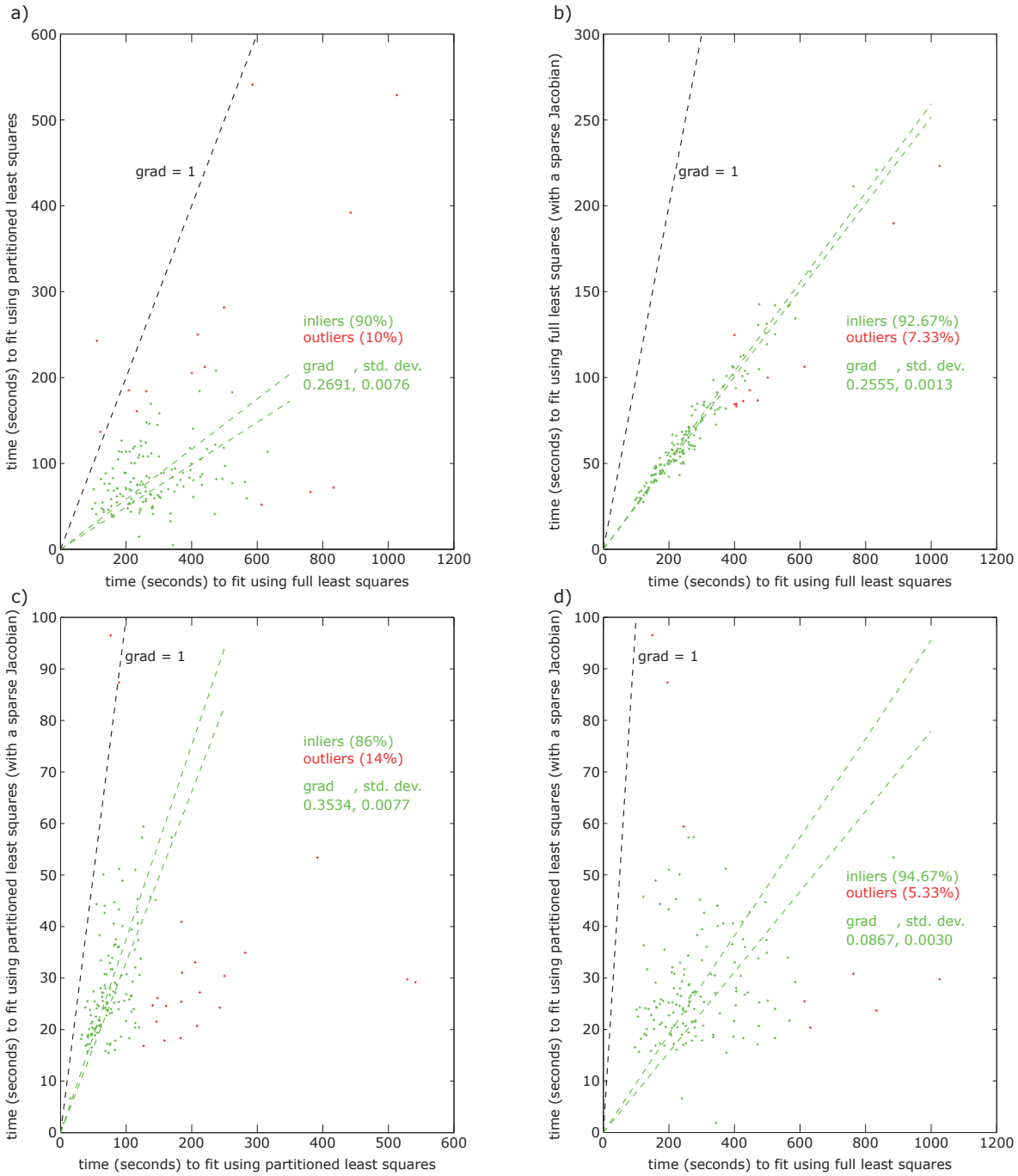


**Figure 3.7:** Initial fitting algorithm execution times. A 150 frame movie was initially fitted for spots as described in Section 3.4.3.1. Four algorithms were used, full and partitioned least-squares with and without sparse Jacobians (sections 3.4.1.1, 3.4.1.2 and 3.4.1.3 respectively). The execution times for the largest cluster (Section 3.4.3.1) in each frame were compared. Linear models were fitted to the data-sets (of the form $d_1 - xd_2$ where $d_1$ and $d_2$ are the data sets) using LMS to discard outliers (shown in red) and OLS to fit the model to the inliers (shown in green). Values for the linear gradients plus their estimated standard deviations are shown in the figure legends. Green dashed lines represent the 95% confidence interval for the gradient value. Black dashed lines represent the unit gradient *i.e.* the path of equal execution times. **a)** compares the full least-squares model with the partitioned least-squares model (both without sparse Jacobians). **b)** compares the full least-squares model with and without sparse Jacobians. **c)** compares the partitioned least-squares model with and without sparse Jacobians. **d)** compares the full least-squares model without a sparse Jacobian to the partitioned least-squares model with a sparse Jacobian.

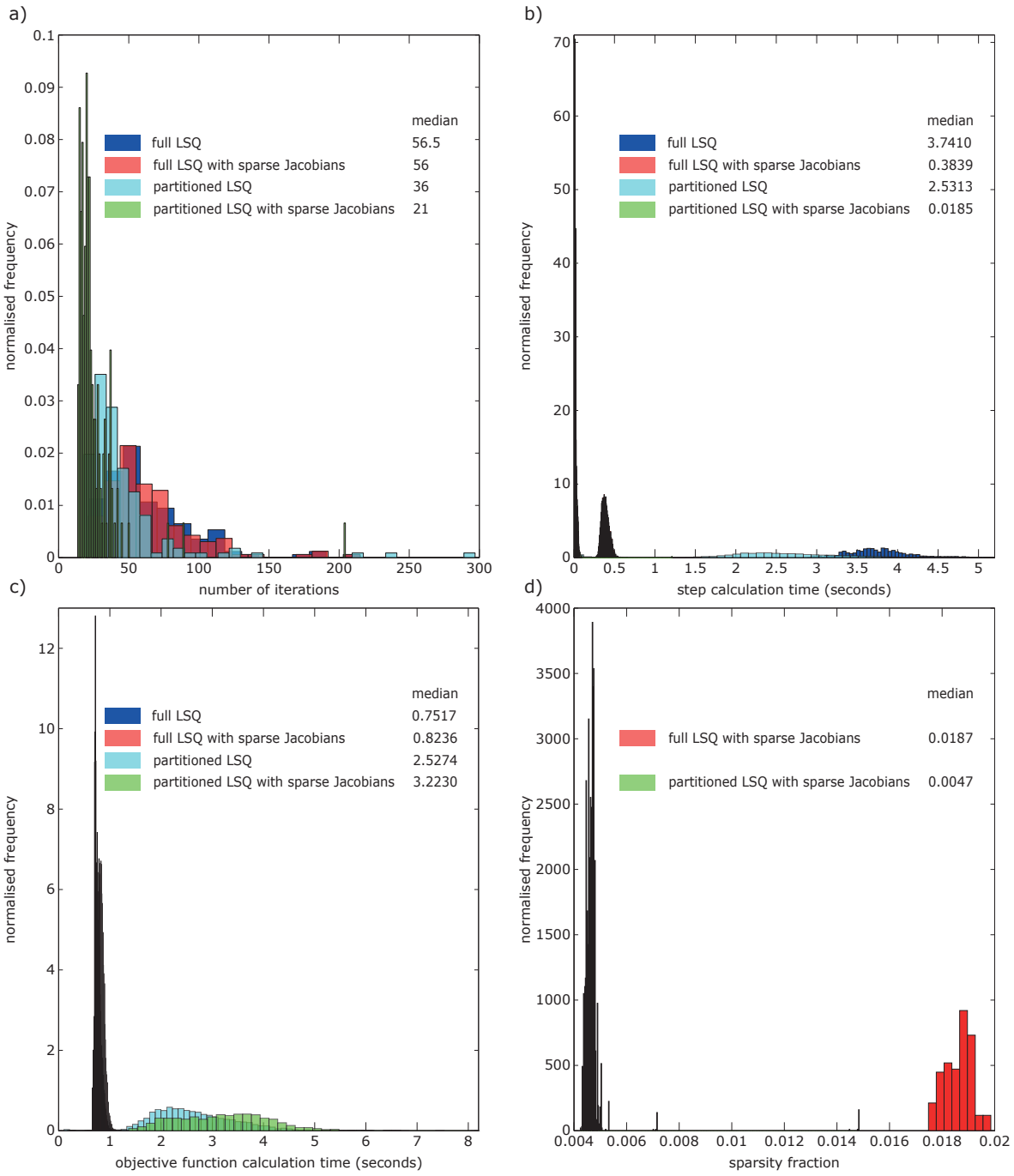


**Figure 3.8:** Initial fitting algorithm iteration times. The algorithm fitting times described in Figure 3.7 broken down into different steps. **a)** Histograms of the number of iterations each algorithm took to converge. **b)** Histograms of the time taken by each algorithm to calculate each subsequent minimisation step. **c)** Histograms of the time taken by each algorithm to calculate its objective function and Jacobian (including the time taken to calculate Jacobian sparsity patterns). **d)** Histograms of the sparsity fractions (fraction of non-zero elements) of each Jacobian. Distribution medians shown in figure legends.

### 3.4.2 Estimating the Point Spread Function of Diffraction Limited Objects

To try and obtain a better estimate of the PSF caused by a sub-resolution object, which may differ from the theoretical value for a number of reasons (object size and rotation, microscope light path complications, non-linear photon response, deconvolution effects etc.) single Gaussian distributions were fitted to isolated local maxima in the image ($> \lceil 10\sigma_x \rceil$ in XY or $> \lceil 10\sigma_z \rceil$ in Z) away from any other local maxima using a similar method described in Section 3.4.1.1 except the Gaussian standard deviations are also made part of the parameter vector, along with the spot positions and amplitudes. Therefore the minimum

$$\min_{v'} \| F(v') \|_2^2$$

was found where

$$v' = \begin{pmatrix} x \\ y \\ z \\ A \\ b \\ \sigma_x \\ \sigma_z \end{pmatrix}$$

Each Gaussian was fitted to a cropped sub-image centred on the local maxima voxel in question. The sub-image extended for $\lceil 5\sigma_x \rceil$ voxels in each direction in XY and $\lceil 5\sigma_z \rceil$ voxels in each direction in Z (isolated local maxima also had to be $> \lceil 5\sigma_x \rceil$ from the edges of the image in XY and $> \lceil 5\sigma_z \rceil$ from the edges of the image in Z). The initial amplitude was taken as the maximum voxel intensity of the 27 central voxels of the cropped image and the initial background was taken as the median intensity of all the edge-voxels of the cropped image. Note that for a single Gaussian kernel the fitting of $\sigma_x$ and $\sigma_y$ is achievable *i.e.* the fitting algorithm converges on a solution, but fitting becomes unstable when jointly fitting more than one kernel [101]. That is why for the

methods detailed in Section 3.4.1 $\sigma_x$ and $\sigma_y$ are kept constant.

The average of the $\sigma_x$ and $\sigma_z$ from all fits are calculated using LMS fitting of the mean (Section 3.2) to discard outliers. This then forms the PSF for the next iteration of isolated spot detection and fitting until both $\sigma_x$ and $\sigma_z$ change by less than 5%. Iterative fitting is abandoned and the theoretical PSF is used if there are not enough isolated spots in the movie or if there are too many outliers detected from the LMS fitting. In practice PSF fitting almost always converges to a solution. Figure 3.9 shows an example of a single fit of an isolated spot and the results of a successful PSF estimation to a single movie.

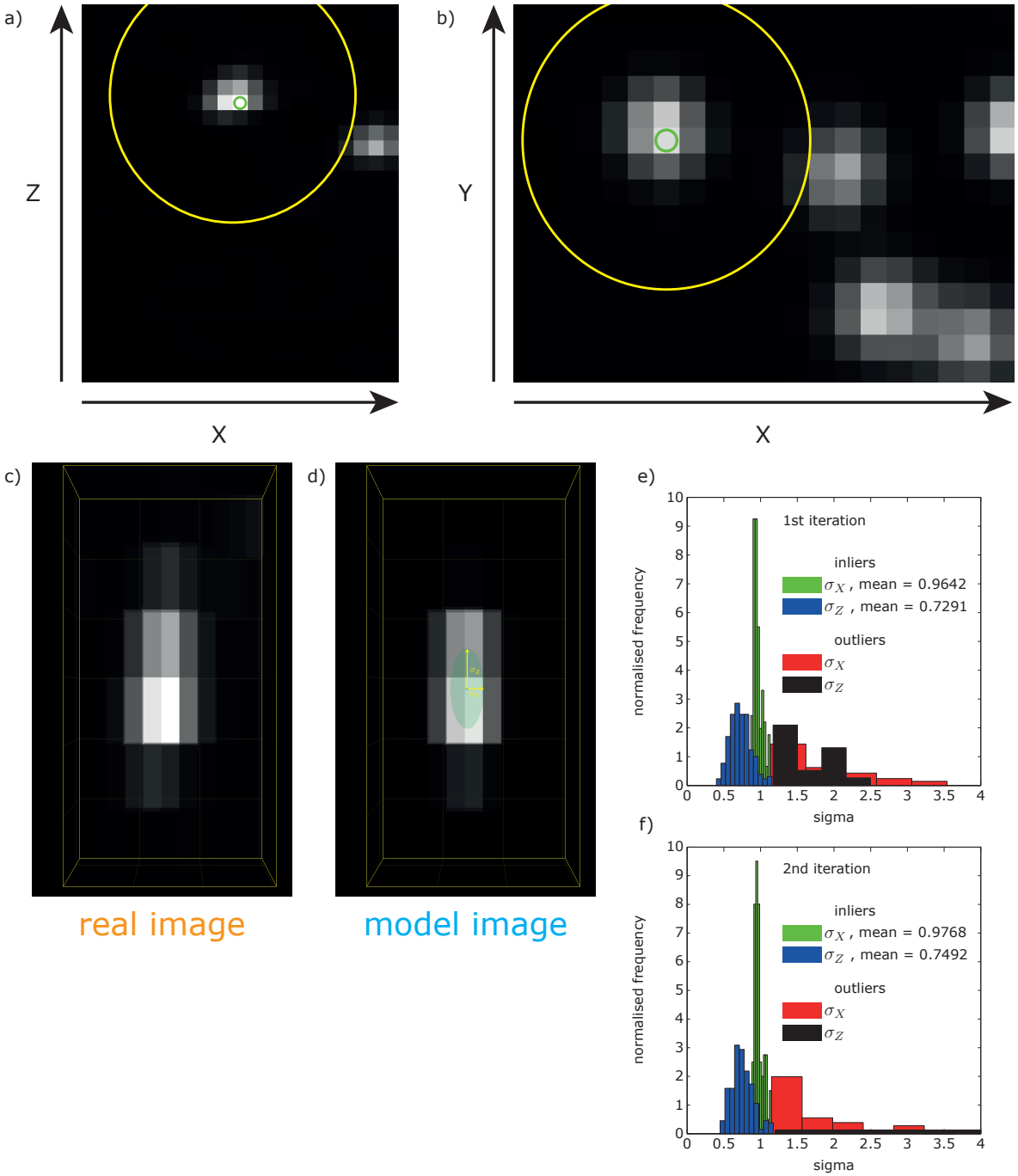


**Figure 3.9:** Illustration of PSF estimation. **a)**, **b)** Example of an isolated local maxima shown as a plane in ZX and XY respectively. Local maxima voxel marked with a green circle, minimum isolation distance marked with a yellow circle. **c)** Cropped 3D image around the voxel in question (voxel dimensions represent real physical voxel dimensions). **d)** Model image of a Single Gaussian fit to the cropped image. Gaussian standard deviations ($\sigma_X$, $\sigma_Z$) marked with yellow arrows. **e)** Results from first iteration of fitting (initial *i.e.* theoretical $\sigma_X, \sigma_Z = 0.8547, 0.8008$ respectively). Data from 225 image fits resulting in 165 and 209 inliers for $\sigma_X$ and $\sigma_Z$ respectively. **f)** Results from second iteration of fitting. Data from 222 image fits resulting in 160 and 207 inliers for $\sigma_X$ and $\sigma_Z$ respectively. Both $\sigma_X$ and $\sigma_Z$ change by less than 5% resulting in an end to iterative fitting. Note that $\sigma_X$ and $\sigma_Z$ given in image space units throughout.

### 3.4.3 Fitting Algorithm

Here the procedure for fitting kinetochore and spindle pole positions within an image is described. Figure 3.10 shows an overview of the algorithm.

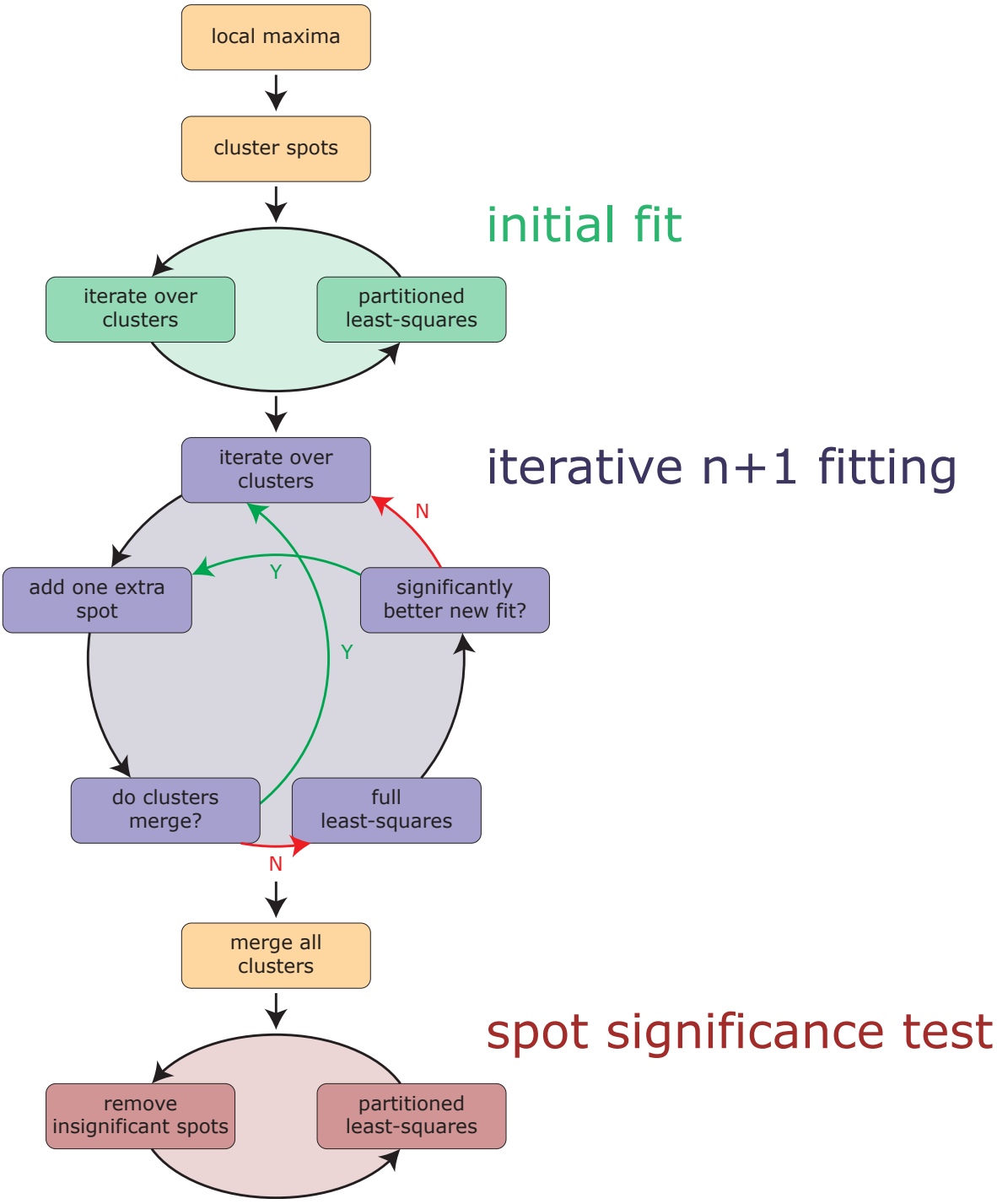


**Figure 3.10:** Overview of the Gaussian mixture-model-fitting algorithm.

#### 3.4.3.1 Initial Fitting

Maxima locations within each image are clustered based on their separations. Local maxima are grouped with others that are both within $\lceil 9\sigma_x \rceil$ in XY and $\lceil 9\sigma_z \rceil$ in Z of each other. Then the clusters are processed separately while the spots within each cluster are jointly fitted. Only image voxels within the relevant cluster are used during the fitting, a voxel is considered part of the cluster if it is both within $\lceil 4\sigma_x \rceil$ in XY and $\lceil 4\sigma_z \rceil$ in Z of any cluster spot (note that this means a voxel can only belong to one and only one cluster). Each cluster is then fitted using partitioned least squares fitting as described in Section 3.4.1.2, with the positions of the local maxima used as the initial starting point. The advantage of using partitioned least-squares fitting over full least-squares fitting is that the function being minimised takes less input arguments ($3n$ as opposed to $4n + 1$) so in general fitting takes less time to converge to a solution (see Figure 3.8). Also spot amplitudes and the background amplitude do not have to be estimated before fitting. Figure 3.11 shows an example of image clustering on a single frame, indicating the image voxels assigned to each cluster.

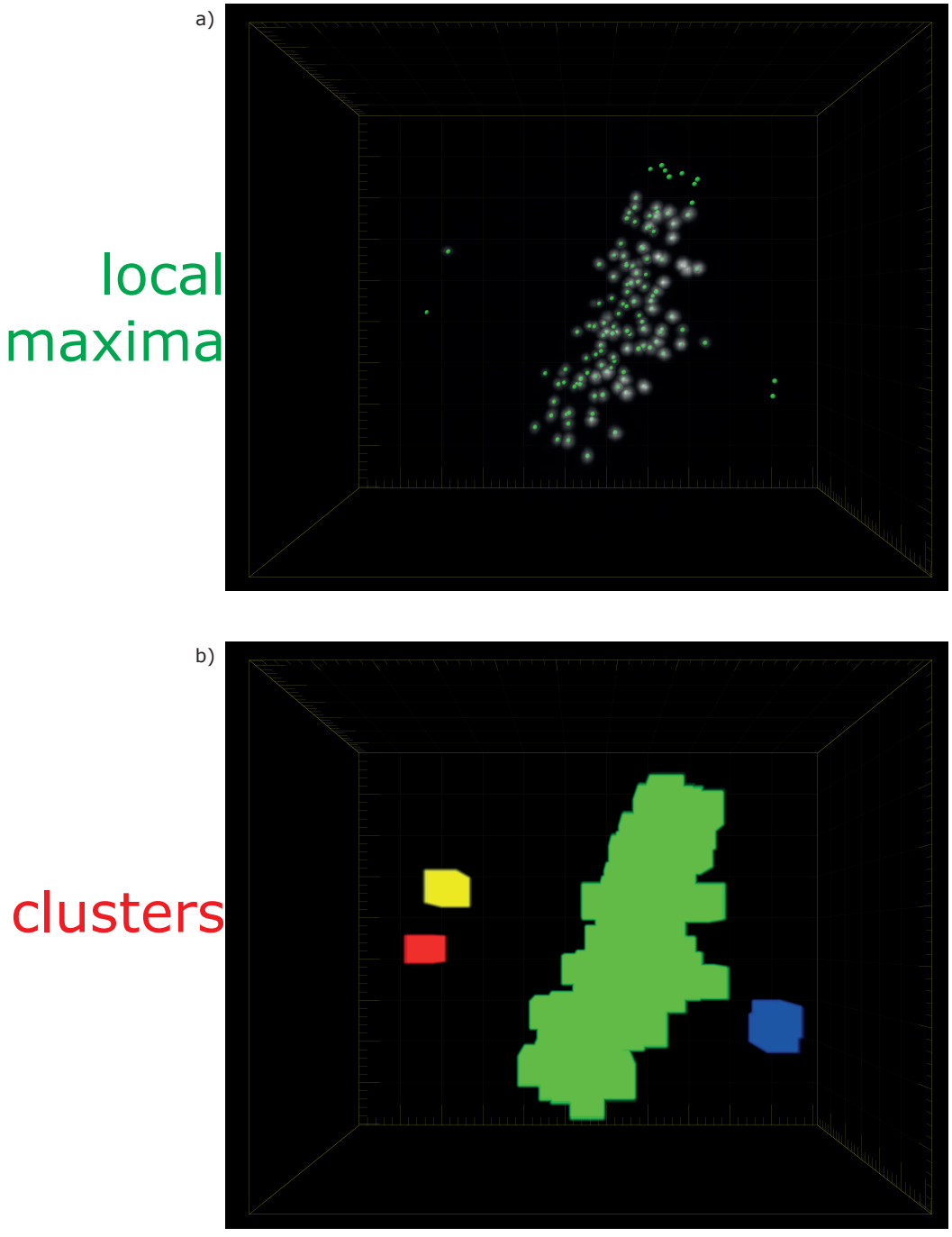


**Figure 3.11:** Feature clustering example. **a)** Example frame with local maxima marked with green spots. **b)** Clustering local maxima as described in Section 3.4.3.1 results in four clusters shown in green, red, blue and yellow.

#### 3.4.3.2 Iterative $n+1$ Kernel Fitting

Due to the conservative method of finding local maxima and the occasional close proximity of spots some features in each cluster could easily have been missed in the first round of fitting. So, to test for 'missing information' for each cluster one more spot is added at the voxel corresponding to the minimum of $F$ (Equation (3.5)) *i.e.* the point where the real image had its intensity highest over the model image. The new spot's spatial parameter upper and lower bounds are set to the maximum and minimum spatial range of the whole cluster respectively and the fitting is re-done. This gives two fitting attempts,

$$F_{\text{original}},\ \text{dof}_{\text{original}} \quad \text{and} \quad F_{\text{new}},\ \text{dof}_{\text{new}}$$

To test whether the new fit is significantly better the residual variance of the new fit is tested against the residual variance of the original fit. If a new spot has been found then the residual variance will be significantly lower in the new fit. The residual variances of the fits are

$$\text{R} = \frac{\|F\|_2^2}{\text{dof}}$$

because $R$ is generated by a sum of squares it is chi-squared distributed. If the new fit did not find a new spot $R_{\text{new}}$ should not be significantly different from $R_{\text{original}}$ and the ratio of the two $T = \frac{R_{\text{new}}}{R_{\text{original}}}$ should be F distributed with $\text{dof}_{\text{original}}$ and $\text{dof}_{\text{new}}$ degrees of freedom. Otherwise if the new fit did find a spot then $T$ will have an extreme value, the test is then a one-sided F-test

$$p = \mathit{fcdf}(T, \text{dof}_{\text{original}}, \text{dof}_{\text{new}})$$

where $\mathit{fcdf}(T, d1, d2)$ is the F cumulative distribution function of $T$ with $d1$ and $d2$ degrees of freedom and $p$ is the $p$-value of the test.

If $p$ is below a significance threshold (chosen to be 5%) then the test is said to have failed *i.e.* $R_{\text{new}}$ is significantly lower than $R_{\text{original}}$ and the new fit is accepted. The new

fit then becomes the original fit and the process is repeated until a new fit is found not to be significantly better, whereupon the new fit is rejected and the original fit is kept.

Before fitting a new spot the cluster is checked to make sure it contains enough voxels for the fitting since there may be voxels within $\lceil 4\sigma \rceil$ of the new spot that were not part of the original cluster for example if the new spot is near an edge of the cluster. If the cluster has to be resized then the previous fit is recalculated on the newly sized cluster for a fair comparison with the new fit. If a cluster is resized and the new fit is accepted then it is checked whether or not it has now merged with any existing clusters. If clusters do merge together then iterative fitting is performed for the new larger cluster.

For partitioned least squares fitting each evaluation of $F$ requires an OLS optimisation to calculate spot and background amplitudes (see Section 3.4.1.2), something which is not required when performing full least squares fitting. During iterative $n+1$ fitting most spots will be at or very close to their final positions and amplitudes *i.e.* $\|F\|_2^2$ should be close to its minimum (within tolerance). Because of this it becomes advantageous to use full least squares fitting when testing potential new spots; the cost of longer convergence times is minimal when fewer evaluations are needed and in fact is outweighed by the time saved in not calculating all spot and background amplitudes during each evaluation. Figure 3.12 shows an example of the $N+1$ fitting procedure.

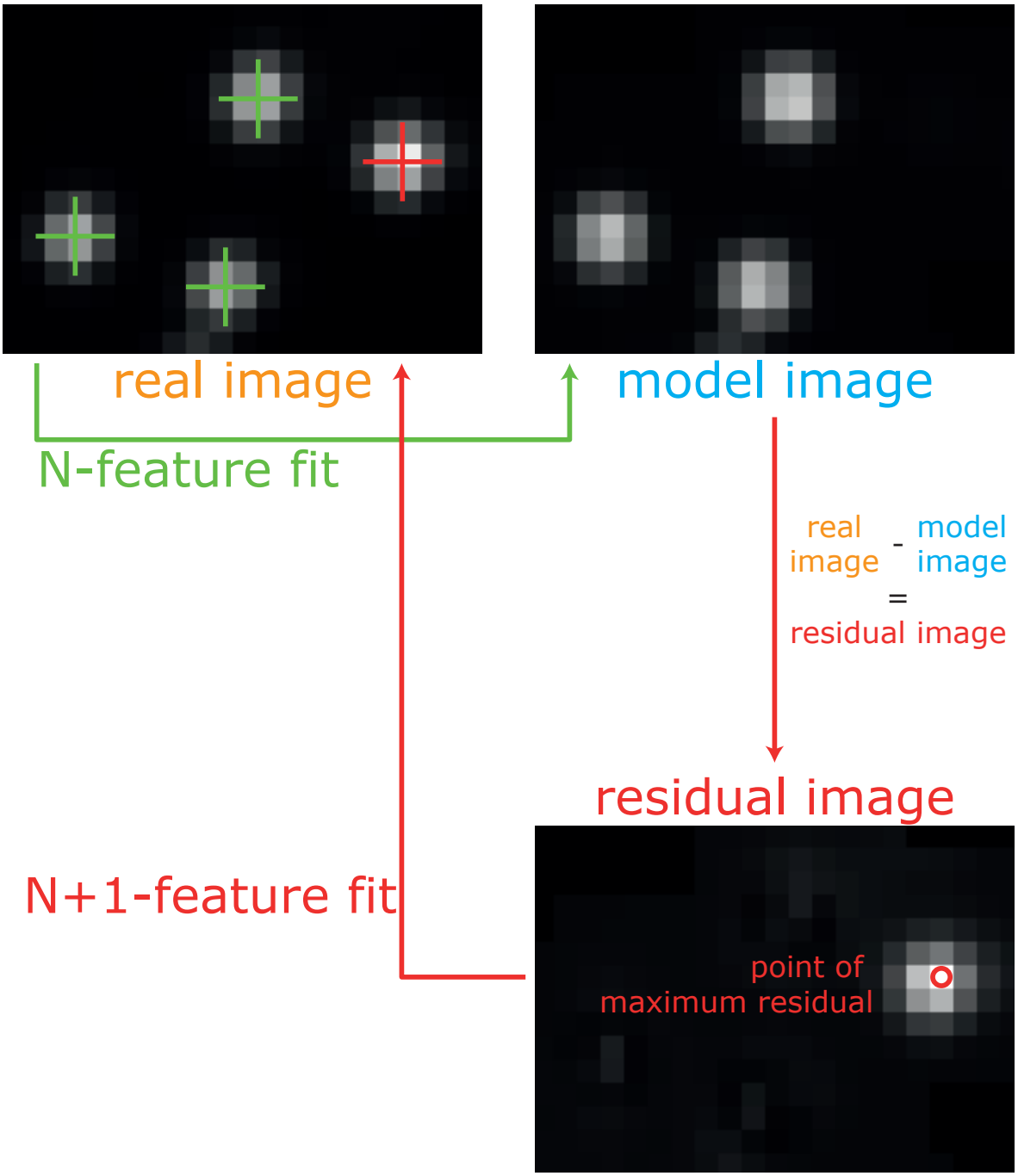


**Figure 3.12:** N+1 spot fit example. The real image is first fit with the 3 spots marked with green crosses. From the residual image *i.e.* the difference between the real image and the 3-spot model image the voxel with the highest residual is chosen as the estimated location of a 4th spot (marked with a red circle). The fit of the 4th spot is marked with a red cross.

#### 3.4.3.3 Finial Fitting plus Test of Spot Significance

After iterative $n+1$ fitting is complete for all clusters, all spots within the image are jointly re-fitted and each spot is tested for significance. Specifically each spot is tested for a significant amplitude (relative to its variance) and each pair of spots is tested for significant separation (relative to their joint variance). This is important because a spot cannot be said to be detectable if it does not have a significant amplitude and it cannot be said to be separable from another spot if it does not have a significant displacement from that spot.

The covariance matrix $c$ of all the spot parameters is calculated after the joint fit by (3.22). The testing procedure is as follows:

First the amplitudes are tested. The test statistic for each spot is

$$T_i^{\text{amp}} = \frac{a_i}{\sqrt{c_{a_i a_i} + R}}$$

where $a_i$ is the amplitude of spot $i$, $c_{a_i a_i}$ is the variance of the amplitude of spot $i$ (from the main diagonal of the covariance matrix) and $R$ is the residual variance of the least-squares fit (the variance of the overall fit contributes to the variance in the amplitude *i.e.* the amplitude of a spot should be significant compared to the variance of the overall fit as well). $T_i^{\text{amp}}$ is assumed to be Student's $t$-distributed with the same degrees of freedom as the least-squares fit. The test is then

$$p_i^{\text{amp}} = 1 - tcdf(T_i^{\text{amp}}, \text{dof})$$

where $tcdf(T_i^{\text{amp}}, d)$ is the Student's $t$ cumulative distribution function of $T_i^{\text{amp}}$ with $d$ degrees of freedom and $p_i^{\text{amp}}$ is the $p$-value of the test. After all spots are tested if any spot has a $p$-value above a threshold (chosen to be 5%) the spot with the largest $p$-value is removed and the fitting is re-done. This is then repeated until no spot has a $p$-value above the threshold.

Secondly the spot separations are tested. The test statistic for each pair of spots is

$$T_{ij}^{\text{dis}} = \frac{d_{ij}}{\text{std}_{ij}^{\text{dis}}}$$

where $d_{ij}$ is the distance between spots $i$ and $j$

$$d_{ij} = \sqrt{(x_i - x_j)^2 + (y_i - y_j)^2 + (z_i - z_j)^2}$$

and $\text{std}_{ij}^{\text{dis}}$ is the estimated standard deviation of the distance between spots $i$ and $j$. $\text{std}_{ij}^{\text{dis}}$ is calculated using the standard linear Gaussian propagation of errors, that is given a value $w$ created by an operation on $x$, $w = Hx$ the covariance of $w$ is $Q = HCH^T$ where $C$ is the covariance of $x$. In this case

$$x = \begin{pmatrix} x_i \\ y_i \\ z_i \\ x_j \\ y_j \\ z_j \end{pmatrix},$$

$$H = \begin{pmatrix} x_i - x_j & y_i - y_j & z_i - z_j & x_j - x_i & y_j - y_i & z_j - z_i \end{pmatrix} \frac{1}{d_{ij}}$$

and

$$C = \begin{bmatrix} c_{x_i x_i} & c_{x_i y_i} & c_{x_i z_i} & c_{x_i x_j} & c_{x_i y_j} & c_{x_i z_j} \\ c_{y_i x_i} & c_{y_i y_i} & c_{y_i z_i} & c_{y_i x_j} & c_{y_i y_j} & c_{y_i z_j} \\ c_{z_i x_i} & c_{z_i y_i} & c_{z_i z_i} & c_{z_i x_j} & c_{z_i y_j} & c_{z_i z_j} \\ c_{x_j x_i} & c_{x_j y_i} & c_{x_j z_i} & c_{x_j x_j} & c_{x_j y_j} & c_{x_j z_j} \\ c_{y_j x_i} & c_{y_j y_i} & c_{y_j z_i} & c_{y_j x_j} & c_{y_j y_j} & c_{y_j z_j} \\ c_{z_j x_i} & c_{z_j y_i} & c_{z_j z_i} & c_{z_j x_j} & c_{z_j y_j} & c_{z_j z_j} \end{bmatrix}$$

where

$c_{x_i x_j}$ is the covariance between $x_i$ and $x_j$ etc. So

$$\mathrm{std}_{ij}^{\mathrm{dis}} = \sqrt{HCH^T}$$

$T_{ij}^{\mathrm{dis}}$ is assumed to be Student's $t$-distributed with the same degrees of freedom as the least-squares fit. The test is then

$$p_i^{\mathrm{dis}} = 1 - tcdf\left(T_i^{\mathrm{dis}}, \mathrm{dof}\right)$$

After all pairs of spots are tested if any have a $p$-value above a threshold (chosen to be 5%) then of the pair that had the largest $p$-value the spot with the lowest amplitude is removed and the fitting is re-done. This is then repeated until no pairs of spots have a $p$-value above the threshold.

### 3.4.4 Gaussian Spot Fitting Accuracy

Uncertainties in spot positions from Gaussian fitting are determined directly from the covariance of the model fit (see Section 3.4.1.5); the uncertainty in the spot parameters is defined as the square-root of the parameter variances, so for parameter $i$

$$\eta_i = \sqrt{\mathrm{c}_{ii}}$$

where c is the covariance matrix of the fit.

Figure 3.13 shows the uncertainties of spot positions across a range of cells. Position uncertainties in X and Y are grouped together as they are equivalent and have a median value of 5nm with a tail stretching out to approximately 40nm. Uncertainties in Z have a much broader distribution due to the greater voxel dimension in Z compared to X and Y (500nm versus 139nm); the distribution has a median value of 16.3nm with a tail stretching out to approximately 140nm.

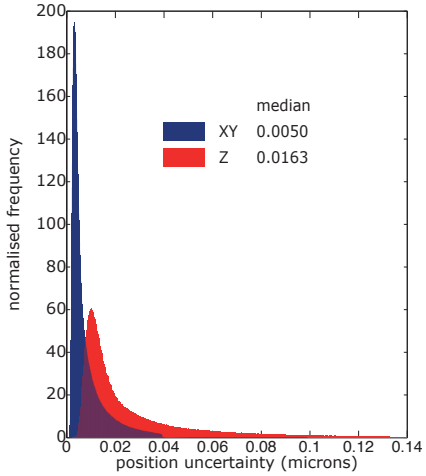


**Figure 3.13:** Uncertainties in Gaussian fitted spot positions. Histograms of the uncertainly in position of Gaussian fitting spots in XY (blue) and Z (red) determined as described in Section 3.4.4. Distribution medians shown in figure legend. Data acquired from 2,689,550 spot fits to 21,144 image frames from 145 movies of untreated cells.

## 3.5 Frame Alignment by Metaphase Plate Fitting

To measure kinetochore dynamics along their principle direction of motion *i.e.* towards and away from the metaphase plate the position and rotation of the plate was estimated in each movie frame. Fitting a metaphase plate in each movie frame also allowed the main problems associated with rotations to be mostly removed, which aided with frame to frame particle assignments during tracking. Plane fitting was carried out using the method used in [96] with an extra step in the initial estimation of the aligned feature set *i.e.* feature clustering.

### 3.5.1 Estimation of Aligned Feature Set

First the kinetochores that had been identified in a frame were divided into two populations: those that were aligned to the metaphase plate and those that weren't. To estimate the population of aligned kinetochores, firstly the located spots in each frame were clustered together with spots that were within 3$\mu$m of each other. Kinetochores aligned to the plate were expected to form one cluster with other clusters formed by distant outlying kinetochores and/or spindle-poles. Starting with the largest population cluster (since the majority of kinetochores were expected to be aligned) a plate fit was attempted on each set. If a plate could not be fit to a cluster the next largest was tested until either a plate was fitted or no plate was assigned to the frame. The population of aligned kinetochores was then refined to remove additional unaligned kinetochores by analysing the distribution of the mean distance between a kinetochore and its five nearest neighbours $d_5^{nn}$ within the cluster. The majority of kinetochores were expected to be aligned and have a small nearest neighbour distance to at least 5 other aligned kinetochores. Therefore any outliers in the distribution of $d_5^{nn}$ would indicate spots that weren't aligned. Outliers were filtered using LMS fitting of the mean (Section 3.2). Figure 3.14 gives an example of an initial aligned feature estimation for a single frame. Figure 3.14a and b show the feature positions within a frame and their clustering based on connectivity with other features less than 3$\mu$m away. Of the resulting three clusters the first cluster (shown in green) is tested first for a metaphase plate (which is successful). Figure 3.14c and d show the removal of potentially unaligned features based on the mean distance between each feature and its five nearest

neighbours. LMS fitting was used to remove outliers, shown in red.

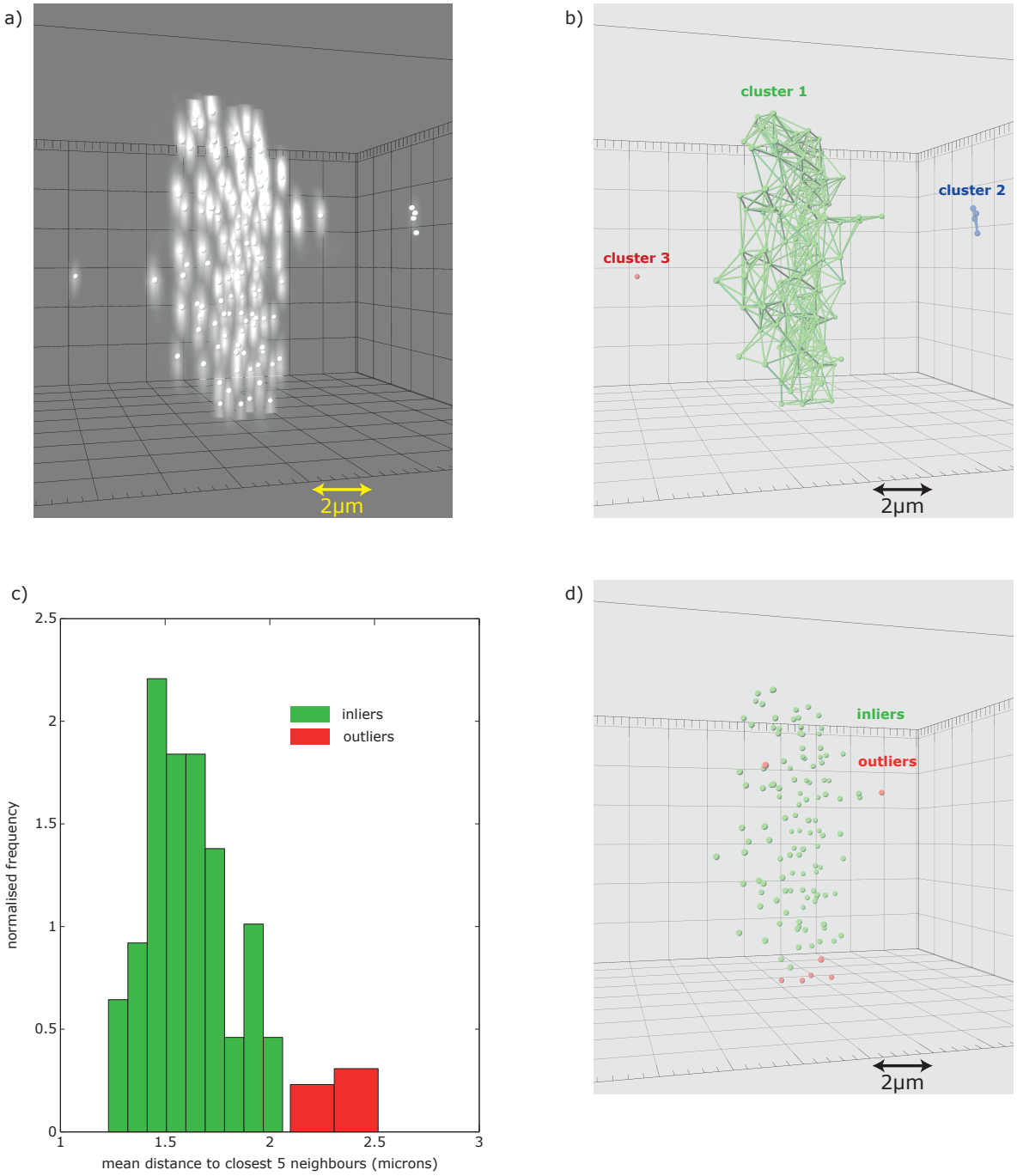


**Figure 3.14:** Metaphase plate fit: feature clustering. **a)** Rendered 3D image of a single frame with spot positions overlaid with silver spheres. **b)** Clustering of features based on connectivity. Features were connected with other features less than 3$\mu$m away (connections shown in figure), with the resulting sub-graphs forming clusters. Clusters were tested for a metaphase plate in descending order of feature number (*i.e.* starting with cluster 1 shown in green). **c)** Histogram of mean distance to the five nearest neighbours for all features in cluster 1; outliers (red) were removed by LMS fitting of the distribution mean. **d)** Inlier (green) and outlier (red) feature positions (based on LMS fitting of the distribution mean). Only the inliers were used for initial plate fitting.

### 3.5.2 Metaphase Plate Fitting by Eigenvalue Decomposition

The centre of the metaphase plate in each frame was taken as the centre of mass of the inlying kinetochores. The orientation of the plate was calculated by the eigenvalue decomposition of the covariance matrix of aligned kinetochore positions. The resultant eigenvectors described the orthogonal directions of scatter of the aligned kinetochores and the corresponding eigenvalues parameterised the degree of scatter in that direction. Kinetochores aligned at the metaphase plate would be expected to show weak scatter in one direction (normal to the plate) compared to the other two. Therefore a plate was fitted to a cluster if the ratio between the smallest eigenvalue and the mean of the other two was smaller than a given threshold, chosen to be 1/3. To determine a consistent normal direction to the fitted plate the eigenvectors were mapped between frames by minimising the global rotation of the vectors. The normal direction to the plate was then chosen as the eigenvector that had the lowest cost $c = \sum_{\text{frames}} (r/g)$ where $r$ was the modulus of the vector's rotation angle between the current and previous frame and $g$ was the geometric mean difference between the vector's corresponding eigenvalue and the other two eigenvalues in the current frame. The cost function for the normal direction was structured this way since the eigenvector representing the normal direction of the metaphase plate was expected to show a larger difference in eigenvalues compared to the other two vectors and was expected to undergo smaller rotations compared to the other two vectors. Figure 3.15 gives an example of eigenvector assignment between frames and selecting the normal direction based on the eigenvector cost.

In frames where a plate was fitted the normal direction to the plate was the eigenvector selected via the cost function described above. One of the in-plane vectors describing the plate was set parallel to the XY plane in raw coordinates and the other was set perpendicular to the first and the normal *i.e.* if the normal direction is described by the normalised vector $n$ where

$$n = \begin{pmatrix} x_n \\ y_n \\ z_n \end{pmatrix}$$

then the plane vector $p_1$ parallel to the XY plane is

$$p_1 = \begin{pmatrix} x_{p1} \\ y_{p1} \\ z_{p1} \end{pmatrix} = \begin{pmatrix} -y_n \\ x_n \\ 0 \end{pmatrix} \frac{1}{\sqrt{x_n^2 + y_n^2}}$$

and the other plane vector $p_2$ is

$$p_2 = \begin{pmatrix} x_{p2} \\ y_{p2} \\ z_{p2} \end{pmatrix} = \begin{pmatrix} x_n \\ y_n \\ z_n \end{pmatrix} \times \begin{pmatrix} x_{p1} \\ y_{p1} \\ z_{p1} \end{pmatrix} = \begin{pmatrix} -z_n x_n \\ -z_n y_n \\ x_n^2 + y_n^2 \end{pmatrix} \frac{1}{\sqrt{x_n^2 + y_n^2}}$$

Together these vectors form the matrix $S$ that defines the plane coordinate system

$$S = \begin{bmatrix} n & p_1 & p_2 \end{bmatrix} = \begin{bmatrix} x_n & x_{p1} & x_{p2} \\ y_n & y_{p1} & y_{p2} \\ z_n & z_{p1} & z_{p2} \end{bmatrix} \tag{3.23}$$

The inverse of $S$ forms the rotation matrix that transforms raw coordinates to rotated coordinates

$$\begin{pmatrix} x_r \\ y_r \\ z_r \end{pmatrix} = S^{-1} \times \begin{pmatrix} x - c_x \\ y - c_y \\ z - c_z \end{pmatrix} \tag{3.24}$$

where $c_x$, $c_y$ and $c_z$ are the centre of mass components in X, Y and Z respectively.

Spot coordinates were rotated relative to this plate. Spots were then redefined as either aligned or unaligned based on their distance from the plate. Unaligned spots were those whose distance from the plate was an outlier (again found by LMS fitting of the mean with $k = 2.5$). The aligned or unaligned grouping was used in frame to frame tracking of features, allowing different tracking parameters to be used for aligned features compared to unaligned ones, which were expected to display different dynamics. For the vast majority of movies of kinetochores during metaphase a plate was fitted to every frame before anaphase, however in cases where a plate was not fit the coordinate system was taken from the previous frame, or from the next frame for

any time-points before the first plate-fit. For these frames all spots were considered to be aligned for the purposes of assigning tracking parameters. Figure 3.16 gives an example of a final plate fit to a frame and the re-classification of aligned and unaligned features based on the normal distance to the plate.

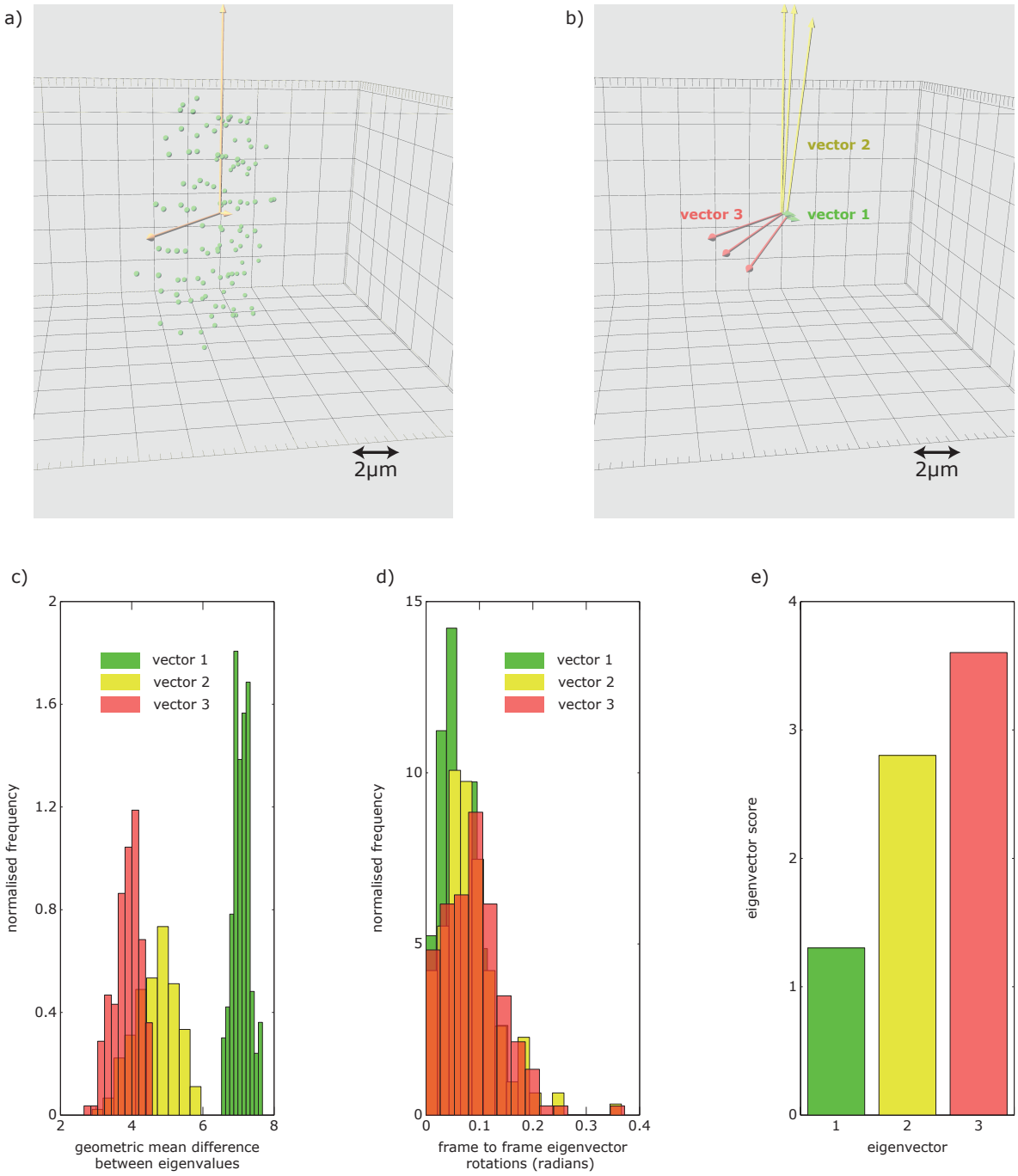


**Figure 3.15:** Metaphase plate fit: calculating and assigning eigenvectors. **a)** Inlier spot positions (from Figure 3.14d) marked with green spheres along with eigenvectors of the spots' covariance matrix indicated by orange arrows (origin taken as the centre of mass of the inlier spots). Relative vector magnitudes proportional to their relative eigenvalue sizes. **b)** Eigenvectors from three subsequent frames. Vectors paired with corresponding vectors in subsequent frames by minimising global rotation of all three vectors between frames. The three vector groups are distinguished with different colours (green, yellow and red). **c)** Histograms of the geometric mean difference between the eigenvalues of each eigenvector group. **d)** Histograms of the frame to frame rotation of each eigenvector group. **e)** Score of each eigenvector group ($\sum_{\text{frames}}(r/g)$ where $r$ is the frame to frame rotation and $g$ is the geometric mean difference in eigenvalues). Vector 1 (green) has the lowest score therefore is assigned as the normal direction to the metaphase plate in each frame.

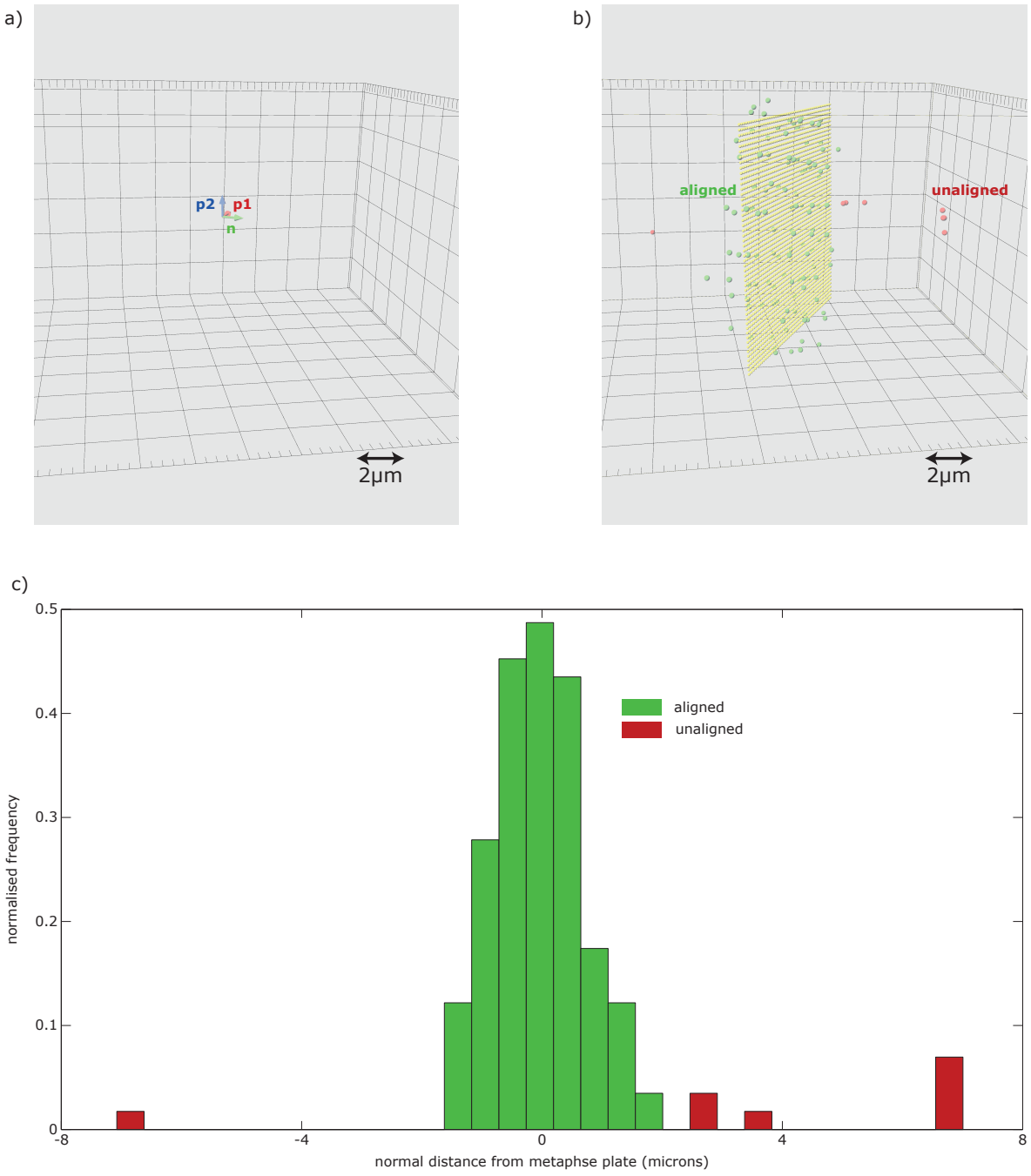


**Figure 3.16:** Metaphase plate fit: final plate fit. **a)** Metaphase plate vectors for a single frame. Normal direction $n$ (green) calculated by eigenvector fit (Figure 3.15). In-plane vector $p_1$ (red) perpendicular to $n$ and parallel to the microscope (raw coordinate) XY plane. In-plane vector $p_2$ (blue) perpendicular to both $n$ and $p_1$. **b)** The metaphase plate fit (yellow) along with all spots in the frame. Final spot classification based on normal distance to the plate. Aligned features marked in green and unaligned features marked in red. **c)** Histogram of spot distances from the metaphase plate. LMS mean fitting (with $k = 2.5$) used to identify outliers *i.e.* unaligned features.

### 3.5.3 Initial Estimation of Anaphase Frames

Automatic estimation of movie frames where a cell has entered anaphase is an important step since kinetochore dynamics and their spatial distribution change abruptly at the onset of anaphase, which could potentially affect downstream steps such as correctly identifying sister kinetochore pairs. Also there is a need for time-points of kinetochores in anaphase to be separated or filtered out from the final data output since ultimately interest is in oscillation dynamics that cease at anaphase onset. The initial detection of any anaphase frames was carried out using the method in [96]. The movie was searched for a set of frames lasting from time $t$ until the end of the movie where the standard deviation of spot distances from the metaphase plate in each frame $S_t$ was larger than the value over the five previous frames, $S_t > S_{t-i} \quad i = \{1, 2, 3, 4, 5\}$ . If this set existed then all member frames were labelled as anaphase.

## 3.6 Initial Frame to Frame Feature Tracking

Frame to frame tracking of features was carried out using the multiple hypothesis tracking (MHT) algorithm as presented in [152] using a similar set-up as presented in [96] with modification to some of the tracking parameters. Features were tracked in their rotated (plate fitted) coordinate system. The algorithm first assigned features between consecutive frames, allowing for birth and death of track segments, by formulating the assignment as a linear assignment problem (LAP) solved using the algorithm presented in [153]. Assignments were spatially optimal but temporally greedy since linking was solved on a frame-by-frame basis. Allowing for birth and death of all track segments made assignments robust to particle disappearances. Costs of linking features were derived from Brownian models of the particles' previous motion, see [152] and its associated supplementary information. The maximum search radius for potential feature links was based on the particles' previous motion and the particles' nearest neighbour density with a user-set maximum cut-off, see [152] supplementary information. The maximum search radius for unaligned features was set higher than for aligned features. Finally track segments were linked together, again by formulating the assignment as a LAP, in a globally (spatially and temporally) optimal manner. This allowed par-

ticle tracking to account for temporary particle disappearances. Figure 3.17 shows a diagram representing features assignments using MHT.

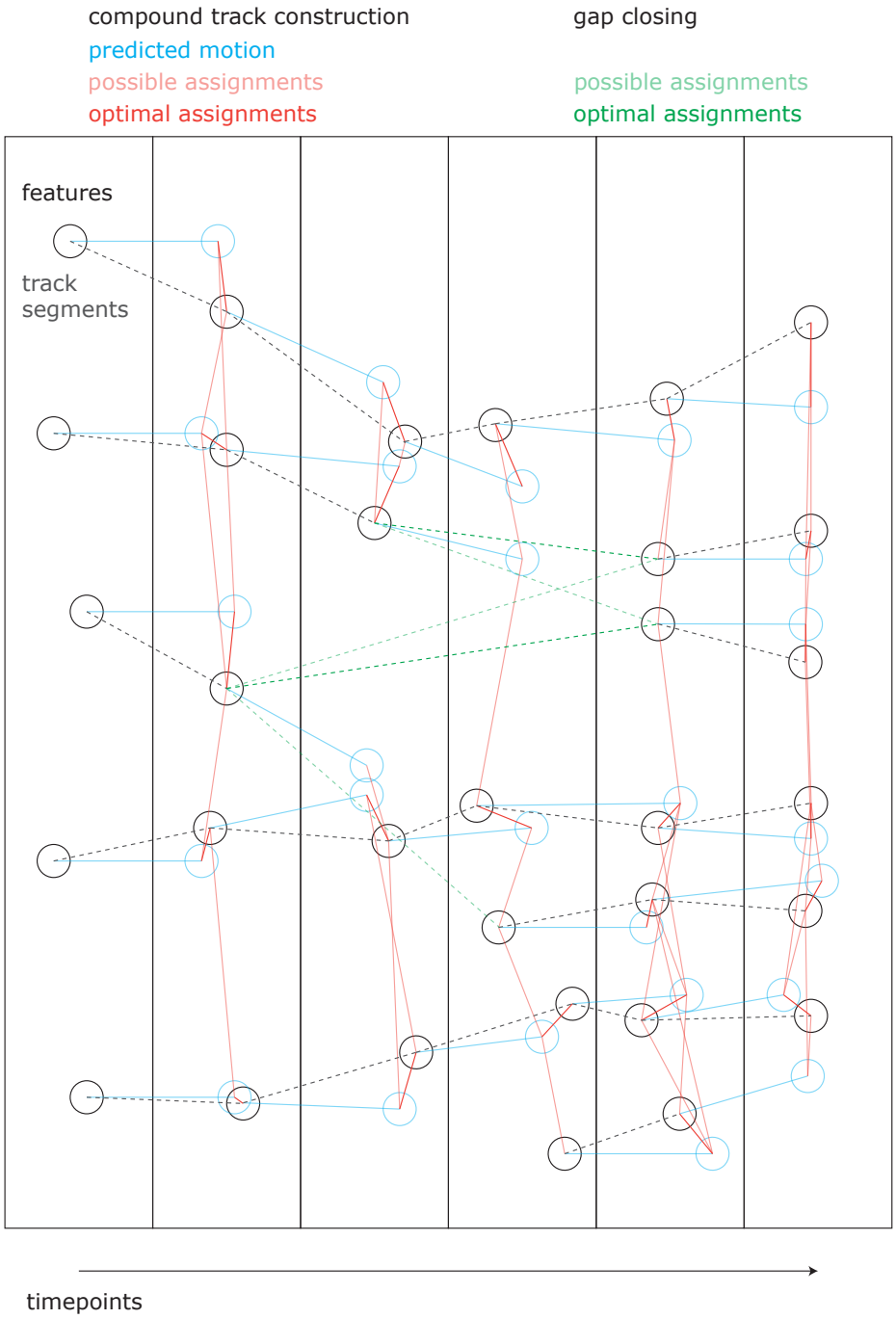


**Figure 3.17:** Diagram of multiple hypothesis frame to frame tracking. Features at each timepoint (black circles) are first linked frame-to-frame. Compound tracks (black dashed lines) have their positions in the next frame predicted based on their previous dynamics (blue lines and circles). Potential assignment of features (light red lines) in each frame based on displacements between predicted and actual features (up to a cutoff). Optimal assignments (red lines) result in the lowest sum of displacements in each frame. Gaps in tracks are closed where possible. Assignments between incomplete tracks (light green dashed lines) based on the distance between track ends and the angle between track segments (up to appropriate cutoffs). Optimal assignments (green dashed lines) results in the lowest sum of displacements.

## 3.7 Frame Alignment by Minimisation of Frame to Frame Displacements

Frame alignment by metaphase plate fitting can potentially suffer due to four reasons: 1) Since the entire metaphase plate is not captured in each movie frame there is the possibility of some ambiguity when assigning the direction of least scatter by eigenvalue decomposition. This could result in an artificial 'wobble' of the fitted plate, adding noise to the rotated particle positions over time. 2) The rotation of the plate around its normal direction cannot be determined by eigenvalue decomposition and is always set parallel to the XY plane in raw coordinates. This means that global rotations of features around the normal axis cannot be removed from feature tracking or trajectory analysis. 3) Because of the possibility of temporary particle disappearances the estimate of the centre of the coordinate system *i.e.* the centre of mass of the aligned kinetochores could potentially suffer. This could also add noise to the rotated particle positions over time. 4) Any frames that did not have a plate fitted did not have a specifically estimated coordinate system, just a copy of the previous / next frame's coordinate system. In addition, conditions that did not have a metaphase plate had no estimated coordinate system.

To further refine the global metaphase coordinate system for a movie, each frame had its coordinate system rotated to minimise the sum of square displacements of features between itself and its target frame. Note that the metaphase plate is then defined as $x = 0$ in the aligned coordinate system. Of the frames with fitted plates the one with the smallest ratio of normal-direction eigenvalue to the mean of its other two eigenvalues was determined as the frame with the 'best' plate fit. Or, if no plates were fit for the movie the first frame was chosen. This frame was the starting frame for minimisation. Working away from the starting frame in time each frame was rotated to match its corresponding target frame *i.e.* if the chosen starting frame was at time $t$ frames $t + 1$ and $t - 1$ were targeted to frame $t$, then frame $t + 2$ was targeted to frame $t + 1$ and frame $t - 2$ was targeted to frame $t - 1$ etc. until all frames were processed.

To rotate a frame's coordinate system to match a target frame, tracked features between

the two frames were selected. Features that were classified as unaligned in either frame were discarded. The current rotated coordinates of the features were taken and the displacements in X, Y and Z were calculated for each feature and pooled together. The mean displacement was calculated using LMS fitting (Section 3.2) and any features that were identified as outliers were discarded, this was to ensure that when displacement minimisation was being carried out that unusually large displacements wouldn't skew the results.

The frame's coordinate system was then linearly-shifted and rotated to minimise the sum of squares of the vector $D(r)$.

$$\min_r \| D(r) \|_2^2 \tag{3.25}$$

$D$ is a $3n$ length vector of combined $n$ feature displacements between the frame and its target frame.

$$D = \begin{pmatrix} x_1^\tau - x_1^t \\ \vdots \\ x_n^\tau - x_n^t \\ y_1^\tau - y_1^t \\ \vdots \\ y_n^\tau - y_n^t \\ z_1^\tau - z_1^t \\ \vdots \\ z_n^\tau - z_n^t \end{pmatrix} \tag{3.26}$$

where $\{x_i^\tau, y_i^\tau, z_i^\tau\}$ are the $\{\mathrm{X}, \mathrm{Y}, \mathrm{Z}\}$ coordinates of feature $i$ after transformation and $\{x_i^t, y_i^t, z_i^t\}$ are the $\{\mathrm{X}, \mathrm{Y}, \mathrm{Z}\}$ coordinates of feature $i$ in the target frame.

The vector $r$ in (3.25) is a set of position and rotation transforms to be applied to the feature coordinates.

$$r = \begin{pmatrix} s_x \\ s_y \\ s_z \\ \phi \\ \theta \\ \psi \end{pmatrix} \tag{3.27}$$

$s_x$, $s_y$ and $s_z$ are linear shifts to be applied to the feature coordinates in X, Y and Z respectively. $\phi$, $\theta$ and $\psi$ are Euler angles for rotations to be applied to the feature coordinates around the X, Y and Z axes respectively.

$$\begin{pmatrix} x_i^\tau & y_i^\tau & z_i^\tau \end{pmatrix} = \begin{pmatrix} x_i + s_x & y_i + s_y & z_i + s_z \end{pmatrix} \times R \tag{3.28}$$

where

$$R = \begin{bmatrix} \cos\psi & -\sin\psi & 0 \\ \sin\psi & \cos\psi & 0 \\ 0 & 0 & 1 \end{bmatrix} \times \begin{bmatrix} \cos\theta & 0 & \sin\theta \\ 0 & 1 & 0 \\ -\sin\theta & 0 & \cos\theta \end{bmatrix} \times \begin{bmatrix} 1 & 0 & 0 \\ 0 & \cos\phi & -\sin\phi \\ 0 & \sin\phi & \cos\phi \end{bmatrix} = \begin{bmatrix} \cos\psi\cos\theta & \cos\psi\sin\theta\sin\phi - \sin\psi\cos\phi & \sin\psi\sin\phi + \cos\psi\sin\theta\cos\phi \\ \sin\psi\cos\theta & \cos\psi\cos\phi + \sin\psi\sin\theta\sin\phi & \sin\psi\sin\theta\cos\phi - \cos\psi\sin\phi \\ -\sin\theta & \cos\theta\sin\phi & \cos\theta\cos\phi \end{bmatrix} \tag{3.29}$$

The Jacobian of $D$, $J_D$ is also calculated, as it is required for minimisation of $\|D\|_2^2$.

$$J_D = \begin{bmatrix} \frac{\partial D_1}{\partial s_x} & \frac{\partial D_1}{\partial s_y} & \frac{\partial D_1}{\partial s_z} & \frac{\partial D_1}{\partial \phi} & \frac{\partial D_1}{\partial \theta} & \frac{\partial D_1}{\partial \psi} \\ \vdots & \vdots & \vdots & \vdots & \vdots & \vdots \\ \frac{\partial D_{3n}}{\partial s_x} & \frac{\partial D_{3n}}{\partial s_y} & \frac{\partial D_{3n}}{\partial s_z} & \frac{\partial D_{3n}}{\partial \phi} & \frac{\partial D_{3n}}{\partial \theta} & \frac{\partial D_{3n}}{\partial \psi} \end{bmatrix} \tag{3.30}$$

The first column of $J_D$ are the partial derivatives of $D$ with respect to the linear shift in X, which is just the X component of the rotation matrix *i.e.* the first row of $R$.

$$\begin{pmatrix} \frac{\partial D_1}{\partial s_x} \\ \vdots \\ \frac{\partial D_n}{\partial s_x} \\ \frac{\partial D_{n+1}}{\partial s_x} \\ \vdots \\ \frac{\partial D_{2n}}{\partial s_x} \\ \frac{\partial D_{2n+1}}{\partial s_x} \\ \vdots \\ \frac{\partial D_{3n}}{\partial s_x} \end{pmatrix} = \begin{pmatrix} R_{1,1} \\ \vdots \\ R_{1,1} \\ R_{1,2} \\ \vdots \\ R_{1,2} \\ R_{1,3} \\ \vdots \\ R_{1,3} \end{pmatrix} = \begin{pmatrix} \cos\psi\cos\theta \\ \vdots \\ \cos\psi\cos\theta \\ \cos\psi\sin\theta\sin\phi - \sin\psi\cos\phi \\ \vdots \\ \cos\psi\sin\theta\sin\phi - \sin\psi\cos\phi \\ \sin\psi\sin\phi + \cos\psi\sin\theta\cos\phi \\ \vdots \\ \sin\psi\sin\phi + \cos\psi\sin\theta\cos\phi \end{pmatrix}$$

Similarly the second and third columns are the partial derivatives of $D$ with respect to the linear shift in Y and Z respectively, which are the Y and Z components of the rotation matrix respectively *i.e.* the second and third rows of $R$.

$$\begin{pmatrix} \frac{\partial D_1}{\partial s_y} \\ \vdots \\ \frac{\partial D_n}{\partial s_y} \\ \frac{\partial D_{n+1}}{\partial s_y} \\ \vdots \\ \frac{\partial D_{2n}}{\partial s_y} \\ \frac{\partial D_{2n+1}}{\partial s_y} \\ \vdots \\ \frac{\partial D_{3n}}{\partial s_y} \end{pmatrix} = \begin{pmatrix} R_{2,1} \\ \vdots \\ R_{2,1} \\ R_{2,2} \\ \vdots \\ R_{2,2} \\ R_{2,3} \\ \vdots \\ R_{2,3} \end{pmatrix} = \begin{pmatrix} \sin\psi\cos\theta \\ \vdots \\ \sin\psi\cos\theta \\ \cos\psi\cos\phi + \sin\psi\sin\theta\sin\phi \\ \vdots \\ \cos\psi\cos\phi + \sin\psi\sin\theta\sin\phi \\ \sin\psi\sin\theta\cos\phi - \cos\psi\sin\phi \\ \vdots \\ \sin\psi\sin\theta\cos\phi - \cos\psi\sin\phi \end{pmatrix}$$

$$\begin{pmatrix} \frac{\partial D_1}{\partial s_z} \\ \vdots \\ \frac{\partial D_n}{\partial s_z} \\ \frac{\partial D_{n+1}}{\partial s_z} \\ \vdots \\ \frac{\partial D_{2n}}{\partial s_z} \\ \frac{\partial D_{2n+1}}{\partial s_z} \\ \vdots \\ \frac{\partial D_{3n}}{\partial s_z} \end{pmatrix} = \begin{pmatrix} R_{3,1} \\ \vdots \\ R_{3,1} \\ R_{3,2} \\ \vdots \\ R_{3,2} \\ R_{3,3} \\ \vdots \\ R_{3,3} \end{pmatrix} = \begin{pmatrix} -\sin\theta \\ \vdots \\ -\sin\theta \\ \cos\theta\sin\phi \\ \vdots \\ \cos\theta\sin\phi \\ \cos\theta\cos\phi \\ \vdots \\ \cos\theta\cos\phi \end{pmatrix}$$

The fourth, fifth and sixth columns of $J_D$ are the partial derivative of $D$ with respect to the rotation angles $\phi$, $\theta$ and $\psi$ respectively; these values are calculated by multiplying the shifted coordinates by the derivative of the rotation matrix $R$ with respect to the angle in question.

$$\frac{\partial D}{\partial \phi} = \begin{pmatrix} x + s_x & y + s_y & z + s_z \end{pmatrix} \times \frac{\partial R}{\partial \phi}$$

where, from (3.29)

$$\frac{\partial R}{\partial \phi} = R^{\phi} = \begin{bmatrix} \cos\psi & -\sin\psi & 0 \\ \sin\psi & \cos\psi & 0 \\ 0 & 0 & 1 \end{bmatrix} \times \begin{bmatrix} \cos\theta & 0 & \sin\theta \\ 0 & 1 & 0 \\ -\sin\theta & 0 & \cos\theta \end{bmatrix} \times \begin{bmatrix} 0 & 0 & 0 \\ 0 & -\sin\phi & -\cos\phi \\ 0 & \cos\phi & -\sin\phi \end{bmatrix} =$$

$$\begin{bmatrix} 0 & \sin\psi\sin\phi + \cos\psi\cos\theta\cos\phi & \sin\psi\cos\phi - \cos\psi\sin\theta\sin\phi \\ 0 & \sin\psi\sin\theta\cos\phi - \cos\psi\sin\phi & -\cos\psi\cos\phi - sin\psi\sin\theta\sin\phi \\ 0 & \cos\theta\cos\phi & -\cos\theta\sin\phi \end{bmatrix} \tag{3.31}$$

$$\frac{\partial R}{\partial \theta} = R^{\theta} = \begin{bmatrix} \cos\psi & -\sin\psi & 0 \\ \sin\psi & \cos\psi & 0 \\ 0 & 0 & 1 \end{bmatrix} \times \begin{bmatrix} -\sin\theta & 0 & \cos\theta \\ 0 & 0 & 0 \\ -\cos\theta & 0 & -\sin\theta \end{bmatrix} \times \begin{bmatrix} 1 & 0 & 0 \\ 0 & \cos\phi & -\sin\phi \\ 0 & \sin\phi & \cos\phi \end{bmatrix} = \begin{bmatrix} -\cos\psi\sin\theta & \cos\psi\cos\theta\sin\phi & \cos\psi\cos\theta\cos\phi \\ -\sin\psi\sin\theta & \sin\psi\cos\theta\sin\phi & \sin\psi\cos\theta\cos\phi \\ -\cos\theta & -\sin\theta\sin\phi & -\sin\theta\cos\phi \end{bmatrix} \tag{3.32}$$

$$\frac{\partial R}{\partial \psi} = R^{\psi} = \begin{bmatrix} -\sin\psi & -\cos\psi & 0 \\ \cos\psi & -\sin\psi & 0 \\ 0 & 0 & 0 \end{bmatrix} \times \begin{bmatrix} \cos\theta & 0 & \sin\theta \\ 0 & 1 & 0 \\ -\sin\theta & 0 & \cos\theta \end{bmatrix} \times \begin{bmatrix} 1 & 0 & 0 \\ 0 & \cos\phi & -\sin\phi \\ 0 & \sin\phi & \cos\phi \end{bmatrix} = \begin{bmatrix} -\sin\psi\cos\theta & -\cos\psi\cos\phi - \sin\psi\sin\theta\sin\phi & \cos\psi\sin\phi - \sin\psi\sin\theta\cos\phi \\ \cos\psi\cos\theta & \cos\psi\sin\theta\sin\phi - \sin\psi\cos\phi & \sin\psi\sin\phi + \cos\psi\sin\theta\cos\phi \\ 0 & 0 & 0 \end{bmatrix} \tag{3.33}$$

A list of transformed coordinates multiplied by a rotation matrix is given by

$$\begin{bmatrix} x_1 + s_x & y_1 + s_y & z_1 + s_z \\ & \vdots & \\ x_n + s_x & y_n + s_y & z_n + s_z \end{bmatrix} \times \begin{bmatrix} R_{1,1} & R_{1,2} & R_{1,3} \\ R_{2,1} & R_{2,2} & R_{2,3} \\ R_{3,1} & R_{3,2} & R_{3,3} \end{bmatrix} = \begin{bmatrix} q(1,1) & q(1,2) & q(1,3) \\ & \vdots & \\ q(n,1) & q(n,2) & q(n,3) \end{bmatrix}$$

where

$$q(i,j) = R_{1,j}(x_i + s_x) + R_{2,j}(y_i + s_y) + R_{3,j}(z_i + s_z)$$

so using (3.31) the fourth column of the Jacobian $J_D$ is

$$\begin{pmatrix} \frac{\partial D_1}{\partial \phi} \\ \\ \vdots \\ \frac{\partial D_n}{\partial \phi} \\ \\ \frac{\partial D_{n+1}}{\partial \phi} \\ \\ \vdots \\ \frac{\partial D_{2n}}{\partial \phi} \\ \\ \frac{\partial D_{2n+1}}{\partial \phi} \\ \\ \vdots \\ \frac{\partial D_{3n}}{\partial \phi} \\ \\ \end{pmatrix} = \begin{pmatrix} (\sin\psi\sin\phi + \cos\psi\cos\theta\cos\phi)\,(y_1 + s_y) + \\ (\sin\psi\cos\phi - \cos\psi\sin\theta\sin\phi)\,(z_1 + s_z) \\ \vdots \\ (\sin\psi\sin\phi + \cos\psi\cos\theta\cos\phi)\,(y_n + s_y) + \\ (\sin\psi\cos\phi - \cos\psi\sin\theta\sin\phi)\,(z_n + s_z) \\ (\sin\psi\sin\theta\cos\phi - \cos\psi\sin\phi)\,(y_1 + s_y) + \\ (-\cos\psi\cos\phi - sin\psi\sin\theta\sin\phi)\,(z_1 + s_z) \\ \vdots \\ (\sin\psi\sin\theta\cos\phi - \cos\psi\sin\phi)\,(y_n + s_y) + \\ (-\cos\psi\cos\phi - sin\psi\sin\theta\sin\phi)\,(z_n + s_z) \\ (\cos\theta\cos\phi)\,(y_1 + s_y) + \\ (-\cos\theta\sin\phi)\,(z_1 + s_z) \\ \vdots \\ (\cos\theta\cos\phi)\,(y_n + s_y) + \\ (-\cos\theta\sin\phi)\,(z_n + s_z) \end{pmatrix}$$

and the fifth column from (3.32) is

$$\begin{pmatrix} \frac{\partial D_1}{\partial \theta} \\ \vdots \\ \frac{\partial D_n}{\partial \theta} \\ \frac{\partial D_{n+1}}{\partial \theta} \\ \vdots \\ \frac{\partial D_{2n}}{\partial \theta} \\ \frac{\partial D_{2n+1}}{\partial \theta} \\ \vdots \\ \frac{\partial D_{3n}}{\partial \theta} \end{pmatrix} = \begin{pmatrix} (-\cos\psi\sin\theta)(x_1+s_x)+(\cos\psi\cos\theta\sin\phi)(y_1+s_y)+ \\ (\cos\psi\cos\theta\cos\phi)(z_1+s_z) \\ \vdots \\ (-\cos\psi\sin\theta)(x_n+s_x)+(\cos\psi\cos\theta\sin\phi)(y_n+s_y)+ \\ (\cos\psi\cos\theta\cos\phi)(z_n+s_z) \\ (-\sin\psi\sin\theta)(x_1+s_x)+(\sin\psi\cos\theta\sin\phi)(y_1+s_y)+ \\ (\sin\psi\cos\theta\cos\phi)(z_1+s_z) \\ \vdots \\ (-\sin\psi\sin\theta)(x_n+s_x)+(\sin\psi\cos\theta\sin\phi)(y_n+s_y)+ \\ (\sin\psi\cos\theta\cos\phi)(z_n+s_z) \\ (-\cos\theta)(x_1+s_x)+(-\sin\theta\sin\phi)(y_1+s_y)+ \\ (-\sin\theta\cos\phi)(z_1+s_z) \\ \vdots \\ (-\cos\theta)(x_n+s_x)+(-\sin\theta\sin\phi)(y_n+s_y)+ \\ (-\sin\theta\cos\phi)(z_n+s_z) \end{pmatrix}$$

and the sixth column from (3.33) is

$$\begin{pmatrix} \frac{\partial D_1}{\partial \psi} \\ \vdots \\ \frac{\partial D_n}{\partial \psi} \\ \frac{\partial D_{n+1}}{\partial \psi} \\ \vdots \\ \frac{\partial D_{2n}}{\partial \psi} \\ \frac{\partial D_{2n+1}}{\partial \psi} \\ \vdots \\ \frac{\partial D_{3n}}{\partial \psi} \end{pmatrix} = \begin{pmatrix} (-\sin\psi\cos\theta)(x_1+s_x)+(-\cos\psi\cos\phi-\sin\psi\sin\theta\sin\phi)(y_1+s_y)+ \\ (\cos\psi\sin\phi-\sin\psi\sin\theta\cos\phi)(z_1+s_z) \\ \vdots \\ (-\sin\psi\cos\theta)(x_n+s_x)+(-\cos\psi\cos\phi-\sin\psi\sin\theta\sin\phi)(y_n+s_y)+ \\ (\cos\psi\sin\phi-\sin\psi\sin\theta\cos\phi)(z_n+s_z) \\ (\cos\psi\cos\theta)(x_1+s_x)+(\cos\psi\sin\theta\sin\phi-\sin\psi\cos\phi)(y_1+s_y)+ \\ (\sin\psi\sin\phi+\cos\psi\sin\theta\cos\phi)(z_1+s_z) \\ \vdots \\ (\cos\psi\cos\theta)(x_n+s_x)+(\cos\psi\sin\theta\sin\phi-\sin\psi\cos\phi)(y_n+s_y)+ \\ (\sin\psi\sin\phi+\cos\psi\sin\theta\cos\phi)(z_n+s_z) \\ 0 \\ \vdots \\ 0 \end{pmatrix}$$

The starting point for minimisation *i.e.* the initial state of $r$ (3.27) was set as follows: the linear shifts $s_x$, $s_y$ and $s_z$ were initially set to the current displacements between the components of the centre's of mass between the two frames

$$s_x = com_x^t - com_x$$

$$s_y = com_y^t - com_y$$

$$s_z = com_z^t - com_z$$

where $com$ is the centre of mass of the coordinate system of the current frame and $com^t$ is the centre of mass of the coordinate system of the target frame. The initial rotation angles were set by the current rotation between the two frame's coordinate systems. Given the coordinate systems of the current frame and the target frame, $S$ and $S^t$ respectively from (3.23), the rotation between the two $r$ was given by

$$r = S^t \times S^{-1}$$

the initial rotation angles $\{\phi, \theta, \psi\}$ between the two frames were calculated from the rotation matrix $r$

$$\{\phi,\theta,\psi\} \rightarrow \begin{cases} \theta = -\arcsin\left(r_{3,1}\right) & \\ \phi = atan2\left(\frac{r_{3,2}}{\cos\theta}, \frac{r_{3,3}}{\cos\theta}\right) & \text{if } |r_{3,1}| \neq 1 \\ \psi = atan2\left(\frac{r_{2,1}}{\cos\theta}, \frac{r_{1,1}}{\cos\theta}\right) & \\ & \\ \psi = 0 & \\ \theta = \frac{\pi}{2} & \text{if } r_{3,1} = -1 \\ \phi = atan2\left(r_{1,2}, r_{1,3}\right) & \\ & \\ \psi = 0 & \\ \theta = \frac{-\pi}{2} & \text{if } r_{3,1} = 1 \\ \phi = atan2\left(-r_{1,2}, -r_{1,3}\right) & \end{cases}$$

where

$$atan2(x,y) = 2\arctan\left(\frac{x}{\sqrt{x^2+y^2}+y}\right)$$

Minimisation of $\|D\|_2^2$ was performed with the *lsqnonlin* function in MATLAB using a trust-region reflective algorithm [149, 150] with a tolerance of $10^{-10}$ set for changes in the input parameters and for changes in $\|D\|_2^2$ (see Section 3.4.1.4). The result $r^*$ was a set of linear transforms and rotations relative to the target frame's coordinate system that would define the new coordinate system for the frame in question.

$$r^* = \begin{pmatrix} s_x^* \\ s_y^* \\ s_z^* \\ \phi^* \\ \theta^* \\ \psi^* \end{pmatrix}$$

The frame's new coordinate system centre of mass was set by

$$com = com^t - \begin{pmatrix} s_x^* & s_y^* & s_z^* \end{pmatrix}$$

The rotation matrix $r^*$ was defined from $\{\phi^*, \theta^*, \psi^*\}$ using (3.29). The frame's coordinate system $S$ was set by

$$S = r^{*-1} \times S^t$$

Figure 3.18 shows the results of frame alignments for a single movie. Figure 3.18a shows that the centre of mass of each frame undergoes an additional shift of 0.1$\mu$m on average. Figure 3.18b shows that the plate normal undergoes an additional rotational shift of 0.02 radians (approximately 1°) on average each frame. Figure 3.18 compares the frame to frame displacements of all tracked objects between the original metaphase plate fit and the aligned plate fit. It shows a reduction in the average displacements from 0.16$\mu$m to 0.10$\mu$m on average.

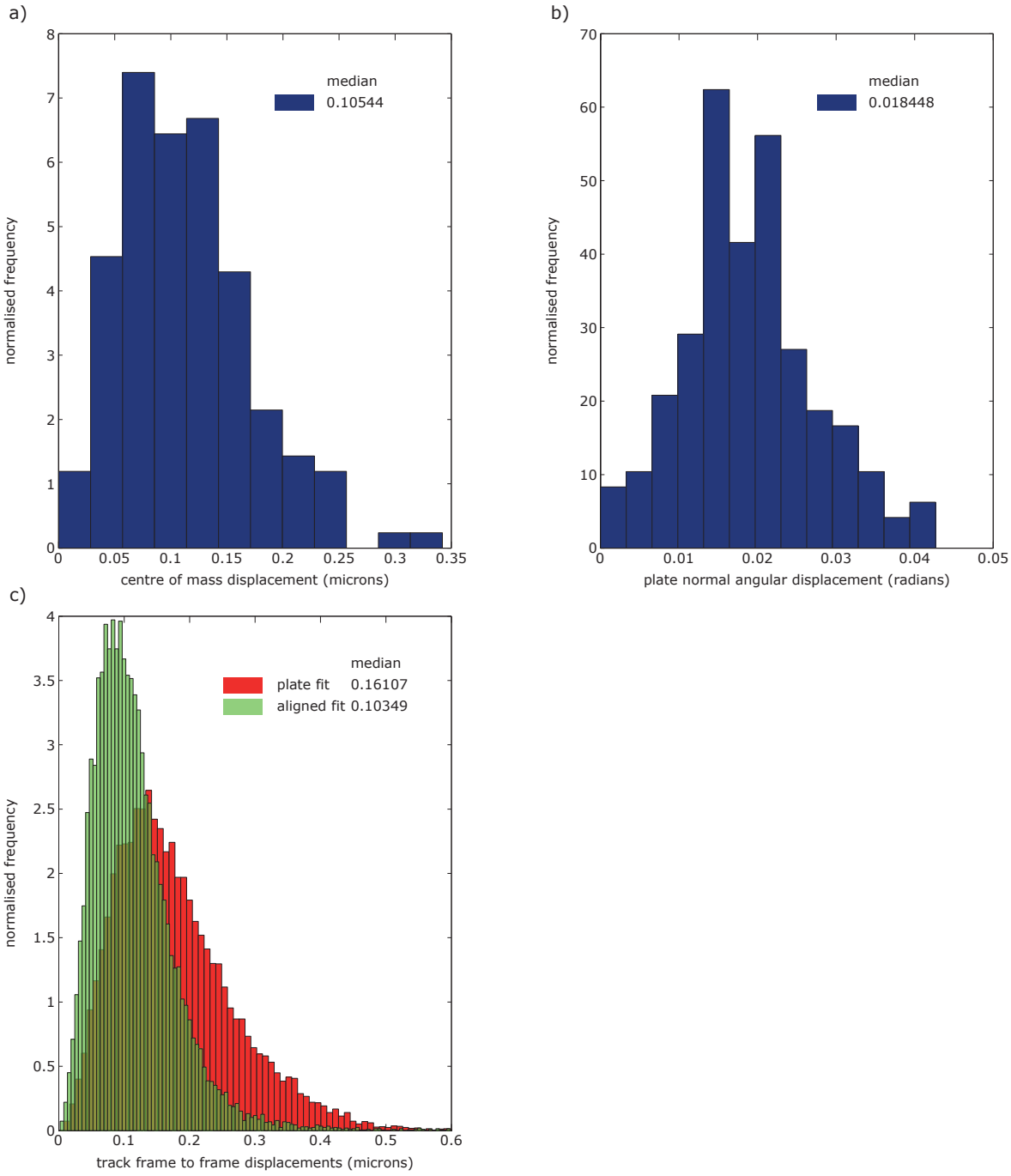


**Figure 3.18:** Example of frame alignment by displacement minimisation. Results from a single movie. **a)** Histogram of frame centre of mass absolute shifts. **b)** Histogram of plate normal absolute angular shifts. **c)** Histograms of the frame to frame displacements for all tracks under the original plate coordinate system (red) and the aligned coordinate system (green). Distribution medians shown in all figure legends.

## 3.8 Improved Frame-to-Frame Feature Tracking using Improved Frame Alignment

Section 3.7 describes a method of improved frame alignment based on the feature displacements between frames, features that are tracked between frames using the method described in Section 3.6. By iterating these two methods an optimal set of tracks can be found by aligning each frame's coordinate system based on existing tracks, then tracking features using the new coordinate system in each frame. In practice after each frame's coordinate system has been aligned features are re-tracked using the new coordinate system. If a different set of tracks are produced then the process is iterated until either re-tracking does not produce a different set of tracks, or up to a maximum number of iterations (set to 10). An optimal set of tracks was almost always found after one or two iterations.

## 3.9 Sister Kinetochore Track Pairing

Sister kinetochore track pairing was carried out as in [96] with some modifications. For each pair of tracks with an overlap of at least 40 frames the separation between tracks, $s_t$ and the angle made by the tracks with the metaphase plate, $a_t$ was calculated for each frame where both tracks existed before anaphase. For frames where either track feature was unaligned with respect to the metaphase plate the angle value was updated to $\min(a_t, 0.99 \times a_{\max})$ where $a_{\max}$ was an adjustable tracking parameter (see Table 3.1 for tracking parameters used). This was because unaligned pairs were not necessarily orientated along the normal to the metaphase plate. The average track separation $\langle s \rangle$, the variance in separation $v$ and the average angle $\langle a \rangle$ were then calculated. If $\langle a \rangle < a_{\max}$ and $\langle s \rangle < s_{\max}^{\text{avg}}$ where $s_{\max}^{\text{avg}}$ was an adjustable tracking parameter (see Table 3.1 for tracking parameters used) the two tracks were considered for possible pairing with a cost $c = \langle s \rangle * v * \langle a \rangle$. All tracks that had a possible pairing partner were also allowed to not pair to anything with a cost $c_{\text{np}} = 1.1 \times \max_{\text{pairs}}(c)$. Tracks were paired in a way that resulted in the lowest overall global cost, $\min_{\text{pairs}} \sum_{i=1}^{\text{no. pairs}} c_i$ (where tracks can only be paired with one other track). Figure 3.19 shows an example of sister kinetochore track pairing in a single cell.

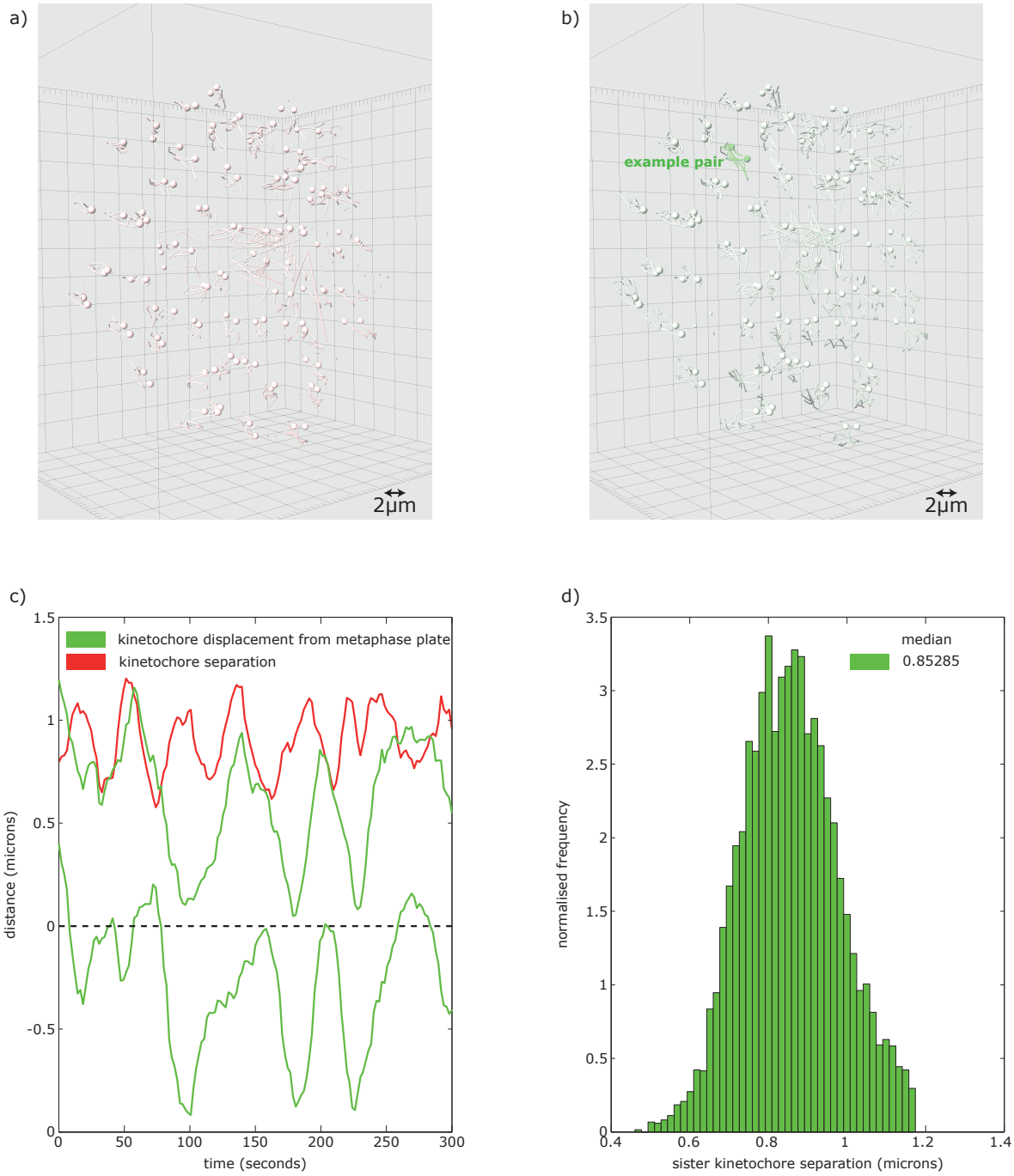


**Figure 3.19:** Sister kinetochore track pairing. Example of sister kinetochore track pairing in a single cell. **a)** All tracked features in the cell. Feature positions marked with red spheres and feature tracks over the previous ten frames marked with red tails. **b)** Track-pairs. Feature tracks successfully paired. Feature positions marked with green spheres and feature tracks over the previous twenty frames marked with green tails. A typical example track-pair highlighted in a dark green. **c)** Example kinetochore track-pair (highlighted in **b**) plotted relative to the aligned metaphase plate in each frame (green). Sister kinetochore separation (in 3D) also plotted (red). **d)** Histogram of all sister kinetochore separations from the cell over all timepoints (8171 data points from 61 track-pairs). Distribution median shown in the figure legend.

## 3.10 Improved Detection of Anaphase Frames

Detection of anaphase frames can be refined by examining the change in inter-sister distances over time. At the onset of anaphase sister kinetochores begin to separate therefore inter-sister distances will rapidly increase. For each frame with time $t$ in the set $\{1 \dots t^a - 1\}$ where time $t^a$ is the current first frame of anaphase, the mean inter-sister distance over all sister-pairs in the current frame $s_t$ was calculated (mean over sister-pairs at a single timepoint) using LMS to fit the mean (Section 3.2). The mean distance $\langle s \rangle$ was then calculated (mean $s_t$ over time) again using LMS to fit the mean and to detect outliers. If there exists a set of frames that last from time $t'$ until $t^a - 1$ whose $s_t$ values are all outliers and for all $s_t > \langle s \rangle$ then those frames are also labelled as anaphase *i.e.* $t^a = t'$.

## 3.11 Improved Frame to Frame Feature Tracking: Integration of Spatial and Temporal Information

Construction of sister kinetochore tracks described so far has separated spatial (spot detection) and temporal (track assignment) aspects. There exists, however, the potential to extract more spatio-temporal information from the image sequence by utilising prior temporal knowledge *i.e.* in this case gaps in sister-kinetochore tracks can be searched for missing spots. For example the position of a missing kinetochore can be inferred from the dynamics of its sister. Potential spots can either be taken from the pool of available spots not currently assigned to a sister-kinetochore track-pair or by re-fitting for new spot positions (Section 3.4.1). The ability to test fitted spots for significance (Section 3.4.3.3) makes this process robust to spurious fits. In brief the procedure goes as follows:

1. Search for any potential tracking errors in each sister-kinetochore track and remove these time-points, see Section 3.11.1.

2. Breakup sister-kinetochore track-pairs at time-points where both kinetochore

time-points are missing (internal missing time-points *i.e.* complete breaks). A track-pair with $n$ complete breaks would be broken into $n + 1$ track-pairs.

3. Iterate forward through time searching for any track-pairs that have a single missing time-point *i.e.* one missing sister in the current frame. Infer the positions of each missing spot in the frame based on the previous dynamics of their sisters, see Section 3.11.2. Search for potential candidates for the missing spots from the current available spots, see Section 3.11.2.1.

4. Repeat step 3 iterating back in time.

5. Iterate forward through time searching for any track-pairs that have double missing time-points *i.e.* both sisters missing in the current frame. Infer the centre points between each missing pair in the frame based on their previous dynamics, see Section 3.11.3. Search for potential candidates for the missing spots from the current available spots, see Section 3.11.3.1.

6. Repeat step 5 iterating back in time.

7. Merge together any track-pairs that share a common spot in a frame. Form two new track-pairs out of the merger, see Section 3.11.4.

8. Resolve any spot assignment conflicts. For any set of track-pairs that share spot assignments in any frame remove the track-pair that has either the most missing time-points or the largest variance in inter-sister distance. Repeat this step until there are no conflicts, see Section 3.11.5.

9. Repeat steps 3, 4, 5 and 6 but keep a record of the locations of potential new spots for each frame instead of searching for potential candidate spots.

10. For any frames with potential new spots re-fit those frames (Section 3.4.1.2). Test each spot for significance (Section 3.4.3.3), remove insignificant spots and re-fit until all spots pass the significance test, see Section 3.11.6.

11. If any frames have new spots return to step 3.

12. In each frame remove any spots that are part of a sister-kinetochore track. Re-track the remaining spots (Section 3.8) and attempt to pair up those tracks (Section 3.9). If any more sister tracks are found return to step 1, see Section 3.11.8.

13. Re-fit metaphase plates (Section 3.5), re-align frames (Section 3.7) and re-check for anaphase frames (Section 3.10), see Section 3.11.9.

Figure 3.20 gives an overview of the extra spot assignment and fitting algorithm.

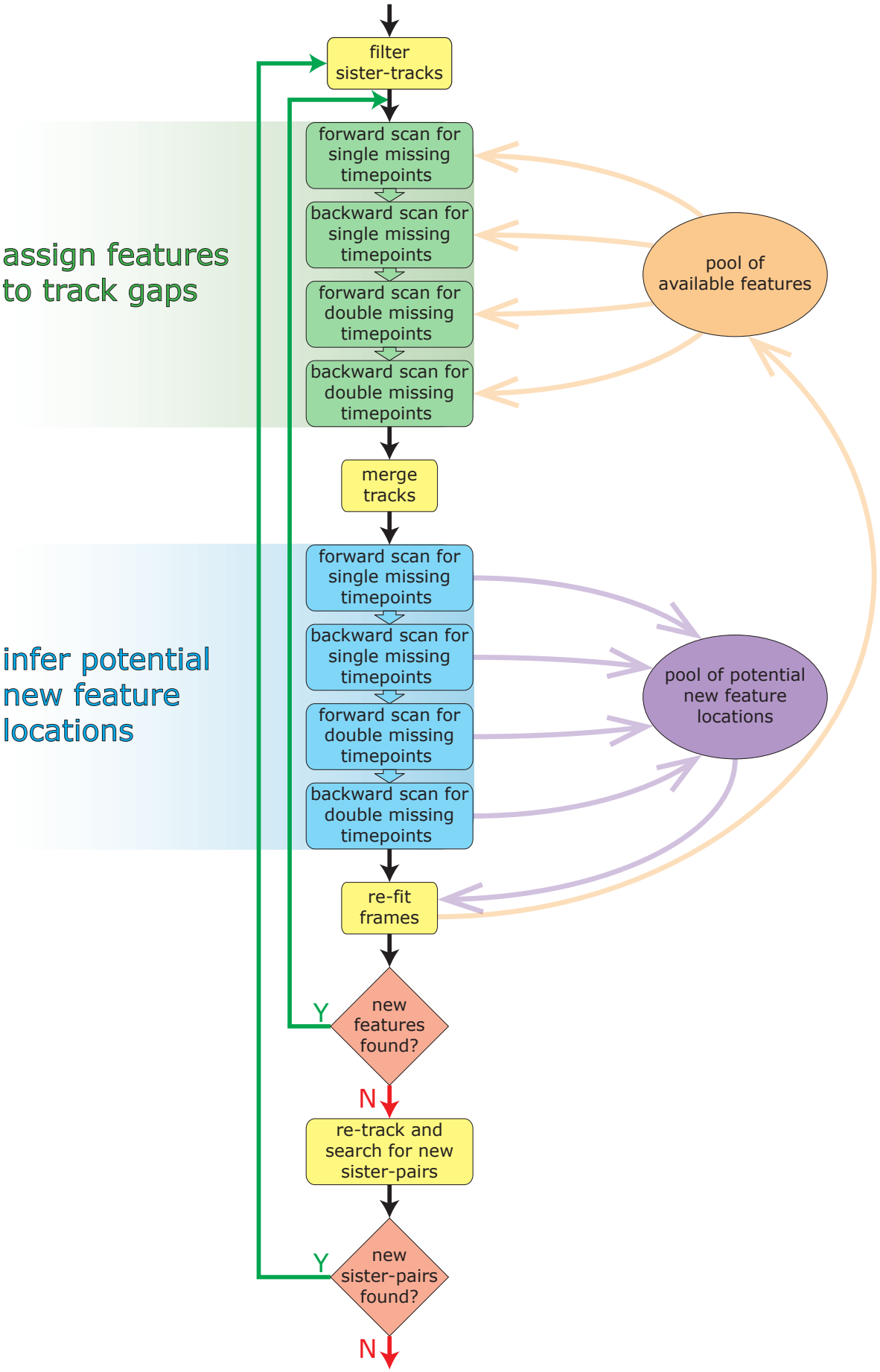


**Figure 3.20:** Overview of extra spot assignment and fitting algorithm. Black / red / green arrows show algorithm flow. Orange / purple arrows show feature information flow.

### 3.11.1 Tracking Error Detection

A tracking error occurs because of an incorrect assignment in frame to frame tracking resulting in a characteristically unusually large jump in the frame to frame kinetochore displacements in at least one spatial dimension. To filter for any erroneous tracking the change in position of each kinetochore (in a trajectory pair) was examined in each spatial dimension using LMS fitting of the mean with $k = 6$ to detect outliers (Section 3.2). The mean change in inter-kinetochore distance was also fitted using LMS with $k = 6$ to detect outliers. Trajectories were also filtered for any time-points prior to anaphase onset (if detected) where the inter-sister distance was larger than $s_{\max}$, an adjustable tracking parameter.

### 3.11.2 Inferring Single Missing Kinetochore Positions

Frames were searched (iterating forward or backward through time) for any sister-pairs where 1) one of the kinetochore positions was missing and 2) both kinetochore positions existed in the previous frame (previous frame was the frame one time-point in the past/future if iterating forward/backward through time respectively). The position of the missing kinetochore was inferred by taking the position vector of the other sister-kinetochore between the previous and current frame and applying it to the kinetochore in question's position in the previous frame (note that positions were all taken in aligned coordinate space as opposed to raw coordinate or image space).

#### 3.11.2.1 Selecting Potential Single Missing Kinetochore Positions

For each frame with an inferred single missing kinetochore position, potential matches were selected as follows. From the pool of available spots *i.e.* any feature spots in the current frame excluding each kinetochore in question's sister spot, a cost of matching was calculated. The cost was defined as

$$c = d\left|1 - \frac{s}{s_p}\right|$$

where $d$ is the distance between the inferred spot position and the target spot position,

$s$ was the sister separation between the target spot and the sister kinetochore in the current frame and $s_p$ was the sister separation between the kinetochores in the previous frame. The cost was structured so to minimise the distance from the inferred positions and to minimise the change in sister separation between frames. Constraints were imposed on potential spot selection. Potential spots were only considered if 1) $s < s_{\max}$ if the current frame was not an anaphase frame, 2) $d < 0.5\mu$m, 3) $|s - s_p| < 0.4\mu$m and 5) $|a - a_p| < 20^\circ$ where $a$ was the angle between the potential kinetochore vector and the X-axis and $a_p$ was the angle between the kinetochore vector and the X-axis in the previous frame. Matches were chosen to minimise the total cost.

### 3.11.3 Inferring Double Missing Kinetochore Positions

Frames were searched (iterating forward or backward through time) for any sister-pairs where 1) both the kinetochores were missing and 2) both kinetochore positions existed in the previous frame (previous frame was the frame one time-point in the past/future if iterating forward/backward through time respectively). The centre point between the missing kinetochores was inferred taking the centre point between the kinetochores in the previous frame. (note that positions were all taken in real, aligned coordinate space as opposed to raw coordinate or image space).

#### 3.11.3.1 Selecting Potential Double Missing Kinetochore Positions

For each frame with inferred double missing kinetochore positions potential matches were selected as follows. A pool of available spots was created, which consisted of all feature spots in the current frame excluding spots that belonged to current sister tracks that did not start in the current frame. The centre point between every suitable pair of potential spots was calculated (all possible pairings). For frames before anaphase pairs of spots were considered suitable only if their separation was less than $s_{\max}$. A cost was then assigned to each possible pairing of inferred centre points and potential centre points with a cost

$$c = d\left|1 - \frac{s}{s_p}\right|$$

where $d$ was the distance between the inferred centre point and the potential centre point. $s$ was the sister separation between the two potential spots and $s_p$ was the sister separation in the previous frame. Constraints were imposed on the potential centre point selection. Spots were only considered for pairing if 1) $d < d_{\max}$ where $d_{\max}$ was the maximum allowed frame to frame spot displacement (an adjustable tracking parameter). The value of $d_{\max}$ depended on if features being considered were aligned to the metaphase plate or not (see Section 3.6), centre points were considered unaligned if either pair of spots were unaligned. If either relevant centre point was unaligned then $d_{\max}$ was assigned the unaligned value. 2) $|s - s_p| < 0.4\mu$m and 3) $|a - a_p| < 20^\circ$ where $a$ was the angle between the target spots vector and the X-axis and $a_p$ was the angle between the spots vector and the X-axis in the previous frame. Matches were chosen to minimise the total cost.

### 3.11.4 Merging Kinetochore Tracks

During track construction, tracks (of different kinetochore-pairs) may conflict over features *i.e.* share a feature in a frame. For each instance of a conflict the track-pairs in question are merged forming two new compound track-pairs. For two sister-pairs $i$ and $j$ with sister-kinetochore tracks $i_1$, $i_2$ and $j_1$, $j_2$ respectively. If for example tracks $i_1$ and $j_2$ have a conflict at time $t'$ then one new track-pair formed will consist of features from track $i_1$ from time $t = \{1 \dots t'\}$ and features from track $j_2$ from time $t = \{t' + 1 \dots \text{end}\}$ for one sister and features from track $i_2$ from time $t = \{1 \dots t'\}$ and features from track $j_1$ from time $t = \{t' + 1 \dots \text{end}\}$ for the other sister. The other track-pair will consist of features from track $j_2$ from time $t = \{1 \dots t'\}$ and features from track $i_1$ from time $t = \{t' + 1 \dots \text{end}\}$ for one sister and features from track $j_1$ from time $t = \{1 \dots t'\}$ and features from track $i_2$ from time $t = \{t' + 1 \dots \text{end}\}$ for the other sister. These new tracks are added to the list of current tracks. Conflicts between track-pairs will then be resolved in the next step (Section 3.11.5).

### 3.11.5 Resolving Track Conflicts

For each set of sister-tracks that are in conflict at any time-point the track-pair with the greatest number of missing time-points is removed until no more conflicts exist. If

any track-pairs have the same number of missing time-points the pair with the largest variance in inter-sister distance is removed.

### 3.11.6 Inferring Potential New Feature Locations

Gaps in sister kinetochore tracks may be due to features that have not been detected. Initial estimates for the locations of missing features can be made based on existing kinetochore dynamics. Estimates for the locations of single missing time-points in each frame can be made by repeating the procedure detailed in Section 3.11.2.1. Estimates for the locations of double missing time-points in each frame can be made by repeating the procedure detailed in Section 3.11.2.1. For each frame with locations of potential new spots, any new spots that are less than 0.2$\mu$m from already existing spots are removed since kinetochores are not expected to exist that close to each other. For any pair of new spots that are less than 0.2$\mu$m from each other, the spot with the smallest average distance to the other new spots is removed. This removes new spot locations that are too close to each other. At each iteration the locations of the estimated new spots in each frame are recorded. Any new spot that is less than 0.05$\mu$m from a previous location estimate is removed, this avoids repeated fitting of new spot locations that are ultimately not kept.

### 3.11.7 Fitting New Spot Locations

For each frame with potential new spot locations the new spots were fitted using the methods described in Section 3.4.1.2. New spot coordinates were first transformed from aligned coordinates to image coordinates,

$$s' = \frac{((S \times s) + com)}{vox}$$

where: $s'$ are image coordinates; $s$ are aligned coordinates; $S$ is the coordinate system of the frame (Equation (3.23)); $com$ is the centre of mass of the frame and $vox$ are the voxel dimensions. This is the inverse of Equation (3.24) with additional scaling by the voxel dimensions to transform into image coordinates. New spot coordinates were combined with the pre-existing spot coordinates and used as a starting point for spot

fitting. Fitting was repeated until all spots passed the test for significance as described in Section 3.4.3.3.

### 3.11.8 Re-tracking Remaining Spots

Once no more new spots are found in any frame (and track gaps have been closed) any remaining features that are not part of a current sister-kinetochore track are re-tracked (as described in Section 3.8 using the currently existing coordinate system for each frame) *i.e.* all current sister-kinetochore track spots are removed from the set of features in each frame and the remaining features tracked. These new tracks are paired together as described in Section 3.9. If any new sister kinetochore track-pairs are found these new track-pairs are added to the current list of kinetochore track-pairs (starting with the tracing error filter as described in Section 3.11.1). The algorithm is repeated until no more new sister kinetochore track-pairs are discovered. Once the new spot fitting algorithm is complete the coordinate systems for each frame are re-defined for the final set of features in each frame, first by plate fitting as described in Section 3.5 and then by frame alignment as described in Section 3.7.

### 3.11.9 Finalising Tracking Results

Once the new spot fitting process is complete the coordinate systems for each frame are re-defined for the final set of features in each frame, first by plate fitting as described in Section 3.5 and then by frame alignment as described in Section 3.7. The movie is also re-checked for anaphase frames as described in Section 3.10. Figure 3.21 gives an overview of the extra feature fitting process. Figure 3.21g shows the number of sister pairs found before and after this extra feature analysis is used. The number of sister pairs are plotted as a function of their degree of completion *i.e.* the fraction of the $2n$ time-points (where $n$ is the number of frames) of the sister pair that are non-empty. The plot shows that more sister pairs are found after extra feature fitting and that the sister pair tracks have less missing time-points. Figure 3.22 shows eight example sister-kinetochore trajectories before and after extra feature fitting indicating where gaps have been filled.

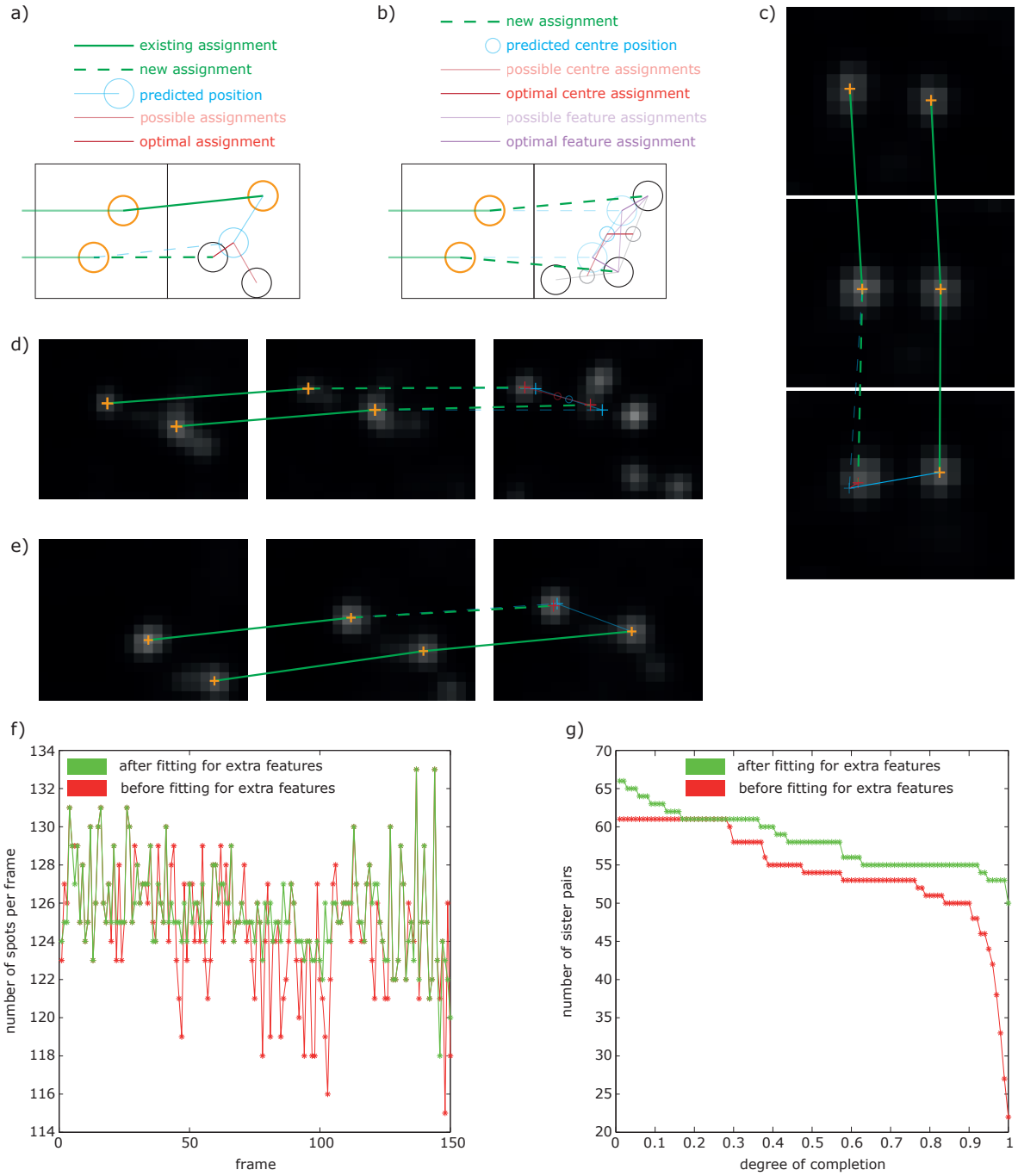


**Figure 3.21:** Overview of extra spot assignment and fitting. **a)** Diagram of assigning single missing features in kinetochore pair tracks. Expected position is the projection of the kinetochore position in the previous frame relative to its sister. Assignment of features optimises cost functions. **b)** Diagram of assigning double missing features in kinetochore pair tracks. Expected sister centre position is the sister centre position in the previous frame projected froward in time. Suitable potential feature pair assignments have their centre positions calculated. Assignments optimise cost functions. **c)** Example of assignment of a feature to a single missing data point. **d)** Example of assignment of features to a double missing data point. **e)** Example of successfully fitting a new spot position based on the expected position of a single missing feature. **f)** Plot of the number of features per frame from a single movie before (red) and after (green) fitting for extra features. **g)** Plot of the number of sister pair tracks with a certain minimum degree of completion (fraction of non-empty data points) from a single movie before (red) and after (green) fitting for extra features.

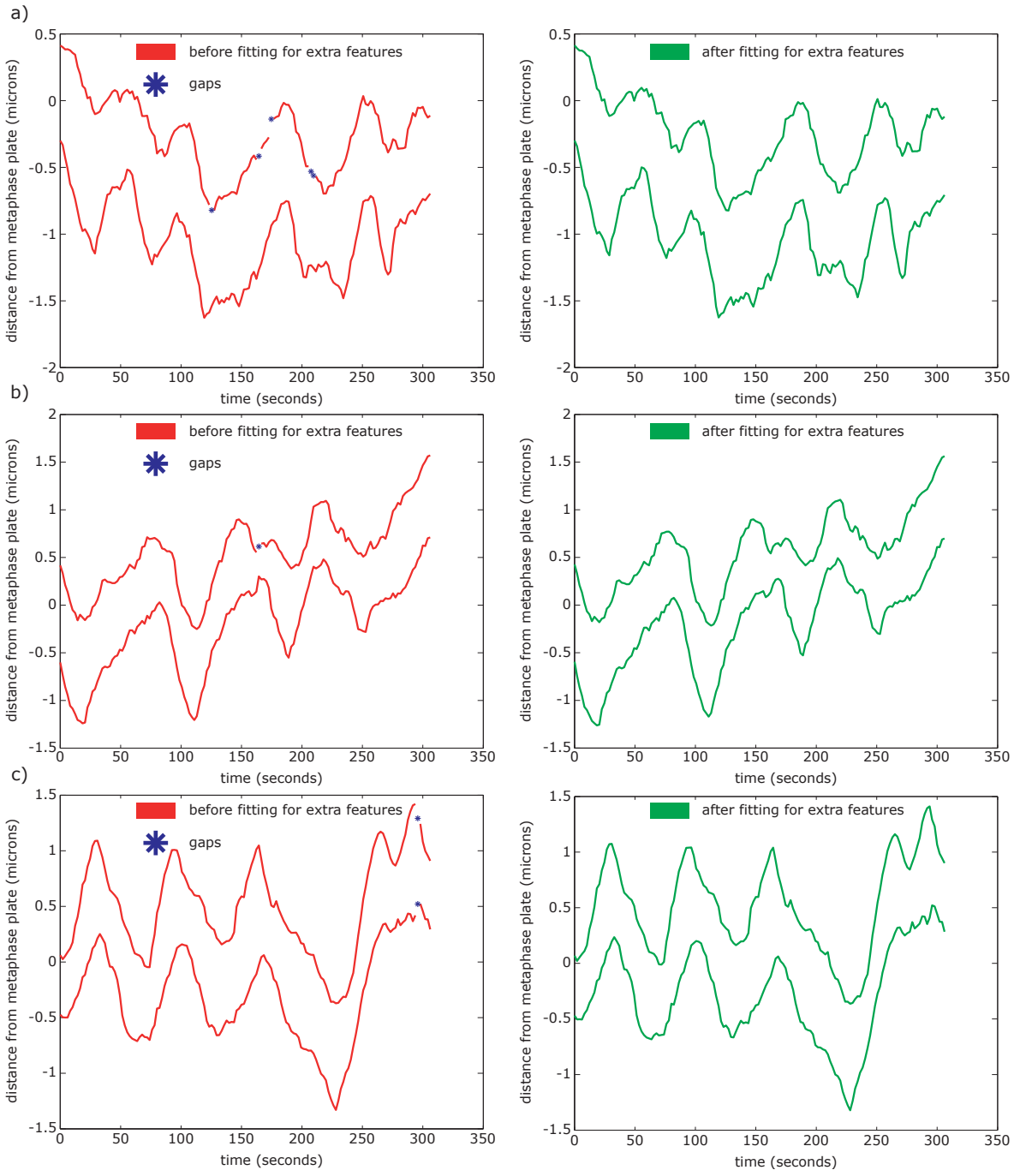


**Figure 3.22:** Examples of sister-kinetochore tracks before and after extra feature assignment/fitting. **a)** to **c)** Sister kinetochore tracks before (red) and after (green) filling gaps (blue stars) by extra feature fitting and assignment. *cont*

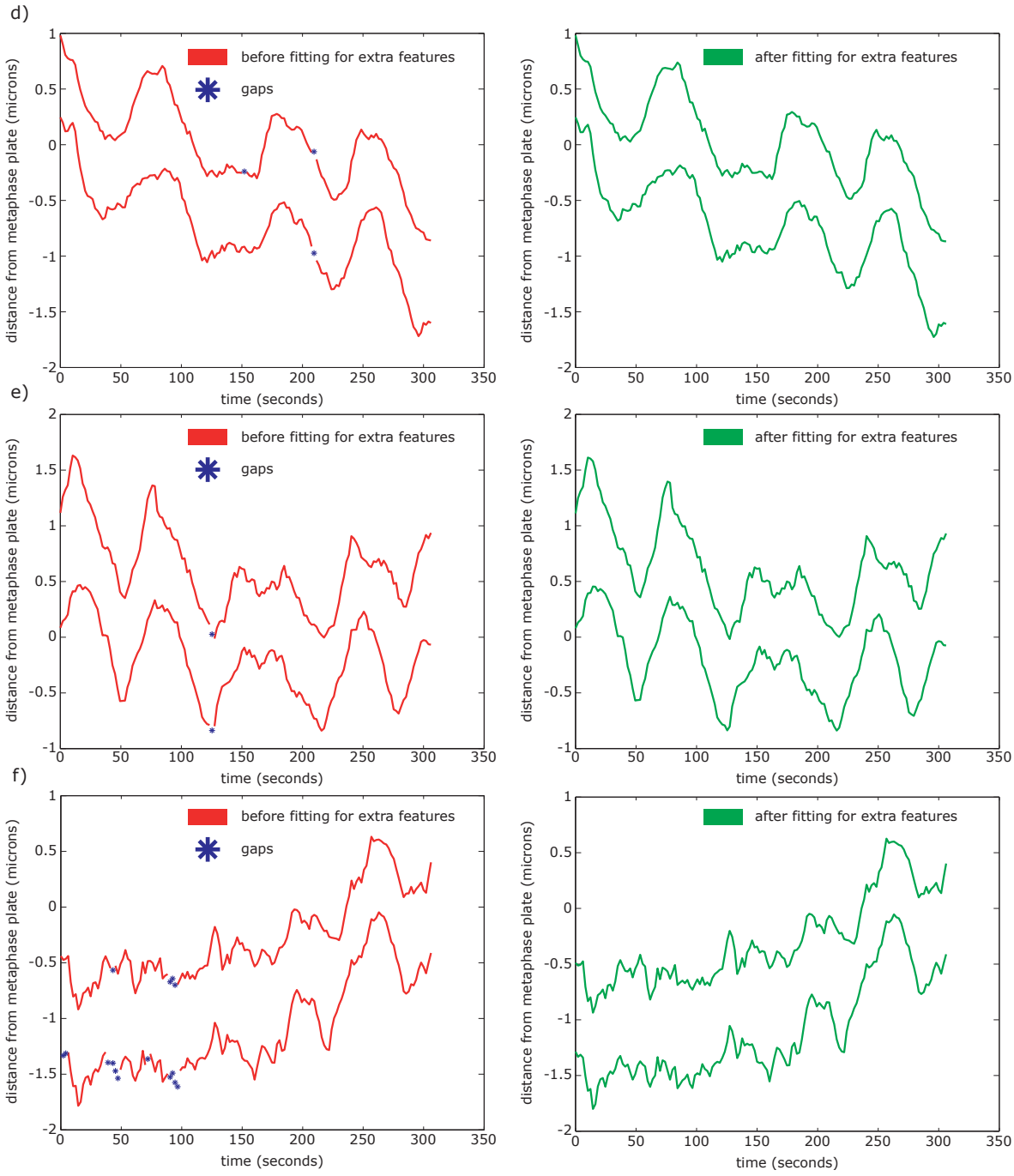


**Figure 3.22:** *cont* **d)** to **f)** Sister kinetochore tracks before (red) and after (green) filling gaps (blue stars) by extra feature fitting and assignment. *cont*

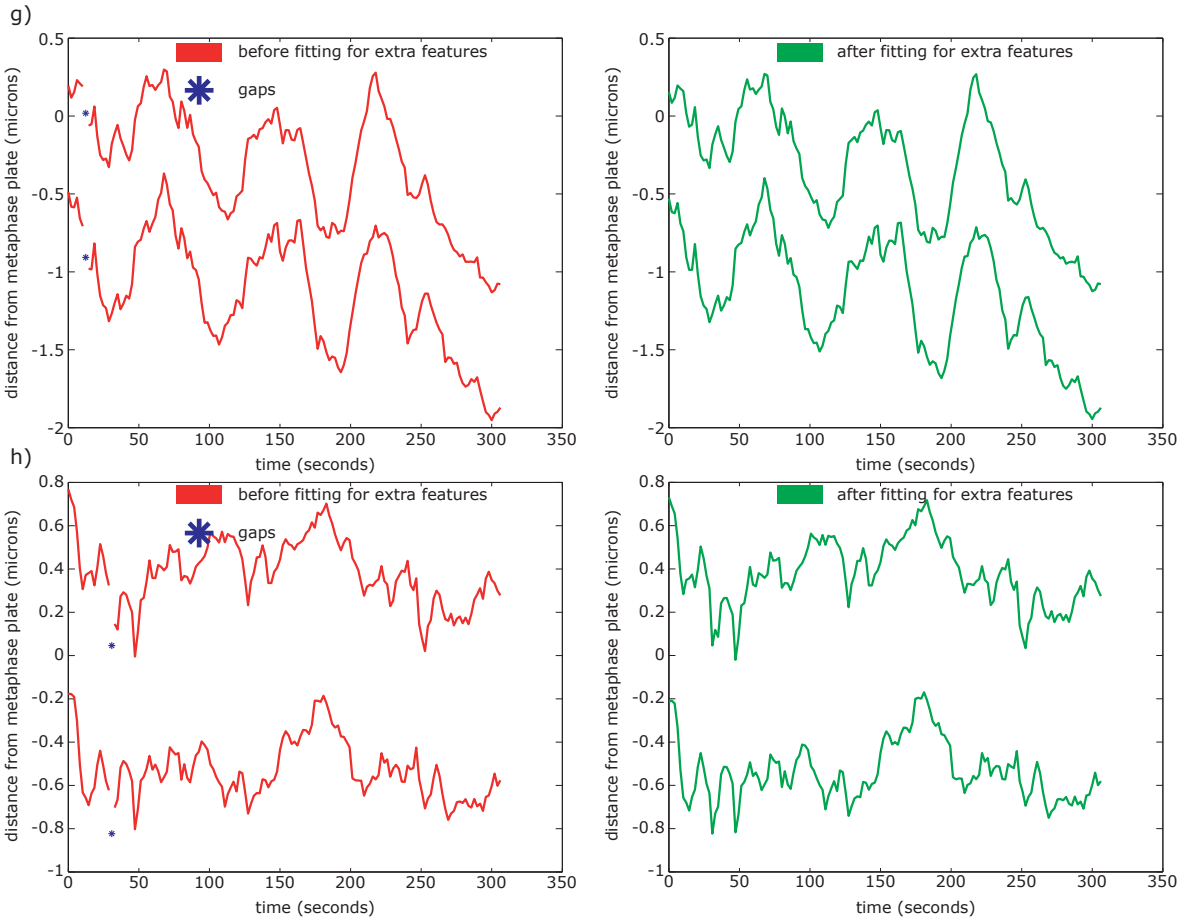


**Figure 3.22:** *cont* **g)** and **h)** Sister kinetochore tracks before (red) and after (green) filling gaps (blue stars) by extra feature fitting and assignment.

## 3.12 Spindle-Pole Track Identification

Spindle-pole tracks were identified by assigning a cost to each pair of tracks as described in [154]. Briefly, the cost was defined as $c = |d - s| * a$ where $d$ was the average distance between the tracks, $s$ was the expected average spindle length, set to 11$\mu$m and $a$ was the average angle between the tracks and the metaphase plate. Tracks were only considered if $d$ was greater than 5$\mu$m and $a$ was smaller than 30°, also tracks were only considered if both tracks were unaligned from the metaphase plate throughout their lifetimes. The pair of tracks with the lowest cost were identified as two spindle-poles. Since both centrioles in each pole were tagged the second centriole track for each pole was found by assigning a cost $c = g^{-1}$ where $g$ was the cross correlation between the pole track and the candidate track. Tracks were only considered if $g$ was greater than 0.9 and if the average distance between the tracks was less than 1$\mu$m. The track with the lowest cost was chosen for each pole as its respective second centriole. Figure 3.23 shows an example of identified spindle-pole tracks and the pole to pole distance over time.

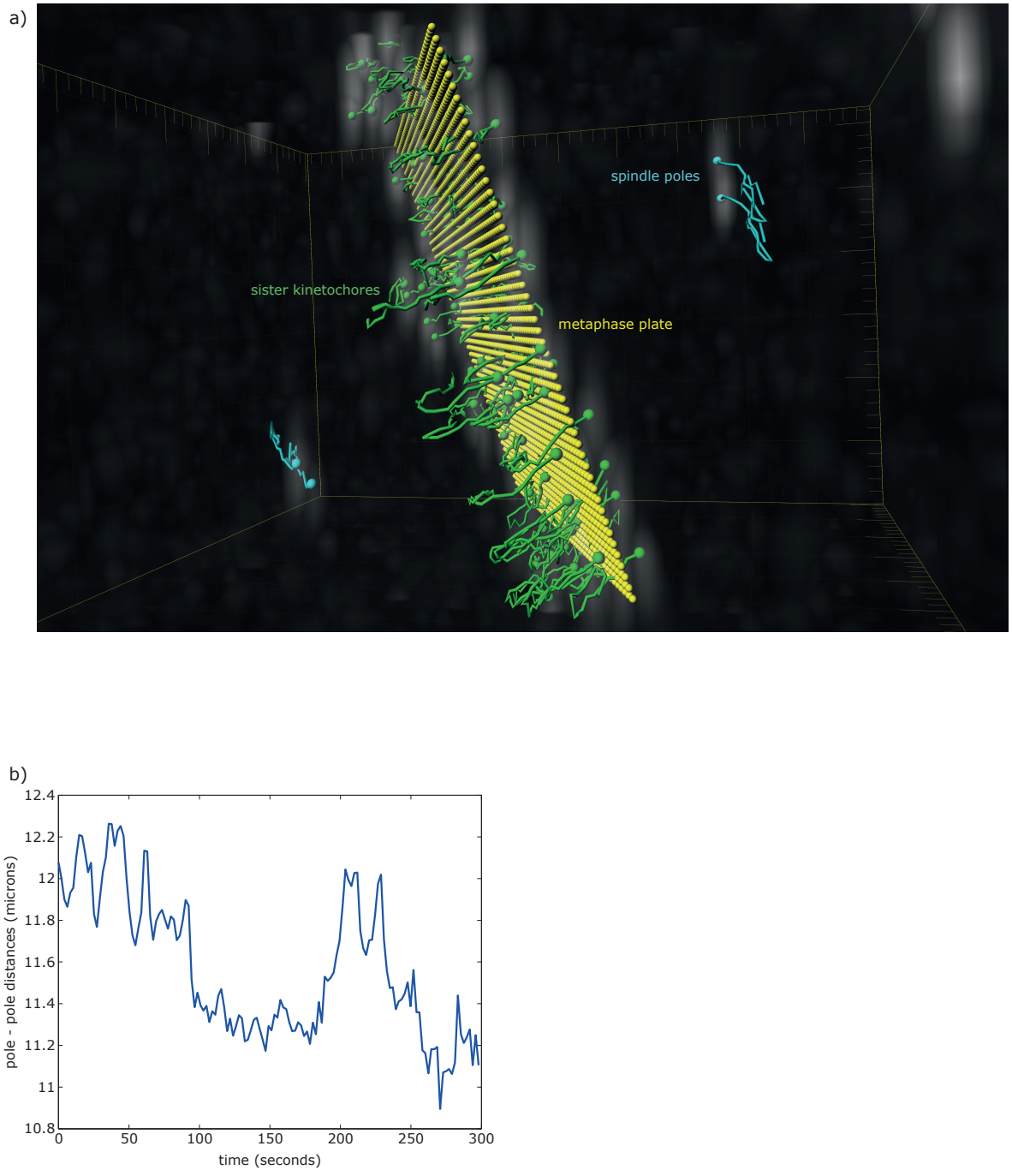


**Figure 3.23:** Identifying spindle-pole tracks. **a)** Example of spindle-pole tracks (blue) along with sister-kinetochore tracks (green) and metaphase plate (yellow). **b)** Pole to pole distances over time.

## 3.13 Spot Alignment to Spindle Axis Coordinate System

If spindle-poles were defined throughout a movie then a spindle coordinate system was defined. For each time point the average point between the two poles (if both centrioles had been found for a pole then the pole position was taken as the average for the two centriole positions) defined the centre point of the coordinate system. The vector between the two poles then defined a plane normal to this vector that passed through the centre point. Spot coordinates were then given relative to the plane in each frame the same way the metaphase plate coordinate system was defined, Section 3.5. Figure 3.24 shows an example of a spindle axis coordinate system and a comparison to the metaphase plate coordinate system examining a plot of a sister-kinetochore track-pair in both systems.

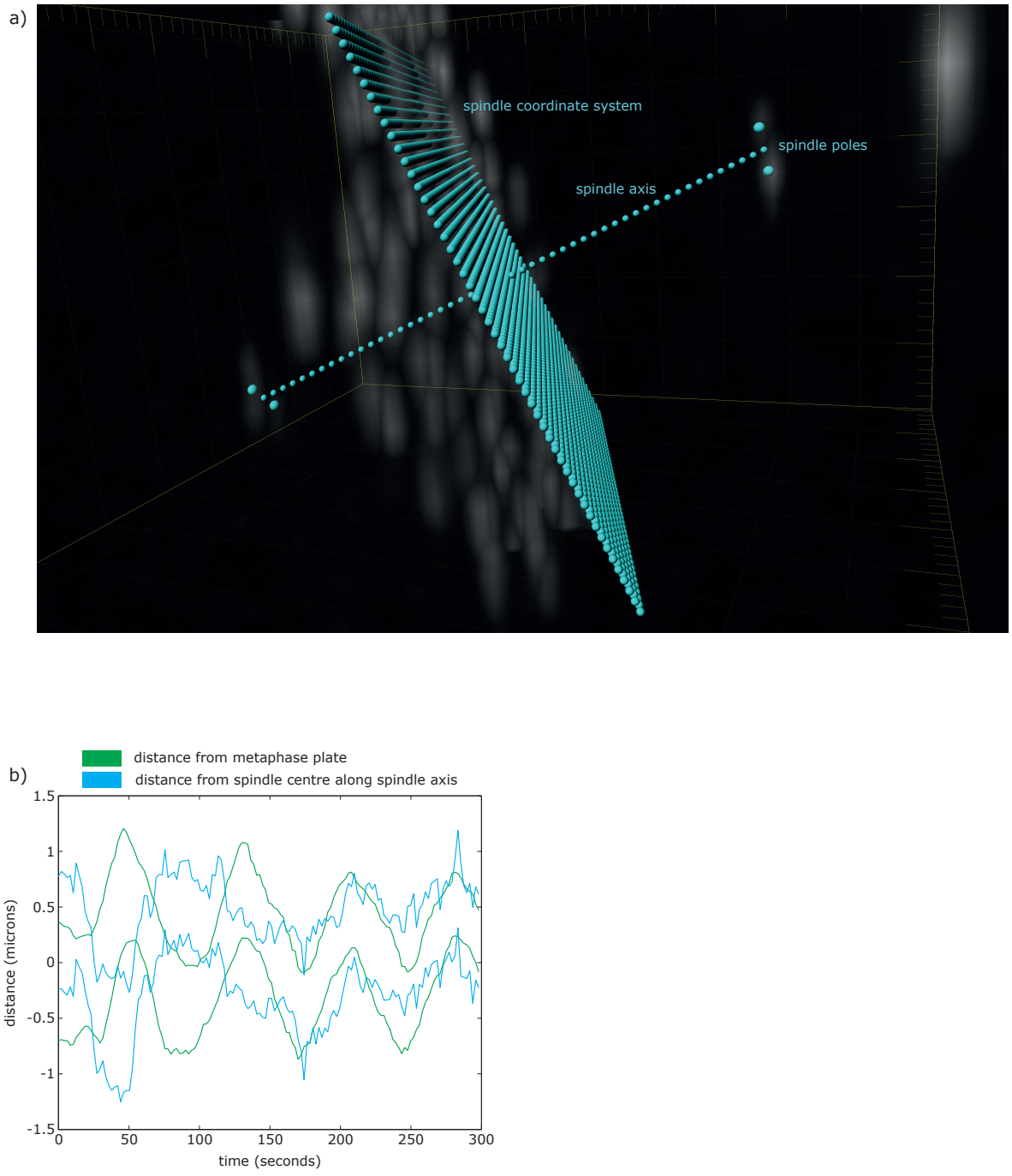


**Figure 3.24:** Spindle axis coordinate system. **a)** Example of a spindle coordinate system and spindle axis defined by spindle-poles. **b)** Example of a sister-kinetochore track-pair with coordinates given in a metaphase plate (green) and spindle axis (blue) coordinate systems.

## 3.14 Verification of Kinetochore Tracking Data

Kinetochore tracking data produced from the assay described in this chapter (metaphase plate coordinate system) was verified against previous work [96] for consistency. Specifically tracking data from the analysis of untreated cells was used to calculate a distribution of sister-kinetochore separations and of sister-kinetochore centre displacement auto-correlations. Results are shown in Figure 3.25; the distribution of sister-kinetochore separations is consistent with previously reported values, [96]. The auto-correlation of sister-kinetochore centre displacements relative to the metaphase plate normal was used to infer oscillatory behaviour in the analysed time-series as described in [96]. Note that in [96], sister centre displacements were taken every frame recorded at a time-lapse of 7.5 seconds per frame. For a fair comparison in this case sister centre displacements were calculated over every four frames (at a time-lapse of 2 seconds per frame) giving sister displacements over 8 seconds, close to the 7.5 seconds used in [96]. The characteristic negative lobe indicated by the red arrow in Figure 3.25b is an indication of the presence of oscillations in the kinetochore trajectories; the time-lag value of the lobe is an indication of half the value of the average period of the oscillations, in this case around 30 seconds (a full period time of approximately 60 seconds). This result is consistent with [96].

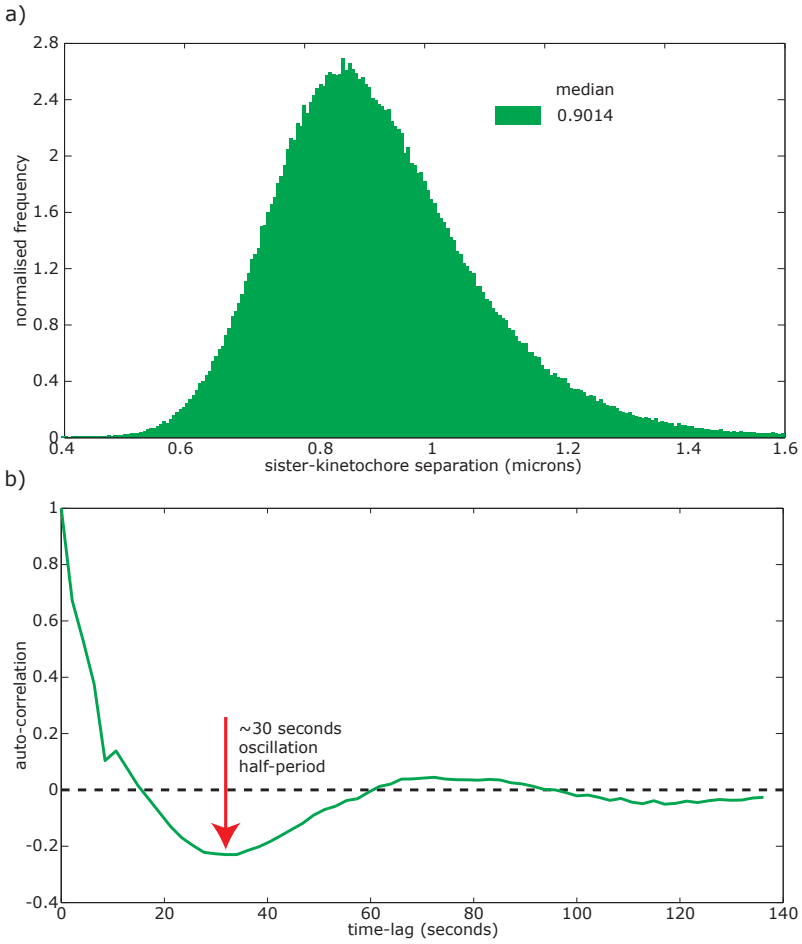


**Figure 3.25:** Summary statistics of kinetochore tracking data. **a)** Histogram of the measured 3D sister-kinetochore separations. Data from 5503 untreated sister pair trajectories pooled across all time points. Distribution median shown in the figure legend. **b)** Auto-correlation of the displacements of sister-kinetochore centres (from 5503 untreated sister pair trajectories). Displacements are taken along the normal to the metaphase plate and over a time period of 4 time points (8 seconds).

## 3.15 Comparison of Coordinate Systems

Although a spindle-axis based coordinate system was not able to be established in every imaged cell due to the reliance on sufficient spindle-pole tracking, a relatively high number of cells were successfully processed. Figure 3.26a shows a histogram of all the measured spindle-axis length measurements on untreated cells. The possibility of measuring kinetochore tracks relative to their cell's spindle axis as well as a 'self-defined' metaphase plate allows the latter results to be validated against the former. Figure 3.26b shows a comparison of the mean sister-kinetochore centre displacement autocorrelation measured on identical trajectories expressed in both coordinate systems. The correlation curve of the plate-based system has the characteristic shape indicative of oscillatory-type behaviour (Figure 3.25b). Although also present in the correlation curve of the spindle-axis based system the main trough is distinctly weaker with a more noisy profile, indicating that although kinetochore-oscillations are still detectable when measured relative to the spindle-axis the signals are corrupted by noise, most likely introduced by the relative random motion of the spindle-poles themselves plus the compounded effect of having the coordinate-system based on only (up to) four spatial positions per frame (four centrioles) rather than typically 100 kinetochores. Figure 3.26c-l show examples of kinetochore-pair trajectories expressed in both coordinate systems. The noisiness of the pole-based coordinates can be seen in these example plots.

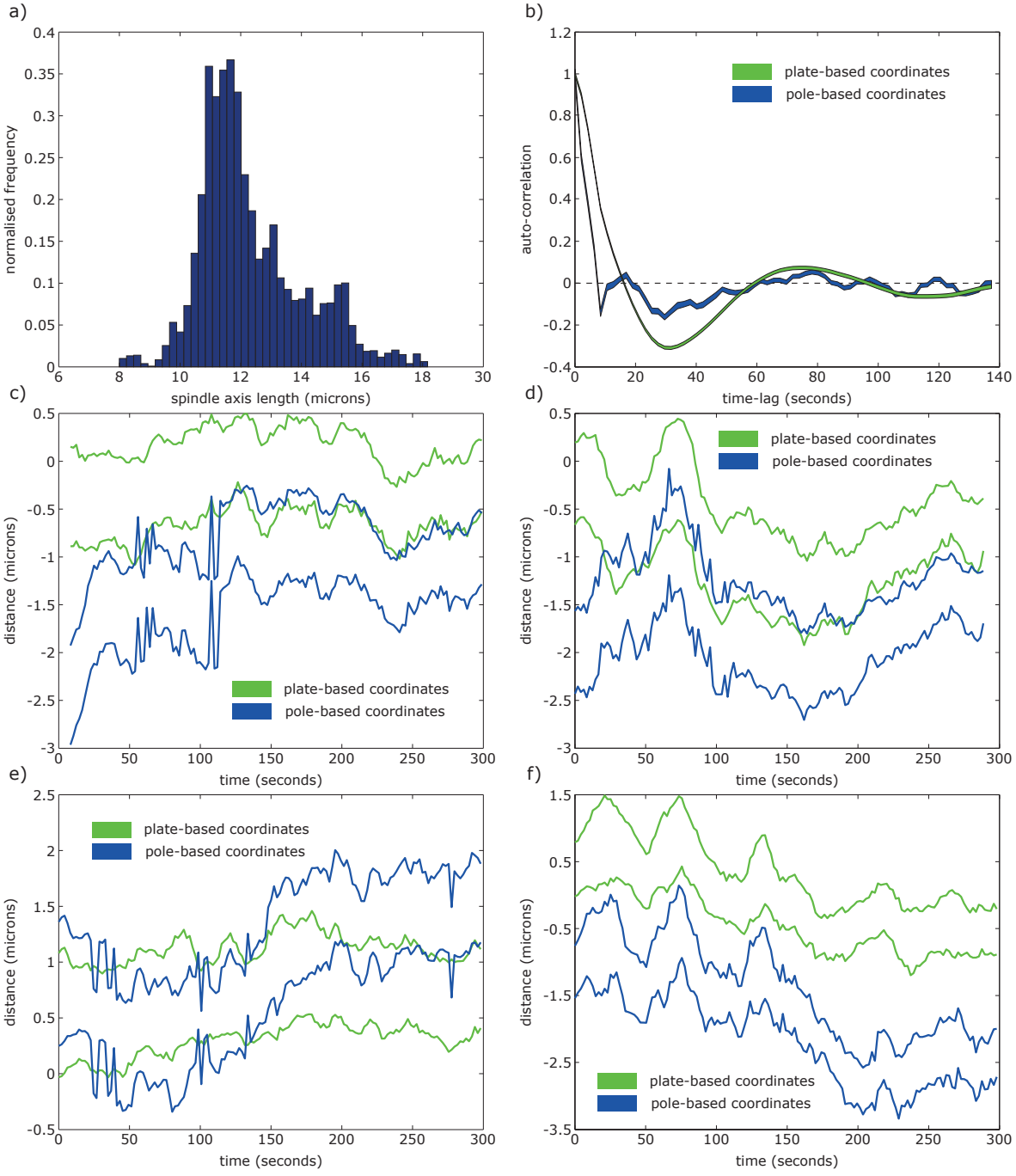


**Figure 3.26:** Comparison of metaphase plate and spindle-pole coordinate systems. **a)** Histogram of spindle axis length (pole to pole distance; data pooled over all time-points). 5554 data-points from 89 cells with identified spindle-poles. **b)** Kinetochore centre normal displacement autocorrelation ($\Delta$t over 4 time-points) measured in the metaphase-plate (green) and spindle axis (blue) based coordinates. Line thickness represents 95% confidence interval of correlation value. Data from 2012 trajectory pairs from 66 cells. **c) - f)** Example trajectory pairs expressed in the metaphase-plate (green) and spindle axis (blue) coordinate systems. *cont*

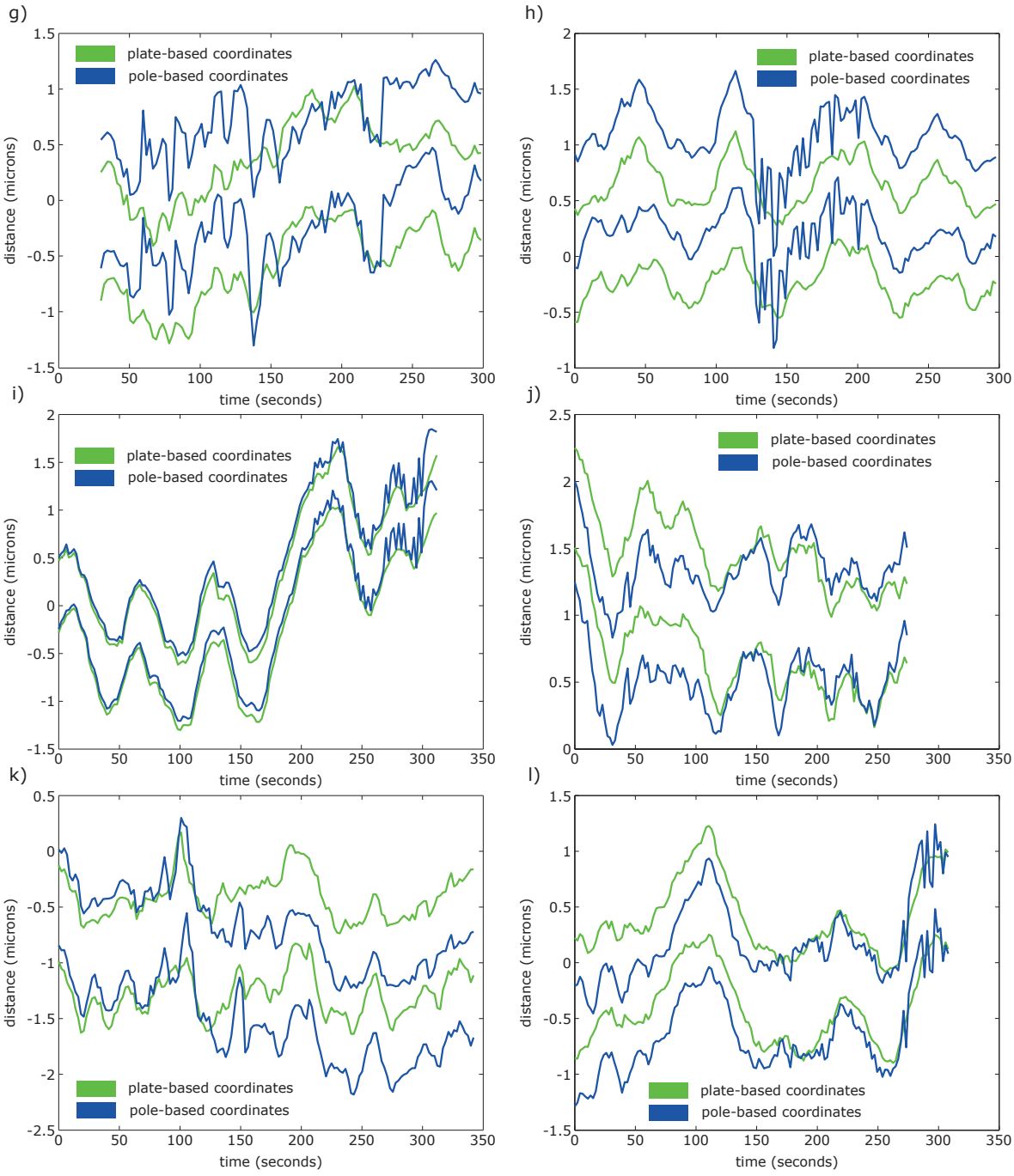


**Figure 3.26:** *cont* **g) - l)** Example trajectory pairs expressed in the metaphase-plate (green) and spindle axis (blue) coordinate systems.

## 3.16 Final Summary

The procedures and algorithms presented in this chapter describe a fully automatic assay taking movies of fluorescently tagged kinetochores in human cells as input and producing sister-kinetochore trajectory data normalised relative to an inferred metaphase plate. A combination of high sampling frequency, spinning-disk confocal microscopy and model-based spot localisation track human kinetochore trajectories to an unprecedented spatio-temporal resolution. Statistics on trajectories produced are consistent with previous results. Tracked spindle-poles give an alternative coordinate system that can be used for confirming the results produced. The high-throughput nature of the assay allows for a large number of kinetochore trajectories to be collected in an unbiased manner. Data produced by this assay will go on to be used in a data-driven statistical modelling framework designed to investigate the nature of human kinetochore dynamics at metaphase.

# Tables

**Table 3.1:** Tracking parameters

| Parameter | Default | Exceptions |
|---|---|---|
| **Adjustable tracking parameters** | | |
| Gap-closing time window | 4 frames* | none |
| Search radius upper limit - aligned ($\mu m$) | 0.8 | Nuf2 siRNA (2.0)*‡ |
| Search radius upper limit - unaligned ($\mu m$) | 3.0* | none |
| **Adjustable sister pairing parameters** | | |
| Maximum average distance ($\mu m$) | 1.5* | (siRNA untreated / Control siRNA) + nocodazole (1.0)* |
| | | Nuf2 siRNA (1.3)* |
| | | CAPD2 siRNA (1.9)* |
| Maximum average angle with normal (°) | 30* | none |

∗ Taken from [96] supplementary information.

‡ Conditions without metaphase plate, thus no aligned versus unaligned kinetochore classification. Therefore, all kinetochores get the same tracking parameters.

# References

[96] Khuloud Jaqaman et al. "Kinetochore alignment within the metaphase plate is regulated by centromere stiffness and microtubule depolymerases". In: *J Cell Biol* 188.5 (Mar. 2010), pp. 665–79.

[99] Xiaohu Wan et al. "The coupling between sister kinetochore directional instability and oscillations in centromere stretch in metaphase PtK1 cells." In: *Molecular biology of the cell* (Feb. 2012).

[101] D Thomann et al. "Automatic fluorescent tag detection in 3D with super-resolution: application to the analysis of chromosome movement." In: *Journal of microscopy* 208.Pt 1 (Oct. 2002), pp. 49–64.

[146] P. J. Rousseeuw and A. M. Leroy. *Robust Regression and Outlier Detection*. New York: John Wiley & Sons, 1987, p. 202.

[147] G Danuser and M Stricker. "Parametric model fitting: from inlier characterization to outlier detection". In: *IEEE Transactions on Pattern Analysis and Machine Intelligence* (1998).

[148] Paul L Rosin. "Unimodal thresholding". In: *Pattern Recognition* 34.11 (July 2001), pp. 2083–2096.

[149] Mary Ann Branch, Thomas F. Coleman, and Yuying Li. "A Subspace, Interior, and Conjugate Gradient Method for Large-Scale Bound-Constrained Minimization Problems". In: *Siam Journal on Scientific Computing* (1999).

[150] Richard H. Byrd, Robert B. Schnabel, and Gerald A. Shultz. "Approximate solution of the trust region problem by minimization over two-dimensional subspaces". In: *Mathematical Programming* 40.1-3 (1988), pp. 247–263.

[151] T. Coleman and Y. Li. "An Interior Trust Region Approach for Nonlinear Minimization Subject to Bounds". In: *SIAM Journal on Optimization* 6.2 (1996), pp. 418–445.

[152] Khuloud Jaqaman et al. "Robust single-particle tracking in live-cell time-lapse sequences". In: *Nat Methods* 5.8 (Aug. 2008), pp. 695–702.

[153] Roy Jonker and Anton Volgenant. "A shortest augmenting path algorithm for dense and sparse linear assignment problems". In: *Computing* 38.4 (1987), pp. 325–340.

[154] Liam P Cheeseman et al. "Specific removal of TACC3-ch-TOG-clathrin at metaphase deregulates kinetochore fiber tension." In: *Journal of Cell Science* 126.Pt 9 (May 2013), pp. 2102–2113.

# Chapter 4

# A Biologically-Motivated Model for Sister Kinetochore Dynamics

## 4.1 A Basic Mechanical Model Appropriate for Statistical Inference

This chapter describes the development of a stochastic biologically-motivated model for kinetochore sister dynamics designed to allow direct fitting to sister trajectory data. The model thus differs from previous mechanistic models that were constructed to demonstrate how oscillatory dynamics emerges from molecular interactions. These models are unfortunately restricted to qualitative comparisons [118, 138] because of the large number of parameters. Moreover the computational technology to fit such models is underdeveloped whilst fits would be uninformative since trajectory data does not determine all the parameters. The model incorporates the basic mechanical processes acting on the kinetochores: K-fibre polymerisation and depolymerisation, PEF that align the sisters to the metaphase plate and a spring connecting the two sister kinetochores.

## 4.2 Kinetochore Dynamics Model

### 4.2.1 Binary-State Kinetochores

Kinetochore dynamics from prometaphase through to the end of anaphase are mainly governed by the action of kinetochore-bound microtubules, or K-fibres. Many kinetochore components facilitate microtubule binding and/or stabilisation *e.g.* the KMN outer-kinetochore complex. A bi-orientated kinetochore-pair is defined as a sister kinetochore-pair where one kinetochore is attached via K-fibres to one and only one centrosome and its sister kinetochore is attached via K-fibres to the other centrosome only. Microtubules are observed to exist in either polymerising (growing) or depolymerising (shrinking) states; also during prometaphase and metaphase kinetochore oscillations are characterised by periods of poleward / anti-poleward movement with fairly uniform velocities separated by sharp reversals of direction. It is assumed that during a period of a kinetochore-pair oscillation the anti-poleward moving kinetochore is attached to polymerising microtubules growing away from its respective centrosome and that the poleward moving kinetochore is attached to depolymerising microtubules shrinking towards its respective centrosome. It therefore becomes natural to model oscillating kinetochores as being in one of two possible states $\sigma = \{+, -\}$ at any given time. Therefore a kinetochore-pair can be in one of four possible states at any given time $\{\sigma_1\sigma_2\} = \{++, --, +-, -+\}$. Given the observed periods of constant velocity during oscillations it is natural to assign an intrinsic velocity to a kinetochore depending on its state $v_\sigma = \{v_+, v_-\}$ (note that dynamics are only being considered here in one dimension, relative to a metaphase plate alignment). The source of these velocity states can be assumed to be the direct action of polymerising / depolymerising K-fibres on the kinetochores, but the nature of kinetochore dynamics is not considered here with any finer abstraction other than two constant velocity states. The observed dynamics of a kinetochore-pair at any given time are therefore the consequence of their internal states at that time plus any external effects.

### 4.2.2 High Viscosity Kinematics of Kinetochores

All dynamics are assumed to occur in a very high viscous limit [88]. That is kinetochores are assumed to flow in the cytoplasm with a very low Reynolds number ($\mathrm{R_e} << 1$). The Reynolds number is a dimensionless quantity characterising fluid flow around an object and is defined as

$$\mathrm{R_e} = \frac{vL}{\nu}$$

where $v$ is the relative velocity of the object to the fluid flow, $L$ is the characteristic length of the object and $\nu$ is the kinematic viscosity of the fluid. Typical kinetochore velocities during oscillations are assumed to be on the order of $10^{-7}\mathrm{ms}^{-1}$ [96]. The length scale of a human kinetochore is assumed to be on the order of $10^{-7}\mathrm{m}$ [155]. The kinematic viscosity of pure water at 37°C is on the order of $10^{-1}\mathrm{m}^2\mathrm{s}^{-1}$. Therefore the Reynolds number of an oscillating kinetochore is estimated to be $\approx \frac{10^{-7}10^{-7}}{10^{-1}} = 10^{-13} << 1$. The low Reynolds number assumption holds even if the estimate of the Reynolds number is too small by several orders of magnitude. Under a low Reynolds number flow the viscous drag force $\mathrm{F_d}$ on an object is given by Stokes' law and is directly proportional to the relative velocity $v$ between the object and the fluid.

$$\mathrm{F_d} = -\gamma v$$

where the drag coefficient $\gamma$ depends both on the properties of the fluid and the size and shape of the object. It is proportional to the dynamic viscosity of the fluid $\mu$ and the characteristic length of the object $L$, $\gamma \propto \mu L$ (note that the fluid dynamic viscosity $\mu$ is the product of the kinematic viscosity $\nu$ and the fluid density $\rho$, $\mu = \nu\rho$).

Consider an object initially at rest in a highly viscous fluid under the action of a constant external force $\mathrm{F}_a$. The net force on the object is the sum of the external force and the drag force $\mathrm{F_{net}} = \mathrm{F}_a + \mathrm{F_d}$. The net force on an object is equal to the rate of change of momentum of the object (Newton's 2$^{\mathrm{nd}}$ law). Assuming the object maintains a constant mass the net force on the object is equal to the product of the object's mass and its rate of change of velocity.

$$\mathrm{F}_a - \gamma v = m\frac{dv}{dt}$$

where $v$ is the velocity of the object and $m$ is the mass of the object. The solution to this equation in terms of $v$ is given by

$$v\left(t\right) = c\exp\left(\frac{-\gamma t}{m}\right) + \frac{\mathrm{F}_a}{\gamma}$$

where $c$ is an arbitrary constant. Assuming the object is initially moving with a velocity $v_0$ the constant $c$ can be solved for

$$v\left(t=0\right) = v_0 = c\exp\left(\frac{-\gamma \times 0}{m}\right) + \frac{\mathrm{F}_a}{\gamma}$$

therefore

$$c = v_0 - \frac{\mathrm{F}_a}{\gamma}$$

Finally, solving for $v$

$$v\left(t\right) = v_0\exp\left(-kt\right) + \frac{\mathrm{F}_a}{\gamma}\left(1 - \exp\left(-kt\right)\right) \tag{4.1}$$

where

$$k = \frac{\gamma}{m}$$

Thus the velocity makes a transition between the initial value of $v_0$ and the final value of $\frac{\mathrm{F}_a}{\gamma}$ with a decay constant $k$. (4.1) can be rearranged to give

$$\Delta v\left(t\right) = \Delta V\left(1 - \exp\left(-kt\right)\right)$$

where $\Delta v\left(t\right) = v\left(t\right) - v_0$ *i.e.* the difference in velocity over time. $\Delta V = \frac{\mathrm{F}_a}{\gamma} - v_0$ *i.e.* the difference in initial and final velocities.

Figure 4.1 shows solutions to (4.1) changing between an initial and final velocity value. Velocity values are shown as functions of $\log_{10}(t)$ for different values of $k$. The plots show that the velocity values sharply asymptote towards their final values, effectively remaining constant. A typical time scale for the transition between the initial and final velocities can be given in terms of $k$. If the final steady state velocity is said to be reached when the decay factor $\exp(-kt) = 0.1\%$ then $t_{\text{decay}} = -\ln(0.001)\,k^{-1} \approx 7k^{-1}$.

Calculating a value for $k$ for a human kinetochore is extremely difficult but a fairly reasonable value can be estimated accurate to within a few orders of magnitude. [156] reported an effective drag coefficient $\gamma = 6 \times 10^{-6}\text{Nsm}^{-1}$ for chromosome velocities observed in newt lung cells (newt lung cells have the advantage over human cells in that their relatively large size and small chromosome density allow direct micromanipulation experiments, the results of which can be used to estimate physical parameters such as drag coefficients). Assuming human kinetochores have roughly similar properties this value will be assumed to be within a few orders of magnitude of the value for human kinetochores. The mass of the human kinetochore - chromosome system is extremely difficult to estimate accurately given the current lack of structural detail available, however a simple estimate can be made. The main component of mass is assumed to be the DNA of the chromosome and its 'enslaved' water. A human chromosome is estimated to be approximately $4\mu$m in length; with kinetochores assumed to be approximately $1\mu$m apart the kinetochore - chromosome system is approximated as a cuboid with a volume of $4\mu\text{m}^3 = 4 \times 10^{-18}\text{m}^3$. Experiments have estimated the the mass density of mitotic chromosomes [157] to be approximately $0.2\text{pg}\,(\mu\text{m})^{-3} = 0.2 \times 10^3\text{kgm}^{-3}$. Water has a mass density of $10^3\text{kgm}^{-3}$ so assuming a 1:1 ratio of DNA and water the combined mass density is $1.2 \times 10^3\text{kgm}^{-3}$. Therefore the estimated mass of the kinetochore - chromosome system is $1.2 \times 10^3 \times 4 \times 10^{-18}\text{kg} \approx 10^{-14}\text{kg}$, this value is likely accurate to within a few orders of magnitude. Therefore the estimate for the decay factor $k \approx \frac{6\times10^{-6}\text{Nsm}^{-1}}{10^{-14}\text{kg}} \approx 10^9\text{s}^{-1}$. Even if this value is several orders of magnitude too large the decay time scale will still be much smaller than one second, $t_{\text{decay}} \sim k^{-1} << 1\text{s}$. Since kinetochore positions are measured on the scale of seconds, $t \sim 1\text{s}$ then it is appropriate to consider applied forces resulting in constant velocities $v = \frac{\text{F}_a}{\gamma} \rightarrow v \propto \text{F}_a$.

In Section 4.2.1 it was concluded to model kinetochores as being in one of two states $\{+,-\}$, each with an intrinsic velocity. These constant intrinsic velocity states can now be considered to be the result of a constant applied force in the high viscosity limit.

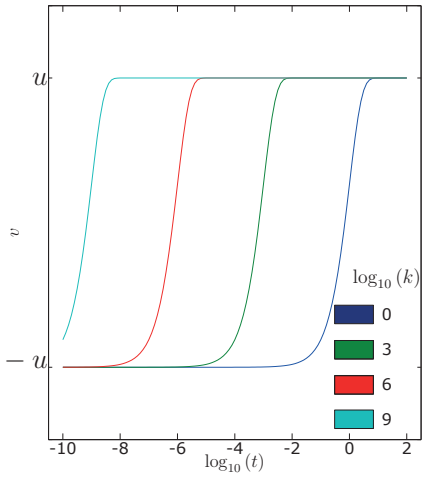


**Figure 4.1:** Velocity transitions of an object under a constant external force in a highly viscous medium in one dimension. Solutions of (4.1) with initial and final velocities given by $v_0 = -u$ and $\frac{\mathrm{F}_a}{\gamma} = u$. Solutions shown as functions of $\log_{10}(t)$ with four different values of $k$ (represented by different values of $\log_{10}(k)$.)

### 4.2.3 Stochastic Frame to Frame Displacement Model

Kinetochore sisters are described by their position normal to the metaphase plate *i.e.* by the coordinate pair $(X_t^1, X_t^2)$, where sister 1 is to the right of sister 2 ($\hat{X}^1 > \hat{X}^2$ on average). Position is measured relative to the plate *i.e.* the plate is positioned at $x = 0$. Thus the K-fibre of sister 1 lies in $x > X_t^1$ and that of sister 2 $x < X_t^2$ at time $t$. The (projected) inter-sister distance is thus $X^1 - X^2$ and is typically positive but could be negative under an extreme twist. The system is in a high viscous limit so inertial forces are ignored. Thus the following force balance applies for each kinetochore

$$F_{\text{drag}} + F_{\text{KF}} + F_{\text{spring}} + F_{\text{PEF}} + F_{\text{noise}} = 0$$

where the drag force is proportional to the kinetochore velocity $F_{\text{drag}} = -\gamma \frac{dX}{dt}$ with an (effective) drag coefficient $\gamma$, the force from the kinetochore $F_{\text{KF}}$ is either anti-poleward (polymerising $F_+$) or poleward (depolymerising $F_-$), the spring force is assumed to be in the linear regime $F_{\text{spring}} = \kappa_0 (X^1 - X^2 - L\cos\theta)$ (where it is projected on to the metaphase plate normal, subtended angle $\theta$) and the polar ejection force (PEF) is

linearised around the metaphase plate $F_{\text{PEF}} = -\alpha_0 X^1$, moving the kinetochore towards the plate. $\kappa_0$ is the spring constant, $L$ the spring's natural length and $\alpha_0$ a coefficient parameterising the linear PEF dependence on position. The last force $F_{\text{noise}}$ is the random force coming from molecular collisions and would result in Brownian motion of the kinetochore if it was otherwise unconstrained. This gives for sister 1

$$\gamma \frac{dX^1}{dt} = -F_{\sigma^1} - \kappa_0 \left(X^1 - X^2 - L\cos\theta\right) - \alpha_0 X^1 + \sqrt{(2\gamma k_B T)}\zeta_t$$

constituting forces from the K-fibre, spring, PEF and random noise respectively. The K-fibre force term comes with a minus sign because sister 1 lies towards positive infinity and $F_\pm$ are defined as the force from a polymerising and depolymerising K-fibre respectively. Here $\sigma^1$ is the state of the attached K-fibre ($+/-$, polymerising, depolymerising respectively), $k_B$ is Boltzmann's constant, $T$ temperature (in Kelvins) and $\zeta_t$ is white noise (time derivative of Wiener noise, $\zeta_t = \frac{dW_t}{dt}$) satisfying $\langle \zeta_t \rangle = 0$ and $\langle \zeta_t \zeta_{t'} \rangle = \delta(t - t')$. The noise coefficient is determined by the fluctuation-dissipation theorem [158]. The drag coefficient is extremely difficult to measure or estimate and would have large variance; thus it is not separated out and it is absorbed into the parameters,

$$\frac{dX^1}{dt} = -\gamma^{-1} F_{\sigma^1} - \kappa \left(X^1 - X^2 - L\cos\theta\right) - \alpha X^1 + \sqrt{\frac{2k_B T}{\gamma}}\zeta_t$$

where $\kappa = \kappa_0/\gamma$, $\alpha = \alpha_0/\gamma$. All these terms have dimensions of speed, in particular $\gamma^{-1}F_{\sigma^1}$ is a velocity and in absence of the other forces $\frac{dX^1}{dt} = -\gamma^{-1}F_{\sigma^1}$ *i.e.* the kinetochore would move at speed $-\gamma^{-1}F_{\sigma^1}$. $v_\pm$ is defined as $v_\pm = \gamma^{-1}F_\pm$ thus parameterising the action of the K-fibre by an effective velocity. The system thus has two speeds $v_\pm$ and two 'force parameters' $\kappa\,(s^{-1})$ and $\alpha\,(s^{-1})$. Finally measurements are made over constant time-steps, therefore the equation is integrated over intervals of $\Delta t$. The forces are likely to be slowly varying over the time interval thus the force integral is approximated as follows $\int_t^{t+\Delta t} F(X_t)\,dt = F(X_t)\,\Delta t$, accurate up to orders $O(\Delta^2)$. Integrating over the time interval $[t, t+\Delta t]$ the approximate displacement over a time interval $\Delta t$ is obtained

$$X^1_{t+\Delta t} = X^1_t - v_{\sigma_t}\Delta t - \kappa\Delta t \left(X^1_t - X^2_t - L\cos\theta_t\right) - \alpha\Delta t X^1_t + \Delta t N\left(0, s^2\right)$$

(Wiener noise over an interval is Gaussian, $W_{t+\Delta t} - W_t \sim N(0, |\Delta t|)$). $s^2 = 2k_BT/(\gamma \Delta t)$ where $s$ has dimensions of speed (for instance Einstein's relation would give $\gamma = k_BT/D$, $D$ the effective diffusion coefficient of the kinetochore). Retaining the parameterisation in terms of speeds is useful since it is physically meaningful.

The basic model for kinetochore displacements ($\Delta X_t = X_{t+1} - X_t$) over the interval $\Delta t$ is thus the following:

$$\begin{aligned} \left(X^1_{t+1} - X^1_t\right)/\Delta t &= -v_{\sigma^1_t} - \kappa\left(X^1_t - X^2_t - L\cos\theta_t\right) - \alpha X^1_t + N(0, s^2) \\ \left(X^2_{t+1} - X^2_t\right)/\Delta t &= v_{\sigma^2_t} - \kappa\left(X^2_t - X^1_t + L\cos\theta_t\right) - \alpha X^2_t + N(0, s^2) \end{aligned} \tag{4.2}$$

where $\sigma^k_t$ is the kinetochore state ($+/-$, polymerising or depolymerising respectively) at time $t$, $\theta_t$ is the measured twist of the sister axis relative to the metaphase plate normal, and $v_+/v_-$ are the polymerisation/depolymerisation velocities of the K-fibres, $\kappa$ is the centromeric spring constant, $L$ the spring's natural length and $\alpha$ parameterises the PEF (linearised around the metaphase plate). The noise is assumed Gaussian with variance $s^2$; hereafter the precision $\tau = s^{-2}$ will be used to parameterise this noise. Figure 4.2 shows a schematic of the model.

The sisters switch state independently under a coherence-incoherence model. Specifically the state $\sigma_t$ is a hidden Markov Chain (hMC) where the rate of switching is

$$\begin{aligned} r\left(\sigma^k \to -\sigma^k | \sigma^2 \neq \sigma^1\right) &= b_c \\ r\left(\sigma^k \to -\sigma^k | \sigma^2 = \sigma^1\right) &= b_{ic} \end{aligned} \tag{4.3}$$

*i.e.* the rate depends on if the sisters are *coherent* (states $+/-$ or $-/+$), when they would both move to the right/left respectively, or *incoherent* ($+/+$, contracting, $-/-$ expanding). Oscillations require $b_c < b_{ic}$, since coherent periods are longer. Recall $+$ is polymerising (trailing) and $-$ is depolymerising (leading) during coherence runs. Coordinated switching occurs since coherence is restored quickly, either as a sustained switching (both sisters switch direction) or as a switching reversal (first sister switching again). Crucially the sister who switches is chosen at random *i.e.* there is no bias in the model. Simulations of this model exhibit quasi-periodic oscillations similar to

observed sister pair dynamics (Figure 4.3). The model however lacks any feedback or regulatory processes, either mechanistic such as an applied force dependence for the K-fibre transition rate between depolymerisation and polymerisation, or through a biochemical sensing circuit [140]. The model's simplicity within a context of biological realism allows it to be fitted to experimental data and used to infer which mechanisms are supported by the actual data. In particular since there is no implicit sister preference to the switching order in the model any biases present in the data can be determined.

A Markov chain Monte Carlo (MCMC) algorithm was developed to compute the posterior distribution of the parameters and the unknown (hidden) sister states. Each trajectory had sufficient information to fit all the parameters except for the natural length $L$ that suffered from an identifiability issue, see Section 4.4.

#### 4.2.3.1 Model simulation

The model was simulated (Figure 4.3) by firstly simulating the sister states as per (4.3), and then simulating displacements as per (4.2). The model was simulated in 1D *i.e.* $\theta = 0$ for all time. Parameters were chosen based on runs of the model on real data. Parameters for Figure 4.3 are $b_c = 0.06s^{-1}, b_{ic} = 0.8s^{-1}$ for the hidden sister states and $v_+ = 0.05\mu m s^{-1}, v_- = -0.03\mu m s^{-1}, L = 0.8\mu m, \kappa = 0.05s^{-1}, \alpha = 0.03s^{-1}$ and $\tau = 1000s^2\mu m^{-2}$.

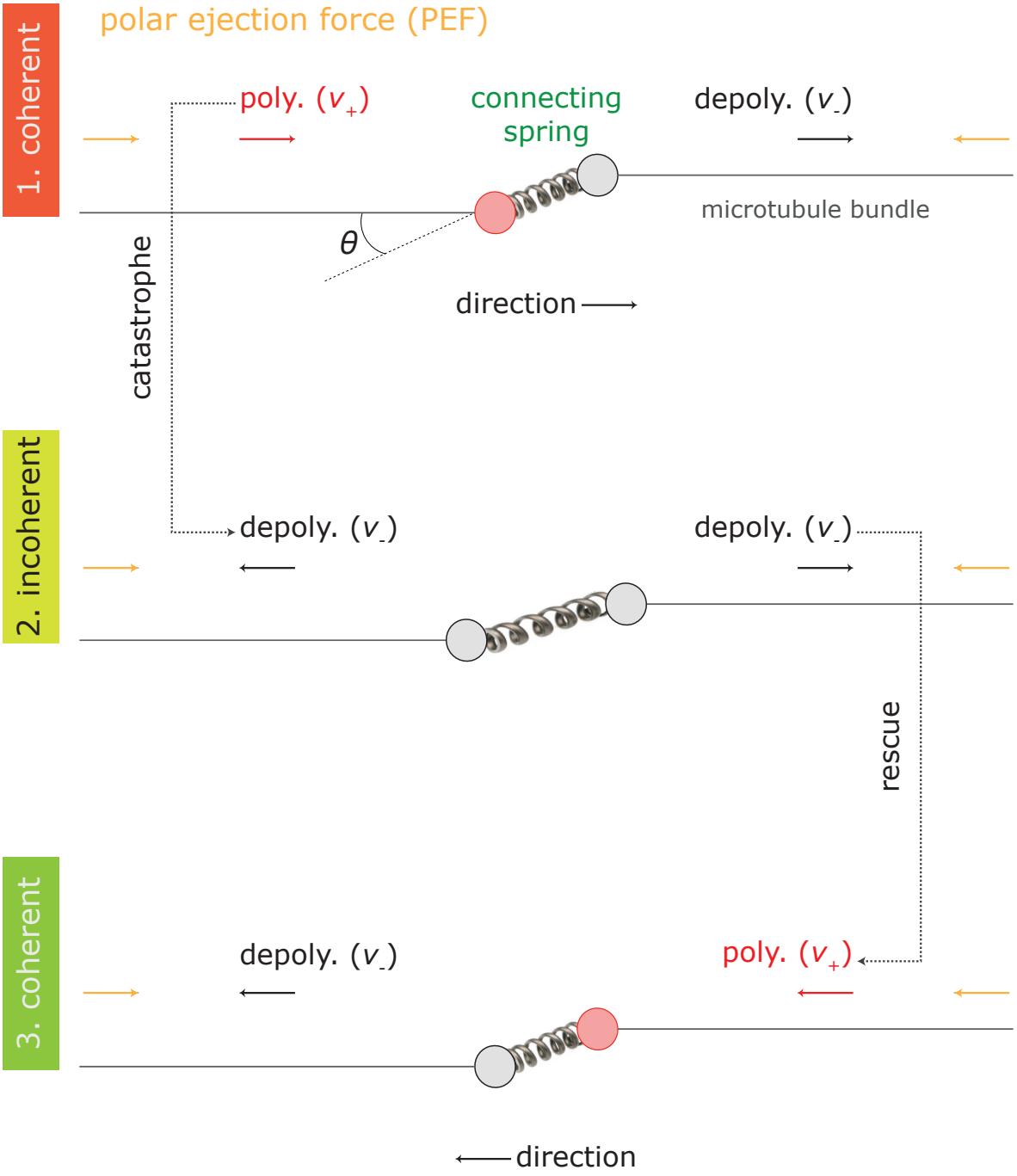


**Figure 4.2:** Kinetochore dynamic model schematic. Net force acting on each kinetochore of a sister kinetochore-pair at any single time-point is equal to the sum of: 1) the intrinsic force acting on each kinetochore depending on the state of the kinetochore at that time $\{v_+, v_-\}$ (polymerising / depolymerising) (red / black), 2) the force caused by the deformation of a linear Hookean spring connecting both sisters (spring force taken as the component acting along the direction of kinetochore motion) and 3) the polar ejection force (orange) assumed to scale linearly with distance from the centre of the coordinate system. Kinetochores are assumed to switch stochastically between polymerising and depolymerising states, Equation (4.3).

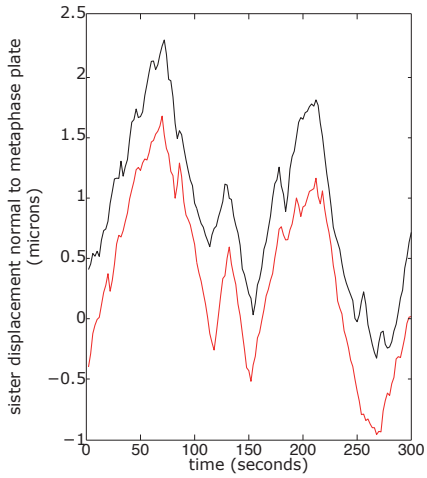


**Figure 4.3:** Simulation of the Kinetochore Dynamics Model. See Section 4.2.3.1 for simulation details. Black / red are simulated trajectories of sister-kinetochores 1 / 2 respectively.

## 4.3 MCMC Methodology

A Bayesian methodology was implemented using a Markov chain Monte Carlo (MCMC) algorithm to compute the posterior probability $\pi\left(v_{\pm},\kappa,L,\alpha,\tau,\sigma_t^k|x_t^k,\theta_t\right)$ of the parameters and the hidden states $\left(\sigma_t^k\right)$ given the observed data $(x_t^1,x_t^2,\theta_t)$. The data is measured at equally spaced time points therefore time was identified with frame number, indexed by $i$. From this distribution all the required moments can be computed *e.g.* mean and variance, switching times can be found and the distribution can be used to answer hypotheses *e.g.* compute the support for $|v_-|>v_+$. The model is fitted to each pair of sister trajectories separately. In the following inter-sister is defined as distance $d_i=x_i^1-x_i^2$ and kinetochore frame displacement $dx_i^k=x_{i+1}^k-x_i^k$. The likelihood given the data and the hidden states is

$$\begin{aligned}\pi\left(x|\sigma,\tau,L,\kappa,v_{\pm},\alpha\right) &= \tau^{n-1}\prod_{k=1,2}\exp\left(-\tfrac{\tau}{2}\sum_{i=1}^{n-1}\left(dx_i^k-\Delta t\, f_i^k\left(\sigma\right)\right)^2\right),\\ f_i^k\left(\sigma\right) &= (-)^k v_{\sigma_i^k}+(-)^k\kappa\left(d_i-L\cos\left(\theta_i\right)\right)-\alpha x_i^k,\end{aligned} \tag{4.4}$$

In the following $\Delta t$ is absorbed into $v_{\pm},\kappa,\alpha$ for simplicity; time is effectively measured in frames. Here $f^k$ is proportional to the force on the sister $k$ at time (frame) $i$, up to the drag coefficient.

### 4.3.1 Priors and Posterior

Conjugate priors were used as follows: $v_{\pm}\sim N\left(\pm\mu,s_v^2\right)$, $\tau\sim\Gamma\left(c,d\right),\kappa\sim N\left(\mu_\kappa,s_\kappa^2\right)$, $L\sim N\left(\mu_L,s_L^2\right)$, $\alpha\sim N\left(\mu_\alpha,s_\alpha^2\right)$ and a Beta distribution on the hMC transition probabilities, parameterised by the probability of remaining in the same state (no change) per frame, $p_c\sim Beta\left(a_c,b_c\right)$ whilst the sisters are coherent and $p_{ic}\sim Beta\left(a_{ic},b_{ic}\right)$ whilst incoherent. These are related to the rates above by $p_c=e^{-\Delta t b_c},p_{ic}=e^{-\Delta t b_{ic}}$. Very weak priors were used, see Table 4.3, except for $p_c,p_{ic}$ where a prior was used that shifts the probability of no change per frame away from 0, and for $L$ a prior was used that was informed from nocodazole treated cells (microtubules are totally depolymerised), Figure 4.4. This prior on $L$ was required since the model has an *a posteriori* identifiability problem (Section 4.4). The posterior follows from Bayes theorem and is given

by (up to proportionality),

$$\begin{aligned}\pi\left(\sigma,\tau,L,\kappa,v_{\pm},\alpha|x\right) \quad \propto \quad & \pi_{\alpha}\pi_{v_{+}}\pi_{v_{-}}\pi_{\tau}\pi_{\kappa}\pi_{L} \\ & p_{c}^{a_{c}+N_{c}-K_{c}-1}\left(1-p_{c}\right)^{b_{c}+K_{c}-1}p_{ic}^{a_{ic}+N_{ic}-K_{ic}-1}\left(1-p_{ic}\right)^{b_{ic}+K_{ic}-1} \\ & \tau^{n-1}\prod_{k=1,2}\exp\left(-\tfrac{\tau}{2}\sum_{i=1}^{n-1}\left(x_{i+1}^{k}-x_{i}^{k}-f_{i}^{k}\left(\sigma\right)\right)^{2}\right)\end{aligned} \tag{4.5}$$

comprising the priors, the hMC state dynamics and the data components respectively. Here $N_c, K_c$ are the number of coherence time points and the number of switches to incoherence respectively, and similarly $N_{ic}, K_{ic}$. Of course $N_c + N_{ic} = n - 1$ ($n$ being the number of time-points), the last time-point not being assigned a state since there is no displacement information.

### 4.3.2 Updates

Variables were updated separately as follows:

**Precision** $\tau$. The conditional on $\tau$ is Gamma distributed giving an update

$$\tau\big|_{.} \quad \sim \quad \Gamma\left(c+n-1,d+\tfrac{1}{2}\sum_{k,i}\left(x_{i+1}^{k}-x_{i}^{k}-f_{i}^{k}\right)^{2}\right)$$

**Velocities** $v_{\pm}$. The conditionals on $v_{\pm}$ are Gaussian distributed; for $v_+$ there is a conditional,

$$\begin{aligned}\pi\left(v_{+}|\cdot\right) \quad \propto \quad & \exp-\tfrac{1}{2}\left(\tfrac{1}{s_{v}^{2}}\left(v_{+}-\mu\right)^{2}+\tau\sum_{k}\sum_{i|\sigma_{i}^{k}=+}\left(x_{i+1}^{k}-x_{i}^{k}-\left(-\right)^{k}v_{+}-\left(-\right)^{k}\right. \\ & \left.\kappa\left(x_{i}^{1}-x_{i}^{2}-L\cos\left(\theta_{i}\right)\right)+\alpha x_{i}^{k}\right)^{2}\Big)\end{aligned}$$

Completing the square,

$$\begin{aligned}v_{\pm}\big|_{.} \quad \sim \quad & N\Big(\left(\tau_{v}^{\pm}\right)^{-1}\Big(\pm\mu s_{v}^{-2}+\tau\sum_{k}\sum_{i|\sigma_{i}^{k}=\pm}\Big(\left(-\right)^{k}\left(x_{i+1}^{k}-x_{i}^{k}+\alpha x_{i}^{k}\right)- \\ & \kappa\left(x_{i}^{1}-x_{i}^{2}-L\cos\left(\theta_{i}\right)\right)\Big)\Big),\left(\tau_{v}^{\pm}\right)^{-1}\Big)\end{aligned}$$

with $\tau_v^{\pm} = \tau n_{\pm} + s_v^{-2}$. Here $n_{\pm}$ are number of time points in state $\pm$ respectively combined over both sister trajectories; $n_+ + n_- = 2(n-1)$ since the last time point is irrelevant. A Metropolis-Hasting rejection sampler is used to impose the constraints $v_+ > 0, v_- < 0$, using the above as a proposal.

**Spring constant** $\kappa$. The conditional on $\kappa$ is Gaussian. It reads,

$$\begin{aligned}\pi(\kappa|\cdot) \quad \propto \quad & \exp -\tfrac{1}{2}\left(\tfrac{1}{s_\kappa^2}(\kappa-\mu_\kappa)^2 + \tau\textstyle\sum_{k,i}\left(x_{i+1}^k - x_i^k - (-)^k v_{\sigma_i^k} - (-)^k\right.\right. \\ & \left.\left.\kappa\left(x_i^1 - x_i^2 - L\cos\theta_i\right) + \alpha x_i^k\right)^2\right)\end{aligned}$$

Completing the square gives the update, ignoring positivity,

$$\begin{aligned}\kappa\big|_{\cdot} \quad \sim \quad & N\left(\tau_\kappa^{-1}\left(\mu_\kappa s_\kappa^{-2} + \tau\textstyle\sum_{k,i}\left((-)^k\left(x_{i+1}^k - x_i^k + \alpha x_i^k\right) - v_{\sigma_i^k}\right)\right.\right. \\ & \left.\left.\left(x_i^1 - x_i^2 - L\cos\theta_i\right)\right), \tau_\kappa^{-1}\right)\end{aligned}$$

with $\tau_\kappa = s_\kappa^{-2} + 2\tau\sum_{i=1}^{n-1}\left(x_i^1 - x_i^2 - L\cos\theta_i\right)^2$. $\kappa \geq 0$ was imposed using the above as a proposal with a Metropolis-Hasting acceptance step (rejection sampler).

**Spring natural length** $L$. The natural length $L$ has conditional,

$$\begin{aligned}\pi(L|\cdot) \quad \propto \quad & \exp -\tfrac{1}{2}\left(\tfrac{1}{s_L^2}(L-\mu_L)^2 + \tau\textstyle\sum_{k,i}\left(x_{i+1}^k - x_i^k - (-)^k v_{\sigma_i^k} - (-)^k\right.\right. \\ & \left.\left.\kappa\left(x_i^1 - x_i^2 - L\cos\left(\theta_i\right)\right) + \alpha x_i^k\right)^2\right)\end{aligned}$$

Completing the square gives the update,

$$\begin{aligned}L\big|_{\cdot} \quad \sim \quad & N\left(\tau_L^{-1}\left(\mu_L s_L^{-2} + \tau\kappa\textstyle\sum_{k,i}\cos\left(\theta_i\right)\left((-)^{k+1}\left(x_{i+1}^k - x_i^k + \alpha x_i^k\right) + v_{\sigma_i^k} + \right.\right.\right. \\ & \left.\left.\left.\kappa\left(x_i^1 - x_i^2\right)\right)\right), \tau_L^{-1}\right)\end{aligned}$$

with $\tau_L = s_L^{-2} + 2\tau\kappa^2\sum_i \cos^2\left(\theta_i\right)$. The sum on $i$ is over $1...n-1$ (excluding last time point). Again positivity is imposed with a rejection sampler.

**Antipoleward force parameter** $\alpha$. For $\alpha$ the conditional $\pi(\alpha|\cdot)$ is a truncated

Gaussian,

$$\begin{aligned}\pi(\alpha|\cdot) \quad \propto \quad & \exp -\tfrac{1}{2}\left(\tfrac{1}{s_\alpha^2}(\alpha-\mu_\alpha)^2+\tau\textstyle\sum_{k,i}\left(x_{i+1}^k-x_i^k+(-)^{k+1}v_{\sigma_i^k}+(-)^{k+1}\right.\right.\\ & \left.\left.\kappa\left(x_i^1-x_i^2-L\cos\theta_i\right)+\alpha x_i^k\right)^2\right)\end{aligned}$$

with $\alpha > 0$. This gives a conditional posterior,

$$\begin{aligned}\alpha|\cdot \quad \sim \quad & N\left(\tau_\alpha^{-1}\left(\mu_\alpha s_\alpha^{-2}-\tau\textstyle\sum_{k,i}x_i^k\left(x_{i+1}^k-x_i^k+(-)^{k+1}v_{\sigma_i^k}+(-)^{k+1}\right.\right.\right.\\ & \left.\left.\left.\kappa\left(x_i^1-x_i^2-L\cos\theta_i\right)\right)\right),\tau_\alpha^{-1}\right)\end{aligned}$$

with $\tau_\alpha = s_\alpha^{-2}+\tau\sum_{i,k}\left(x_i^k\right)^2$ and truncated to $\alpha > 0$ by a rejection sampler.

**State transition probabilities** $p_c, p_{ic}$. The conditionals on $p_c, p_{ic}$ are Beta distributed as follows (Equation (4.5)), $p_i\Big|_{\cdot} \sim Beta\left(a_c+N_c-K_c, b_c+K_c\right)$ where $N_c, K_c$ are the number of coherence time points and the number of switches to incoherence respectively for the current sister hidden states $\sigma$ and similarly $p_{ic}\Big|_{\cdot} \sim Beta\left(a_{ic}+N_{ic}-K_{ic}, b_{ic}+K_{ic}\right)$.

**Hidden states** $\sigma_t^k$. This hidden MC can be updated by a Gibbs move locally at each time point [159]. Define $a_{rs}$ as the transition matrix between the states $(+,-)$ with $p_c, p_{ic}$ the probabilities of no change $a$ depending on the current state. The conditional for state $\sigma_i^k$ on sister $k$ is then given by,

$$\pi\left(\sigma_i^k=r|\cdot\right) \propto a_{\sigma_{i-1}^k r}\left(\sigma_{i-1}^{\hat{k}}\right)\phi\left(\Delta X_i^k|\sigma_i^k=r,\cdot\right)a_{r\sigma_{i+1}^k}\left(\sigma_i^{\hat{k}}\right)$$

where $\phi$ is the Gaussian pdf of $\Delta X_i^k$ depending on $\sigma_i^k$, and dependence of $a$ is indicated on the other sister $\hat{k}$ (determining whether the sisters are coherent/incoherent). The first and last time points are slightly different, as there is no preceding/following state. This conditional is easily normalised for a Gibbs update (or a Metropolis-Hasting always proposing a change) running consecutively over sisters and through time.

However this algorithm has poor mixing; on the Gelman-Rubin convergence statistic [160] the noise $\tau$ is the slowest to converge because of poor convergence of the hMC. Performance is improved by using two moves. Firstly doing a joint update of both sisters at each time point *i.e.* the above conditional (product over sisters)

is used to compute the probabilities of states $++, +-, -+, --$ at each time point followed by a Gibbs update. Secondly a block move of length $w$ is used for each sister separately. This is computationally time consuming taking about 4 times longer than the joint sister update. It was found that a 20% mix of the block move $w$ randomly selected over 4...10 gave as good convergence as a full block move. The block move is constructed as follows. Define row vectors $u_0, u_1$ associated with current states $0, 1$ at position $i$. Then iteratively move to the next time point reconstructing $u_r = \left(u_0 a_{0r} \phi\left(\Delta X_i^k | \sigma_i^k = 0, \cdot\right)\right) \oplus \left(u_1 a_{1r} \phi\left(\Delta X_i^k | \sigma_i^k = 1, \cdot\right)\right)$ on sister $k$, thereby doubling the length of $u_r$. This works through the window. Initialise the vectors by $u_r = a_{sr}$ if $\sigma_{i_1}^k = s$, and then $u_r$ is the unnormalised probability vector of all $2^w$ states if $\sigma_{i_{w+1}}^k = r$. The state in the window is then updated using a Gibbs move. Windows from the start of the time series have a prior on the initial position as above. Computational costs to update over the full time series are similar for $w = 2...11$, thereafter rising.

### 4.3.3 Initial conditions, mixing and convergence

Ten chains were run for each trajectory (sister pair) from over dispersed initial conditions and the Gelman-Rubin convergence statistic was used to test for convergence [160]. Chains were initially run up to 500,000 samples. If they failed to converge (convergence diagnostic $> 1.1$ on any parameter), they were run up to a maximum of 4,371,200 samples. Any trajectory with a convergence statistic still $> 1.1$ was considered unconverged and was discarded from further analysis. See Table 4.2 for number of trajectories that passed convergence. The hidden state is initialised from a simulation of the MC given the initial parameters $p_c, p_{ic}$. 5,000 samples per chain were used for final analysis, the result of a total chain length of either: 500,000; 1,050,100; 2,155,400 or 4,371,200 subsampled by a factor of: 50; 100; 200 or 400 and subject to an initial burn-in (after sub-sampling) of: 5000; 5501; 5777 or 5928 respectively.

## 4.4 Natural Length Identifiability

If the angle $\theta_t$ is constant (in time) there is a parameter symmetry *i.e.* the model is *a priori* unidentifiable. Specifically, the natural length $L$ of the spring can be absorbed into $v_\pm$ since there is the symmetry $L \to L + l/\cos\theta$, $v_\pm \to v_\pm + \kappa l$; thus only the two combinations $v_+ - v_-, v_+ - \kappa L \cos\theta$ (and recombinations of these) are independent of the symmetry and thus identifiable (estimatable). The sign constraints $v_+ > 0, v_- < 0$ limit this identifiability symmetry to $-v_+/\kappa < l < -v_-/\kappa$ in addition to $L + l/\cos\theta > 0$, where $L, v_\pm$ are the true (unknown) values. An informed prior is thus required for $L$ in this case. This symmetry is lost if $\theta_t$ varies over the trajectory; however the low variation of $\theta_t$ leaves an *a posteriori identifiability* problem. To estimate the natural length of kinetochore pairs cells were treated with a high dose of nocodazole overnight (the drug was added after the required siRNA incubation period in the case of RNAi experiments, see Chapter 2 for experimental details). This resulted in cells depleted of microtubules, allowing kinetochore-pairs to be observed in an unattached, tension free state. Cells that had entered prometaphase were imaged as described in Section 2.3 although the Z-spacing was set to $0.2\mu$m $\times$ 31 slices, imaging $6\mu$m in Z. The higher Z resolution was used since kinetochore pairs in cells treated with nocodazole were not necessary aligned with their axis roughly perpendicular to Z as they are when bi-orientated. The imaging conditions still allowed a 3D frame to be recorded every 2 seconds. The reduced spatial range in Z did not cause a problem since no metaphase plate was fitted and only inter-sister distance measurements were analysed. Movies were analysed as described in Chapter 3 following all steps except no metaphase plate was fitted (Section 3.5). Tracking was initially carried out in an unaligned coordinate system corrected for centre of mass shift only (Section 3.6) before frame alignment (Section 3.8). For sister-kinetochore track pairing (Section 3.9) the cost due to track angles was not considered. Sister-kinetochore trajectories from nocodazole treated cells were assumed to be under the influence of thermal fluctuations so trajectories were fitted to a one-dimensional harmonic oscillation model:

$$D_{t+1} = D_t - \kappa\left(D_t - L\right) + N\left(0, s'^2\right) \tag{4.6}$$

where $D_t$ is the separation between trajectories at time $t$. The model was fitted to trajectory pairs using a MCMC methodology similar to the methods discussed in Section 4.3 (without the need to compute any hidden states) to infer the natural inter-kinetochore length for each condition. Cells not treated with siRNA and Control siRNA treated cells were found to have virtually identical natural lengths of around 0.77$\mu$m. An additional condition was used as a control, Nuf2 siRNA (without nocodazole); cells depleted of Nuf2 were unable to make end-on attachments between kinetochores and microtubules. The natural lengths from Nuf2 siRNA cells were virtually identical to lengths from untreated and Control siRNA cells at around 0.78$\mu$m. The natural length of CAPD2 siRNA was found to be larger, at around 0.97$\mu$m and with larger variance, consistent with the idea of sister-kinetochores being attached by a spring with a lower spring constant undergoing thermal fluctuations, see Figure 4.4 for the results.

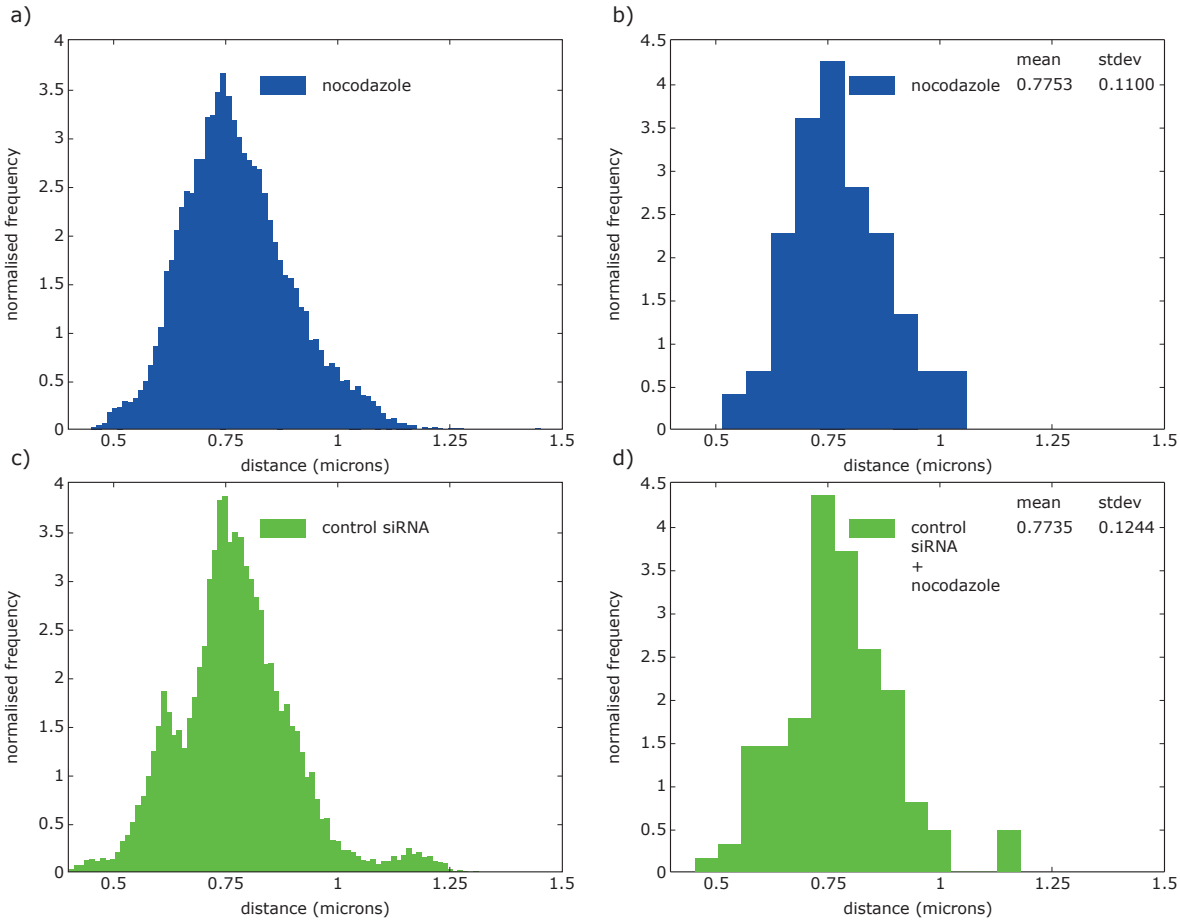


**Figure 4.4:** Natural inter-kinetochore distance as determined by nocodazole treatment. **a,c,e,g)** Measured inter-kinetochore distances. **b,d,f,h)** Natural length inferred by fitting kinetochore trajectories to a 1D harmonic motion model (distribution of trajectory means is shown, computed on EV $>$ 0.25 trajectories under 1D harmonic model). Rows correspond to a,b) no siRNA treatment (142 trajectories), c,d) control siRNA (122 trajectories) *cont*

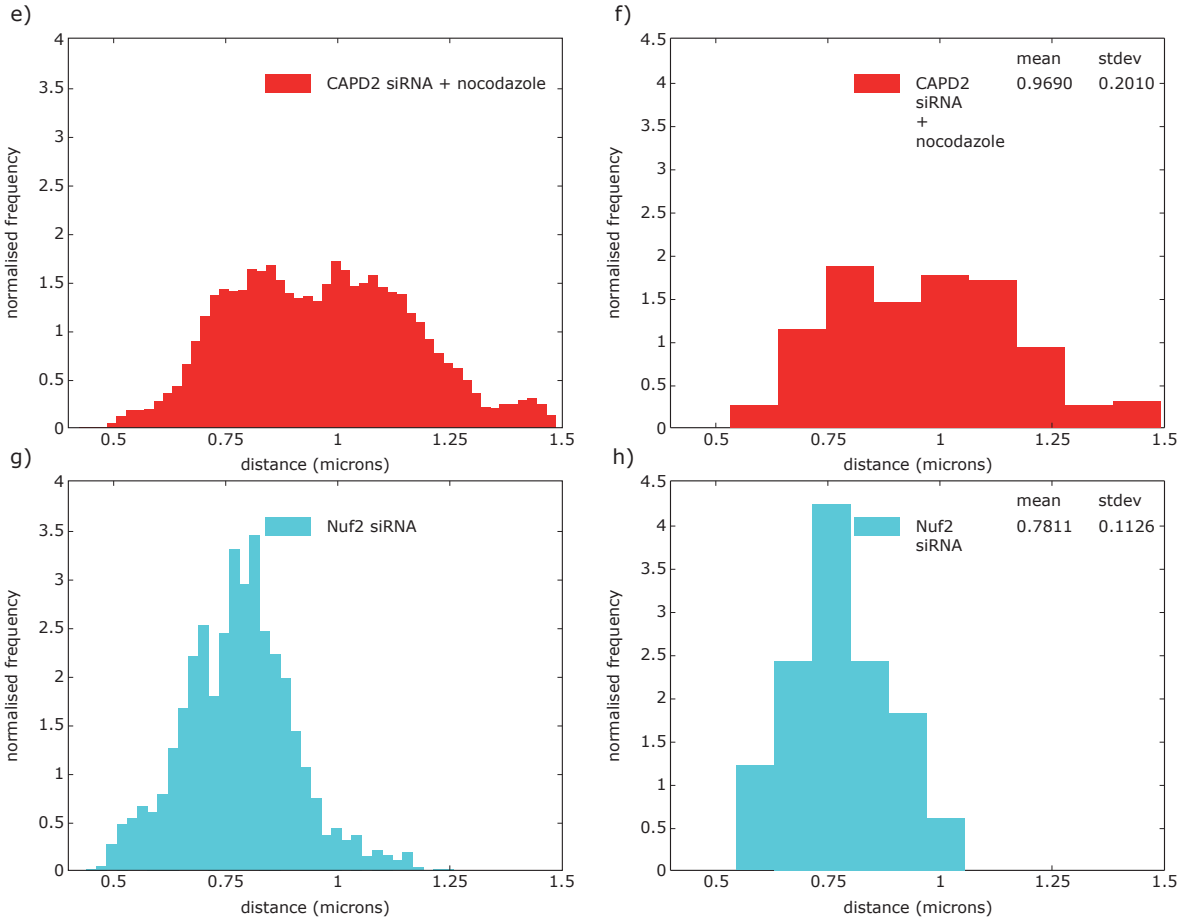


**Figure 4.4:** *cont* e,f) CAPD2 siRNA (187 trajectories), g,h) Nuf2 siRNA (no nocodazole, 21 trajectories).

## 4.5 Explained Variance

Explained Variance is a model-fitting statistic used to measure how well the fitted model parameters and the hidden states explain the observed variance of a trajectory. The explained variance EV is defined as follows. For dynamic model (4.2) analysed data, for model parameters, hidden state and data compute the sum of squares

$$V = \sum_{k=1,2} \sum_{i=1}^{n} (x_{i+1}^k - x_i^k - f_i^k(\sigma))^2, \quad f_i^k(\sigma) = (-)^k v_{\sigma_i^k} + (-)^k \kappa(x_i^1 - x_i^2 - L\cos(\theta_i)) - \alpha x_i^k$$

or for 1D harmonic model (4.6) analysed data, for model parameters and data compute the sum of squares

$$V = \sum_{i=1}^{n} (D_{i+1} - D_i - f_i)^2, \quad f_i = -\kappa(D_i - L)$$

This is the difference between the predicted displacements and the observed displacements. By averaging over the posterior (samples from MCMC) the (average) explained variance is obtained,

$$\text{EV} = 1 - \frac{\mathbf{E}_{posterior}[V]}{V_0} \tag{4.7}$$

where for the dynamic model $V_0$ is the sum of the displacement variances of the two sisters,

$$V_0 = \sum_{k=1,2} \sum_{i=1}^{n} (x_{i+1}^k - x_i^k)^2$$

Strictly the mean displacement should be subtracted in the previous expression but this is small for long time series. Similarly for the 1D harmonic model

$$V_0 = \sum_{i=1}^{n} (D_{i+1} - D_i)^2$$

## 4.6 High Throughput Kinetochore Dynamic Data

Data-driven modelling requires a large number of sister kinetochore trajectories sampled at a high enough resolution to capture key dynamic processes. Using the assay described in Chapter 3 a database of dynamic data consisting of thousands of HeLa-cell sister-kinetochore trajectories was compiled. Experimental details can be found in Chapter 2. Sister kinetochore trajectories were given relative to an aligned metaphase plate coordinate system (see Section 3.7). Before being processed data used for modelling was put through automatic filters on anaphase events, trajectory length and for the detection of any remaining tracking errors as follows (see Table 4.1 for the effect of filters on data throughput):

- **Anaphase Filter:** The model fitted to the trajectory data did not account for the initiation of anaphase therefore trajectories were first filtered of any anaphase time-points. Anaphase frames were detected during the tracking assay (see Section 3.10).

- **Tracking Error Filter:** To remove any possible remaining tracking errors trajectories were filtered using the technique described in Section 3.11.1. Any time-points detected as errors were removed.

- **Trajectory Length Filter:** The MCMC methodology used to fit the model required sufficiently long continuous trajectory pairs. Therefore the database was filtered for trajectory pairs that contained a section of data that continually spanned at least 75% of a 5 minute movie *i.e.* lasted at least 3 minutes 46 seconds or 113 time-points with no internal missing time-points. For trajectories that passed the filter any data outside the continuous set of time-points was discarded.

## 4.7 Final Summary

A basic mechanical model of bi-orientated chromosome oscillations has been introduced based on binary-state kinetochores, a linear spring-like inter-kinetochore connection and an external spatial force gradient biased towards the centre of the cell body. A statistical framework has been established designed to fit the model directly to sister-

kinetochore trajectories. Model-fitting requires strong prior knowledge on the natural length between sister-kinetochores; data which was provided by imaging experiments on nocodazole-treated cells followed by model-fitting. Natural length data was gathered for all conditions that will be used in future experiments.

# Tables

**Table 4.1:** Sample counts

| Condition | Number of Cells Collected | Number of Sister-Pairs from Collected Cells | Number of Unique Cells After Filtering Data* | Number of Sister-Pairs after Filtering Data* |
|---|---|---|---|---|
| Untreated | 161 | 5503 | 85 | 1334 |
| Nocodazole | 170 | 2997 | 19 | 232 |
| Control siRNA | 157 | 6327 | 108 | 1614 |
| Control siRNA + nocodazole | 94 | 2893 | 28 | 344 |
| CAPD2 siRNA | 140 | 5595 | 76 | 1219 |
| CAPD2 siRNA + nocodazole | 154 | 7411 | 70 | 621 |
| Nuf2 siRNA | 95 | 1366 | 19 | 102 |
| Parental | 70 | 3762 | 55 | 1784 |

∗ Data filters described in Section 4.6 (anaphase filter, tracking error filter and trajectory length filter).

**Table 4.2:** Successful convergence counts

| Condition | Number of Sister-Pairs With Successful Model Convergence* |
|---|---|
| Untreated | 1077 |
| Control siRNA | 1465 |
| CAPD2 siRNA | 1006 |
| Parental | 1529 |

∗ See Section 4.3.3 for convergence criteria.

**Table 4.3:** Priors for MCMC inference

| Parameter | $v_{\pm}$ | $\kappa$ | $L$ | $\alpha$ | $\tau$ | $p_c$ | $p_{ic}$ |
|---|---|---|---|---|---|---|---|
| Untreated‡ * | $N(\pm 0.03, 10)$ | $N(0.05, 10^4)$ | $N(0.788, 0.022)$ | $N(0.01, 10^4)$ | $\Gamma(0.5, 10^{-3})$ | $\Gamma(2.5, 1)$ | $\Gamma(2, 1)$ |
| Parental* | | | | | | | |
| Control siRNA‡ | | | $N(0.7735, 0.0155)$ | | | | |
| CAPD2 siRNA‡ | | | $N(0.9690, 0.0404)$ | | | | |

∗ Priors are identical.

‡ Priors are identical except for an informed prior on $L$ estimated from nocodazole treated cells.

# References


[88] R. B. Nicklas. "The forces that move chromosomes in mitosis". In: *Annu Rev Biophys Biophys Chem* 17 (1988), pp. 431–449.

[96] Khuloud Jaqaman et al. "Kinetochore alignment within the metaphase plate is regulated by centromere stiffness and microtubule depolymerases". In: *J Cell Biol* 188.5 (Mar. 2010), pp. 665–79.

[118] Ajit P Joglekar and Alan J Hunt. "A simple, mechanistic model for directional instability during mitotic chromosome movements". In: *Biophysical Journal* 83.1 (July 2002), pp. 42–58.

[138] G. Civelekoglu-Scholey et al. "Dynamic bonds and polar ejection force distribution explain kinetochore oscillations in PtK1 cells". In: *J. Cell Biol.* 201.4 (May 2013), pp. 577–593.

[140] Jian Liu et al. "An integrated mechanobiochemical feedback mechanism describes chromosome motility from prometaphase to anaphase in mitosis". In: *Proceedings of the National Academy of Sciences of the United States of America* 105.37 (Sept. 2008), pp. 13752–13757.

[155] Julie P I Welburn and Iain M Cheeseman. "Toward a Molecular Structure of the Eukaryotic Kinetochore". In: *Developmental Cell* 15.5 (Nov. 2008), pp. 645–655.

[156] Blerta Shtylla and James P. Keener. "A Mathematical Model for Force Generation at the Kinetochore-Microtubule Interface." In: *SIAM Journal of Applied Mathematics* 71.5 (2011), pp. 1821–1848.

[157] M.D. Bennett et al. "DNA density in mitotic and meiotic metaphase chromosomes of plants and animals". In: *Journal of Cell Science* 63.1 (1983), pp. 173–179.

[158] J. Honerkamp. *Statistical Physics: An advanced approach with applications*. Springer, 2002.

[159] C.P Robert, G Celeux, and J Diebolt. "Bayesian estimation of hidden Markov chains: A stochastic implementation". In: *A stochastic implementation. Statistics & Probability Letters* (1993).

[160] A. Gelman and D. Rubin. "Inference from iterative simulation using Multiple sequences." In: *Statistical Science* 7 (1992), pp. 457–511.

# Chapter 5

# Inferring Sister Kinetochore State and Dynamic Parameters through a Model Fit

## 5.1 Statistical Model-Fitting

In Chapter 4 a statistical framework was presented designed to fit a basic mechanical model to sister-kinetochore trajectories. This chapter describes fitting the model to human kinetochore trajectories produced from the high-throughput assay described in Chapter 3. Model fits across a multitude of trajectory-pairs reveals key correlates and dynamics processes especially with regards to directional switches.

## 5.2 Successfully Fitting the Kinetochore Dynamics Model to a Single Trajectory-Pair

The model was first fitted on a sister pair exhibiting strong oscillations (Figure 5.1a) inferring concurrently both model parameters (spring constant $\kappa$; spring natural length $L$; polymerisation $v_+$ and depolymerisation $v_-$ speeds; PEF gradient strength $\alpha$; noise parameter $s^2$) and the unobserved sister states ($v_-/v_-, v_-/v_+, v_+/v_+, v_+/v_-$). On this trajectory the inferred K-fibre (free) polymerisation ($v_+$) and depolymerisation ($v_-$) speeds

are $17\pm4$nm.s$^{-1}$ and $49\pm4$nm.s$^{-1}$ respectively with depolymerisation significantly faster than polymerisation ($p < 10^{-8}$). The corresponding kinetochore speeds during AP (anti-poleward, away from its closest spindle-pole) and P (poleward, towards its closest spindle-pole) runs follow from the combined action of K-fibre (de)polymerisation, the spring force and the PEF on the kinetochore (see (4.2)) and are $24\pm22$nm.s$^{-1}$ and $43\pm25$nm.s$^{-1}$ respectively, shifts of 41% and 12% on average over the trajectory. AP speed remains less than that of a P moving kinetochore, the sister separation therefore increases over a coherent run suggesting that the lead sister is pulling the trailing sister, a result consistent with previous studies in PtK1 cells [99, 100]. Clearly the spring and PEF forces are small compared to those of the K-fibres that provide most of the driving force. All these forces are found to be non-zero (associated parameters are non zero, Figure 5.1f-i), in particular the trailing kinetochore connection with its K-fibre is found to be active ($v_+ > 0$), the kinetochore being pushed away from its spindle-pole. This trajectory shows strong regions of coherence interspersed with short periods of incoherence that correspond to the two sisters both polymerising ($v_+/v_+$) (Figure 5.1e). There is a high confidence in assigning the sister polymerisation state (Figure 5.1c) endowing the trajectory with a high level of deterministic behaviour (strong clear oscillations). In fact this trajectory shows the previously reported [90, 161] deterministic lead sister switching choreography as is evident directly from the sister trajectories (Figure 5.1a-e); the lead sister switching first with a probability of 99% compared to 0% for the trailing sister to switch first (the remaining 1% is joint/coincident switching). These lead sister driven dynamics are responsible for the contracting ($v_+/v_+$) incoherent state observed in between coherent runs giving the classic dynamic profile with the inter-sister distance relaxing at a switching event ($v_+/v_+$) and increasing over the following half-period as the lead sister moves away (Figure 5.1b). The high-resolution 3D measurements also show that the sister axis is dynamic with maximal twist occurring during the incoherent (contracting) phases (Figure 5.1b). During coherence the spring is under increasing stretch which reduces the twist while during the contracting coherence state the twist is high, potentially a combination of thermal fluctuations in the twist angle and actual pushing forces between the kinetochores.

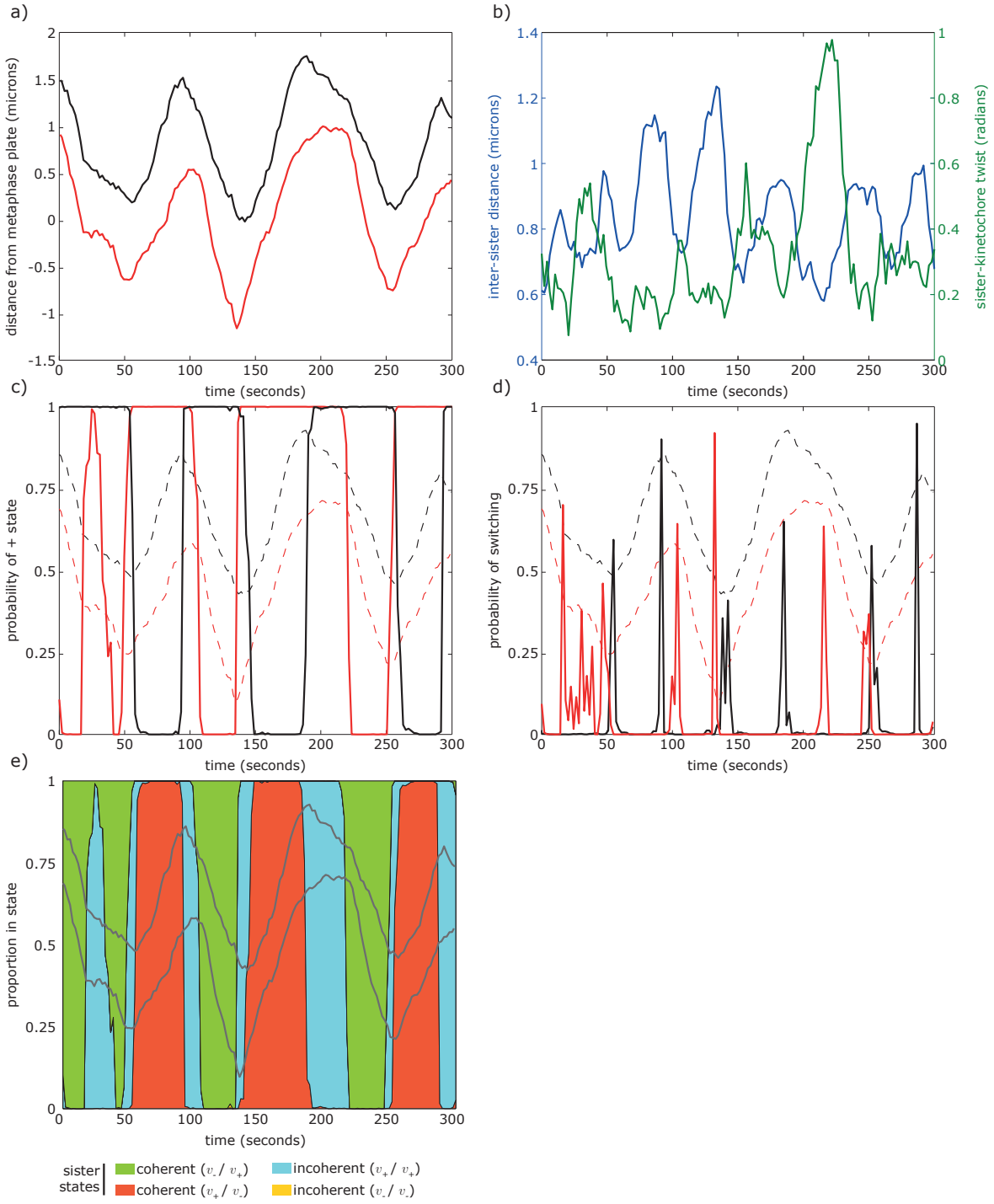


**Figure 5.1:** Single Trajectory Model Fit. **a)** A sister kinetochore trajectory displaying a strong deterministic dynamics (EV = 67%), kinetochore distance measured from metaphase plate. **b)** Inter-sister separation (blue) and sister-kinetochore twist *i.e.* angle with normal to metaphase plate (green). **c)** Inferred probability of each sister being in the polymerising (+) state. Dotted lines represent trajectories from a). **d)** Inferred probability of sisters switching states (per frame). Dotted lines represent trajectories from a). **e)** Inferred sister states. Coherent states green ($v_+/v_-$), red ($v_-/v_+$), incoherent states blue ($v_+/v_+$), yellow ($v_-/v_-$). *cont*

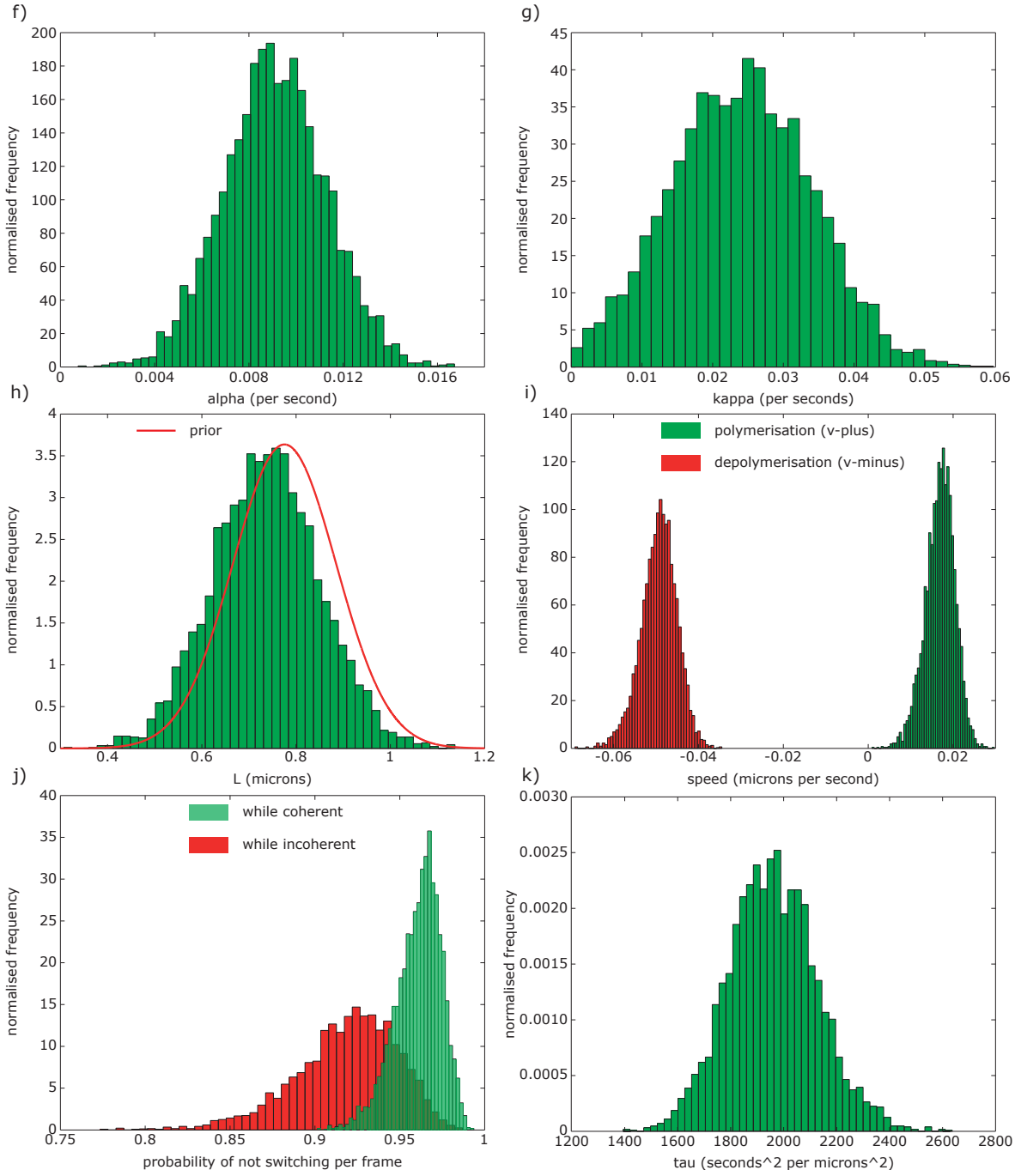


**Figure 5.1:** *cont* Inferred posterior distributions and model parameters. Posterior distributions consist of 25000 samples (from a chain of length 50000 steps after a burnin of 25000 steps). **f)** Posterior distribution of the anti-poleward force gradient $\alpha$. **g)** Posterior distribution of the spring constant $\kappa$. **h)** Posterior distribution of the natural length $L$ in green and the informed Gaussian prior used in the sampler (red) determined through nocodazole treatment. **i)** Posterior distributions for the speeds $v_+$ (green) and $v_-$ (red). **j)** Distributions of the probabilities of not switching state per time-point while coherent (green) and incoherent (red). **k)** Posterior distribution of the noise parameter $\tau = s^{-2}$.

## 5.3 Sister Kinetochore Population Switching Statistics

To ascertain the statistics of kinetochore switching dynamics *in vivo* the model was fitted to 1077 sister pairs across 85 cells; on a further 257 trajectories the model failed to find a fit (failed convergence test, see Table 4.2 and Section 4.3.3) suggesting that the deterministic/oscillatory signal of these trajectories was weak. Only the converged trajectories were used in the following. The fitting method cannot determine the natural length on each trajectory coincidently with all the other parameters but only across the population (from nocodazole treated cells, Section 4.4). Figure 5.2 shows that the posterior distribution for $L$ shifts towards higher values as the prior is weakened (prior variance increases). Given the *a posteriori* lack of identifiability the robustness of parameters was tested with respect to a change in the $L$ prior mean, Figure 5.3. It was found that apart from the inferred speeds almost all other parameters were robust to changes in the $L$ prior mean and did not change significantly (the exception being $\kappa$ when the $L$ prior mean was decreased by 20%). As expected given the nature of the identifiability issue the values of the inferred speeds scaled with changes in the $L$ prior mean. To quantify levels of stochasticity in the trajectories explained variance (EV) (4.7) was used as a statistic (see Section 4.5). EV is essentially a measure of the deterministic (oscillatory) component in the trajectory that is explained by the model. Figure 5.4 shows the EV range of fitted trajectories. EV varies from 0.003 to 0.66. Visual inspection of trajectories suggested that a deterministic switching mechanism is not always at work, see trajectory examples Figures 5.5, 5.6, 5.7 and 5.8 for trajectories organised by EV. Figure 5.9 shows mean sister-centre displacement auto-correlation of trajectories (as in Figure 3.25b) organised by EV. Trajectories with higher EV show more evidence of oscillatory *i.e.* deterministic behaviour. Therefore trajectories were defined as either showing deterministic behaviour with an explained variance EV $> 0.25$ (54% of trajectories) or showing predominantly stochastic behaviour with an EV $< 0.25$ (Figure 5.4). The trajectory shown in Figure 5.1a is the most deterministic trajectory (EV $= 0.66$). Individual cells tend to show a range of trajectory behaviour including those with a highly deterministic component and those that are quite stochastic (Figure 5.4b). Trajectories with low EV were spatially biased towards the edge of the metaphase plate

(Figure 5.4c) consistent with previous observations that chromosomes at the periphery have weaker oscillations [57, 99, 138]. To investigate the mechanism of sister switching focus was placed on the more deterministic trajectories (EV $> 0.25$; $n = 577$). First the magnitude of $v_-$ was confirmed to be larger than $v_+$ (Figure 5.1i, $p = 10^{-182}$, MW) and that coherent and both incoherent (expanding/contracting) sister states occur; $(v_+/v_+)$ 4.8% and $(v_-/v_-)$ 0.9% of the time on EV $> 0.25$ trajectories (Figure 5.11). Further it was confirmed that polymerising K-fibres push the trailing kinetochore; on 56% of all trajectories (71% of trajectories with EV $> 0.25$) the inferred $v_+$ distribution has a mean that is $> 1.65 \times$ standard deviation indicating that support for $v_+ = 0$ is less than 5% (Figure 5.12). This is a conservative test but indicates that in contrast to previous work [100, 128] the trailing (AP) moving kinetochore is active and not solely pulled by their sister.

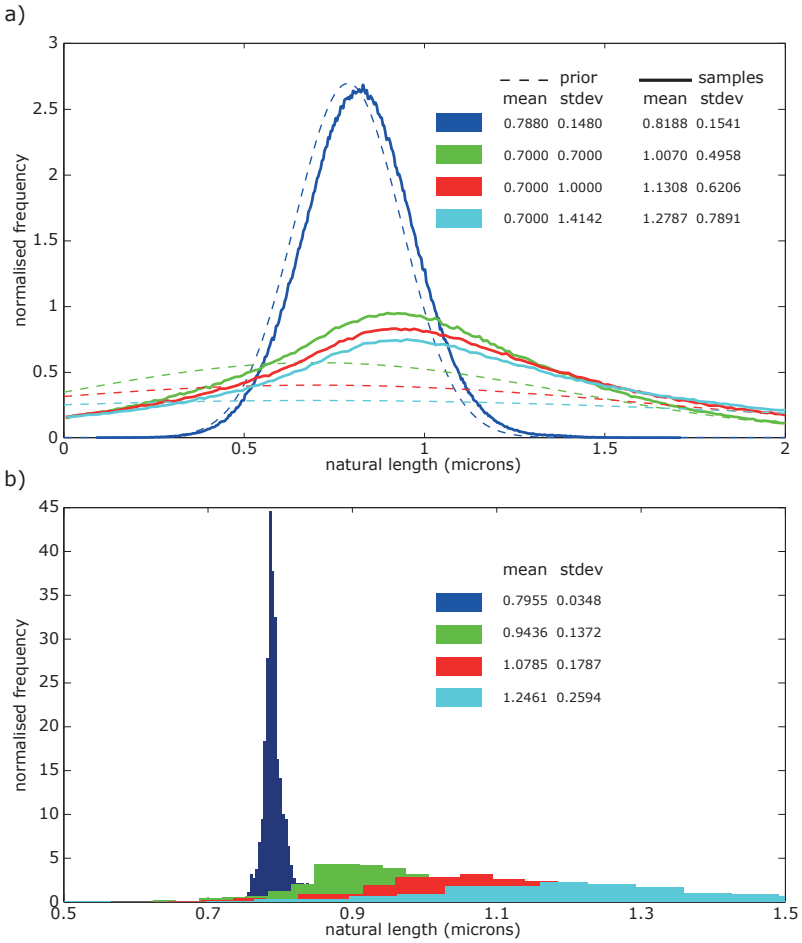


**Figure 5.2:** Analysis of the identifiability of the natural length $L$. Inference was performed with 4 different priors on $L$ with increasing variance, specifically a truncated Gaussian prior with (mean, std) = (0.7880, 0.1480) in blue, the informed prior estimated from nocodazole treatment and used throughout the analysis, Table 4.3, (0.7000 0.7000) green; (0.7000 1.0000) red and (0.7000 1.4142) cyan (means, variances refer to Gaussian before truncation to $L > 0$). **a)** Prior (dashed) and posterior (solid) distributions of $L$, samples pooled from all trajectories (1,670,168 samples from 1334 trajectories). **b)** Distribution of posterior mean of L for the trajectories with an EV $> 0.25$ (517; 521; 518 and 523 trajectories respectively). Statistics shown in legend.

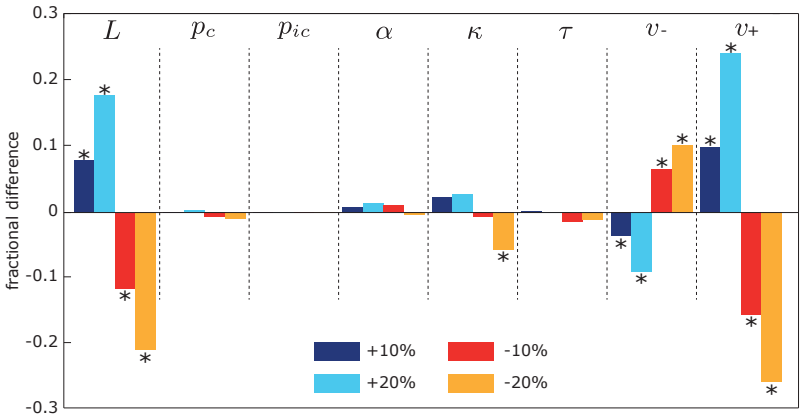


**Figure 5.3:** Parameter robustness analysis for the L prior. Fractional change in median of the distribution of posterior parameter means for trajectories with EV $> 0.25$. The prior mean of $L$ was altered by $\{+10, +20, -10, -20\}$ % (blue, cyan, red, orange) compared to the default value (Table 4.3)); prior variance kept at 0.022. Fractional difference defined as d = (median(new distribution) - median(default distribution))/median(default distribution). Significant differences (5% on MW test) marked with *. Data from 514 (blue), 504 (cyan), 536 (red) and 554 (orange) trajectories respectively.

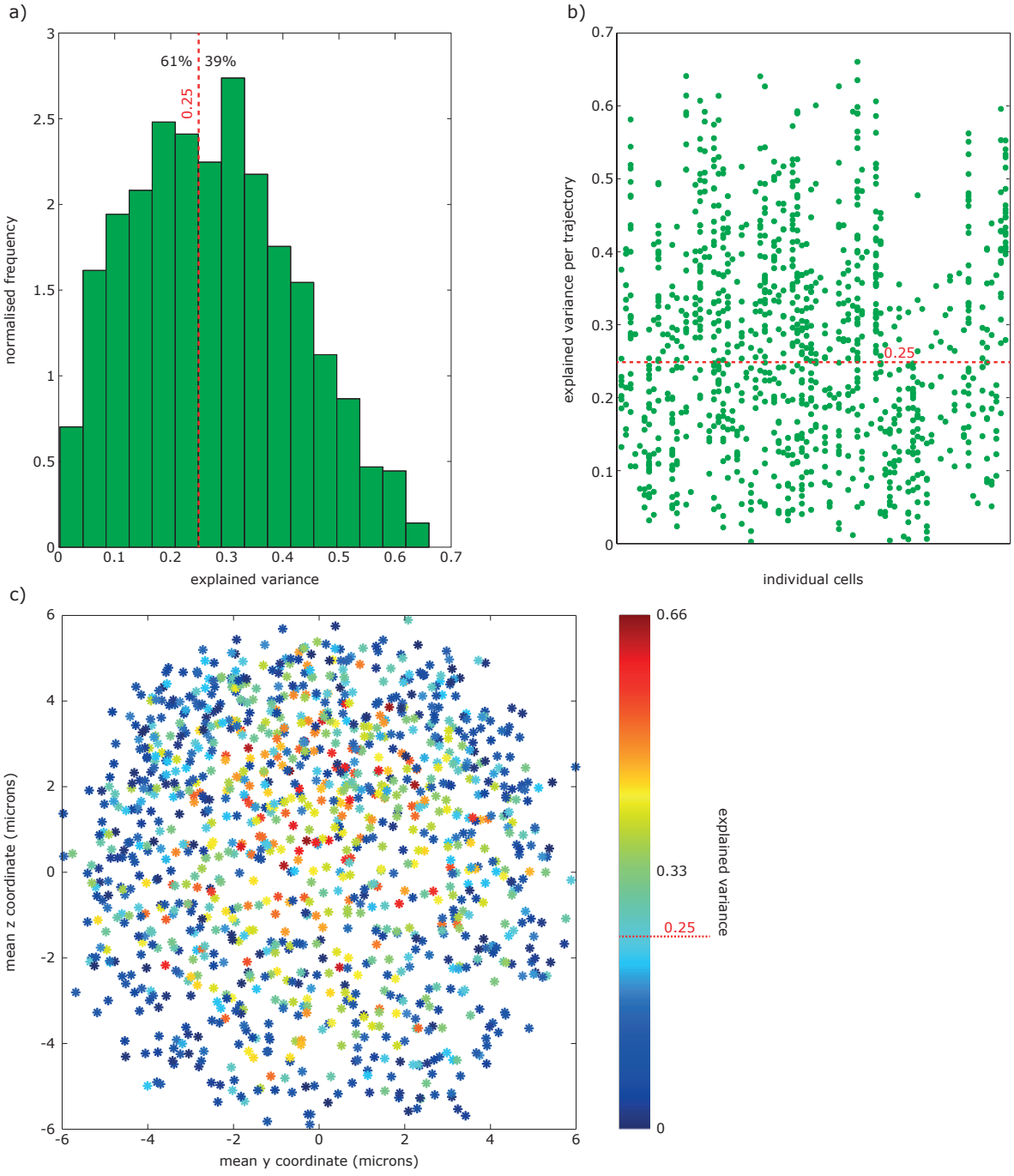


**Figure 5.4:** Multiple Trajectory Explained Variance. **a)** Histogram of explained variance (EV) (4.7) of 1077 trajectory fits from 85 cells. **b)** Plot of explained variance of trajectories grouped vertically by cell. **c)** Mean trajectory position on metaphase plate (mean aligned y and z coordinates). Coloured by explained variance.

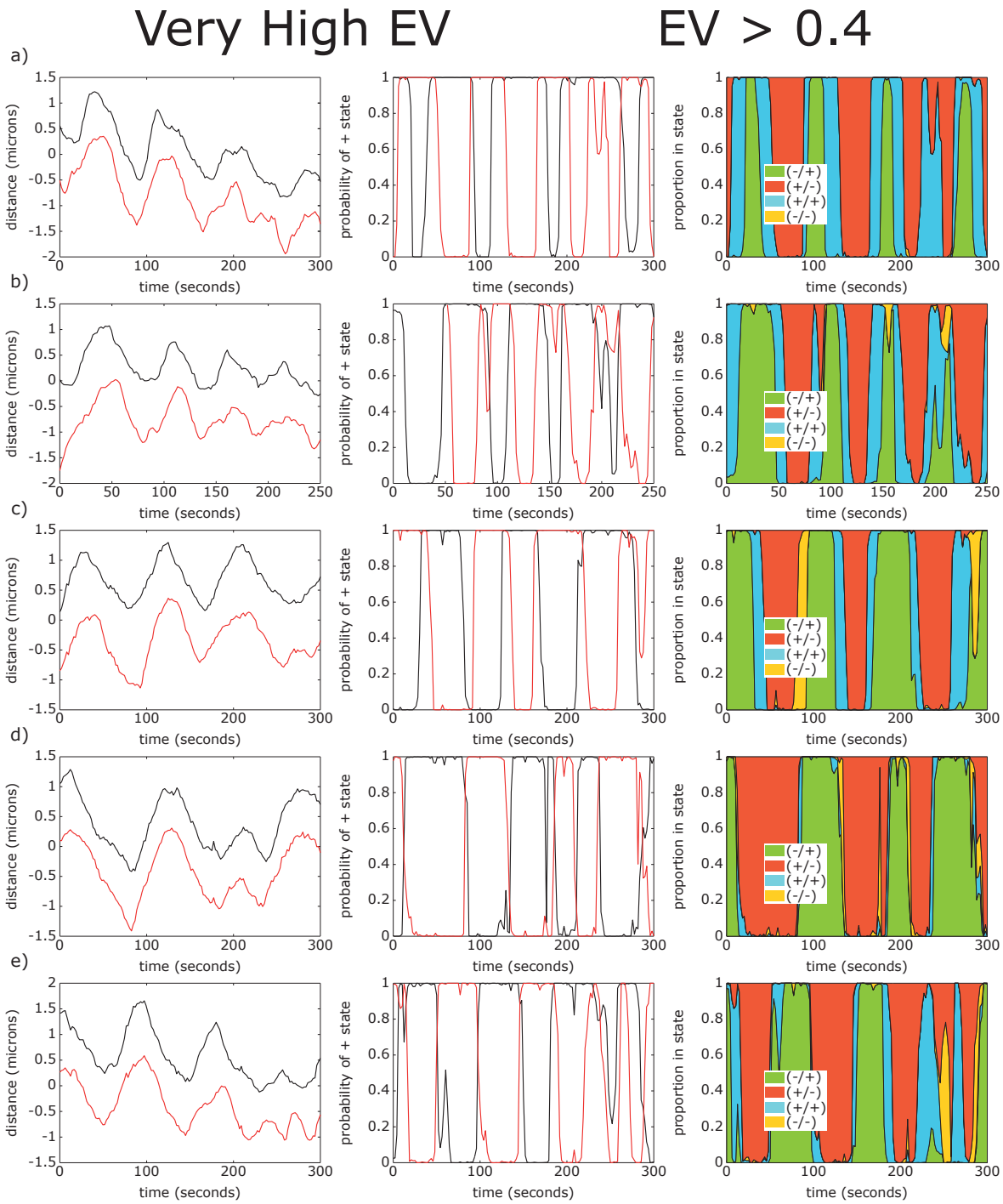


**Figure 5.5:** Examples of Trajectories with Very High EV. Twenty randomly chosen trajectories with explained variance (EV) $> 0.4$. Sub-plots show from left to right trajectories (distance from metaphase plate), probabilities of + (polymerising) state and the proportion of sister-states $(+/-, -/+, +/+, -/-)$. **a)-e)** trajectories one to five *cont*

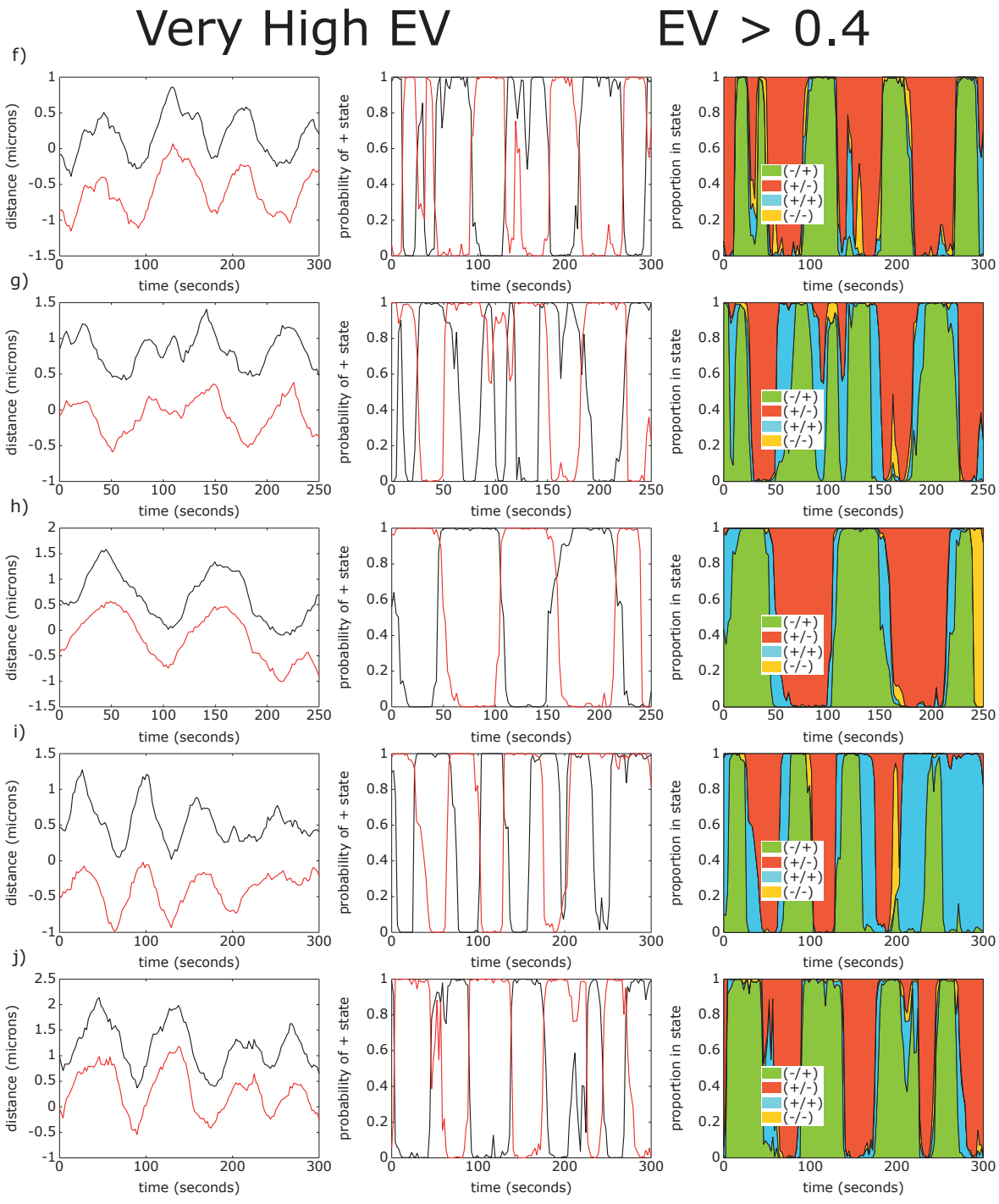


**Figure 5.5:** *cont* **f)-j)** trajectories six to ten *cont*

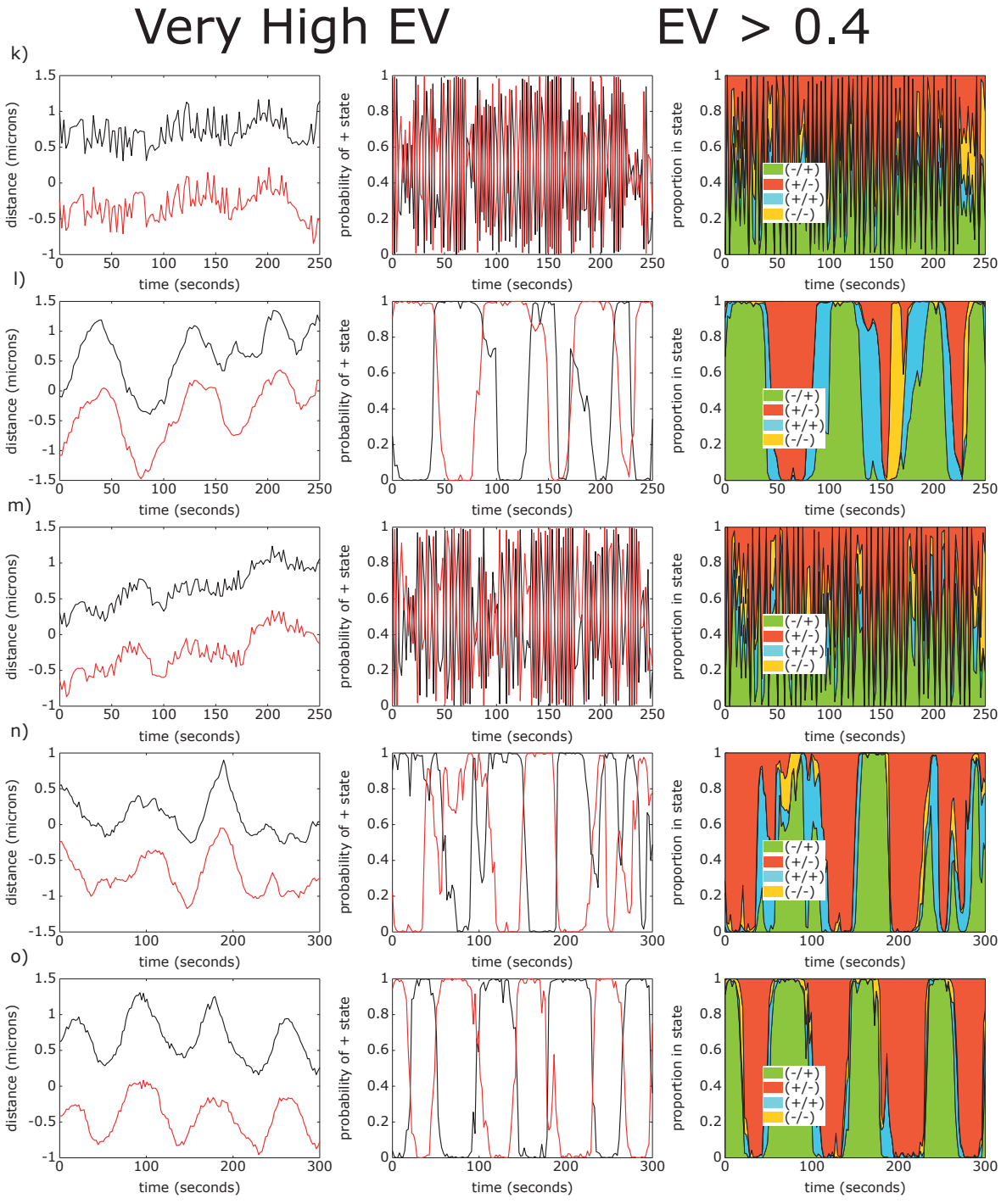


**Figure 5.5:** *cont* **k)-o)** trajectories eleven to fifteen *cont*

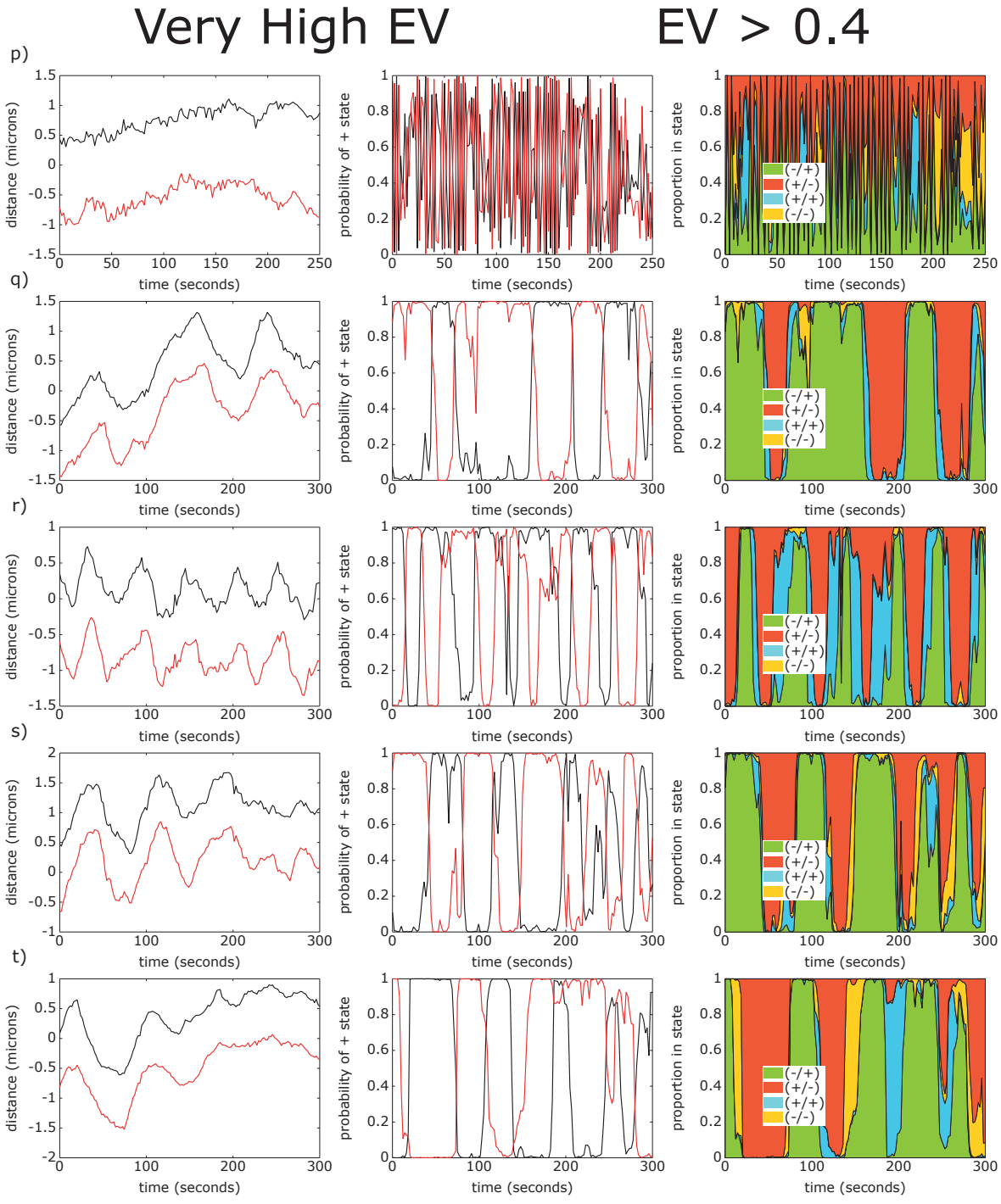


**Figure 5.5:** *cont* **p)-t)** trajectories sixteen to twenty.

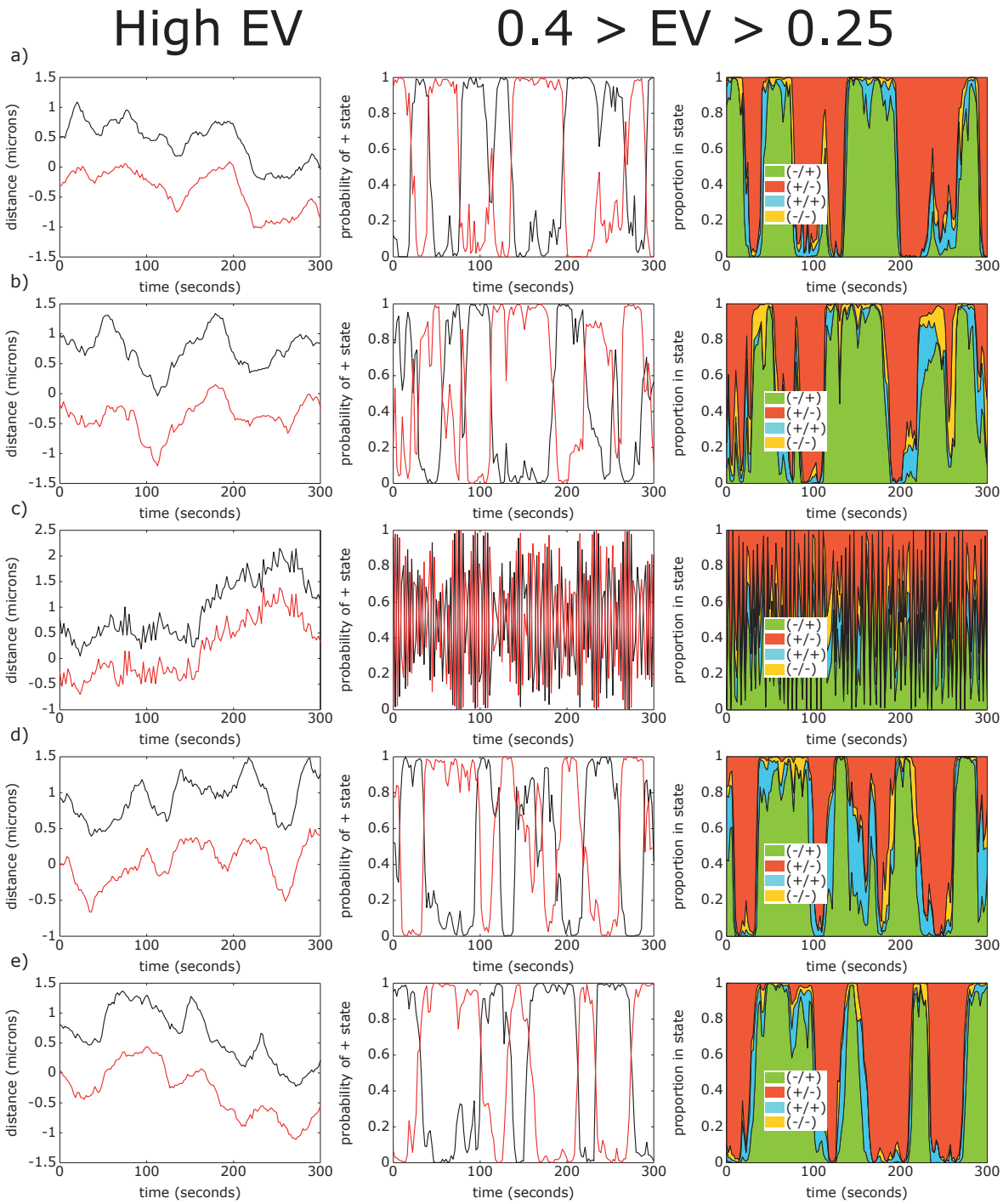


**Figure 5.6:** Examples of Trajectories with High EV. Twenty randomly chosen trajectories with explained variance $0.4 > (\mathrm{EV}) > 0.25$. Sub-plots show from left to right trajectories (distance from metaphase plate), probabilities of + (polymerising) state and the proportion of sister-states $(+/-, -/+, +/+, -/-)$. **a)-e)** trajectories one to five *cont*

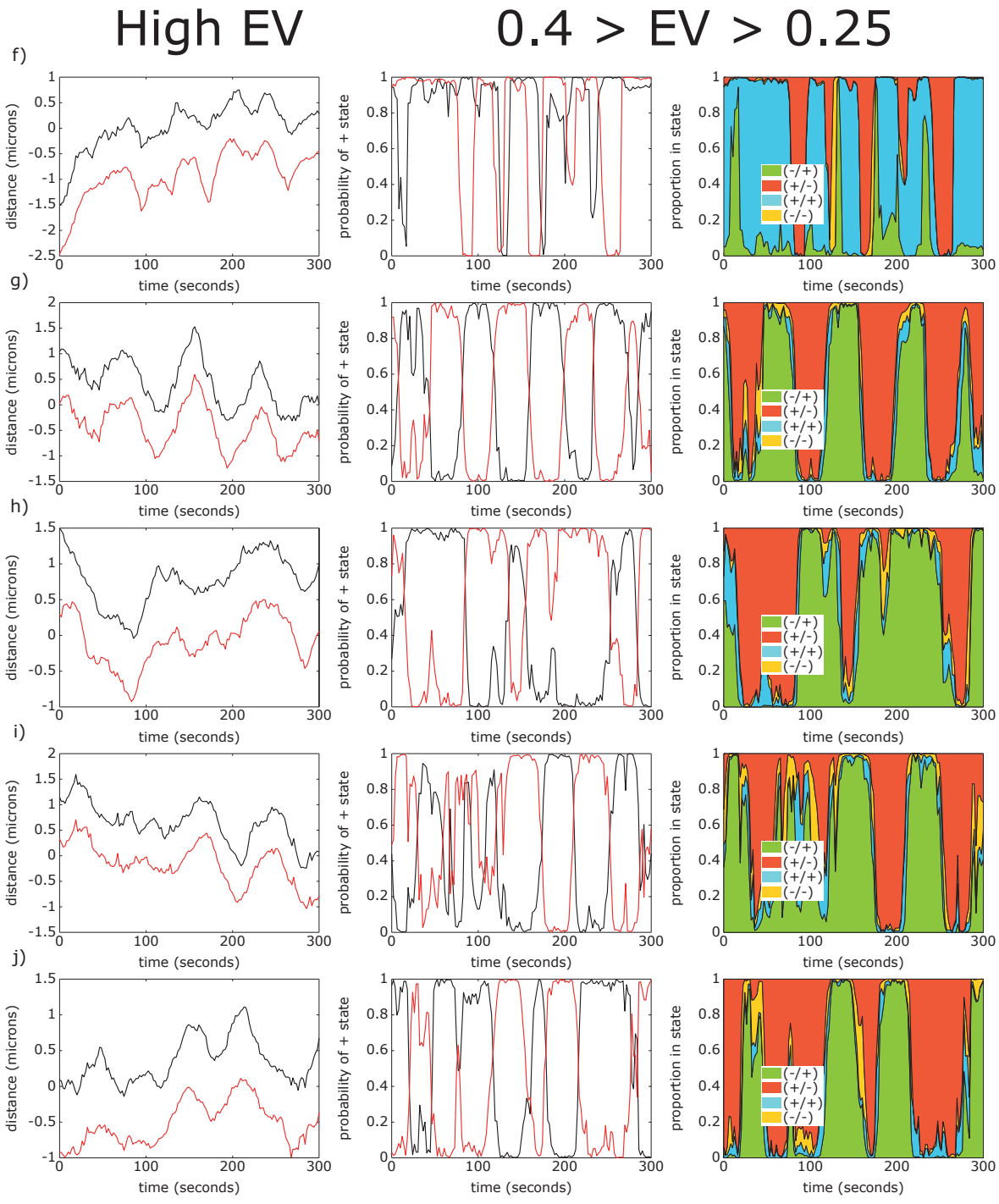


**Figure 5.6:** *cont* **f)-j)** trajectories six to ten *cont*

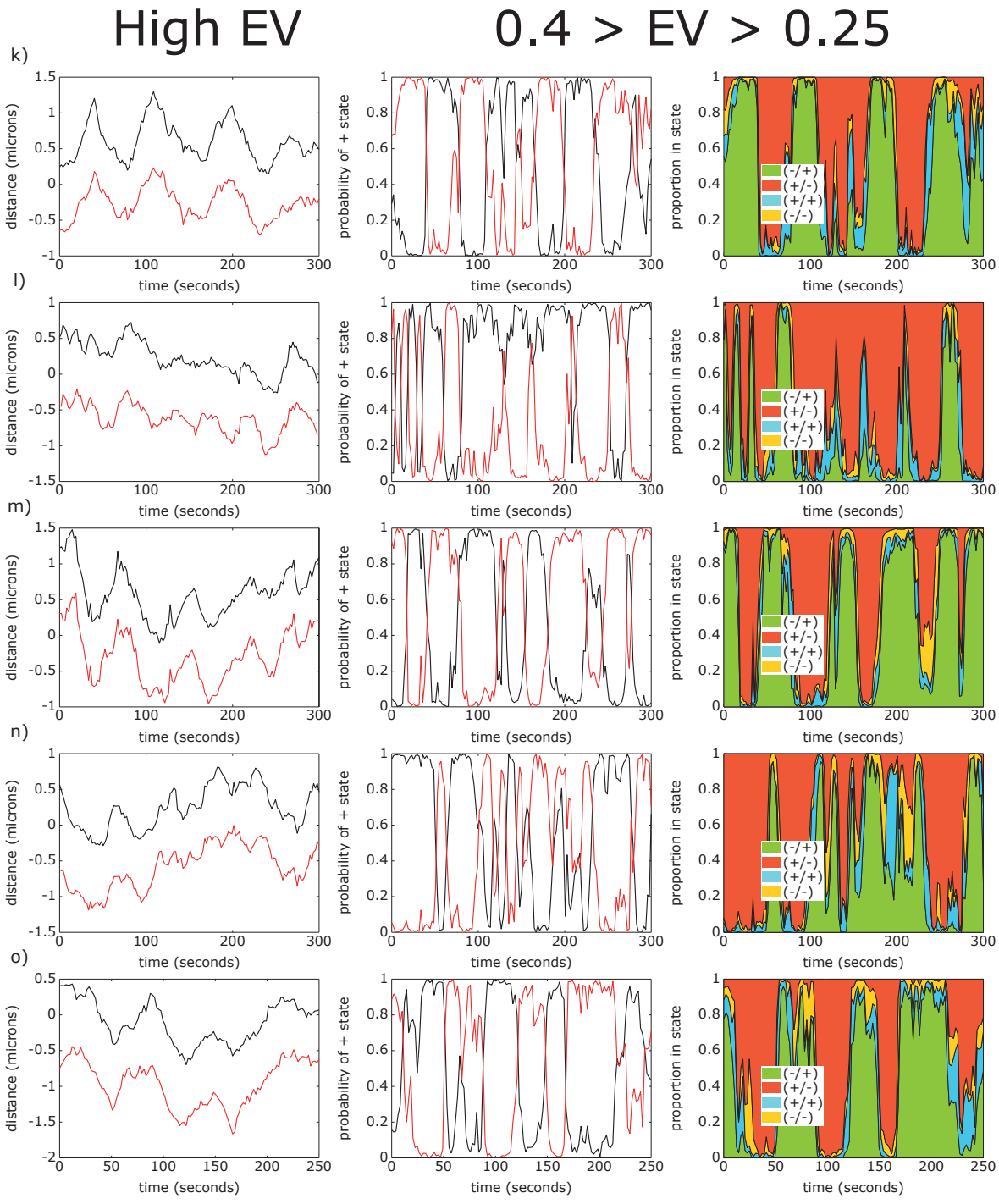


**Figure 5.6:** *cont* **k)-o)** trajectories eleven to fifteen *cont*

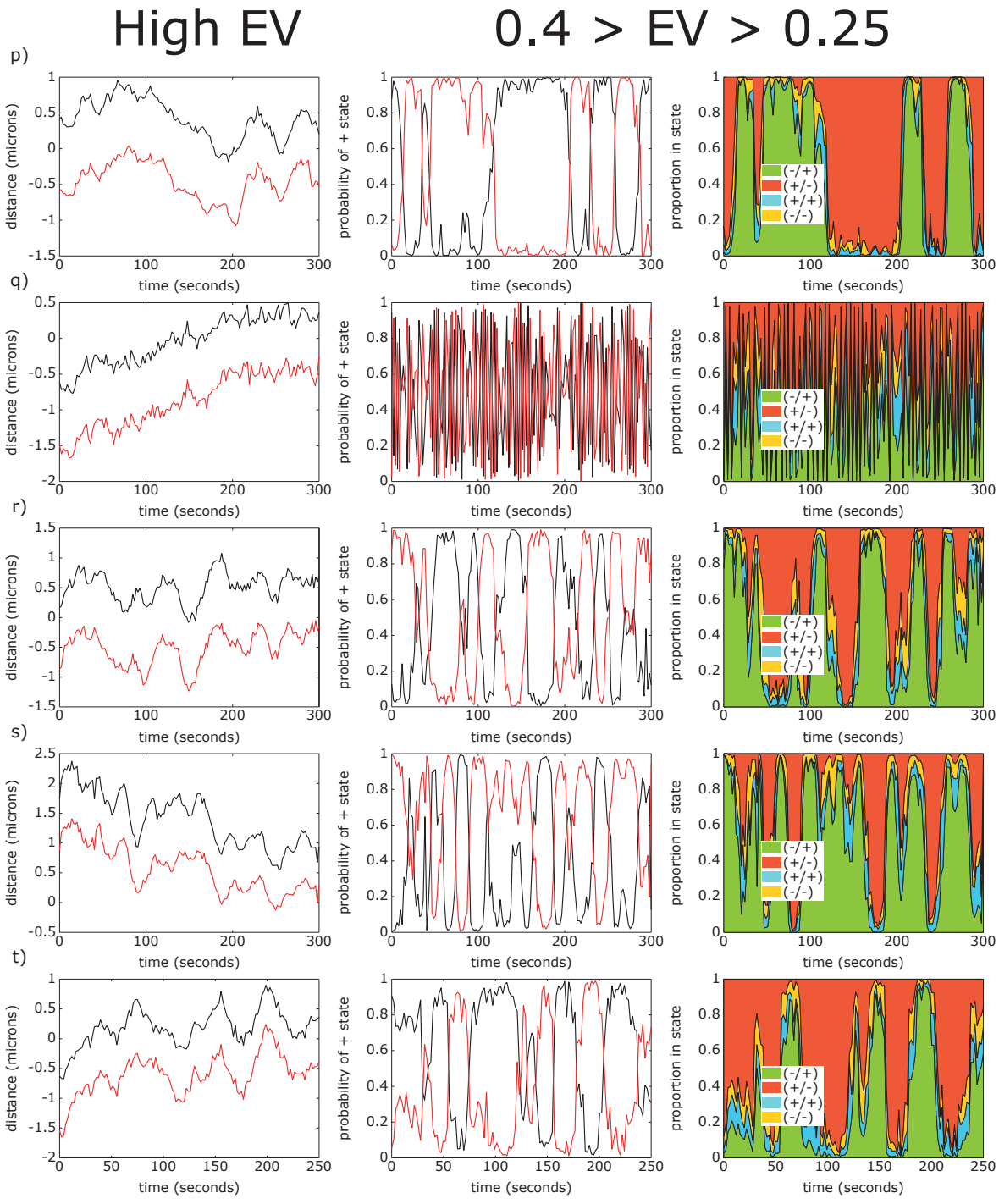


**Figure 5.6:** *cont* **p)-t)** trajectories sixteen to twenty.

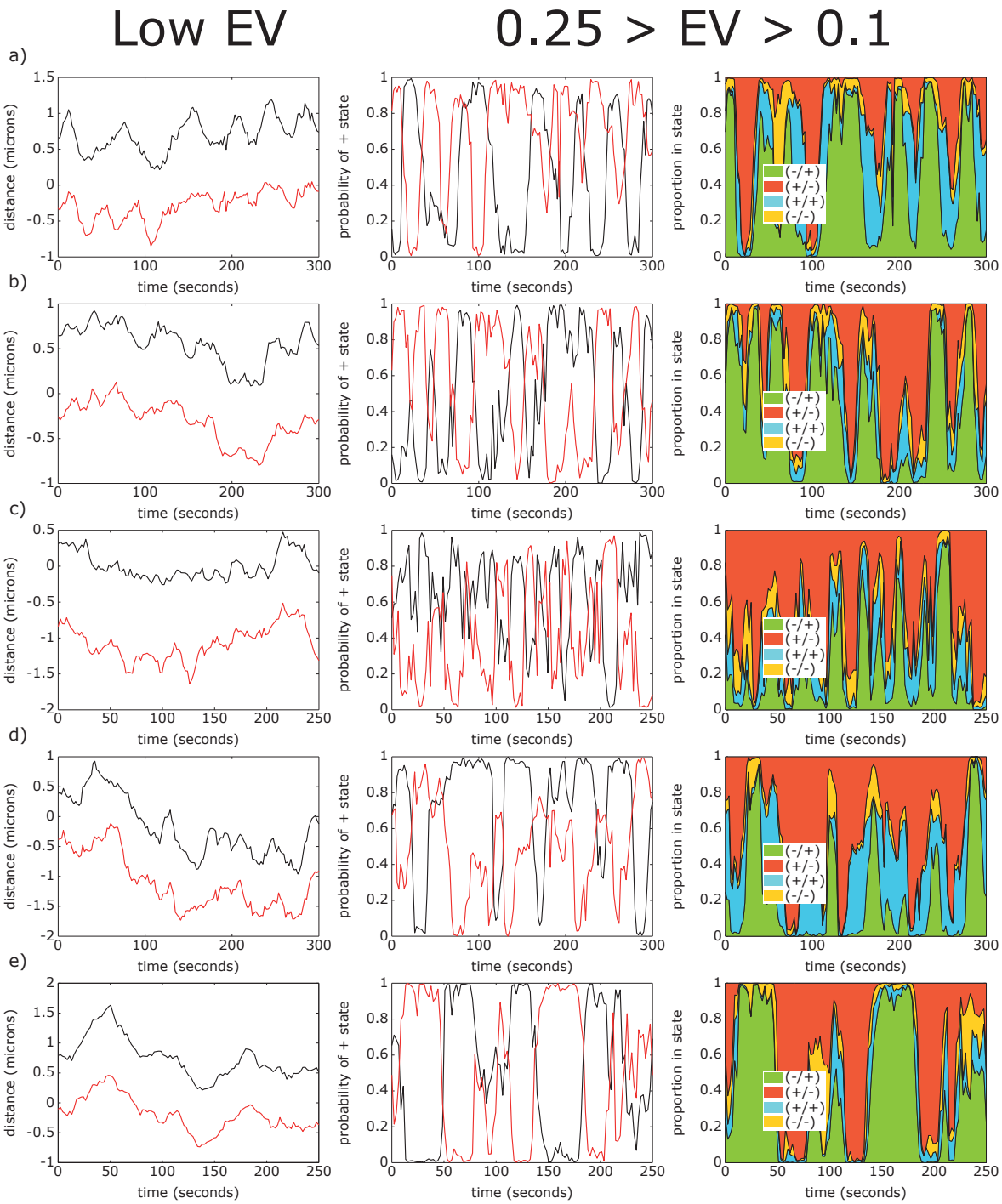


**Figure 5.7:** Examples of Trajectories with Low EV. Twenty randomly chosen trajectories with explained variance $0.25 > (\text{EV}) > 0.1$. Sub-plots show from left to right trajectories (distance from metaphase plate), probabilities of + (polymerising) state and the proportion of sister-states $(+/-, -/+, +/+, -/-)$. **a)-e)** trajectories one to five *cont*

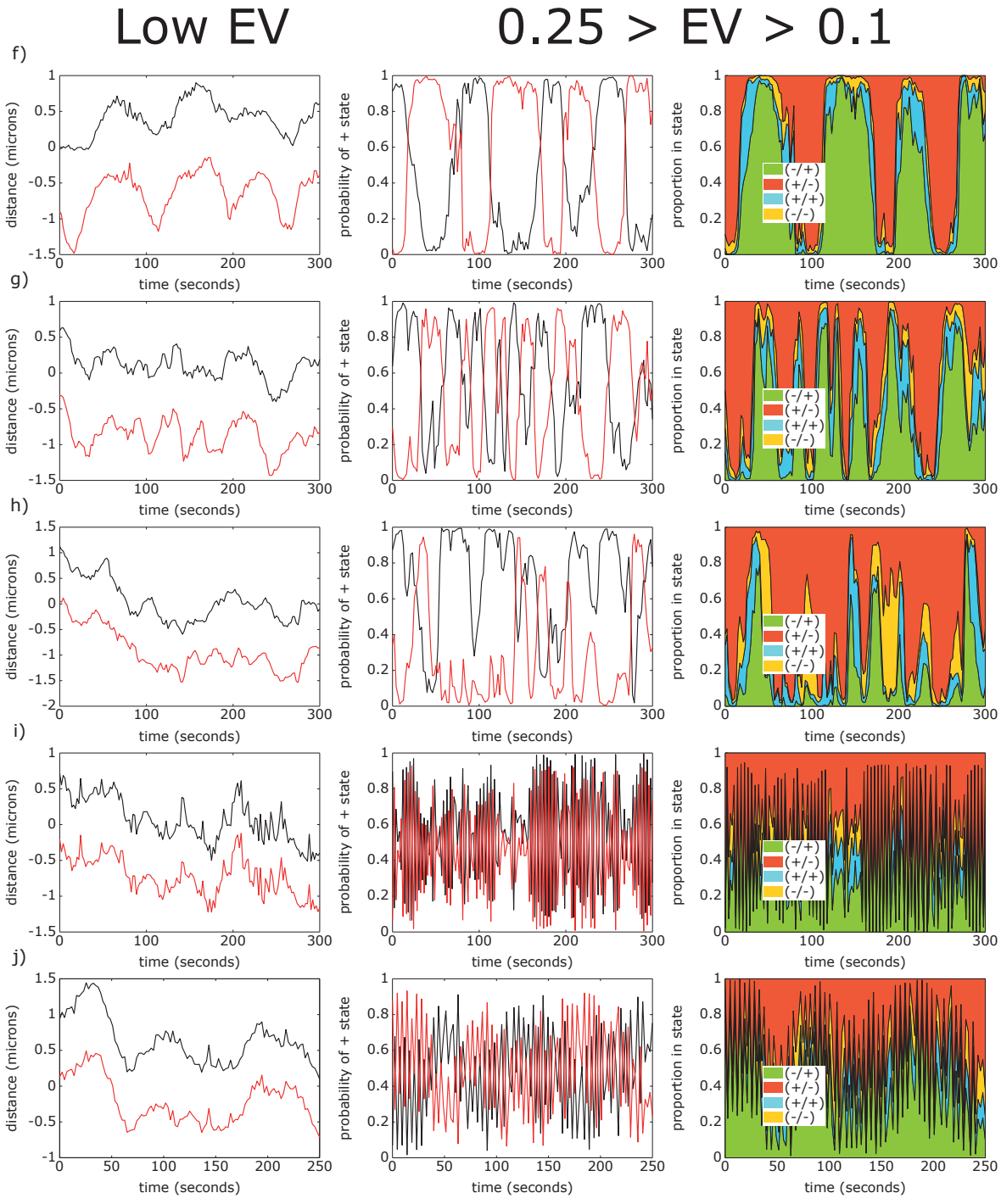


**Figure 5.7:** *cont* **f)-j)** trajectories six to ten *cont*

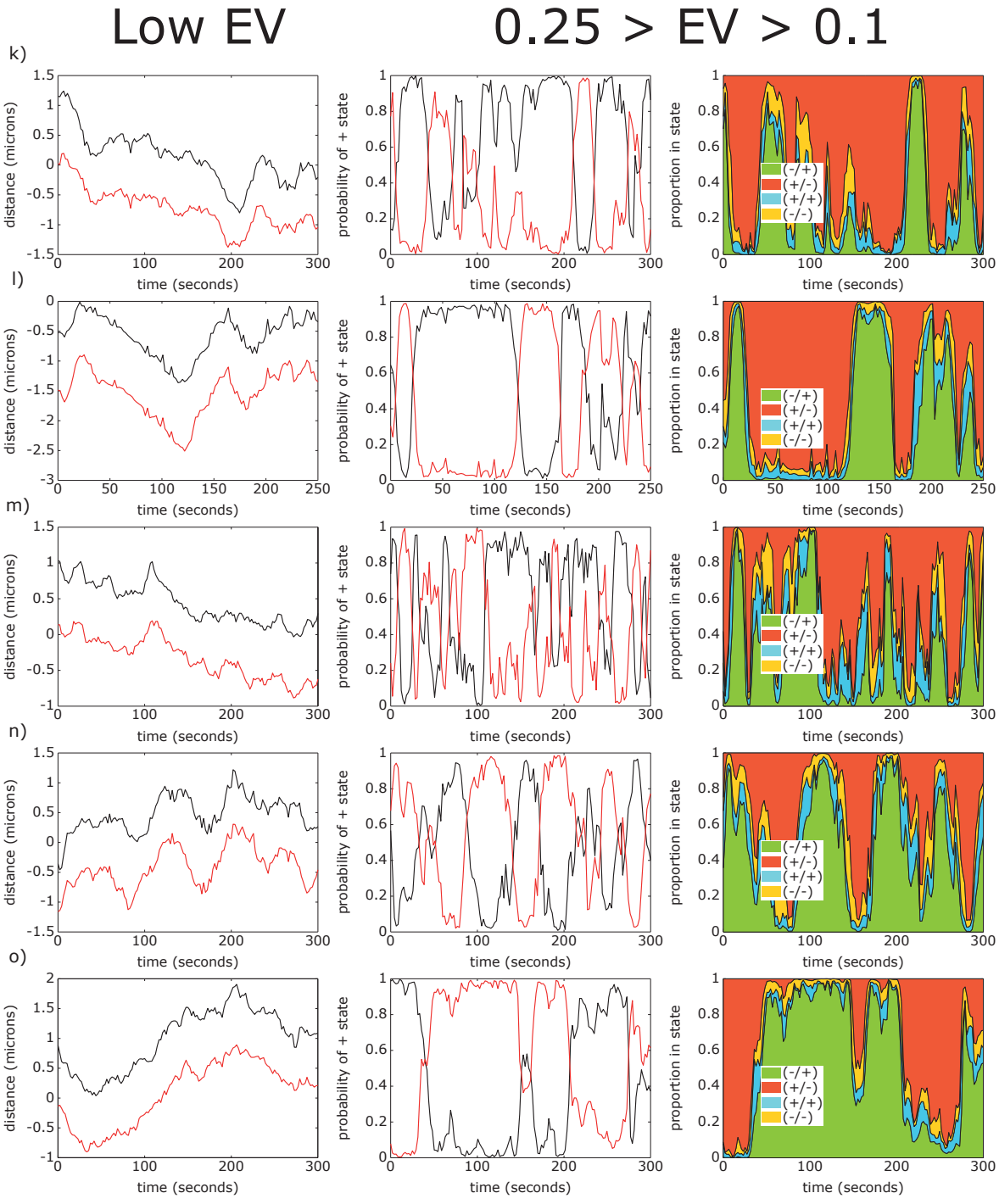


**Figure 5.7:** *cont* **k)-o)** trajectories eleven to fifteen *cont*

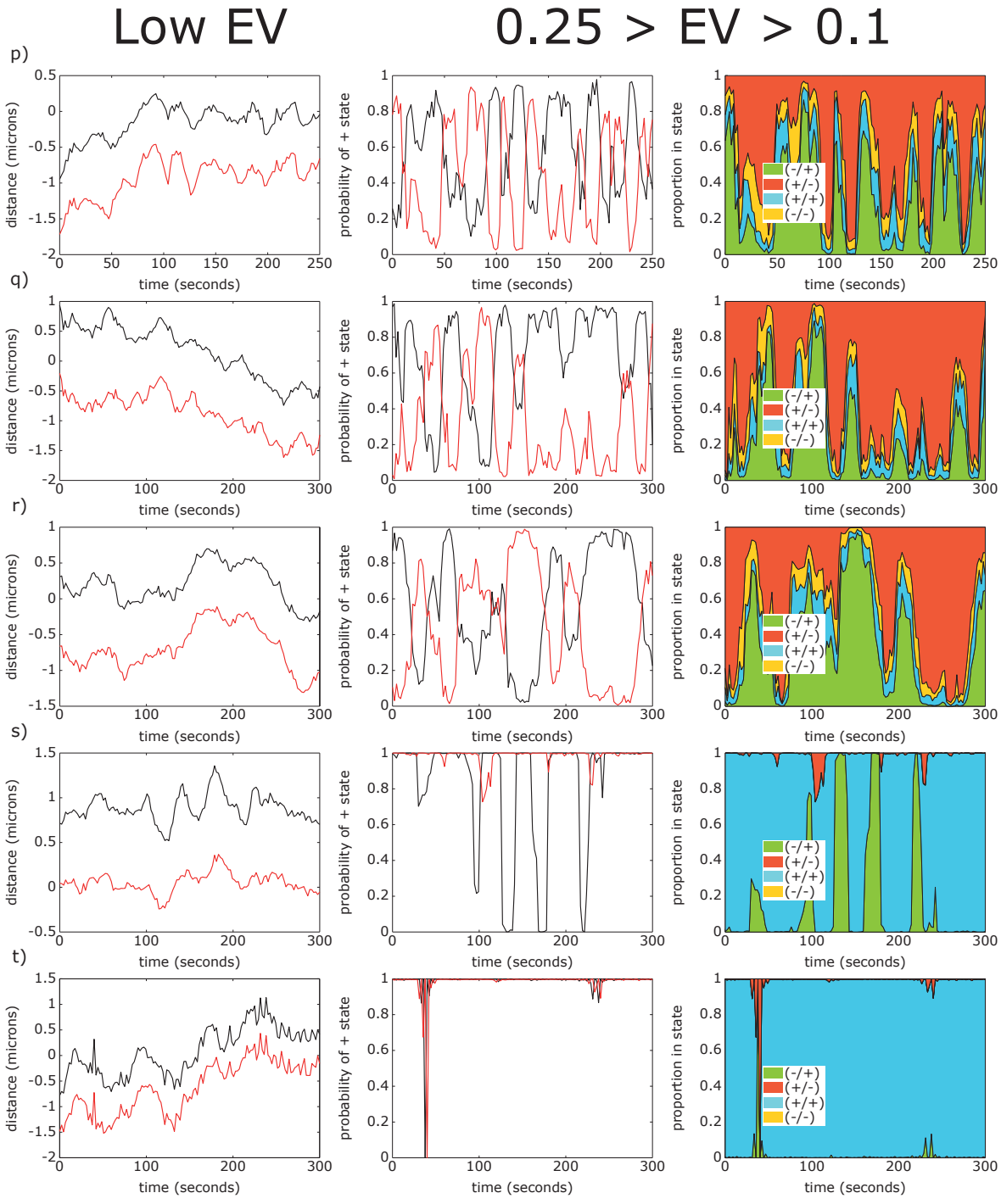


**Figure 5.7:** *cont* **p)-t)** trajectories sixteen to twenty.

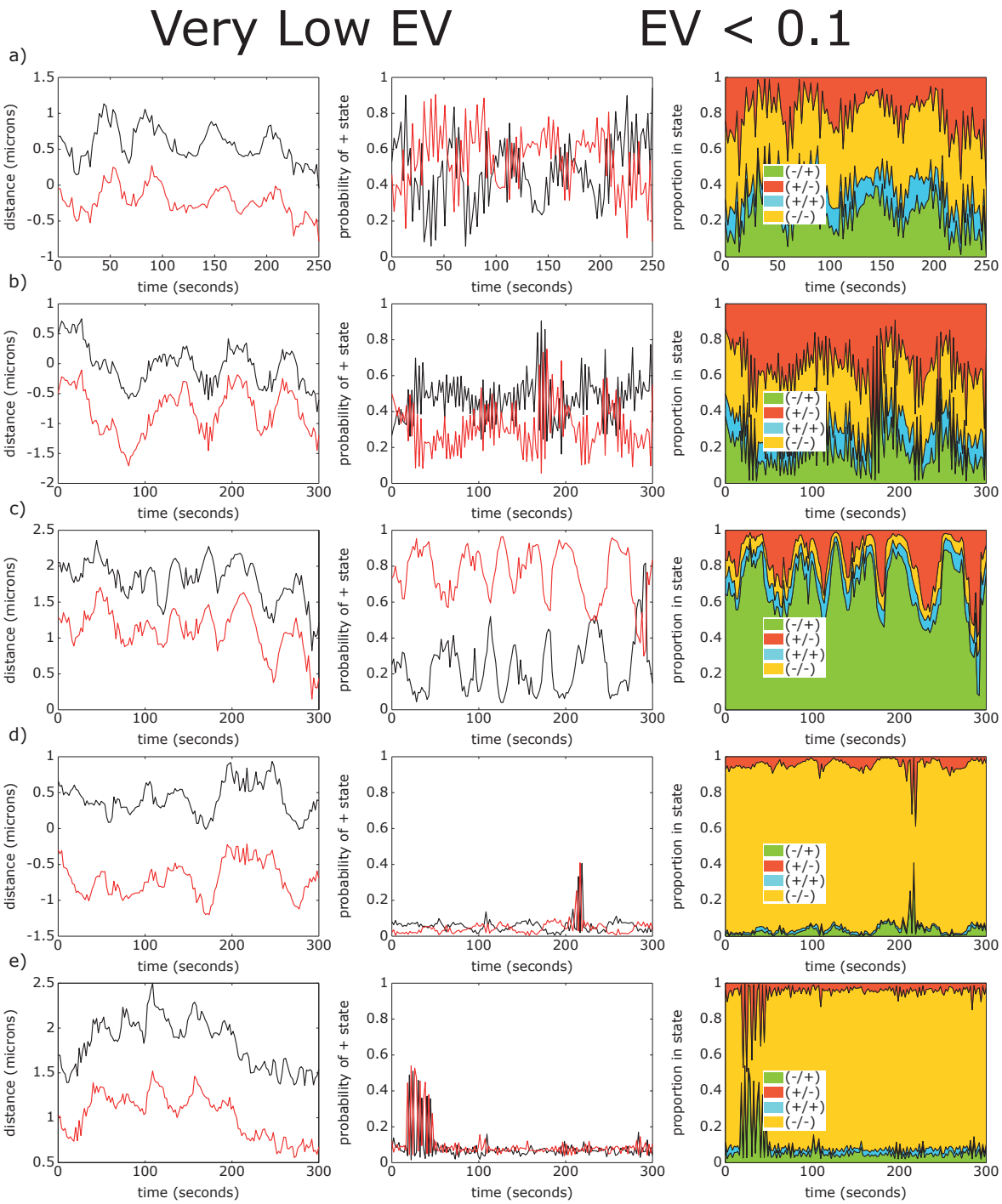


**Figure 5.8:** Examples of Trajectories with Very Low EV. Twenty randomly chosen trajectories with explained variance $0.1 >$ (EV). Sub-plots show from left to right trajectories (distance from metaphase plate), probabilities of + (polymerising) state and the proportion of sister-states $(+/-, -/+, +/+, -/-)$. **a)-e)** trajectories one to five *cont*

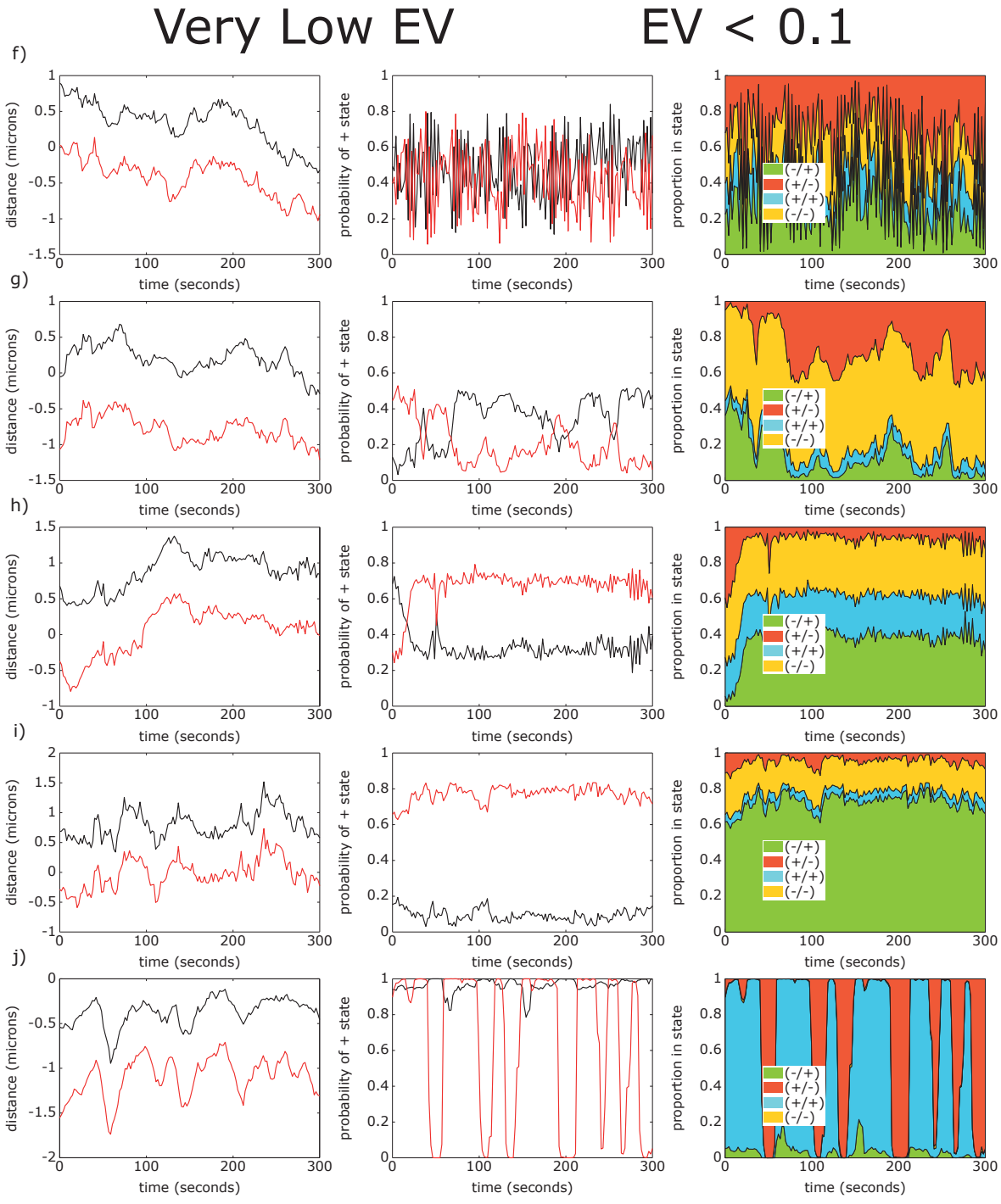


**Figure 5.8:** *cont* **f)-j)** trajectories six to ten *cont*

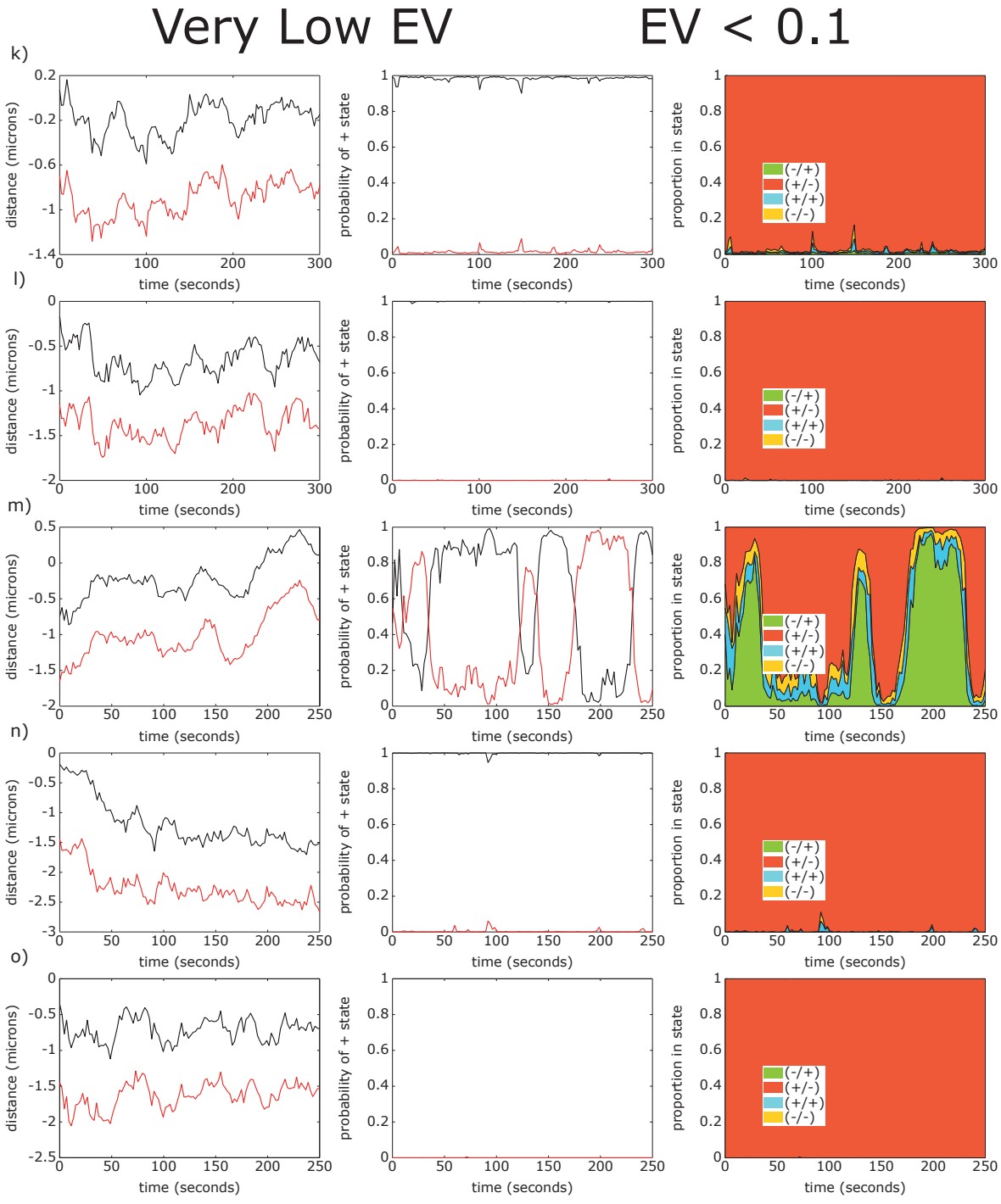


**Figure 5.8:** *cont* **k)-o)** trajectories eleven to fifteen *cont*

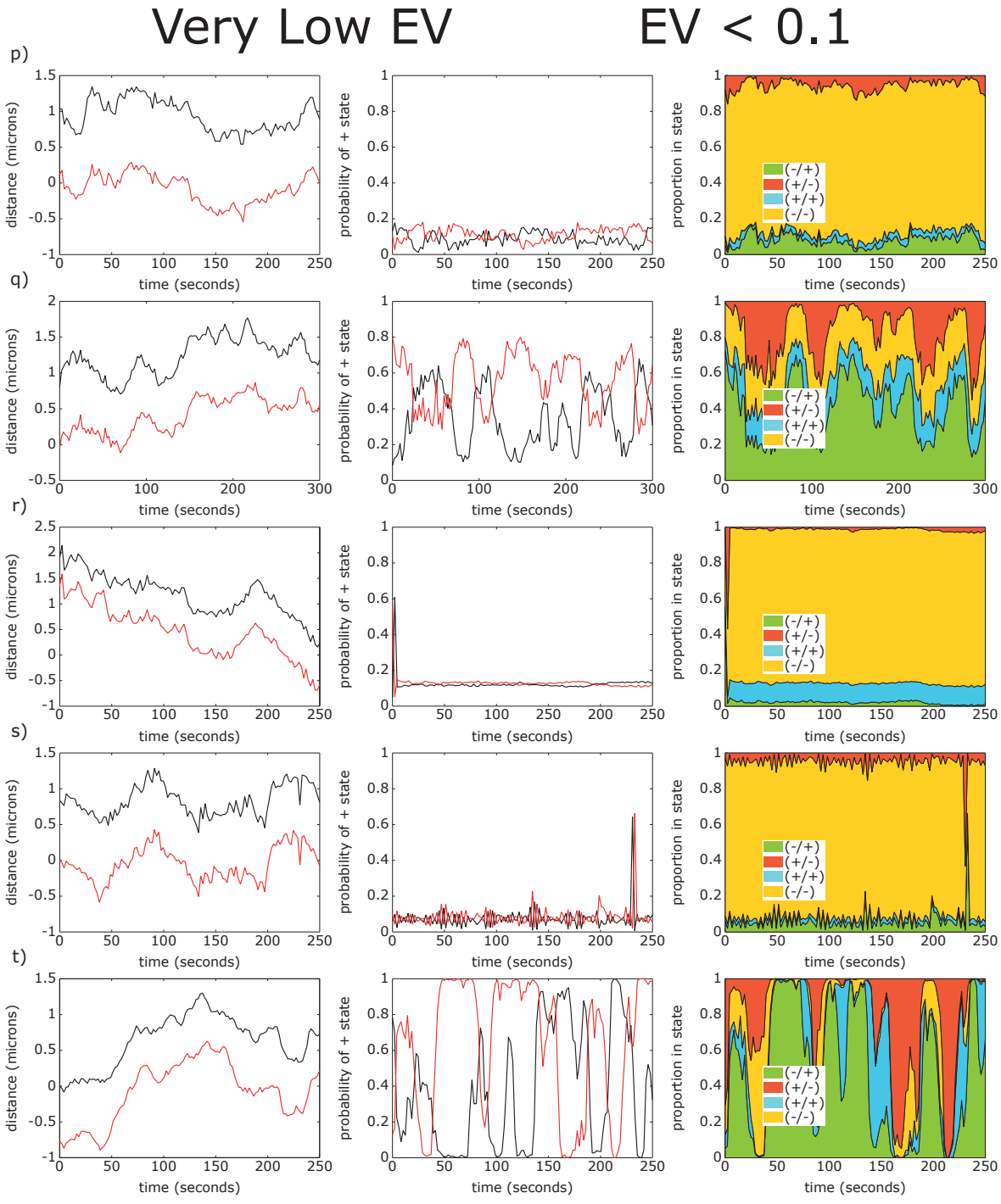


**Figure 5.8:** *cont* **p)-t)** trajectories sixteen to twenty.

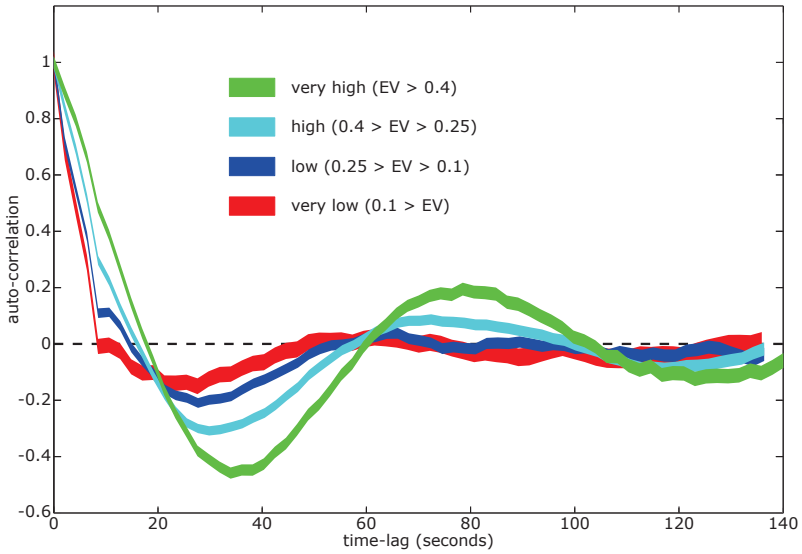


**Figure 5.9:** Sister-centre displacement auto-correlation organised by EV. Trajectories organised into four groups based on EV: EV $>$ 0.4 (green; 226 trajectories from 41 cells); 0.4 $>$ EV $>$ 0.25 (cyan; 351 trajectories from 72 cells); 0.25 $>$ EV $>$ 0.1 (blue; 356 trajectories from 74 cells) and 0.1 $>$ EV (red; 144 trajectories from 55 cells). Line widths represent the 95% confidence interval of the correlation value.

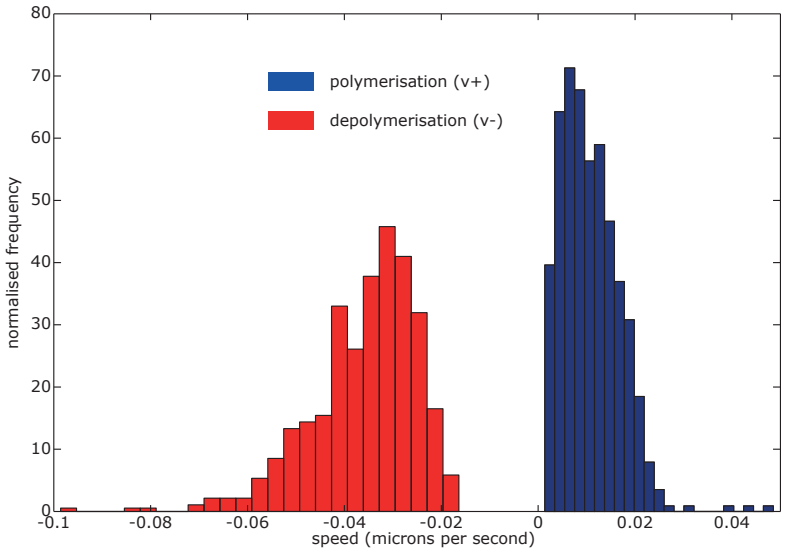


**Figure 5.10:** Posterior mean speeds. Histograms of posterior mean $v_-$ (red) and $v_+$ (blue) for trajectories with EV $> 0.25\,(n = 577)$.

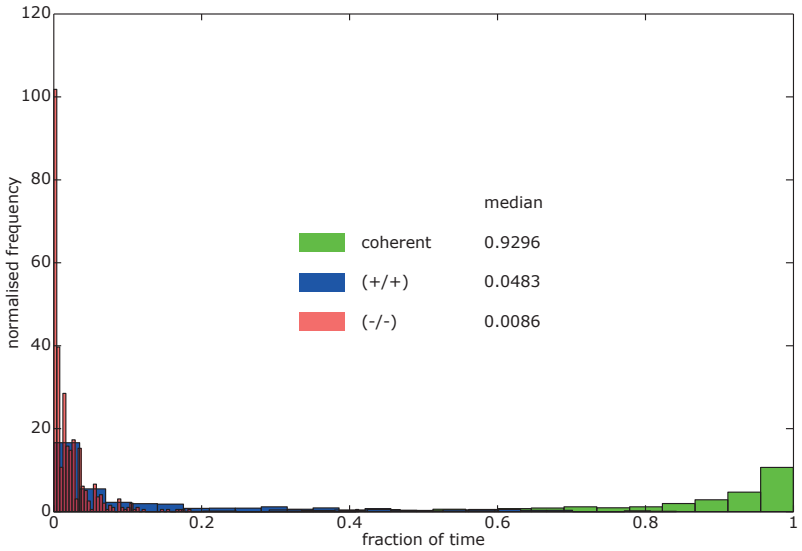


**Figure 5.11:** Fraction of time trajectories from untreated cells spend in a coherent state (green), an incoherent $(+/+)$ state (blue) and an incoherent $(-/-)$ state (red). Fractions calculated by counting time-points of trajectories as either $(+/+)$, $(-/-)$ or coherent depending of which state had the higher probability. Data from 577 trajectories with EV $> 0.25$.

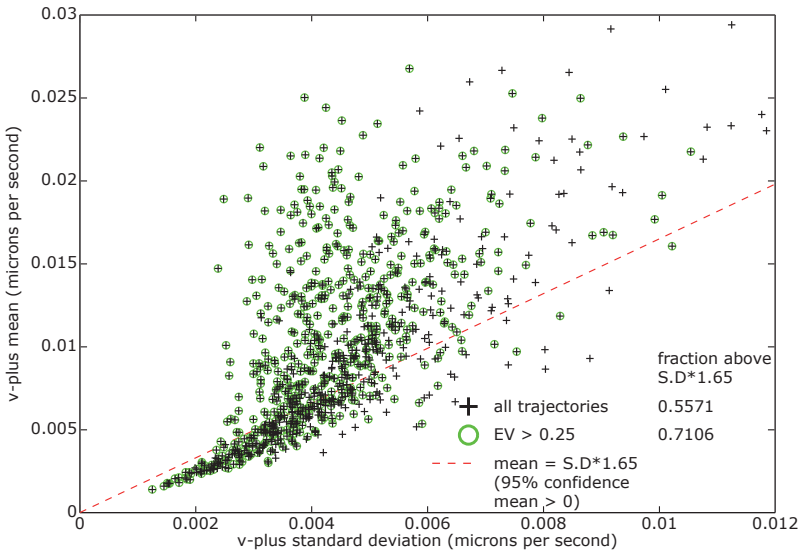


**Figure 5.12:** Evidence for $v_+$ being greater than zero. Posterior mean $v_+$ value versus standard deviation for 1077 trajectories from untreated cells. Trajectories with EV $> 0.25\,(n = 577)$ marked with green circles. Red line indicates mean = s.d. $\times$ 1.65 *i.e.* the 95% confidence limit that $v_+ > 0$. Statistics shown in legend.

## 5.4 Trail Sister Kinetochore Switching First is Strongly Suppressed

The frequency that a lead or trailing sister switch occurs after a coherent run was calculate. To extract this information a period of coherence was defined as a predominantly coherent sequence of time-points (reversals back to the same coherent state within 4 time-points were allowed within a coherent period). A change out of coherence ($v_+/v_-$ or $v_-/v_+$) to $v_+/v_+$ and $v_-/v_-$ correspond to a lead and trail switch respectively. This filters out transient switches that are rapidly reversed and allowed the demarcation of periods of coherence separated by periods of incoherence for each trajectory. The mean coherence and incoherence times are 28.5 (11.8) and 7.5 (8.8) seconds respectively (mean and population standard deviation), Figure 5.13, *i.e.* giving a half period of 36 seconds that is consistent with the autocorrelation analysis, Figures 3.25, 5.9. For a coherent run ($n = 3615$) the probability of the leading or trailing sister switching first was inferred from the model, the confidence of either reflecting the relative dynamics of the two sisters across the event. There was a spread of switching biases across switching events between those with a high probability of the lead sister switching first to those with a high probability of trail switching, Figure 5.14a. A kinetochore switching event was defined as a lead switching event (LSE) if the probability of a lead switch exceeded the probability of a trail switch by 1/3 and a trail switch event (TSE) similarly; the remaining events are defined to have a joint switch/no bias (JSE); respective regions are shown on Figure 5.14a. These criteria illustrate that there was a strong lead bias with the fraction of LSE and TSE being 58.9% and 8.9% respectively, the remaining fraction (32.2%) of events being joint, Table 5.1; a trajectory demonstrating all three event types is shown in Figure 5.14c. This result is similar to the lead switching bias reported in PtK1 cells at 85% : 15%, lead : trail [100]. It was also confirmed that similar distributions of switching probabilities were observed in the parental cell line HeLa-K eGFP-CENP-A (Figure 5.15). It cannot be ruled out that higher sampling ($<$ 2s per frame) would reveal further lead (or trail) bias but attempts to do so indicated that such data is dominated by thermal noise making designation of switching preferences near impossible. For instance the ability to assign a lead or trail preference to an event deteriorates with EV (Figure 5.14b) *i.e.* as noise in the

trajectory increases. Nevertheless these data demonstrate that trailing sister switching is heavily inhibited leaving a weak lead bias and a majority of joint switch events.

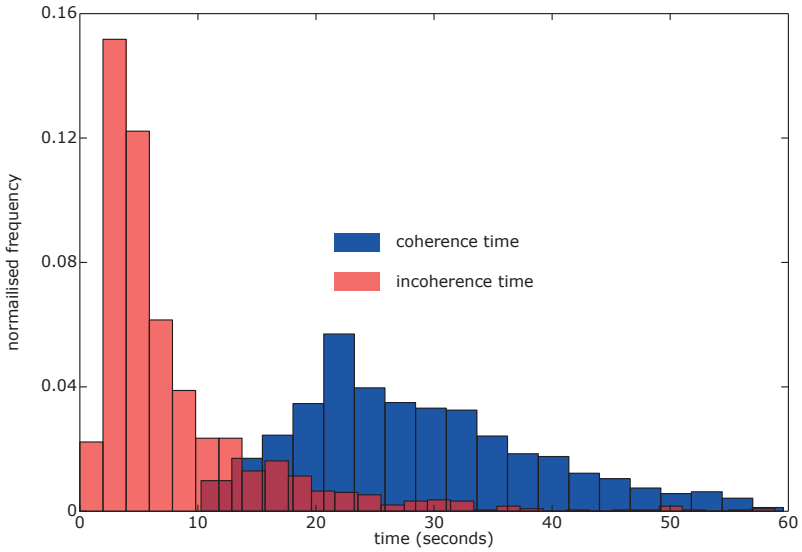


**Figure 5.13:** Histograms of trajectory coherence and incoherence times (EV $> 0.25, n = 577$).

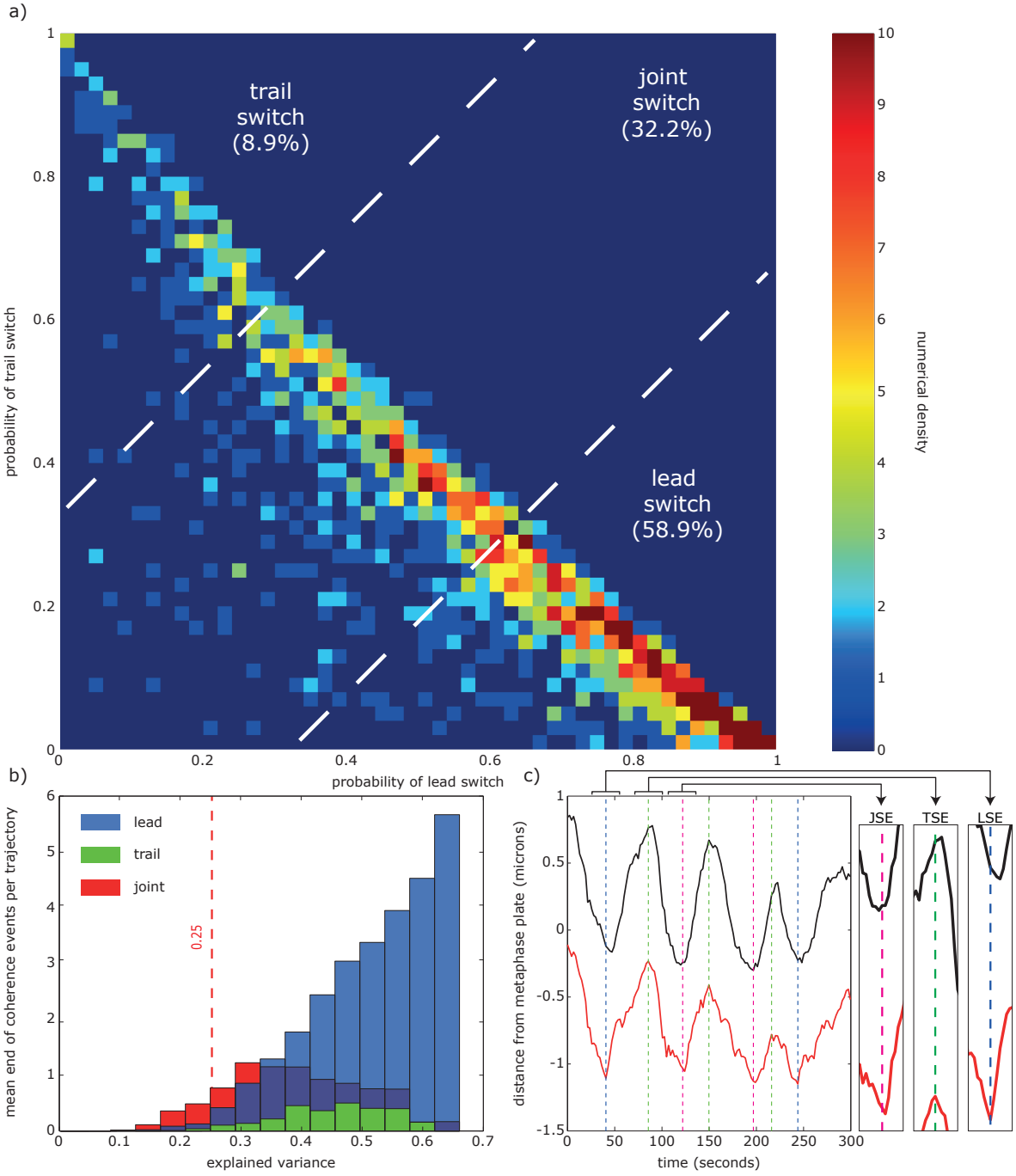


**Figure 5.14:** Coherence to incoherence switch events (cell line: HeLa-K eGFP-CENP-A, eGFP-Centrin1). **a)** Probability of the trailing verses lead sister switching first after a coherence period (EV $>$ 0.25 trajectories; $n$ = 1737 events). Dotted white lines indicate the cut- off where P(lead switches first) is greater than P(trail switches first) by 1/3 and vice versa. **b)** Mean number of LSE (blue), TSE (green) and JSE (red) per trajectory binned by EV. **c)** An example trajectory exhibiting lead switch events (LSE; blue dotted lines), trail switch events (TSE; green dotted lines) and joint switch events (JSE; purple dotted lines).

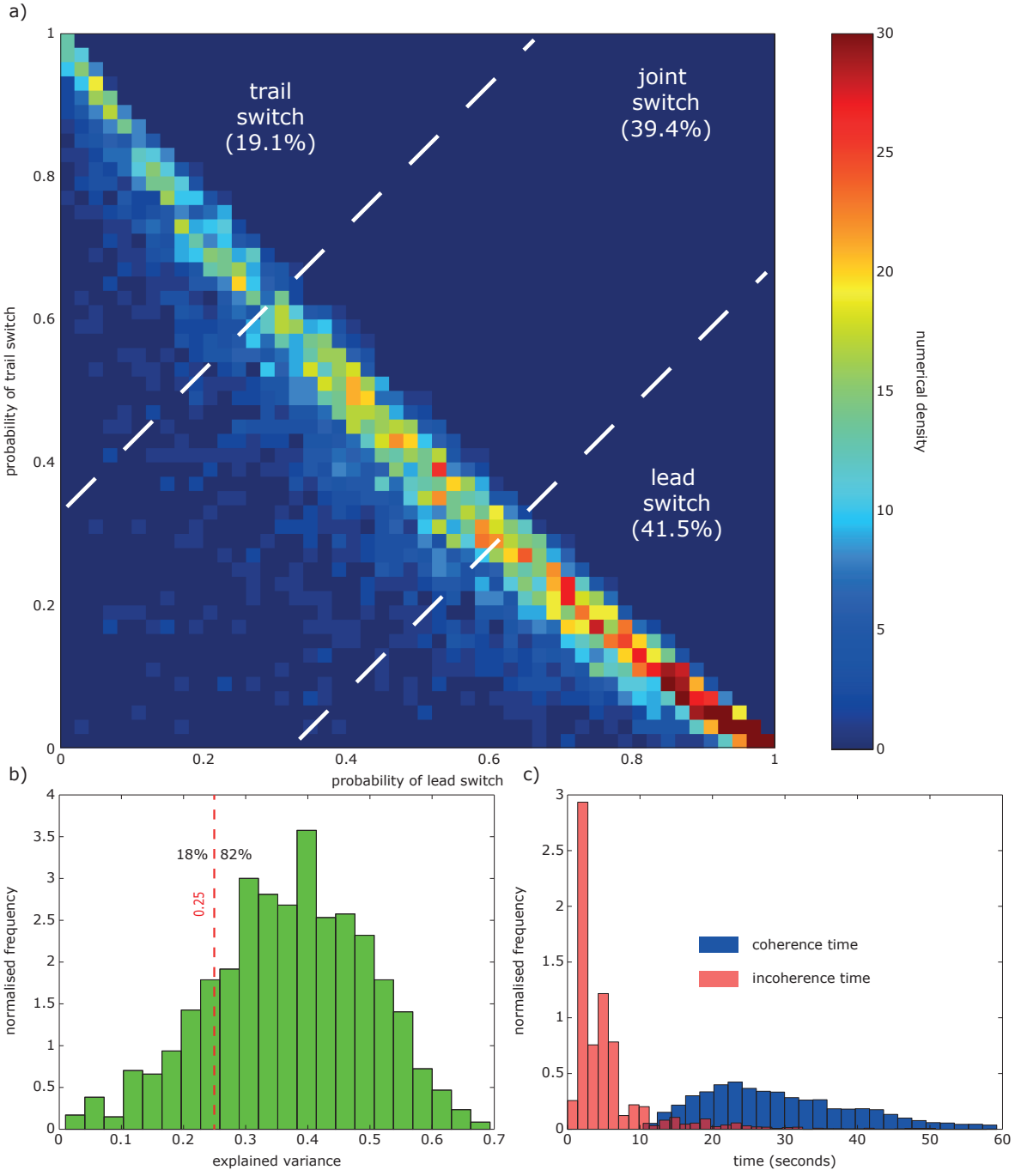


**Figure 5.15:** Event analysis of the parental cell line HeLa-K eGFP-CENP-A. **a)** Probability of trail verses lead sister switching first for end of coherence events. Dotted white lines indicate the cut-off where P(lead switches first) is greater than P(trail switches first) +1/3 and vice versa, defining lead/trail switch events (LSE/TSE) respectively. The remaining population of events are classed as joint switch events (JSE). 5076 events from 1247 trajectories with EV $> 0.25$ from 54 cells. **b)** Histogram of explained variance (EV) (4.7) of 1529 trajectory fits from 54 cells. **c)** Histograms of trajectory coherence and incoherence times (EV $> 0.25, n = 1247$).

## 5.5 Inferred Forces do not Support a Tug-of-War Switching Mechanism

Next it was addressed how the pattern of sister switching is coordinated. The data supports a mechanism orchestrated by a build-up of forces but contradicts a tug-of-war hypothesis (Figure 5.16). In the system the spring is weak, contributing typically less than 13% of the force on a kinetochore whilst the K-fibre generates on average 58% of those forces (Figure 5.16a). The inferred centromere spring constant is low at $0.0302 \pm 0.0007 \mathrm{s}^{-1}$ (mean $\pm$ S.E.M.) *i.e.* the spring contributes a speed of 30nm $\mathrm{s}^{-1}$ under a micron stretch on average. Since the spring length fluctuations are typically within 400nm the spring only makes a small adjustment to the speed of up to 12nm $\mathrm{s}^{-1}$. The PEF force constant is also small at $0.0173 \pm 0.0008 \mathrm{s}^{-1}$ giving an effective speed of 17nm $\mathrm{s}^{-1}$ at a displacement of 1 micron from the metaphase plate; these compare to a depolymerisation speed of $37.4 \pm 0.6$nm $\mathrm{s}^{-1}$ (Figure 5.10). Thus spring forces are small and do not typically build up sufficiently to counter the forces resulting from polymerisation and depolymerisation and hence are insufficient to induce a stall in the leading sister. This does not of course exclude occasional stalls when switching fails to occur, switching times then being substantially longer than the norm. In conclusion switching is not a consequence of a tug-of-war between kinetochore microtubules, spring and PEF forces. However this does not rule out a force-dependent switching mechanism since there are distinct force characteristics to the dynamics (Figure 5.16). For a kinetochore in a leading state (P) the spring and PEF typically pull back on the kinetochore whilst in the trailing state (AP) these combine to increase the speed of the kinetochore (Figure 5.16b,d,f); *c.f.* magnitude of $v_-$ being greater than $v_+$. The PEF and spring forces are periodic, the latter with double the frequency, these forces being in phase just before a switching event (Figure 5.16d,f). The spring force is thus near maximal as the leading sister switches although this is simply a reflection of the fact that the spring is under maximal stretch at that point (Figure 5.1b).

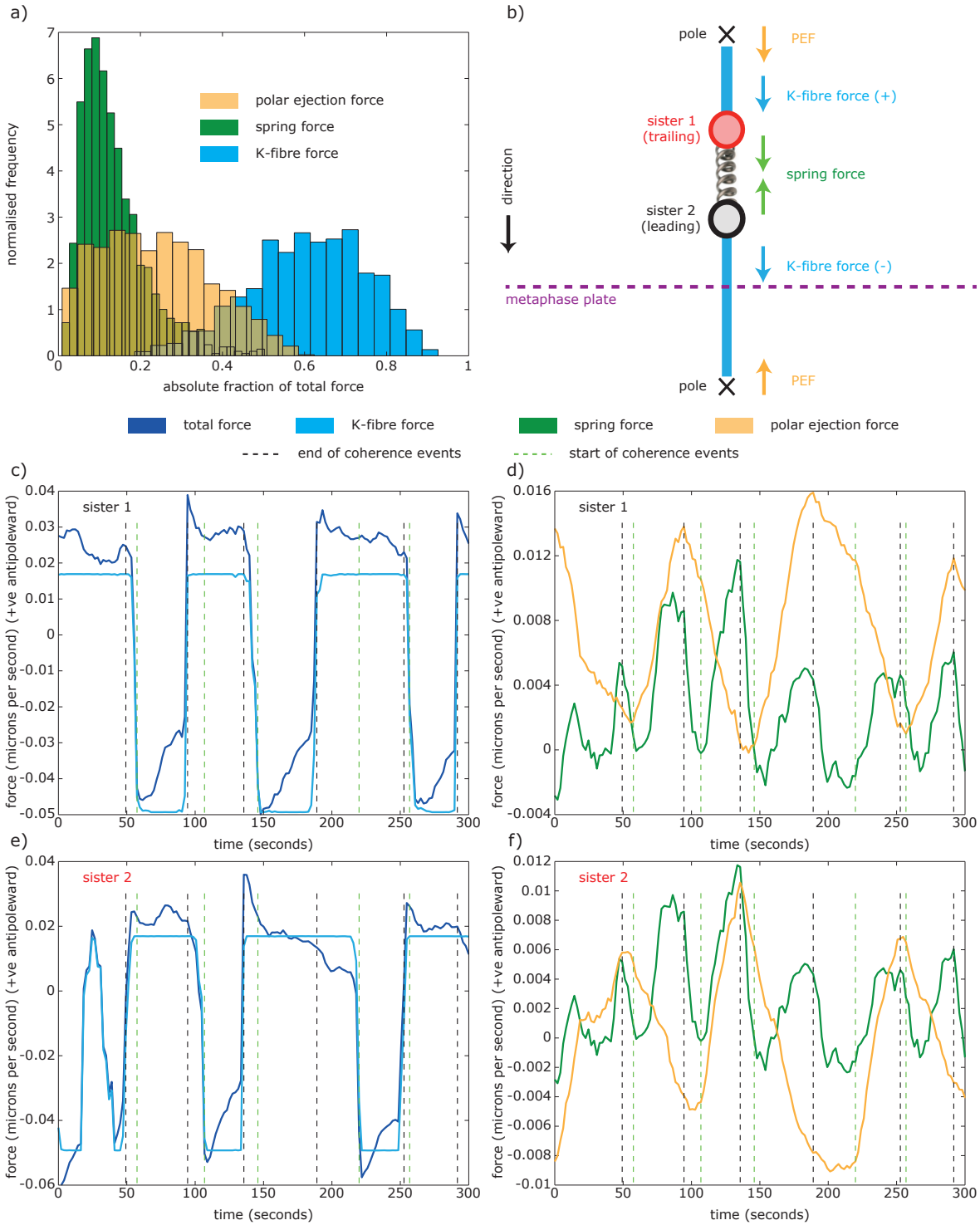


**Figure 5.16:** Temporal force profiles of sister kinetochores. **a)** Histogram of the absolute fraction of total force made up from polar ejection forces (PEF; orange), spring force (green) and K-fibre depolymerisation/polymerisation force (light blue) averaged over trajectories with EV $> 0.25\,(n = 577)$. **b)** Schematic for the forces acting on sisters. **c-f)** Estimated decomposition of kinetochore velocity into its force components over time for the trajectory in Figure 5.1a; **c,d)** sister 1 and **e,f)** sister 2. Polymerisation/depolymerisation force on kinetochores attributable to the K-fibre (light blue); spring force (green); polar ejection forces (orange) and the total force (dark blue). Time-series overlaid with inferred end (black) and start (green) times of coherence periods (runs). Note that forces are positive in the anti- poleward direction.

## 5.6 There is a Strong Causal Signature in the Spring Force for Lead and Trail Switching

To investigate further pre- and post-switch dynamics were examined in TSE and LSE events. By aligning profiles ±40s across the events it can be seen clearly that LSE and TSE have both pre-event (causal) and post-event signatures (Figure 5.17). Specifically the (−10s) pre-event spring tensions (and inter-sister distances) were significantly different ($p = 7 \times 10^{-8}, 7 \times 10^{-11}$, MW) being 39% lower on average in TSE than LSE (Figure 5.17b) whilst the PEF showed no such signature, being very similar under LSE and TSE for both the leading and trailing sisters (Figure 5.17c). For a LSE the spring force increases by 3-fold over the 20s prior to switching, stabilises 4s prior to the switch and then decreases rapidly during the 8s post-switching. This relaxation of the spring prior to the switch appears to be the result of the lead sister slowing down. This would be in-line with the non-linear kinetics of P movement reported in PtK1 cells in which the velocity slows at maximal inter-sister stretch [162]. The spring and PEF forces are also low, (average) peak forces of $6, 14$nm s$^{-1}$ respectively (the latter for the lead sister), confirming that switching is not a result of stalling since their sum is only half of the lead sister depolymerisation speed ($37.4 \pm 0.6$nm s$^{-1}$). Finally, the switching of the second sister (trailing) correlates with a reduction in the spring forces to near zero (Figure 5.17b, red vertical line). The profile for a TSE is distinct: the force in the spring is much lower prior to the switch and builds up more slowly (Figure 5.17b). The profile for a TSE was distinct: the force in the spring is much lower prior to the switch and builds up more slowly (Figure 5.17b). The maximum force is only reached 4s after the switch has occurred. This indicates that the trail switch itself is necessary to build up tension whilst the force reached is similar ($\sim 7$nm s$^{-1}$) to that seen during LSE. These differences in spring force also explain the reduced twisting of the sisters prior to a LSE compared to a TSE, *i.e.* twist is reduced by the higher inter-sister forces whilst the contracting incoherent state after an LSE causes an increase in twist (Figure 5.17d). The post event spring force is also compressive at some time point post LSE (TSE) in 37% (7%) of events while compression of the centromeric chromatin was observed in 38% of coherent runs, typically early after a switch; however distinguishing active compression from a compressive thermal fluctuation is extremely difficult. Note that

JSEs have spring force profiles similar to those of LSE (Figure 5.18) suggesting that there are in fact only two switching choreographies, JSE having a lead bias but with the second sister switching faster than the temporal resolution is able to resolve. Taken together, the data supports the following working model: firstly the trailing sister K-fibre polymerisation state is stabilised by a pulling force from the spring. Secondly the lead sister switching rate is controlled by a tension sensor that responds to forces exerted by the centromeric spring. This model is consistent with that proposed previously [99]. These mechanisms also provide possible explanations for switching resolution. Under TSE the lead sister tension sensor triggers under the escalating spring force post-event (Figure 5.17b) while in LSE the loss of the applied force triggers catastrophe in the trailing sister K-fibre. The latter is a slower process, again suggesting that pulling (expanding) states are suppressed.

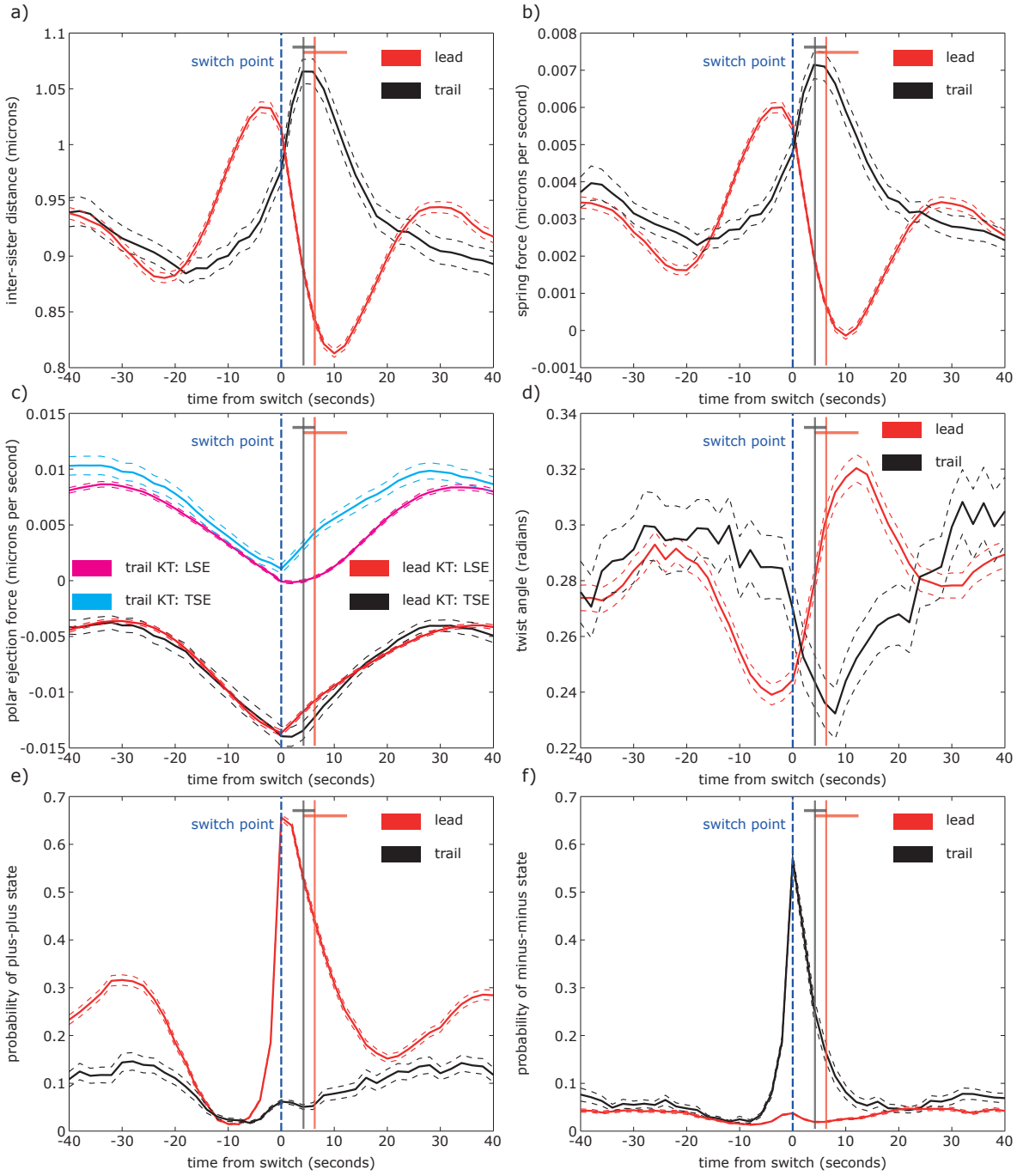


**Figure 5.17:** Signatures in temporal profile distributions during sister kinetochore directional switching. **a)-f)** Time profiles across switching events according to type (LSE, TSE). Events from trajectories with EV $> 0.25$ where lead (LSE, $n = 1024$; red) or trail (TSE, $n = 154$; black) switched first out of coherence were aligned at their median switching time (time origin, vertical dotted blue line). Solid lines indicate mean values over time, dashed lines $\pm$ one S.E.M. **a)** Time-dependent change in inter-sister distance; **b)** spring force; **c)** polar ejection force for the two sisters; **d)** twist angle; **e)** probability of $v_+/v_+$ state and **f)** probability of $v_-/v_-$ state. In c) forces are positive in the direction of motion. Median time at which the second sister switches is indicated by vertical red (trail following LSE) and black (lead following TSE) lines, with the inter-quartile range given as horizontal lines at the top of the figure.

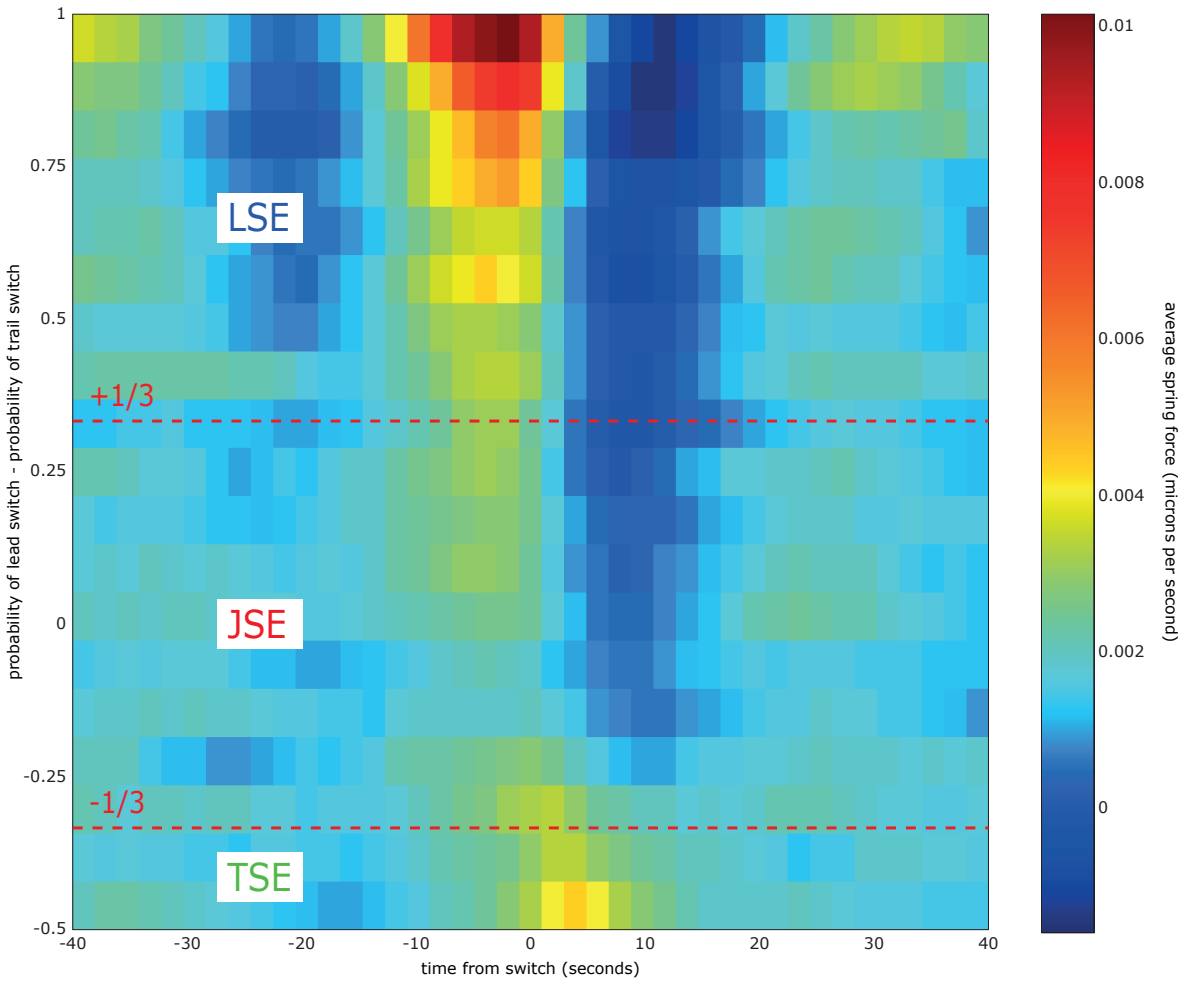


**Figure 5.18:** Spring force profiles as a function of switch type. Average spring force profiles (±40s) for untreated cells centred at switching point as a function of switch type (probability of lead switch - probability of trail switch). Areas corresponding to lead (LSE), joint (JSE) and trail (TSE) switch events marked with horizontal red lines (previously defined, see Figure 5.14 and Section 5.4). Data from 1737 end of coherence events.

## 5.7 Final Summary

Model-fitting to multiple trajectory-pairs revealed a range of population statistics and key correlates in sister-kinetochore dynamics during metaphase oscillations. Kinetochore-pairs exhibited different levels of deterministic- and stochastic-type behaviour quantified by an explained variance statistic. Trajectory-pairs displaying high-stochastic- / low-deterministic-type behaviour *i.e.* low explained variance were biased towards the edge of the metaphase plate, consistent with previous experimental observations that peripheral chromosomes show less oscillatory-like dynamics compared to central ones. The central elastic connection between sister-kinetochores and the PEF were both shown to be relatively weak compared to the intrinsic force produced by poleward or anti-poleward moving kinetochores. Therefore results suggested that directional switches are not due to a kinetochore-pair reaching a point of force-balance between opposing agents but rather due to rapid changes of kinetochore state. The period of time between poleward-directed chromosome movement was referred to as an incoherent state of the kinetochore-pair (as opposed to a coherent state *i.e.* one poleward- and one anti-poleward-moving kinetochore). A strong bias was found for the leading- *i.e.* anti-poleward moving-kinetochore to switch into an incoherent state first. Lead-kinetochore switching suppresses configurations where both kinetochores pull on a chromosome in opposite directions, a state that could be considered dangerous pre-anaphase since it could lead to microtubule detachment. The profiles of inter-kinetochore tension pre- and post-switching event are distinctly different between lead- and trail-switches with lead-switches exhibiting a rapid increase in spring-force pre-event. This suggests that there is an active tension-sensing agent on the lead-kinetochore that triggers a change of state leading to a preferred lead-sister switch that prevents an undesired dual-pulling state of a kinetochore-pair.

# Tables

**Table 5.1:** Event counts in trajectory analysis

| Condition | Number of Lead Switch Events (End / Start) Coherence | Number of Trail Switch Events (End / Start) Coherence | Number of Joint Switch Events (End / Start) Coherence |
|---|---|---|---|
| Untreated | 1050 / 1073 | 160 / 211 | 658 / 1145 |
| Untreated (EV > 0.25) | 1024 / 1022 | 154 / 194 | 559 / 769 |
| Control siRNA | 924 / 1008 | 449 / 612 | 1326 / 2227 |
| Control siRNA (EV > 0.25) | 900 / 945 | 431 / 570 | 1136 / 1529 |
| CAPD2 siRNA | 1269 / 1297 | 990 / 1074 | 611 / 870 |
| CAPD2 siRNA (EV > 0.25) | 1254 / 1249 | 981 / 1039 | 559 / 689 |
| Parental | 2174 / 2175 | 1011 / 1186 | 2190 / 2801 |
| Parental (EV > 0.25) | 2106 / 2097 | 970 / 1126 | 2000 / 2388 |

# References

[57] Jason Stumpff et al. "The Kinesin-8 Motor Kif18A Suppresses Kinetochore Movements to Control Mitotic Chromosome Alignment". In: *Dev Cell* 14.2 (Feb. 2008), pp. 252–62.

[90] R. V. Skibbens, V. P. Skeen, and E. D. Salmon. "Directional instability of kinetochore motility during chromosome congression and segregation in mitotic newt lung cells: a push-pull mechanism". In: *J Cell Biol* 122.4 (Aug. 1993), pp. 859–75.

[99] Xiaohu Wan et al. "The coupling between sister kinetochore directional instability and oscillations in centromere stretch in metaphase PtK1 cells." In: *Molecular biology of the cell* (Feb. 2012).

[100] S. Dumont, E. D. Salmon, and T. J. Mitchison. "Deformations within moving kinetochores reveal different sites of active and passive force generation". In: *Science* 337.6092 (July 2012), pp. 355–358.

[128] A Khodjakov and C L Rieder. "Kinetochores moving away from their associated pole do not exert a significant pushing force on the chromosome." In: *The Journal of Cell Biology* 135.2 (1996), pp. 315–327.

[138] G. Civelekoglu-Scholey et al. "Dynamic bonds and polar ejection force distribution explain kinetochore oscillations in PtK1 cells". In: *J. Cell Biol.* 201.4 (May 2013), pp. 577–593.

[161] S. A. Ribeiro et al. "Condensin regulates the stiffness of vertebrate centromeres". In: *Mol. Biol. Cell* 20.9 (May 2009), pp. 2371–2380.

[162] J. C. Waters et al. "The kinetochore microtubule minus-end disassembly associated with poleward flux produces a force that can do work". In: *Mol. Biol. Cell* 7.10 (Oct. 1996), pp. 1547–1558.

# Chapter 6

# Multiple Force-Dependent Mechanisms Regulate Human Chromosome Directional Switching to Produce Noisy Metaphase Oscillations

## 6.1 Inter-Kinetochore Tension Control of Kinetochore Switching Tested by Perturbation Experiments

The results discussed in Chapter 5 lead to a proposal for kinetochore directional switching where lead-kinetochore switching is favourably-biased and is under the control of a tension-sensing agent sensitive to the inter-kinetochore tension of the centromeric spring. In this chapter that model will be tested by careful perturbation experiments; designed to affect the inter-kinetochore tension whilst not directly interfering with any kinetochore-proteins.

## 6.2 A Stiff Centromere Spring is Required to Bias Switching to the Lead Sister Kinetochore

One prediction of the inter-kinetochore tension sensing model proposed in Chapter 5 is that manipulation of the spring and its associated forces should dramatically affect coordination and oscillatory dynamics. Specifically weakening of the spring should reduce force sensing between the sisters and have no effect on K-fibre polymerisation and depolymerisation speeds. To test this the CAPD2 subunit of condensin I was depleted, which causes decompaction of centromeric chromatin resulting in a reduction in the stiffness of the sister-sister linkage and an increase in the period of oscillation [96, 161, 163] (Figure 6.1e). For comparison purposes a control siRNA treatment was used, which had similar characteristics to the untreated cell line, in particular it retained the LSE bias (Figure 6.2a). It was confirmed that under CAPD2 depletion kinetochore oscillations were retained (Figure 6.1b; Figure 6.1e) while inter-sister distances were largely consistent with a weaker spring (Figure 6.1d). This was in part because of a larger rest length determined by nocodazole treatment (Figure 4.4e,f), consistent with a change in the physical properties of the centromeric spring [163]. Model fits further showed that the spring constant was reduced (by 58%) as expected while other mechanical parameters were affected to a lesser degree, the second largest being $v_+$ that changed by 37% (Figure 6.3d,g; Table 6.1). Basic expectations were thus satisfied and it was concluded that CAPD2 is primarily affecting spring elasticity. An analysis across $n = 1006$ sister pairs (CAPD2 siRNA treatment) compared to $n = 1465$ (Control siRNA treatment) showed that although oscillations had a larger period, Figure 6.1e, and amplitude, Figure 6.1c, they were also more deterministic with the proportion of EV $> 0.25$ increasing to 84% (Figure 6.3a,b). This higher level of deterministic behaviour (trajectory dynamics fit the model better) is likely a consequence of the increased period and amplitude, reducing the effects of limited spatial and temporal resolution. In fact although the coherence time is longer its proportion throughout the period is reduced, with sisters in CAPD2 siRNA treated cells spending longer in incoherence (Figure 6.3i, 6.4). Thus switching takes longer, indicative of reduced levels of inter-sister regulation. An analysis of these trajectories revealed that the switching lead bias was reduced, 1.3:1 compared to 2.0:1 in Control siRNA; Figure 6.2. Thus weaken-

ing the centromeric spring largely abolishes the mechanism that allows communication between sister kinetochores and the resulting lead-first switching choreography.

### 6.2.1 Key Model Parameters are Shown to be Significantly Different Under siRNA Treatment by Statistical Clustering

To test whether observed differences in model parameters under CAPD2 depletion (compared to controls) were significantly different compared with intra-treatment inter-experiment differences statistical clustering was used. Data was initially separated into sets based on treatment (untreated, control siRNA and CAPD2 siRNA) and on individual experiments (imaging days) (Figure 6.5), the latter giving an estimate of variation between experimental batches. Distances between sets were calculated using the Tukey-Kramer range test on the mean ranks of each set calculated using the Kruskal-Wallis one-way analysis of variance. Clustering was performed by combining sets with the lowest distance into one new set and repeating the clustering until only one set remained. Distances between each set were determined as significant or not based on the Tukey-Kramer range test with a 95% confidence interval. Figure 6.5b,c show the clustering of posterior mean values of the spring constant and natural length $(\kappa, L)$ respectively. In both these cases all CAPD2 siRNA experiments belong to a single cluster (of insignificant intra-cluster distances) with the largest overall (significant) distance to any other cluster. In the case of $L$ this is understandable given the strong prior (Section 4.4) and the differences in the mean prior for each condition (Table 4.3). In the case of $\kappa$ however the result strongly suggests that the fitted parameter values under CAPD2 depletion are significantly different to controls even when accounting for inter-experimental variation. No other parameter tested showed complete clustering of a single treatment type suggesting that for other model parameters inter-treatment variation was not significantly different from inter-experimental variation. Clustering analysis of this type is ultimately qualitative in assessment but nerveless serves as a useful indication of the variation in the parameters. The fact that the speed values $(v_+, v_-)$ (Figure 6.5e,f respectively) do not show comparatively significant inter-treatment variation given the differences in the mean prior on $L$ between treatments (Table 4.3) and the sensitivity

of the posterior speed values on the prior natural length (Section 4.4) is an indication that reasonable priors for natural length (especially in the case of CAPD2 depletion) were chosen and that K-fibre (de)polymerisation speed (force) is largely independent of inter-chromatid tension (caused by Condensin).

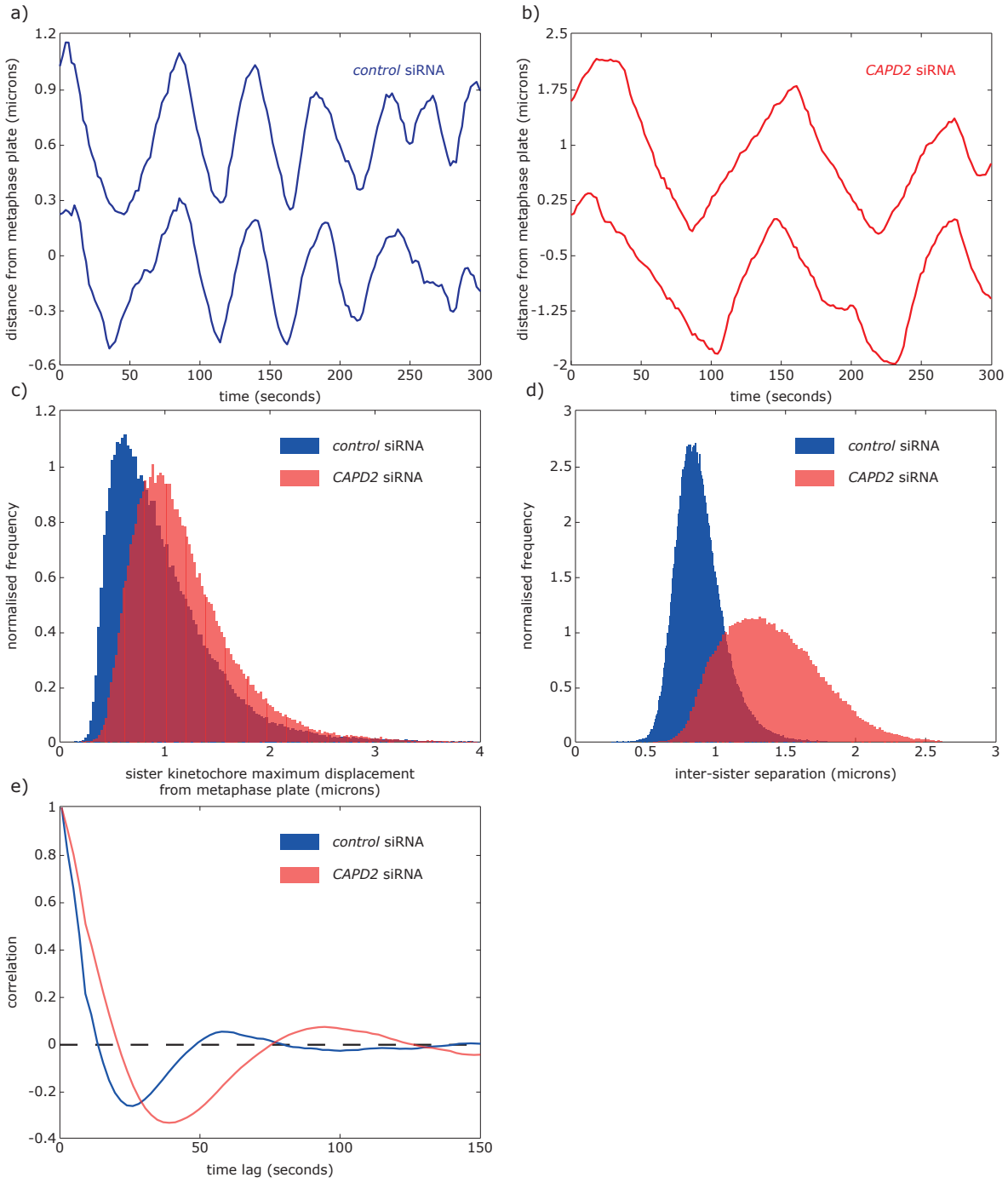


**Figure 6.1:** siRNA depletion of CAPD2. **a)** Typical example of a control siRNA trajectory exhibiting strong oscillations. **b)** Typical example of a CAPD2 siRNA trajectory exhibiting strong oscillations. **c)** Histograms of maximum kinetochore-pair displacement from metaphase plate observed; **d)** histograms of measured inter-sister distances (pooled over trajectories and time points) and **e)** autocorrelation of sister centre displacements ($\Delta x$) over 4 frames (8s) normal to the metaphase plate in control (blue) and CAPD2 siRNA (red) treated cells ($n = 1219, 1614$ trajectories from $108, 76$ cells respectively).

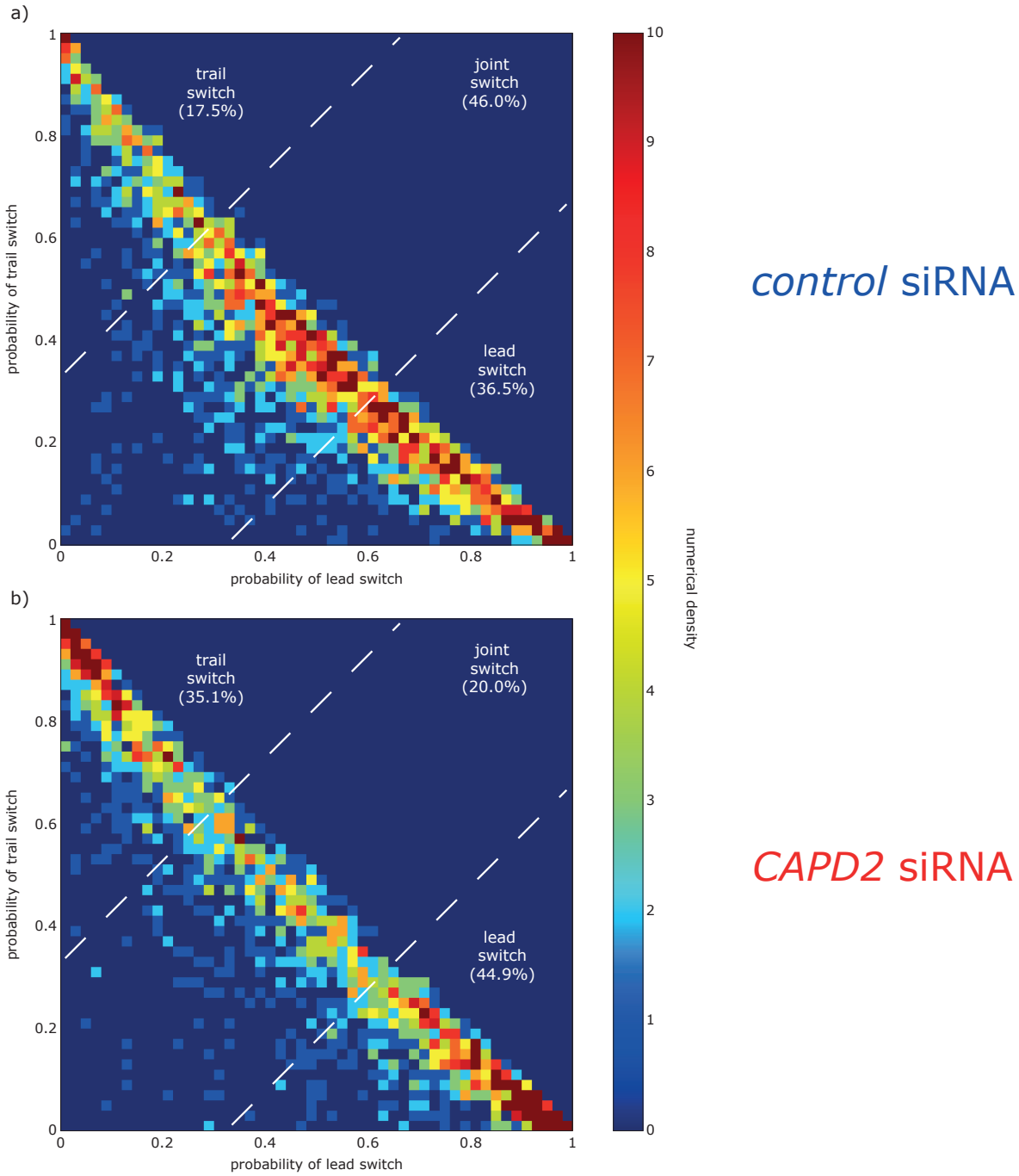


**Figure 6.2:** Coherence to incoherence switch events in siRNA treated cells. Probability of the trailing verses lead sister switching first after a period of coherence in **a)** control and **b)** CAPD2 siRNA treated cells (EV $> 0.25$; $n = 2467, 2794$ events respectively). Dotted white lines indicate the cut-off where P(lead switching first) is greater than P(trail switching first) by 1/3 and vice versa.

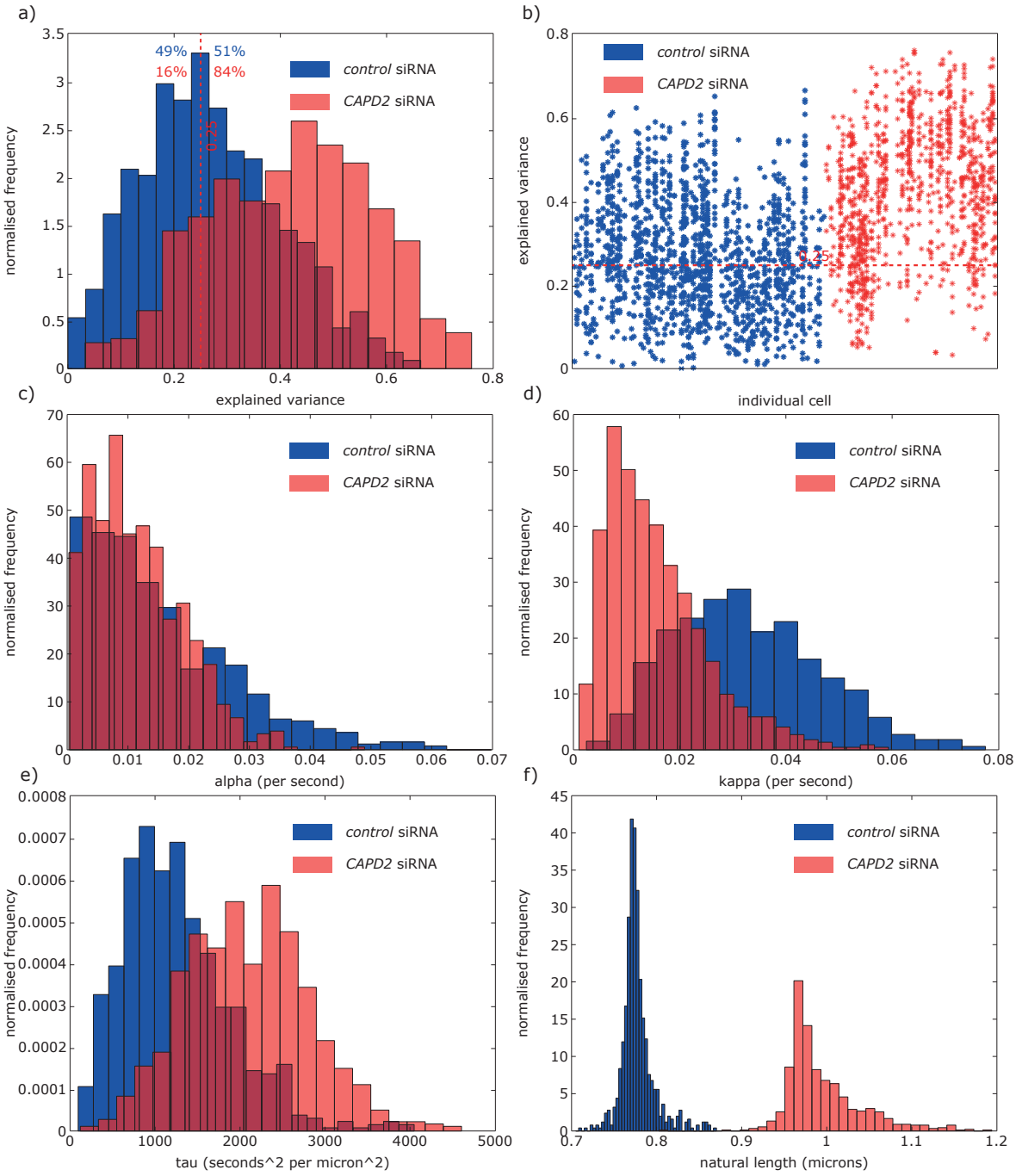


**Figure 6.3:** CAPD2 siRNA model parameters. **a)** Histograms of explained variance (EV) per trajectory with proportions of trajectories above and below EV = 0.25. **b)** Explained variance per trajectory grouped by cell. Horizontal line indicates EV = 0.25. **c)-f)** Distributions of posterior mean model parameters. **c)** Distributions of the anti-poleward force gradient $\alpha$. **d)** Distributions of the spring constant $\kappa$. **e)** Distributions of the noise parameters $\tau$. **f)** Distributions of natural lengths $L$. *cont*

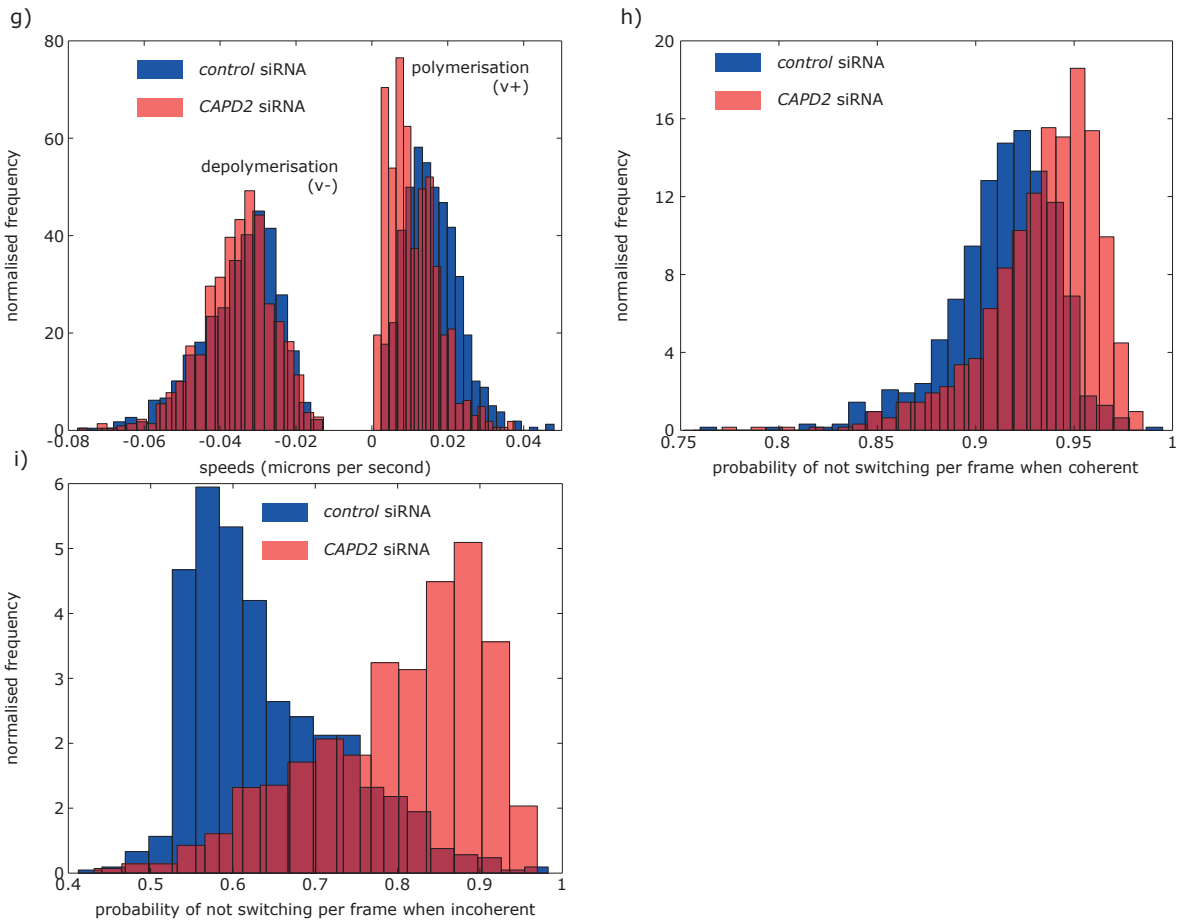


**Figure 6.3:** *cont* **g)-i)** Distributions of posterior mean model parameters. **g)** Distributions of $v_+$ and $v_-$ speeds. **h)** Distributions of the probabilities of not switching states per time-point when coherent. **i)** Distributions of the probabilities of not switching states per time-point when incoherent. Data used in **c)-i)** from trajectories with EV $> 0.25$ (744 Control siRNA trajectories and 850 CAPD2 siRNA trajectories).

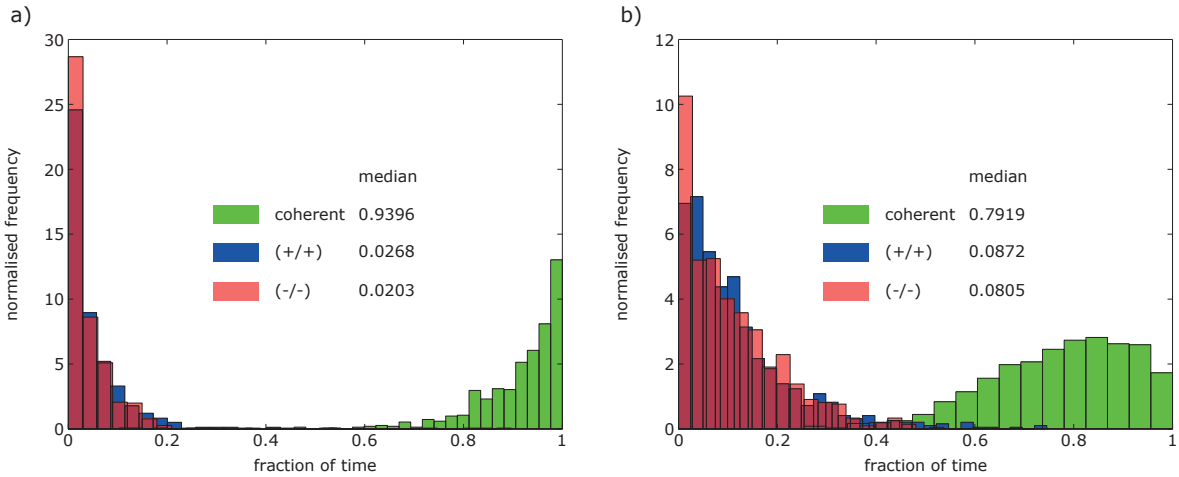


**Figure 6.4:** Fraction of time in (in)coherence states for siRNA treated cells. Fraction of time trajectories from **a)** control siRNA and **b)** CAPD2 siRNA cells spend in a coherent state (green), an incoherent $(+/+)$ state (blue) and an incoherent $(-/-)$ state (red). Fractions calculated by counting time-points of trajectories as either $(+/+)$, $(-/-)$ or coherent depending of which state had the higher probability. Data from 744 Control siRNA and 850 CAPD2 siRNA trajectories filtered by EV $> 0.25$.

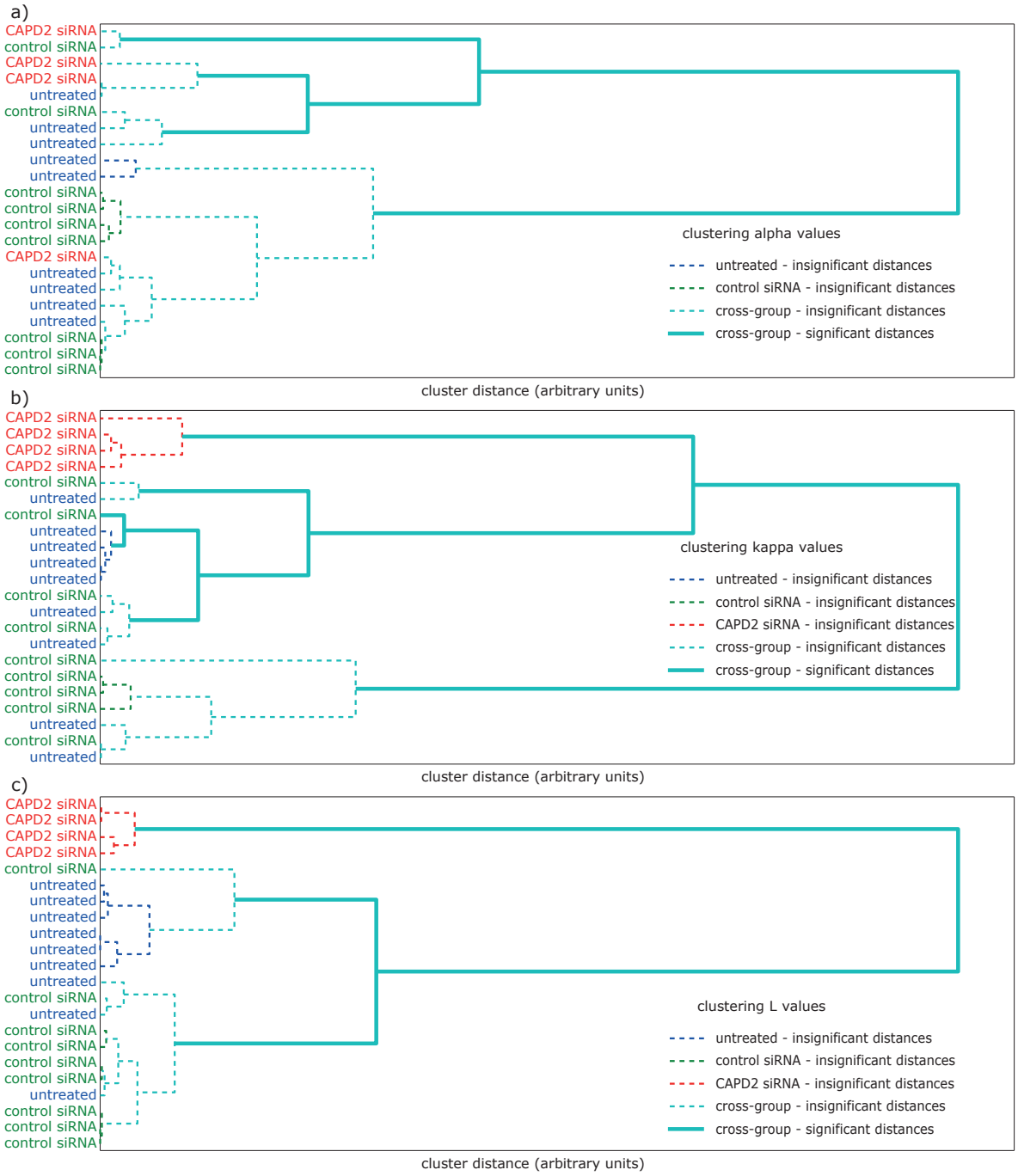


**Figure 6.5:** Clustering of posterior mean model parameters initially grouped by individual experiments. See Section 6.2.1 for details of the clustering algorithm. Insignificant distances between sets shown with dashed lines, significant distances shown with solid lines. Clusters containing only experiments of a single treatment type are coloured appropriately ($\{\text{blue}, \text{green}, \text{red}\}$ for $\{\text{untreated}, \text{control siRNA}, \text{CAPD2 siRNA}\}$ respectively). Clusters containing experiments of different treatment types coloured cyan. Parameter values taken from EV $> 0.25$ trajectories (untreated: 9 experiments $\{\text{no. cells}, \text{no. trajectories}\} = (\{14, 157\}, \{14, 213\}, \{16, 264\}, \{6, 72\}, \{7, 123\}, \{10, 109\}, \{2, 8\}, \{10, 69\}, \{6, 62\})$, control siRNA: 9 experiments $\{\text{no. cells}, \text{no. trajectories}\} = (\{6, 157\}, \{8, 213\}, \{19, 264\}, \{3, 72\}, \{8, 123\}, \{2, 109\}, \{20, 8\}, \{20, 69\}, \{20, 62\})$, CAPD2 siRNA: 4 experiments $\{\text{no. cells}, \text{no. trajectories}\} = (\{21, 157\}, \{21, 213\}, \{16, 264\}, \{14, 72\})$). **a)** Clustering of anti-poleward force gradient $\alpha$. **b)** Clustering of spring constant $\kappa$. **c)** Clustering of natural length $L$. *cont*

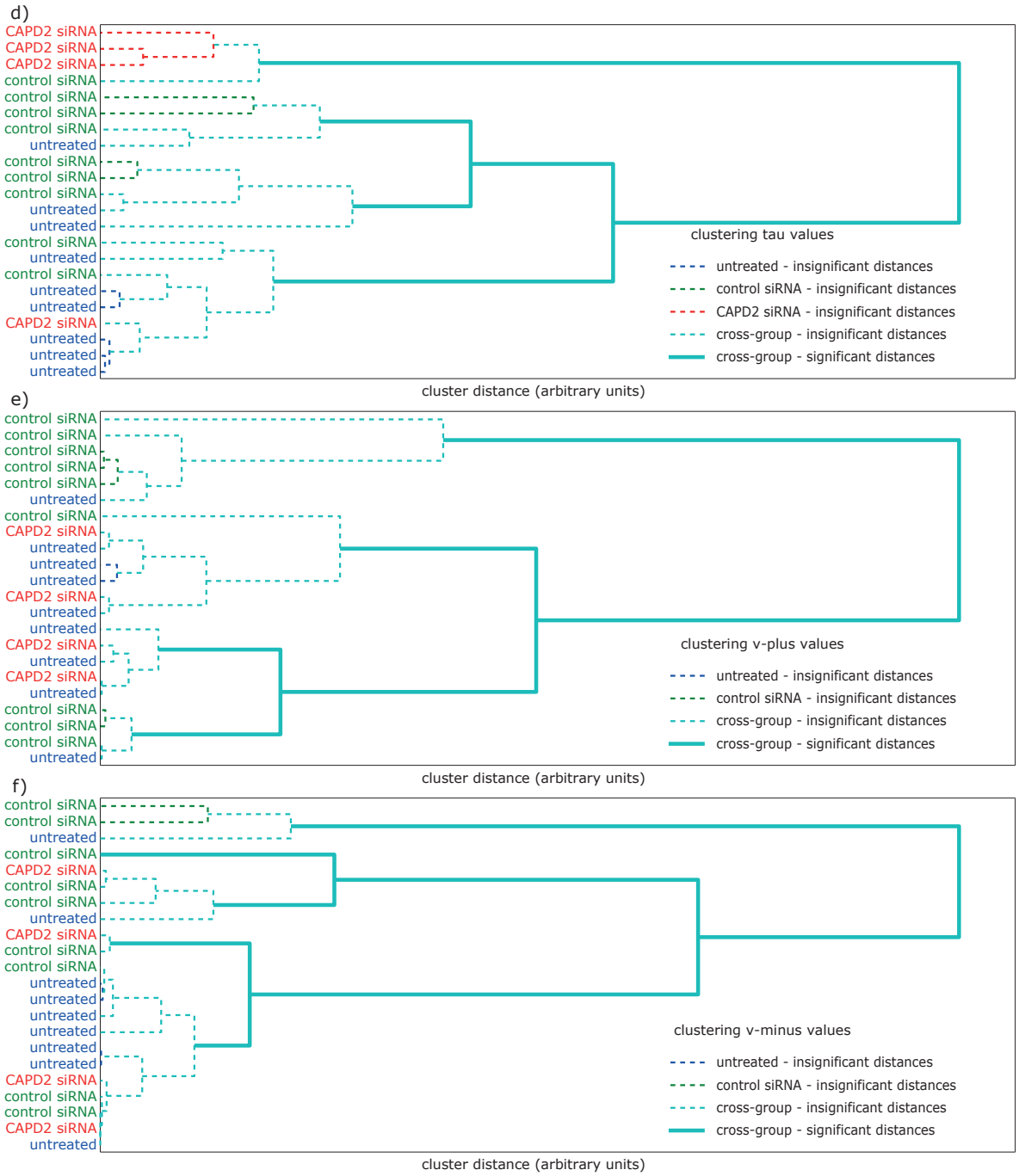


**Figure 6.5:** *cont* **d)** Clustering of noise parameter $\tau$. **e)** Clustering of polymerisation speed $v_+$. **f)** Clustering of depolymerisation speed $v_-$. *cont*

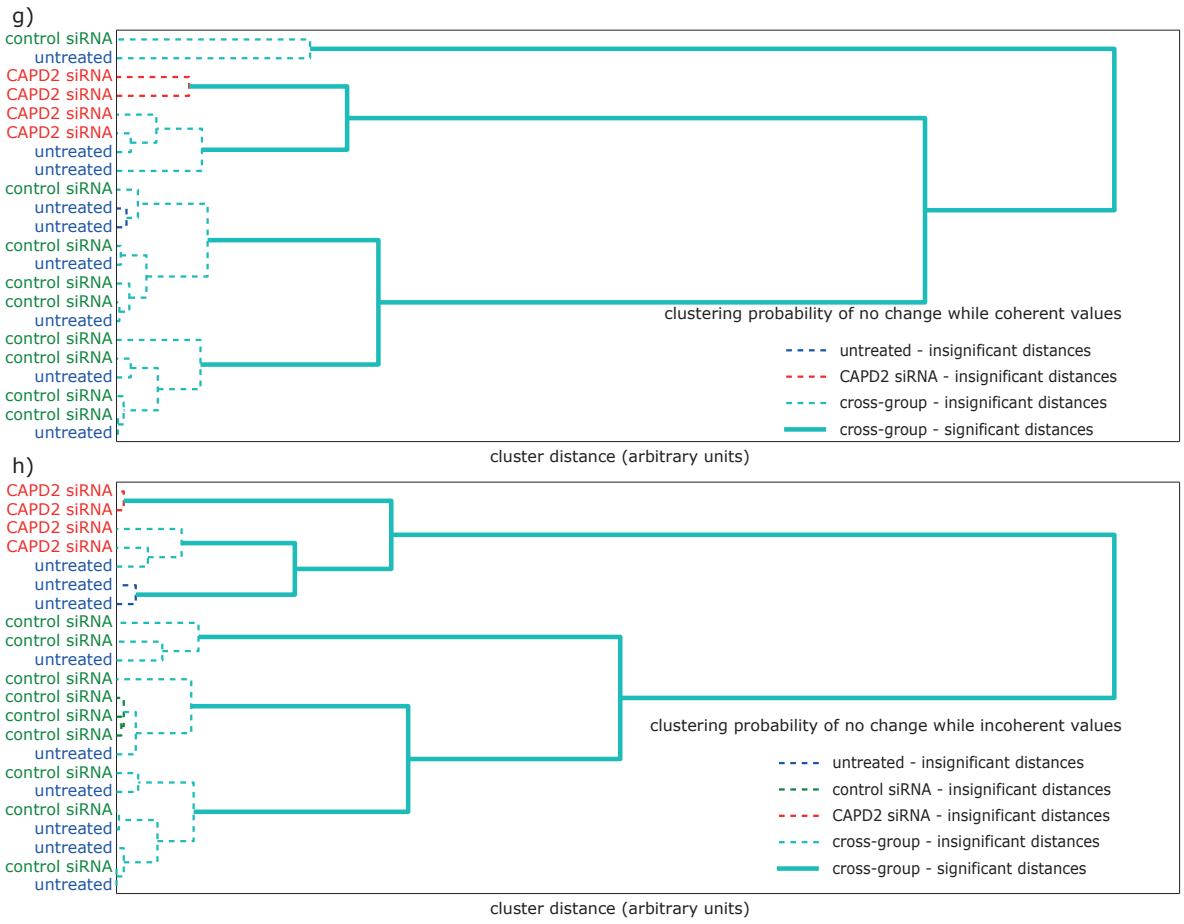


**Figure 6.5:** *cont* **g)** Clustering of probabilities of not switching states per time-point while coherent. **h)** Clustering of probabilities of not switching states per time-point while incoherent.

## 6.3 Evidence for a Tension-Rate Sensor on the Lead Sister Kinetochore

Examination of the causal signatures in the force profiles indicates surprisingly that the spring force profiles were typically higher under CAPD2 depletion, but as predicted pre-event differences for LSE and TSE were reduced (Figure 6.6a,b). The data thus supports the following model: the increased spring force stabilises the trailing sister resulting in a longer half-period (Figure 6.1e). However the higher force in the spring demonstrates that the lead-sister tension sensor cannot be responding to a threshold force as this would be exceeded far earlier than the switching event in CAPD2-depleted cells, suggesting a mechanism based on the rate of change of the tension is present. Examination of the fractional change in the spring force over 10s suggests that the tension sensor fires when a fractional change of 0.5 occurs, the switching event then following within 10s (Figure 6.6c; green dotted line). Therefore it is proposed that the tension sensor continually adapts on a time scale of 10s to the current spring tension. This is a tension-rate-sensor. It is proposed that LSE triggering under CAPD2 depletion is not through the tension-rate-sensor because it fails to trigger under the gentle force profiles seen in these conditions, resulting in fractional changes over 10s that are below 0.5 (Figure 6.6b,d). Instead it is suggested that a second mechanism for microtubule rescue of the leading sister is present whereby the K-fibre has a native switching rate dependent on the balance of polymerising and depolymerising constituent microtubules. Under CAPD2 depletion, thereby removing the trigger for the tension-rate-sensor, a native instability of the K-fibres is revealed so tuned to have similar rates of switching and thus similar proportions of LSE and TSE. Finally the second sister switches in CAPD2 depletion as normal, the tension-rate-sensor triggering under the escalation of the spring force in TSE reaching the 0.5 fractional change threshold (Figure 6.6d), whilst loss of the pulling force causes the trailing sister to switch in LSE due to loss of stabilisation of polymerisation state. These considerations also apply to the untreated cells (Figure 5.17) where the fractional change exceeds 1.5 at its peak, and to the original parental cell line (Figure 6.7). In all these cell lines there is a mixture of lead kinetochore switching mechanisms reflected in the lead:trail bias; the high bias of the untreated cell line indicates near pure lead switching (85%) through tension-

meter firing, whilst the Control siRNA with a lead bias of 2.0:1, only has 50% of LSE attributable to tension-meter firing, compared to 23% in CAPD2 depleted cells. This heterogeneity partially explains the degrading signature of the fractional tension change during LSE since this signature is an average over the two LSE types. Further, switching of the K-fibre takes 10 to 15s in LSE and maximal fractional tension change is not coincident with the kinetochore direction reversal. This is because of a phase of deceleration (10s prior to direction reversal) of the inter-sister spring distance as microtubules within the K-fibre undergo rescue, Figure 6.6c; 6.7. After a TSE the switching of the original lead sister K-fibre appears to be faster, occurring within 3 to 8s. Explaining these fine details will require data on K-fibre microtubule composition and state.

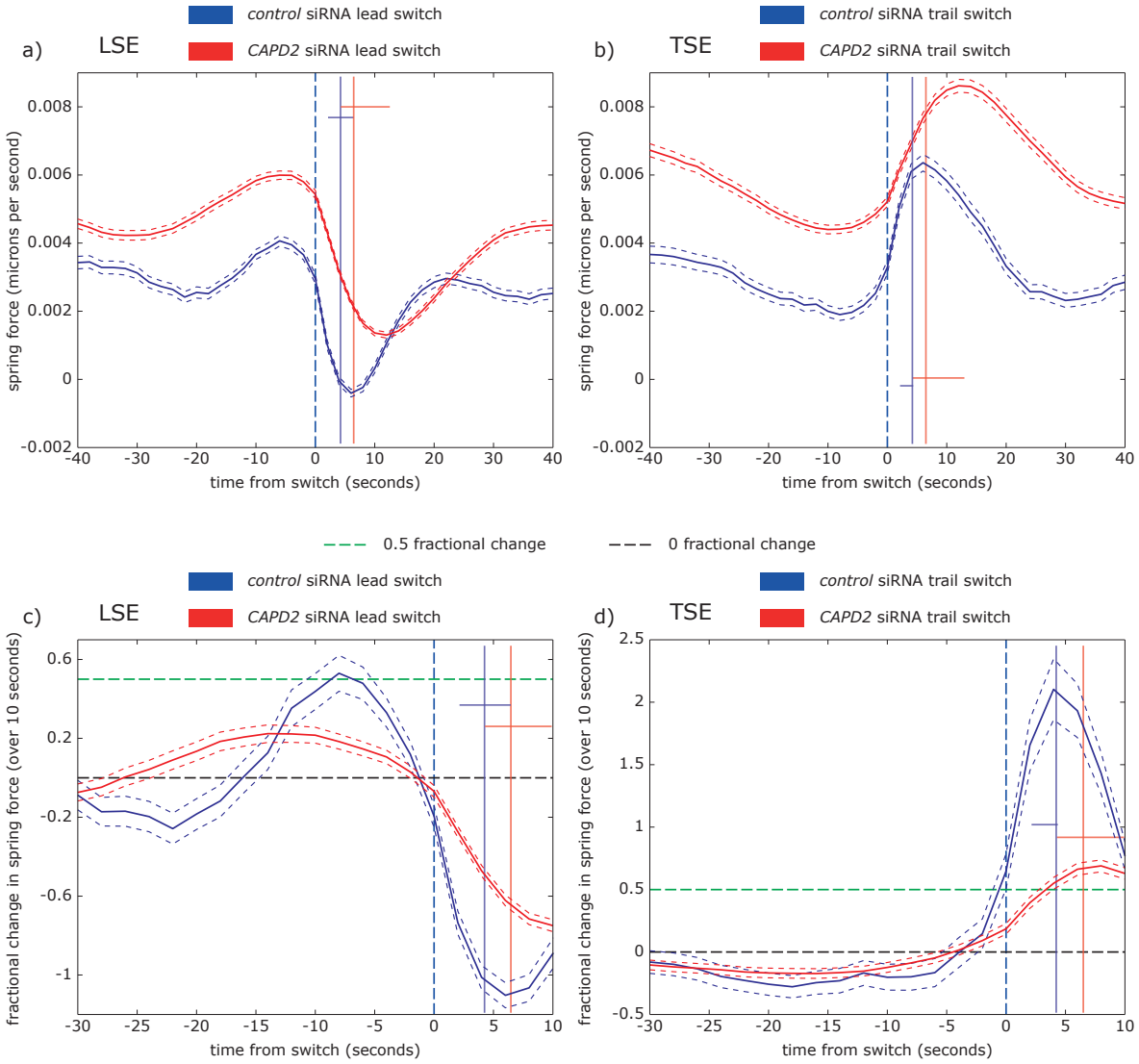


**Figure 6.6:** Force signatures and fractional changes under weakening of the spring. **a)** Aligned profiles for the spring force for LSE in Control (blue) and CAPD2 (red) siRNA treatments around their median switch times (events from trajectories with EV $>$ $0.25, n = 900, 1254$ events respectively). Solid lines represent mean values over time and dashed lines represent $\pm$ one S.E.M. Median time at which the second sister switches is indicated by the vertical blue (Control siRNA) and red (CAPD2 siRNA) lines with the inter-quartile range indicated by horizontal lines. **b)** Same analysis as a) but for TSE ($n = 431, 981$ events respectively). **c)** Fractional change in the spring force over the previous 10s for LSE, data as a). **d)** Fractional change in the spring force over the previous 10s for TSE, data as b). In c), d) second sister switching times as a), b). The green and black horizontal dotted lines indicate the 0.5 and 0 fractional change in spring force, respectively.

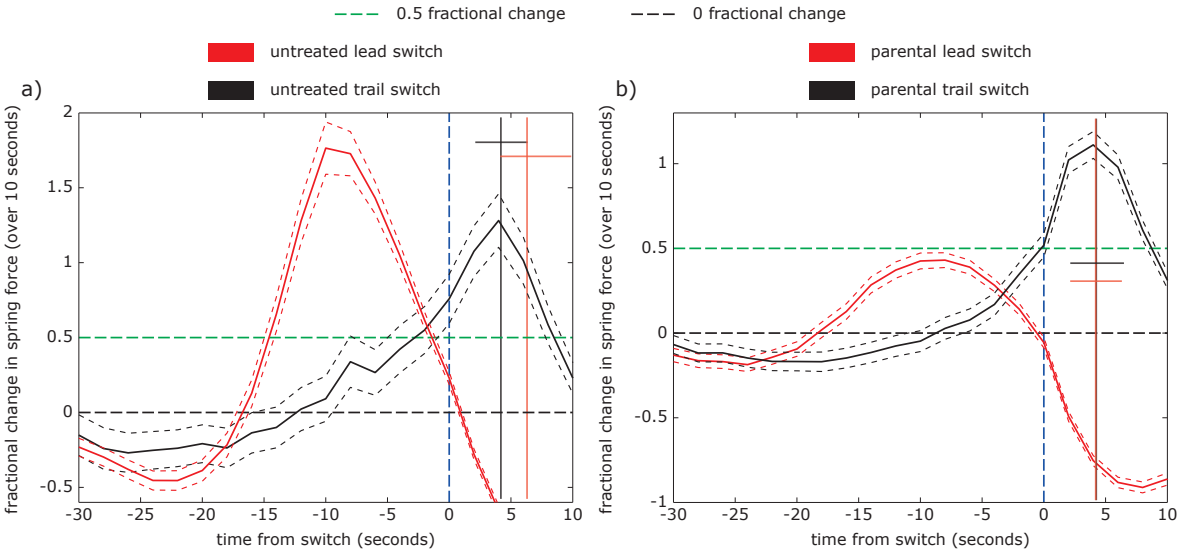


**Figure 6.7:** Fractional changes under weakening of the spring in untreated and parental cell lines. **a)** Fractional change in the spring force over the previous 10s in untreated cells for lead (red) and trail (black) switch events around their median switch times (events from trajectories with EV $> 0.25, n = 1024, 154$ events respectively). Solid lines represent mean values over time and dashed lines represent $\pm$ one S.E.M. Median time at which the second sister switches is indicated by the vertical red (trail following lead) and black (lead following trail) lines with the inter-quartile range indicated by horizontal lines. **b)** Same analysis as a) but for the the parental cell line ($n = 2345, 1081$ events respectively). The green and black horizontal dotted lines indicate the 0.5 and 0 fractional change in spring force, respectively.

## 6.4 Model for Human Kinetochore Switching

Analysis supports a new model of kinetochore switching (see schematic in Figure 6.8) in which the lead sister is connected to the trailing sister by a weak centromeric spring, dynamics regulated so that the spring sustains only low forces throughout metaphase oscillations. This set-up prevents thermal fluctuations and/or stochastic movements of the trailing sister from stalling the lead sister. This is crucial to ensure that directional chromosome movements are robust. By implication the weak spring cannot induce switching by stalling the lead sister. Instead switching is regulated through a local force sensing *i.e.* communication occurs between the sisters through the (small but significant) forces in the connecting spring. A layered mechanism of switching is proposed whereby the multiple microtubules of each K-fibre have a native switching rate, a consequence of the dynamic instability of the constituent microtubules whilst a tension-rate sensor on the lead sister typically results in lead sister switching under escalation of spring force during a coherent run (Figure 6.8). A LSE thus has the following sequence of events: over a coherent run the faster lead sister ($|v_-| > |v_+|$), (Figure 5.10) results in an increased spring force that stabilises the trailing sister state by inhibiting catastrophe whilst tension build up causes the tension-rate sensor to fire at 0.5 relative tension increase over 10s (Figure 6.6c). The lead sister thus switches to polymerisation; the spring force collapses and the trailing sister polymerisation state then becomes unstable because of the age of its constituent microtubules. This age difference can explain the bias towards the previous trailing sister to undergo catastrophe and not the newly switched kinetochore. In a TSE there is a slower build up of inter-sister separation that changes the whole choreography of switching. This slower build up is possibly due to obstacles to chromosome movement or other stochastic events. It results in a gentler spring force profile thus the lower forces fail to stabilise the trailing sister state and the lower fractional change prevents the tension rate sensor firing. Hence the trailing sister switches first due to its native age dependent catastrophe rate; the lead sister then rapidly follows through under firing of the tension-rate sensor as the spring force escalates (Figure 6.6d). Again there is an asymmetry, the original lead sister has an established tension-rate sensor, whilst the new lead sister tension-meter would take 10s to establish a rate measurement. The coherent run time prior to a TSE

is longer by 1.3s on average ($28.5 \pm 11.2$ versus $29.8 \pm 12.3$s), but the large coefficient of variation of these distributions means this is not significant. Finally under weakening of the spring (CAPD2 depletion) the polymerisation and depolymerisation speeds are insufficient to increase the spring force fast enough to switch the tension-rate sensor during a coherent run. Since the spring force is in fact high in CAPD2 depleted cells, because of a high inter-sister distance, the polymerisation state is stabilised and thus the half-period is longer (Figure 6.1b). Switching is then stochastic with a slight bias towards LSE presumably because of a small component of the tension-rate sensor firing whilst the second sister follows a switching mechanism identical to above. The model (Figure 6.8) provides for the first time a (probabilistic) causal mechanistic model explaining how switching events are initiated (first sister switch) and how switching events are resolved (second sister switching) thereby returning the sisters to a coherent state. This model requires three key regulatory mechanisms. Firstly microtubule catastrophe rates increase with age, indeed microtubules have been reported to have a age dependent catastrophe rate [164]. Secondly catastrophe rates of kinetochore microtubules are reduced under applied forces. Such stabilisation by applied force is observed with purified budding yeast kinetochores *in vitro* [46] and micro-manipulation experiments *in vivo* [88]. Thirdly there is a tension-rate sensor on the lead sister kinetochore that fires under a fractional change of 0.5 over 10s. Such dynamic adaptive sensors are known in chemotaxis where the chemotaxis signalling network responds to temporal gradients in the chemo-attractant [165, 166], a property that emerges from the connectivity of the signalling network [167]. Thus the tension-rate sensor could comprise such adaptive signalling networks with force sensing proteins. It is proposed that this layered mechanism has evolved to minimise the likelihood of pulling sister-chromatids apart in pre-anaphase cells by keeping inter-sister forces small. Without the tension-rate sensor (CAPD2 depletion) the sisters have a 35% probability of both entering a pulling state at a switching event (TSE), compared to 17.5% with the tension rate sensor (Control siRNA). Further, TSE have shorter periods of incoherence after switching than LSE ($p = 1.32 \times 10^{-5}$, MW), $4.17 \pm 4.35$ versus $6.26 \pm 5.57$s respectively (untreated cells) suggesting the system has minimised the time spent in the pulling state. In total kinetochores spend 8% of their time in the expanding incoherent state in absence of a tension-rate sensor (Figure 6.4) compared to only 2% with a

tension-rate sensor (Figure 6.4).

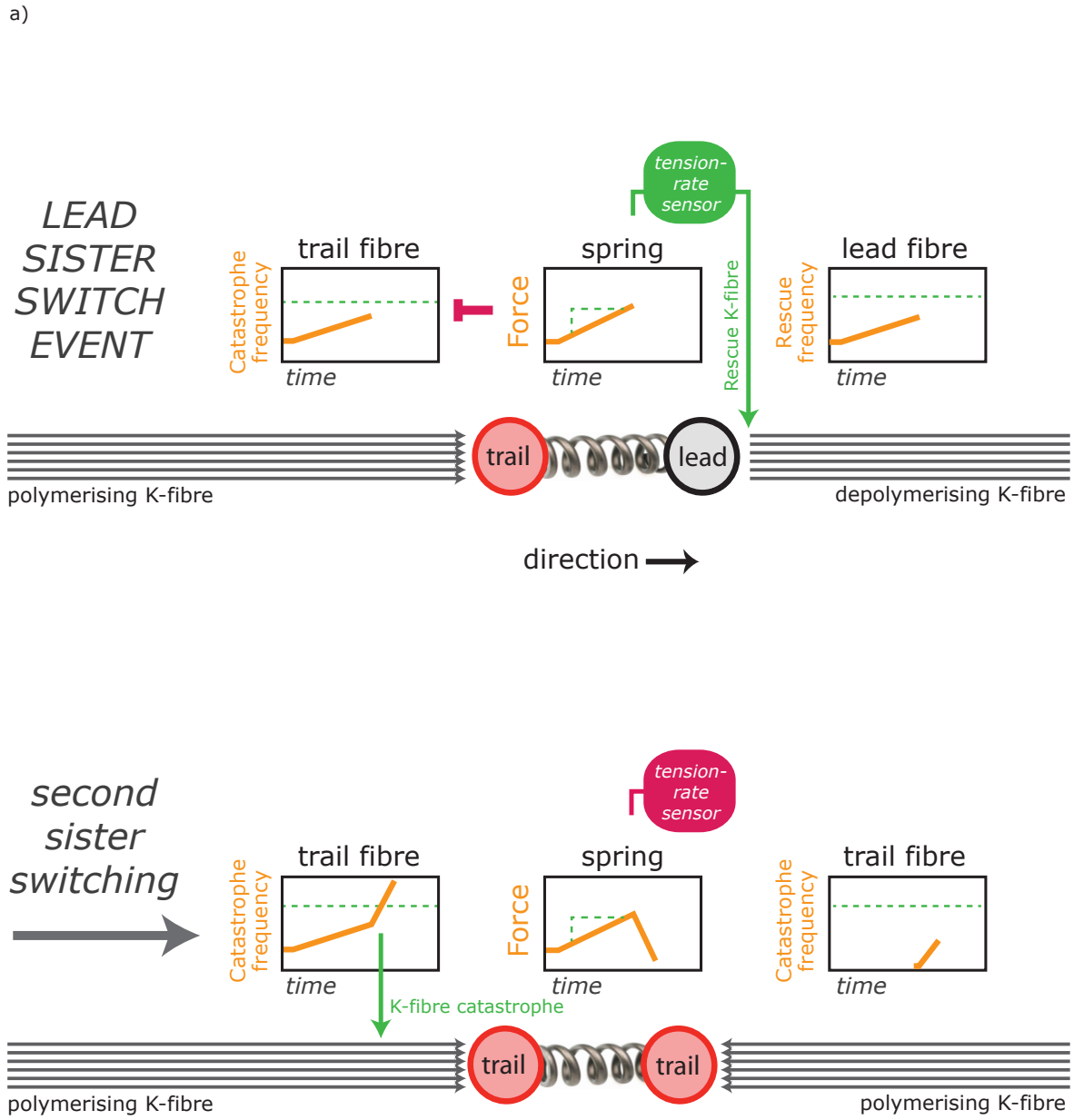


**Figure 6.8:** A tension-rate sensor, force stabilised polymerisation state and a K-fibre ageing process coordinate sister kinetochore switching. Cartoon model summarising the mechanisms that coordinate sister kinetochore switching. Trailing sisters (red outline) and leading sisters (black outline) are shown attached to K-fibres that are polymerising or depolymerising. Sisters are linked by centromeric spring. The inset above the spring illustrates how spring forces (F) are changing with time (orange lines). The insets above the K-fibres illustrate how the rate of catastrophe or rescue of the constituent microtubules evolves over time (ageing). Thresholds for initiating a kinetochore state change are shown by horizontal green dotted lines. **a)** Top panel: The lead sister switches first when the spring force builds up at a sufficient rate to trigger the tension-rate sensor (green) on the lead sister whilst those high spring forces also inhibit the native catastrophe rate of the trailing sister-attached K-fibre. This results in the lead sister switching before the trailing. Bottom panel: Switching of the lead sister results in a rapid reduction of the spring forces, which removes the force stabilisation of the trailing sister-attached K-fibre polymerisation state causing the trailing sister to switch, returning the sisters to a coherent state moving in the opposite direction. *cont*

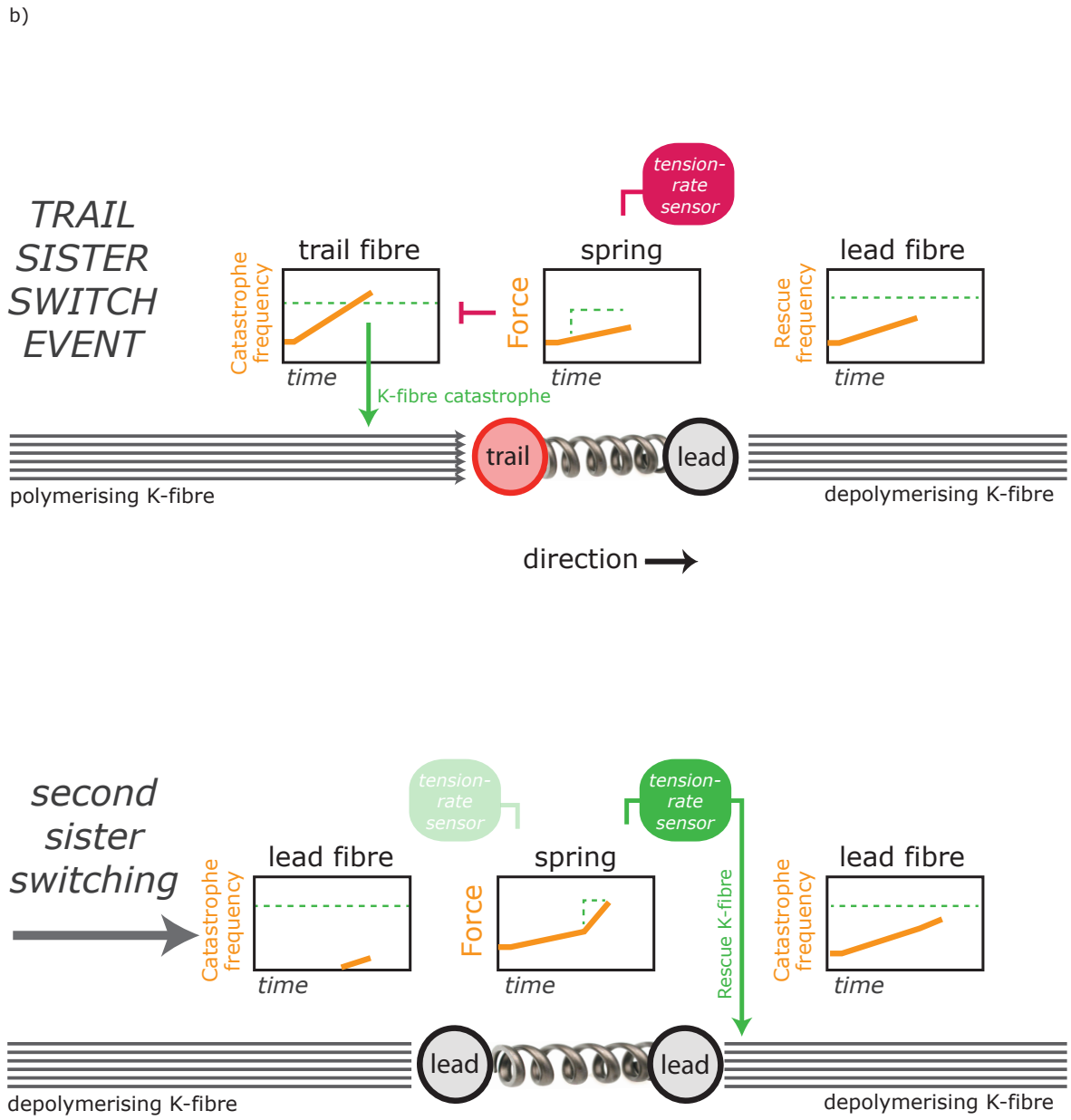


**Figure 6.8:** *cont* Note that the previously lead (just switched) kinetochores does not re-switch in this model because the K-fibre is 'new', compared to the trailing sister attached K-fibre that is old and close to the switching threshold. **b)** Top panel: The trailing sister switches first when the spring force does not build up sufficiently fast to fire the tension-rate sensor, whilst the low force fails to stabilise the K-fibre of the trailing kinetochore thus giving the trailing sister a higher catastrophe rate. A trail switch is thus favoured, rescues being less probable that catastrophes. Bottom panel: Once the trailing sister switches the spring force increases rapidly activating the tension-rate sensor and driving the former lead sister to switch into a trailing state. The failure of the new lead kinetochore to re-switch suggests that the tension-rate sensor is not yet fully active.

## 6.5 Final Summary

Perturbation of the inter-kinetochore centromeric spring by CAPD2 depletion revealed key characteristics of sister-kinetochore coordination at directional switches. Summary statistics (inter-sister distances and sister-centre displacement autocorrelation (Figure 6.1d,e)) on trajectories under CAPD2 depletion were shown to be consistent with previous results [96]. Analysis of the internal mechanical model parameters showed that relative to controls CAPD2 depletion reduced the inter-kinetochore spring constant $\kappa$ the most as predicted. Trajectories under CAPD2 depletion overall exhibited more deterministic behaviour; not an unexpected result since compared to controls trajectories under CAPD2 depletion have longer periods of oscillation hence would be likely to undergo fewer directional switches during identically spaced sampling windows. Few directional switches means longer periods of coherence hence longer periods where the model-fitting procedures can with greater confidence assign probabilities of directional-states to the sister-kinetochores. As predicted by the proposed lead-kinetochore tension-sensing model, weakening of the centromeric spring reduced the lead-kinetochore switch bias when the system enters a period of incoherence. It was found however that spring forces are almost uniformly higher under CAPD2 depletion compared to controls. This suggests that the lead-kinetochore tension-sensor is sensitive not to absolute levels of force but to force-gradients. Such a sensor fits with the notion of an adaptive signalling network in place at a kinetochore-pair and is consistent in behaviour with other signalling networks found throughout biological systems.

# Tables

**Table 6.1:** Model parameters of control siRNA and CAPD2 siRNA trajectories

| Parameter | Control siRNA Mean | Control siRNA Std | CAPD2 siRNA Mean | CAPD2 siRNA Std | Difference‡ |
|---|---|---|---|---|---|
| $\tau$ $(s^2\mu m^{-2})$ | 1264.1646 | 646.8736 | 2086.8355 | 726.3127 | 0.6508 |
| $\kappa$ $(s^{-1})$ | 0.0351 | 0.0205 | 0.0156 | 0.0095 | 0.5557 |
| $v_+$ $(\mu m s^{-1})$ | 0.0167 | 0.0127 | 0.0108 | 0.0064 | 0.3527 |
| $L$ $(\mu m)$ | 0.7769 | 0.0207 | 1.0046 | 0.0745 | 0.2931 |
| $\alpha$ $(s^{-1})$ | 0.0162 | 0.0150 | 0.0115 | 0.0075 | 0.2879 |
| $p_{ic}$ | 0.6384 | 0.0938 | 0.7992 | 0.1069 | 0.2519 |
| $p_c$ | 0.8539 | 0.2045 | 0.9208 | 0.1046 | 0.0784 |
| $v_-$ $(\mu m s^{-1})$ | -0.0354 | 0.0118 | -0.0355 | 0.0100 | 0.0020 |

‡ $\left|\frac{\text{Control siRNA Mean} - \text{CAPD2 siRNA Mean}}{\text{Control siRNA Mean}}\right|$

# References

[46] Bungo Akiyoshi et al. "Tension directly stabilizes reconstituted kinetochore-microtubule attachments". In: *Nature* 468.7323 (Nov. 2010), pp. 576–9.

[88] R. B. Nicklas. "The forces that move chromosomes in mitosis". In: *Annu Rev Biophys Biophys Chem* 17 (1988), pp. 431–449.

[96] Khuloud Jaqaman et al. "Kinetochore alignment within the metaphase plate is regulated by centromere stiffness and microtubule depolymerases". In: *J Cell Biol* 188.5 (Mar. 2010), pp. 665–79.

[161] S. A. Ribeiro et al. "Condensin regulates the stiffness of vertebrate centromeres". In: *Mol. Biol. Cell* 20.9 (May 2009), pp. 2371–2380.

[163] D. Gerlich et al. "Condensin I stabilizes chromosomes mechanically through a dynamic interaction in live cells". In: *Curr. Biol.* 16.4 (Feb. 2006), pp. 333–344.

[164] M. K. Gardner et al. "Depolymerizing kinesins Kip3 and MCAK shape cellular microtubule architecture by differential control of catastrophe". In: *Cell* 147.5 (Nov. 2011), pp. 1092–1103.

[165] H. C. Berg and P. M. Tedesco. "Transient response to chemotactic stimuli in Escherichia coli". In: *Proc. Natl. Acad. Sci. U.S.A.* 72.8 (Aug. 1975), pp. 3235–3239.

[166] R. M. Macnab and D. E. Koshland. "The gradient-sensing mechanism in bacterial chemotaxis". In: *Proc. Natl. Acad. Sci. U.S.A.* 69.9 (Sept. 1972), pp. 2509–2512.

[167] N. Barkai and S. Leibler. "Robustness in simple biochemical networks". In: *Nature* 387.6636 (June 1997), pp. 913–917.

# Chapter 7

# Discussion

Accurate segregation of genetic information during cell-division is vital for proliferation. Mitotic chromosome dynamics are a key process in the structural reorganisation of cellular material required for successful division. Oscillations of chromosomes during metaphase are a distinct emergent macroscopic phenomena, a consequence of undoubtedly multiple, poorly understood mesoscopic and microscopic mechanisms mediated by each kinetochore and the mitotic spindle. It is these mechanisms that ensure accurate and robust chromosome segregation during mitosis. Kinetochore-oscillations offer a method for assessing the mitotic segregation machinery of the cell on a system-wide level. Measurements of kinetochore dynamics in human cells during metaphase were made using a HeLa-K cell line stably expressing fluorescent markers for kinetochores (eGFP-CENPA) and spindle-poles (eGFP-Centrin1). Live cell 4D movies (3D + time) of cells in metaphase were collected; kinetochore dynamics were extracted from movies by a high spatio-temporal resolution automatic high-throughout kinetochore-tracking assay. A precursor assay was used in a previous kinetochore dynamics study [96]. Here the methodology was substantially upgraded including the use of a diffraction-limited fluorescent spot-fitting algorithm that gave kinetochore positions to sub-light resolution accuracy. High-throughput data analysis allowed for a large set of kinetochore-trajectories to be gathered covering a wide-range of dynamic behaviour without introducing observer-bias. The use of a high-throughput data analysis methodology is essential in many areas of biological-study especially image analysis where individual samples tend to exhibit only a small set of possible dynamics and / or are contaminated by substantial noise. Automatic feature-tracking of fluorescently-tagged structures in

image-series represents a key technology for biological research. Feature dynamics can be extracted quickly without any human-based bias that could be introduced by manual image analysis. Robust behavioural-models of the dynamics can be used to aid the extraction of information, for instance: model-based spot fitting (Section 3.4), metaphase-plate fitting (Section 3.5) and trajectory-gap filling (Section 3.11). Care must be taken however to not use models that are too restrictive and therefore bias the feature-tracking to only objects displaying a sub-set of possible dynamics. A high-throughput information extraction methodology was implemented to infer mechanical and kinetic parameters of sister trajectories, linking high resolution tracking to model-fitting. A principled Bayesian methodology was followed for model-fitting, ensuring that model complexity is appropriate for the data type *i.e.* all parameters could be estimated for each trajectory (using nocodazole treatment to estimate the natural spring length). The model in (4.2) is thus necessarily simple but incorporates sufficient biological mechanisms to explain the observed dynamics in the trajectory data. The model demonstrates that oscillations arise from basic principles whilst also indicating that trajectory data can be used to extract biologically relevant information (force decomposition, switching times and switching biases) that allows underlying mechanisms to be inferred. In essence models such as these and their associated fitting algorithms are powerful analysis tools for scrutinising such data. These models are not however designed to explain dynamics at a high-level of mechanistic detail, detail that is included in many previous models [118, 138, 141, 156]. The latter models, for instance incorporating the kinetochore sleeve [120], demonstrate how order *e.g.* oscillations can emerge from dynamics at the microscopic / mesoscopic scale; however their complexity prevents a direct fitting to trajectory data *i.e.* the model parameters could not be completely determined directly from trajectory data.

A key result from this study is the inference of an active trailing (AP moving) sister-kinetochore during an oscillation; moving due to the influence of a force that has a magnitude on average 30% that of the force acting on the leading sister-kinetochore. Consequences of active trailing kinetochores can be seen from the inferred inter-kinetochore spring forces, post switching events; specifically during the incoherence period after an LSE there is a point where the (average) spring force becomes negative (Figure 5.17b (untreated) and Figure 6.6a (control siRNA)), indicating compression of the spring

below its natural length. Dynamics of this kind are explained by both kinetochores actively moving AP and pushing against each other during a switching event. Note that for the majority of the time the spring is under tension *i.e.* stretched above its natural length due to the simple fact that the leading kinetochore moves faster than the trailing kinetochore ($|v_-| > |v_+|$). This conclusion, that of an active trailing kinetochore but a resultant inter-kinetochore connection under tension, was presented by a previous study [168]; however the authors described trailing kinetochore dynamics as so: "the majority of AP movement occurs while the kinetochore is under tension, and therefore not actively pushing". This work contradicts that conclusion since the magnitude of the inferred polymerisation force acting on the trailing kinetochore is much greater than that resulting from the action of the inter-kinetochore spring (Figure 5.16a), therefore the main source of force acting on the trailing kinetochore according to this study is the intrinsic polymerisation force pushing the kinetochore anti-poleward. Previous work however has suggested that trailing kinetochores are not active and are simply pulled passively by the active leading sister. These conclusions were based on: laser microsurgery experiments where severing the linkage between sister-chromatids resulted in the trailing kinetochore stalling and then reversing direction (moving poleward), while the leading kinetochore continued moving towards its pole [128]; and that only on the leading kinetochore is the action of a force evident due to intra-kinetochore stretch [100]. If the trailing kinetochore is passively pulled by the leading kinetochore then the observed decrease in inter-kinetochore distance and ultimate compression of the spring post LSE would require a dominant PEF with a large gradient across the metaphase plate. This follows from the fact that the rate of change of the inter-sister distance does not decrease as the spring approaches the point of compression (Figure 5.17a), which would follow from the dynamics being driven by the spring itself. Previous studies have however concluded that the PEF and its gradient are low across the metaphase plate [127, 130], suggesting that switching dynamics are not driven by the PEF and arguing against the passive trailing kinetochore hypothesis. In addition a high PEF across the metaphase plate would be expected to cause chromosomes to move quickly when crossing the plate, which is contrary to observed motion of aligned chromosomes [90]. In conclusion this study suggests that during an oscillation the main source of force acting on a trailing kinetochore is its polymerising K-fibre actively

pushing it anti-poleward. Contradictions to previous studies that suggest trailing kinetochores are passive warrant further examination; preliminary explanations can be put forward here however. Observations of trailing kinetochores stalling and reversing direction after being artificially separated from their sisters by laser microsurgery [128] could be explained by an induced directional switch. Clearly any protein / chemical control circuitry setup between sister-kinetochores would be severely disrupted by artificial separation, the results of which can only be guessed at given the almost complete lack of any knowledge or understanding of such chemical factors. A study of intra-kinetochore stretch during oscillations inferred that the leading kinetochore is acted upon by a force, but the trailing is not [100]. However the full effects of applied force on the protein architecture of a kinetochore are currently not properly understood and have not been directly tested, either *in vivo* or *in vitro* therefore inference of applied force based on *in vivo* intra-kinetochore measurements at the present time must be treated with some scepticism.

The presence of both active leading and trailing kinetochores results in a switching choreography that is distinct from that in a force-balance model *i.e.* a tug-of-war mechanism. Under a tug-of-war mechanism the net direction of a chromosome during an oscillation is determined by which kinetochore has the greater magnitude of poleward directed forces, therefore once the leading kinetochore looses its poleward drive both kinetochores change direction concurrently. Models that apply tug-of-war force balance [118, 132, 138, 169] are therefore not supported by this study; directional switching occurs in these models due to a load-dependent loss of depolymerising microtubules from the leading K-fibre. Once the leading kinetochore looses sufficient microtubules the trailing kinetochore automatically switches direction due to the applied force from its K-fibre towards the corresponding spindle-pole. In contrast, this study indicates that directional switching comprises an explicit directional reversal of both kinetochores, the leading kinetochore from a depolymerising to a polymerising state and vice versa for the trailing kinetochore. Ultimately the data gathered in this study supports the hypothesis that directional switching is regulated by a force sensing mechanism with communication occurring between sister-kinetochores through the small but significant forces felt through their connecting spring. Specifically the data suggests that the leading kinetochore switches predominantly under a fractional force

change in the centromeric spring of 0.5 over 10s (Figure 6.6c) *i.e.* a tension-rate sensor that adapts to changes in force over time. This model contrasts with a previous model of directional switching control that proposed that switching is initiated by reaching a threshold tension in the centromeric spring, similar to force-induced protein unfolding / dissociation [90, 91, 99, 127]. Under this model the leading kinetochore switches direction due to a relatively high threshold tension value and subsequently the trailing kinetochore switches direction due to a relatively low threshold tension value. Another key result from the study that contradicts this previous model is the observation that the leading kinetochore is not always the first to initiate a directional switch, trailing kinetochore switching first occurs in approximately 10% of cases (untreated cells). A similar observation was made in a previous study [100] without however offering an hypothesis for how trailing kinetochore first switching occurs; the data presented here however does suggest a mechanism for trailing kinetochore initiated switching. The key observation is that directional switches still occur even when the tension-rate sensor is severely inhibited by a reduction in the stiffness of the centromeric spring by CAPD2 depletion, the difference being that under CAPD2 depletion the proportions of leading- and trailing-initiated switches are nearly equal (Figure 6.2b). Thus in addition to the tension-rate sensor two other mechanisms are proposed, force stabilisation of polymerising microtubules [46, 88] and an age dependent increase of catastrophe [164, 170, 171]. Thus two possible switching pathways are resultant, lead-first switching and trail-first switching.

**Lead-first switching**

Over a period of coherence between the sisters the faster leading kinetochore ($|v_-| > |v_+|$) causes an increase in the spring tension that stabilises the trailing kinetochore's K-fibre against catastrophe and hence prevents the trailing kinetochore from switching direction. Eventual tension build-up fires the tension-rate sensor causing the leading kinetochore to switch direction, the adaptive nature of the sensor preventing premature activation due to thermal fluctuations in the spring. Once the leading kinetochore switches to polymerisation the spring tension quickly drops, removing the stabilising effect on the trailing kinetochore. The trailing kinetochore's K-fibre quickly becomes unstable due to its age (its last switch was $\sim$ 30s ago) and switches direction. Note that the recently switched

leading kinetochore that is now the new trailing kinetochore has a relatively 'young' polymerising K-fibre and hence is protected against rapid direction reversal while under relatively low tension at the beginning of the new coherent period of oscillation. This property addresses an outstanding question in the field, that of how a newly switched kinetochore now in a trailing / polymerising state is prevented from rapid switching; a serious flaw in the simple lead-sister high-tension / trail-sister low-tension switching model.

**Trail-first switching**

The rate of build-up of spring tension during a coherent period is lower (Figure 6.6d), possibly due to obstacles in the chromosome path or other stochastic events. The lower tension fails to stabilise the trailing kinetochore's K-fibre while the lower rate fails to switch the leading kinetochore. Therefore the trailing kinetochore switches first due to the K-fibre age dependent catastrophe rate; leading kinetochore switching then follows due to the sudden rapid increase in tension in the centromeric spring that fires the tension-rate sensor. Note that the new leading kinetochore does not rapidly switch back under high tension since the newly established rate-sensor will take $\sim$ 10s to establish a rate measurement.

Under CAPD2 depletion the weaker centromeric spring fails to generate a fast enough increase in tension required to fire the tension-rate sensor. Since the spring force is actually higher under CAPD2 depletion (Figure 6.6a,b) (due to the higher inter-sister distance) the trailing kinetochore's K-fibre is stabilised against switching. Since both switching pathways are delayed the sister-pair remains in a coherent state for longer; hence the longer oscillation period (Figure 6.1e). Eventual switching is stochastic between lead- and trail-first dynamics with a slight bias toward lead-first possible due to a small component of the tension-rate sensor firing; the second kinetochore then switches due to the mechanisms described previously. A key feature of the multi-layered switching mechanism proposed here is the fact that the tension-rate sensor is robust to high-frequency fluctuations in centromeric spring tension, preventing premature directional switches; while the absolute magnitude of the spring force is low compared to the K-fibre forces, preventing premature separation of sister-chromatids pre-anaphase.

Further studies will warrant the integration of additional kinetochore behaviours into this model-based analysis framework, for instance including lead-sister deformations [100], the protein composition of the kinetochore [57, 59] and the status of K-fibre dynamics [27] thus allowing a quantitative understanding of how kinetochores control chromosome movement. Identifying the protein components of the tension-rate sensor is now a major objective whilst additional work is needed to determine how they sense the rate of tension change and how this leads to changes in microtubule dynamics. Finally this work demonstrates how monitoring the rate-of-change and not simply the threshold of a molecular event can be used to control a cell biological process. This has broad implications for how control mechanisms are analysed throughout biological systems.

# References


[27] J Tirnauer et al. "EB1 targets to kinetochores with attached, polymerizing microtubules". In: *Mol Biol Cell* 13.12 (Dec. 2002). 1059-1524 (Print) Journal Article, pp. 4308–16.

[46] Bungo Akiyoshi et al. "Tension directly stabilizes reconstituted kinetochore-microtubule attachments". In: *Nature* 468.7323 (Nov. 2010), pp. 576–9.

[57] Jason Stumpff et al. "The Kinesin-8 Motor Kif18A Suppresses Kinetochore Movements to Control Mitotic Chromosome Alignment". In: *Dev Cell* 14.2 (Feb. 2008), pp. 252–62.

[59] Ana C Amaro et al. "Molecular control of kinetochore-microtubule dynamics and chromosome oscillations". In: *Nat Cell Biol* (Mar. 2010).

[88] R. B. Nicklas. "The forces that move chromosomes in mitosis". In: *Annu Rev Biophys Biophys Chem* 17 (1988), pp. 431–449.

[90] R. V. Skibbens, V. P. Skeen, and E. D. Salmon. "Directional instability of kinetochore motility during chromosome congression and segregation in mitotic newt lung cells: a push-pull mechanism". In: *J Cell Biol* 122.4 (Aug. 1993), pp. 859–75.

[91] R.V. Skibbens, C.L. Rieder, and E.D. Salmon. "Kinetochore motility after severing between sister centromeres using laser microsurgery: evidence that kinetochore directional instability and position is regulated by tension". In: *Journal of Cell Science* 108.7 (1995), pp. 2537–2548.

[96] Khuloud Jaqaman et al. "Kinetochore alignment within the metaphase plate is regulated by centromere stiffness and microtubule depolymerases". In: *J Cell Biol* 188.5 (Mar. 2010), pp. 665–79.

[99] Xiaohu Wan et al. "The coupling between sister kinetochore directional instability and oscillations in centromere stretch in metaphase PtK1 cells." In: *Molecular biology of the cell* (Feb. 2012).

[100] S. Dumont, E. D. Salmon, and T. J. Mitchison. "Deformations within moving kinetochores reveal different sites of active and passive force generation". In: *Science* 337.6092 (July 2012), pp. 355–358.

[118] Ajit P Joglekar and Alan J Hunt. "A simple, mechanistic model for directional instability during mitotic chromosome movements". In: *Biophysical Journal* 83.1 (July 2002), pp. 42–58.

[120] T L Hill. "Theoretical problems related to the attachment of microtubules to kinetochores". In: *Proc Natl Acad Sci USA* 82.13 (July 1985), pp. 4404–8.

[127] CL Rieder and ED Salmon. "Motile kinetochores and polar ejection forces dictate chromosome position on the vertebrate mitotic spindle". In: *The Journal of Cell Biology* 124.3 (1994), pp. 223–233.

[128] A Khodjakov and C L Rieder. "Kinetochores moving away from their associated pole do not exert a significant pushing force on the chromosome." In: *The Journal of Cell Biology* 135.2 (1996), pp. 315–327.

[130] K. Ke, J. Cheng, and A. J. Hunt. "The distribution of polar ejection forces determines the amplitude of chromosome directional instability". In: *Curr. Biol.* 19.10 (May 2009), pp. 807–815.

[132] G Civelekoglu-Scholey et al. "Model of chromosome motility in Drosophila embryos: adaptation of a general mechanism for rapid mitosis". In: *Biophysical Journal* 90.11 (June 2006), pp. 3966–3982.

[138] G. Civelekoglu-Scholey et al. "Dynamic bonds and polar ejection force distribution explain kinetochore oscillations in PtK1 cells". In: *J. Cell Biol.* 201.4 (May 2013), pp. 577–593.

[141] Blerta Shtylla and James P Keener. "A mechanomolecular model for the movement of chromosomes during mitosis driven by a minimal kinetochore bicyclic cascade". In: *Journal of theoretical biology* 263.4 (Apr. 2010), pp. 455–470.

[156] Blerta Shtylla and James P. Keener. "A Mathematical Model for Force Generation at the Kinetochore-Microtubule Interface." In: *SIAM Journal of Applied Mathematics* 71.5 (2011), pp. 1821–1848.

[164] M. K. Gardner et al. "Depolymerizing kinesins Kip3 and MCAK shape cellular microtubule architecture by differential control of catastrophe". In: *Cell* 147.5 (Nov. 2011), pp. 1092–1103.

[168] J. C. Waters, R. V. Skibbens, and E. D. Salmon. "Oscillating mitotic

newt lung cell kinetochores are, on average, under tension and rarely push". In: *J. Cell. Sci.* 109 ( Pt 12) (Dec. 1996), pp. 2823–2831.

[169] G. Gay et al. "A stochastic model of kinetochore-microtubule attachment accurately describes fission yeast chromosome segregation". In: *J. Cell Biol.* 196.6 (Mar. 2012), pp. 757–774.

[170] D. J. Odde, L. Cassimeris, and H. M. Buettner. "Kinetics of microtubule catastrophe assessed by probabilistic analysis". In: *Biophys. J.* 69.3 (Sept. 1995), pp. 796–802.

[171] T. Stepanova et al. "History-dependent catastrophes regulate axonal microtubule behavior". In: *Curr. Biol.* 20.11 (June 2010), pp. 1023–1028.

# Appendix: Published and Submitted Work

**E. Vladimirou et al. "Springs, clutches and motors: driving forward kinetochore mechanism by modelling". In: *Chromosome Res.* 19.3 (Apr. 2011), pp. 409–421**

Chromosome Res (2011) 19:409–421
DOI 10.1007/s10577-011-9191-x

# Springs, clutches and motors: driving forward kinetochore mechanism by modelling

**Elina Vladimirou · Ed Harry · Nigel Burroughs · Andrew D. McAinsh**

Published online: 18 February 2011


**Abstract** As a mechanical system, the kinetochore can be viewed as a set of interacting springs, clutches and motors; the problem of kinetochore mechanism is now one of understanding how these functional modules assemble, disassemble and interact with one another to give rise to the emergent properties of the system. The sheer complexity of the kinetochore system points to a future requirement for data-driven mathematical modelling and statistical analysis based on quantitative empirical measurement of sister kinetochore trajectories. Here, we review existing models of chromosome motion in the context of recent advances in our understanding of kinetochore molecular biology.

**Keywords** chromosome directional instability · kinetochores · mathematical modelling · microtubule · mitosis

Responsible Editors: James Wakefield and Herbert Macgregor

E. Vladimirou · E. Harry · A. D. McAinsh (✉)
Centre for Mechanochemical Cell Biology, Warwick Medical School, University of Warwick, Coventry, UK
e-mail: andrew@mechanochemistry.org

E. Harry
Molecular Organisation and Assembly in Cells (MOAC) Doctoral Training Centre, University of Warwick, Coventry, UK

E. Harry · N. Burroughs
Warwick Systems Biology Centre, University of Warwick, Coventry, UK

**Abbreviations**

| | |
|---|---|
| AP movement | Anti-poleward movement |
| ATP | Adenosine triphosphate |
| DIC | Differential interference contrast |
| GTP | Guanosine triphosphate |
| J&H | Joglekar and Hunt |
| k-fibre | Kinetochore fibre |
| kMT | Kinetochore microtubule |
| MTs | Microtubules |
| P movement | Poleward movement |
| PEF | Polar ejection force |
| 3D | Three dimensional |

## Introduction

Mitosis, the set of processes by which sister chromatid pairs are first captured by spindle microtubules, shuttled into a central position (in metaphase) and subsequently segregated to opposite poles of the cell (in anaphase), is fundamental to all eukaryotic life. This complex series of movements is to a large extent driven by kinetochores, which are adaptive, multilayered mechanochemical machines that assemble at the centromere of each sister chromatid and engage the plus ends of k-fibres, bundles of around 20–25 kinetochore microtubules (kMTs) that emanate from the spindle poles (for review see Cleveland et al. 2003; McAinsh et al. 2003; Santaguida and Musacchio 2009). The connections between k-fibres and kineto-

chores are remarkable in that they allow kinetochores to grip and to exert force on k-fibres during both the growth and shrinkage phases of the k-fibre (Joglekar et al. 2010). Incisive experiments using video-enhanced DIC microscopy made over 17 years ago revealed that once sister kinetochores become attached to MTs emanating from opposite poles (biorientation), they undergo a series of oscillations (Hughes and Swann 1948; Lewis 1939) that involve periods of poleward (P) and anti-poleward (AP) movement at constant velocity—a process termed chromosome directional instability (Skibbens et al. 1993). Recently, single-particle tracking algorithms and fluorescent protein reporters have been deployed to systematically track the 3D position of multiple sister kinetochore pairs over time in living human cells (Jaqaman et al. 2010) revealing semi-regular oscillations indicative of stochasticity in the switching mechanisms (Fig. 1a, c). During oscillations, the sister pair also move towards and away from one another (breathing), and the kinetochore itself undergoes internal deformation between the inner and outer plates (stretching; Maresca and Salmon 2009; Uchida et al. 2009). These oscillations, breathing and internal stretching reflect the adaptive switching of the kinetochores between two different structural and functional states: one that is bound to growing MTs undergoing AP movement, i.e. the trailing sister and one that binds depolymerising MTs undergoing P movement, i.e. the leading sister.

The chromosome–kinetochore–kMT assembly can be viewed as a set of interacting springs, clutches and motors. The physical linkage between the sister kinetochores via centromeric chromatin is generally regarded to be a flexible elastic connection (Nicklas 1988). Consistently, the cross correlation of the two biorientated sisters as they oscillate back and forth during metaphase shows fairly tight, but not complete, motion coupling (Jaqaman et al. 2010). There is, however, evidence that the centromeric linkage is plastic, although this may depend on the attachment state of the kinetochores (i.e. syntelic; Loncarek et al. 2007). In addition the, inherent multi-layered nature of the kinetochore and the observed conformation changes within the structure (Wan et al. 2009) could be thought of as constituting a second flexible elastic connection. In effect, the kinetochore–kMT attachment functions as a dynamic mechanical connection or "molecular clutch" mediated by proteins that can form physical contacts with the microtubule lattice. An attractive hypothesis is that kinetochores translate the forces generated by GTP hydrolysis-dependent growth and shrinkage of kMTs into chromosome movements, essentially rectifying MT dynamic instability into useful work. The regularity of oscillations indicates that kinetochores control force generation through regulation of kMT dynamics. Additional forces are generated by kinetochore-bound plus-end and minus-end translocating ATP-dependent molecular motor proteins directly exerting force on kMTs (Sharp et al. 2000) while external forces within the mitotic spindle also influence kinetochore (chromosome) motion. Most notably, the polar ejection force (PEF) pushes chromosome arms away from the spindle pole whilst depolymerisation of MTs at their minus-ends (spindle pole) generates poleward MT flux, which exerts a poleward force on the chromosome. The PEF is generated by chromosome-bound chromokinesin motors or by polymerizing MTs striking the chromosome arms (Kapoor and Compton 2002). Changes in spindle pole position and the forces exerted by the spindle as a whole also need to be considered (for review see Dumont and Mitchison 2009). Given the level of mechanical complexity in the system and the high degree of coupling between the different components, we will need mathematical models to identify concepts, determine dependencies, integrate multiple datasets consisting of empirical observations and generate novel and testable hypotheses. Here, we set out to review existing models of chromosome directional instability in mammalian cells, relate these models to recent experimental advances and discuss where future efforts are needed.

## Force and feedback

There have been a number of mathematically based studies that demonstrate kinetochore oscillations, which can arise from a number of mechanisms; the key requirements are a spatially dependent force and a feedback process. In essence, as kinetochores move away from the metaphase plate, a restoring force is needed. This is provided by the PEF that increases in strength near the pole, thus increasing the anti-poleward force. However, without a feedback

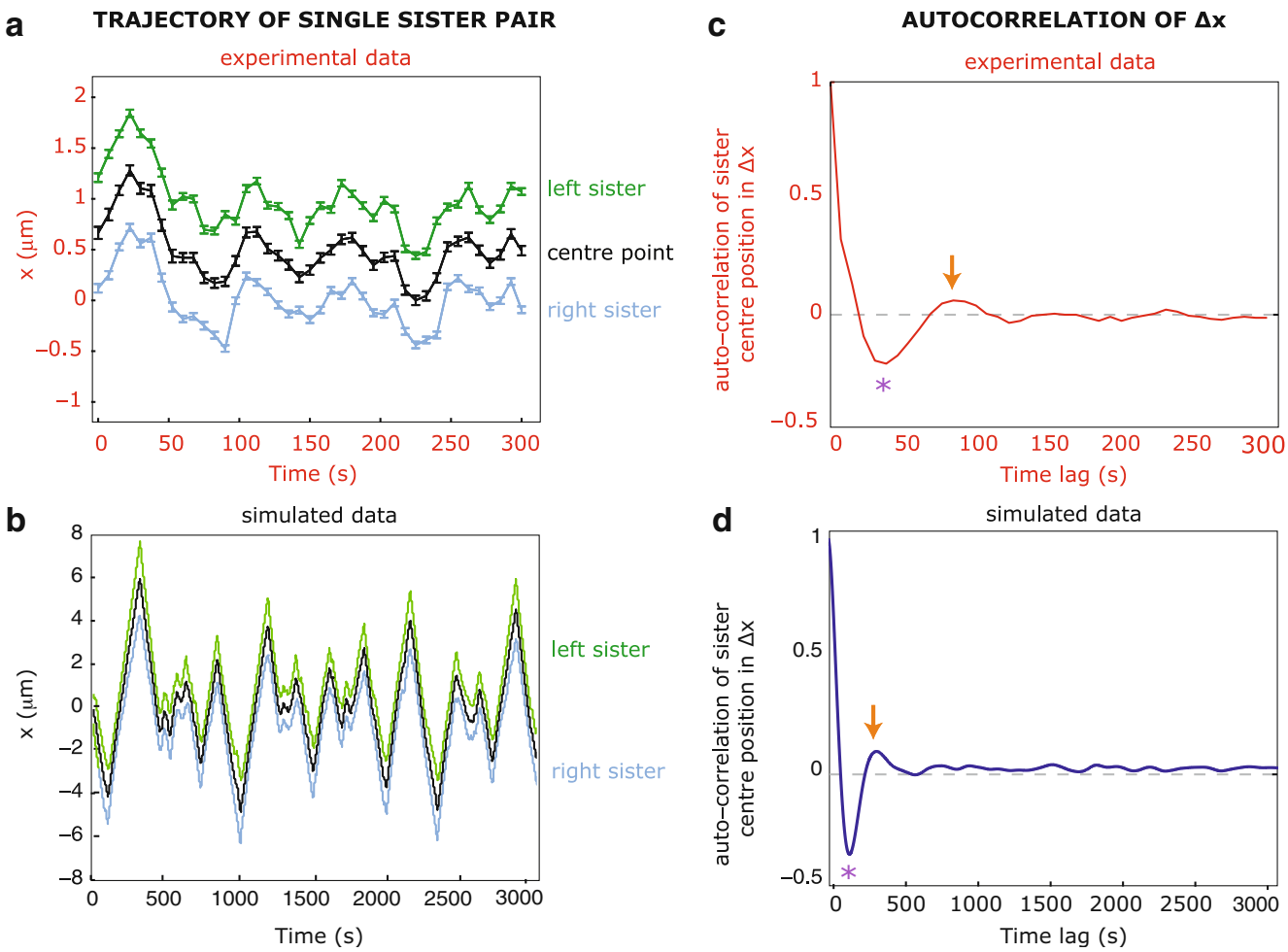


**Fig. 1** Comparison of experimental and simulated data of sister kinetochore oscillations in metaphase. **a** Trajectory of a single sister kinetochore pair undergoing oscillations along the normal ($x$) to the metaphase plate. Coordinate positions of right (*blue line*) and left (*green line*) sisters plus the centre point between them (*black line*) are from experimental data of kinetochores in human HeLa cells (Vladimirou and McAinsh, unpublished data). **b** Trajectory of a single sister kinetochore pair undergoing oscillations in metaphase. Data was simulated using the mathematical model from Joglekar and Hunt 2002, which is largely based on parameters from PTK-1 cells, hence the longer timescale for oscillations compared to human cells. **c, d** Autocorrelation of the centre positions of sister pairs from experimental (50 trajectories; *red line*; **c**) and simulated data (100 trajectories; *blue line*; **d**). The half period (*purple star*) and full period (*orange arrow*) of the oscillation in the autocorrelation curves are indicated

mechanism, this would position the chromosomes stably at the metaphase plate. The models vary fundamentally in whether they incorporate MT dynamic instability, i.e. as a two-state growth/catastrophe model or assume full regulation of MT growth processes by the kinetochore. Most of these models use force balancing either in a set of differential equations or in a mesoscopic simulation model. At the subcellular level viscous forces dominate and inertial effects are negligible, thus all the forces acting on the object can be equated to the viscous drag term that is proportional to velocity. This can be particularly useful as it can be used to calculate the system's position using the condition that the forces must balance. Force balance models have been used extensively in a biological context. For example, a force balance model was developed to explain force generation by polymerising actin filaments (Mogilner and Oster 2003). Also, the steady state pole separation during the early stages of spindle morphogenesis in *Drosophila* embryos was modelled by a force–balance differential equation complemented by equations describing the distribution of MTs, motors and

forces (Cytrynbaum et al. 2003). The assumptions and principles needed to develop such a force–balance model are summarised in box 1 and are described further in (Howard 2005).

**Box 1:** Modelling chromosome directional instability using a force-balance approach

***Step 1: Assumption of overdamped dynamics:*** The equation of motion is given by $m\,d^2x/dt^2 + \gamma\,dx/dt + k\,x = F$ where the first (inertial) term is Newton's second law (the acceleration of a mass is proportional to the force applied to it), the second term is due to viscous forces ($\gamma$ is the drag coefficient and is dependent on the size and the shape of the object as well as the fluid's viscosity) and the third term is due to elastic forces (Hooke's law, the force an object will experience when connected to a spring of stiffness k extending a distance x beyond its resting length $x_0$). F can be any other externally applied force. The above equation can describe a system that can display monotonic or oscillatory motion depending on the strength of the damping. When a microscopic system is strongly damped, the inertial term can be ignored and the equation of motion reduces into $\gamma\,dx/dt + k\,x = F$.

***Step 2: Identifying the antagonistic forces acting on the system:*** All the forces acting on the object are either spring-like (kx) depending on position or of another functional form (F) that may depend on position and/or time. For example the force due to an elastic attachment between one kinetochore and another would depend on the position of the kinetochore relative to the other (kx form). An example of an external force might be due to a molecular motor and could have a stochastic form depending on time. In any case, the net force is opposed by an equal drag force.

***Step 3: Solving the equality to get the system's position and velocity in time as a response to the changing forces:*** In a complex, multicomponent system such as the kinetochore-kMT mechanical unit, predicting the response of the system to the applied forces is not straight forward. By using the assumption that $F - k\,x - \gamma\,dx/dt = 0$ at each point in time and space, this differential equation can be solved to determine the velocity dx/dt and the position x satisfying the force-balance.

## Kinetochore–microtubule attachment complex

For mammalian systems the model of Joglekar and Hunt 2002—from here on called J&H—best reflects our current understanding of how kinetochores work (Gardner and Odde 2006). The heart of the model is a simple force–balance equation between the forces exerted on kinetochores by attached microtubules and the PEFs acting on the chromosome arms (Fig. 2a). This model is built on the work of Terrell Hill, who developed a beautiful model that describes how a kinetochore may follow a depolymerising MT, with the kinetochore being theorised as a sleeve containing binding sites distributed at equal distances (Hill 1985). The length of a sleeve is assumed to be 40 nm, which is the thickness of the outer plate of a kinetochore based on electron micrographs (Brinkley et al. 1992). Since each tubulin heterodimer is 8 nm long, five dimers can penetrate the sleeve lengthwise, and since a microtubule is made up of 13 protofilaments circularly arranged, $5\times13=65$ tubulin dimers can enter a sleeve. There are, therefore, an estimated 65 binding sites per sleeve. As a MT enters a sleeve, it forms more and more bonds lowering the total free energy, so MT movement will be biased to entering the sleeve (Fig. 2b). However, moving further into the sleeve requires breaking all the previously formed bonds, so there is an ever increasing energy barrier for the MT to overcome. A microtubule can move relative to a sleeve either by depolymerising or by the sleeve moving by (forced) diffusion. In the J&H model, the kinetochore sleeves are connected to the chromosome through springs that generate a restoring potential to reposition the sleeve near the chromosome. The MT plus-end position in a sleeve is, therefore, affected by the load on the chromosome and the polymerisation state of the kMT, with a high pulling load tending to move the MT further out of the sleeve (Fig. 2c). The overall result is that a sleeve will shift its position on a MT to balance its free energy against its restoring load. This energy balance endows the sleeve with a crucial property; sleeves tend to follow a depolymerising MT at *a constant rate* until the restoring load causes the sleeve to stall and the MT quickly detaches.

Experimental evidence for such a sleeve structure is growing: The core microtubule binding site in the vertebrate kinetochore is composed of the KNL-1 protein and two 4-subunit protein complexes—Ndc80 and Mis12/MIND—which through multiple protein–protein interactions constitute the KMN network (Cheeseman et al. 2006). The Ndc80 complex can directly bind MTs with low affinity (~3 μM; Wei et al. 2006; Cheeseman et al. 2006). KNL-1 has also been shown to bind to MTs but with very low affinity (Cheeseman et al. 2006), thereby necessitating further

work to define its direct involvement in kinetochore–kMT attachment. Nevertheless, reconstitution of the full KMN network does lead to a synergistic increase in MT binding affinity to ~0.5 μM (Cheeseman et al. 2006). Recent structural studies now show that the Ndc80 complex can bind to both inter- and intra-tubulin dimer interfaces (Alushin et al. 2010). The Ndc80 complex can also self-assemble forming oligomeric arrays via inter-complex interactions suggesting that it could mediate multiple kinetochore–MT interactions (Alushin et al. 2010). Consistently, Salmon and colleagues demonstrated that in vivo there are at least ten copies of Ndc80 complex per microtubule in vertebrates (Johnston et al. 2010; Fig. 2b). Additional binding sites could be provided by the Ska complex, which can oligomerise and form ring-like structures on MTs in vitro with a binding affinity of ~0.3 μM (Welburn et al. 2009). Together, these could provide the tens of binding sites that would be organised into a sleeve-like structure as proposed by Hill. Importantly, both the Ska and Ndc80 complexes have both been shown, in optical trapping experiments, to couple a plastic bead to a depolymerising MT, with the Ndc80 complex being able to form load-bearing attachments (Welburn et al. 2009; Powers et al. 2009). At the same time, there are a multitude of molecular motors, MT-associated proteins and plus-end tracking proteins that could contribute to the interaction surfaces within the kinetochore (for review see Maiato et al. 2004). Thus, molecular evidence supports the idea that a kinetochore sleeve that incorporates multiple low-affinity binding sites (see model in Fig. 2b) can operate as a "molecular clutch" to couple MTs to the chromosome. However, modelling this complex structure and specifically its kinetics and characteristics (elasticity, energy barriers, inter-sleeve connectivity, effects on kMT (de)polymerisation and dynamic instability, length constraints) has proceeded little since the original formulation.

To account for polymerisation of kMTs, J&H modified the Hill sleeve model as follows: During catastrophe, microtubules shrink much faster than kinetochores move, therefore only growing microtubules enter empty sleeves. Once inside a sleeve, the polymerising microtubule will switch to a depolymerising state (catastrophe) with a rate $k_{cat}$. During an oscillation, the leading sister will follow depolymerising kMTs poleward causing greater and greater load on the associated sleeves on the leading sister. The sleeves on the trailing sister attached to polymerising MTs are under low load as they are being led by the chromosome and any depolymerising kMTs are quickly lost out of the sleeves. In this configuration, the leading sister is 'pulling' the chromosome. This is supported by laser surgery experiments in which cutting kMTs of the trailing sister resulted in no change in the poleward velocity; however, cutting the kMTs of the leading sister resulted in the complete abolition of poleward movement (Khodjakov and Rieder 1996). We should also bear in mind that under certain situations the kinetochores can generate pushing forces through poleward microtubule flux (Toso et al. 2009) and that measurement of centromere deformation suggests that AP movement of a kinetochore can produce a pushing force (Skibbens et al. 1993). Eventually, the load on the leading sister's sleeves becomes too great and the depolymerising MTs detach from their sleeves. The other sister that has accumulated depolymerising MTs is now dominant and the chromosome starts to follow the new leading sister. This mechanism is consistent with exciting recent experiments on purified kinetochore particles showing that a threshold force (~4 pN) causes a decrease in the kinetochore particle–kMT attachment lifetime (Akiyoshi et al. 2010). Importantly, this work also shows that increasing the load up to this threshold actually stabilises attachments, a result that is consistent with experiments in living cells (Nicklas 1988). This mechanism is something that can be incorporated into modelling efforts (see discussion below).

The spatial gradient in the PEF is vital to this directional switch, providing the restoring force towards the spindle equator against which the leading sister competes. Since the PEF is proportional to the density of microtubules from the spindle, effectively a point source, it is reasonable to assume the force follows an inverse square distribution (PEF proportional to $1/x^2$ where $x$ is the distance from the poles), although other functional forms have been used suggesting that oscillatory behaviour is robust to its exact form. The role of the PEF in chromosomal directional instability has been tested in newt lung cells by severing the chromosome arms using femtosecond-pulsed lasers (Ke et al. 2009). While the main characteristics of directional instability, such as constant speed remained unaltered, shortening the

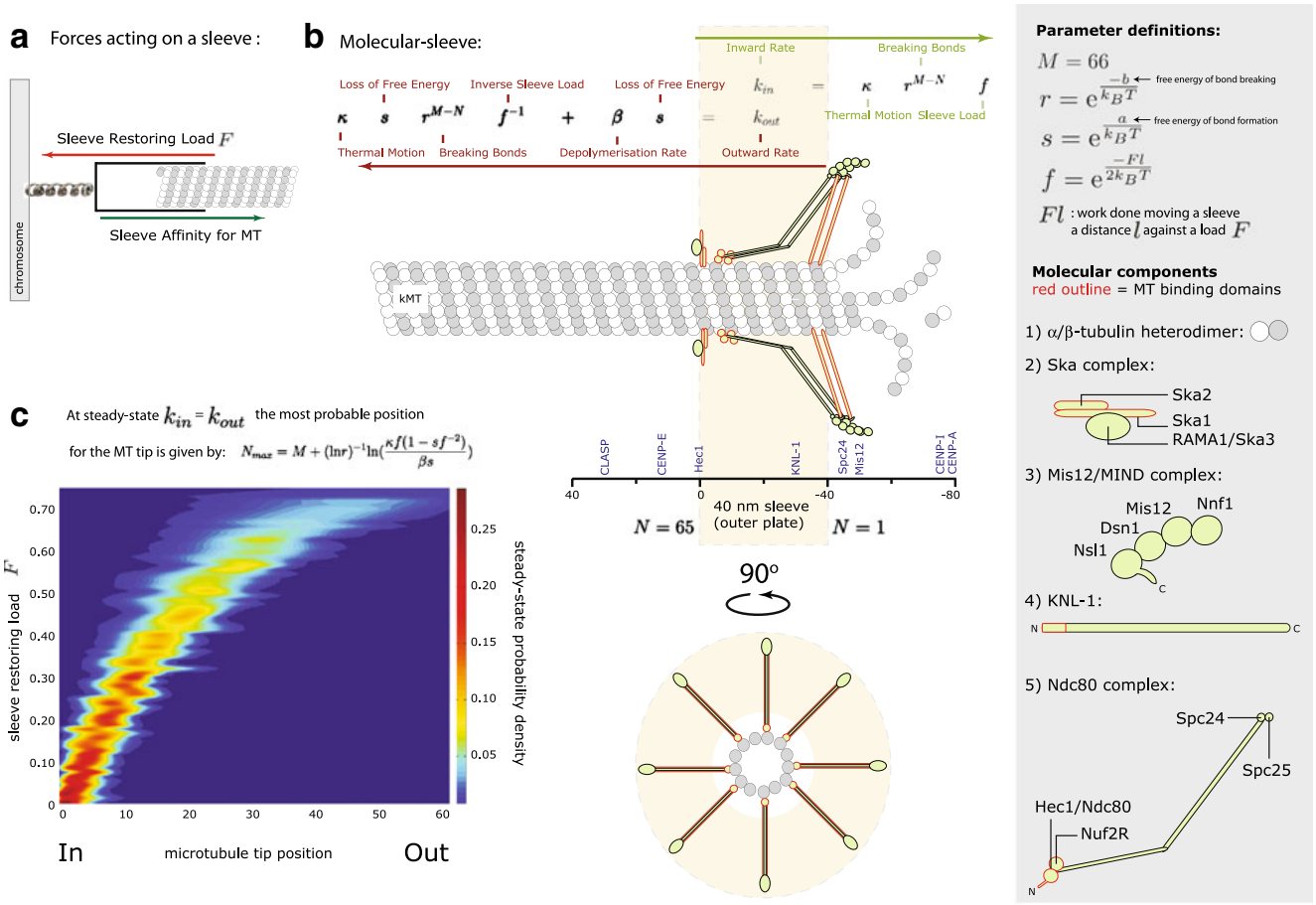
a Forces acting on a sleeve :
Sleeve Restoring Load F
Sleeve Affinity for MT
chromosome
b Molecular-sleeve:
Inward Rate
Breaking Bonds
Loss of Free Energy
Inverse Sleeve Load
Loss of Free Energy
Thermal Motion
Breaking Bonds
Depolymerisation Rate
Outward Rate
Thermal Motion
Sleeve Load
kMT
CLASP
CENP-E
Hec1
KNL-1
Spc24
Mis12
CENP-I
CENP-A
40
0
-40
-80
N = 65
40 nm sleeve
(outer plate)
N = 1
90°
c
At steady-state $k_{in} = k_{out}$ the most probable position
for the MT tip is given by: $N_{max} = M + (\ln r)^{-1} \ln(\frac{\kappa f(1-sf^{-2})}{\beta s})$
sleeve restoring load F
steady-state probability density
microtubule tip position
In
Out
Parameter definitions:
$M = 66$
$r = e^{\frac{-b}{k_B T}}$ ← free energy of bond breaking
$s = e^{\frac{a}{k_B T}}$ ← free energy of bond formation
$f = e^{\frac{-Fl}{2k_B T}}$
$Fl$ : work done moving a sleeve a distance $l$ against a load $F$
Molecular components
red outline = MT binding domains
1) α/β-tubulin heterodimer:
2) Ska complex:
Ska2
Ska1
RAMA1/Ska3
3) Mis12/MIND complex:
Mis12
Nnf1
Dsn1
Nsl1
C
4) KNL-1:
N
C
5) Ndc80 complex:
Spc24
Spc25
Hec1/Ndc80
Nuf2R
N

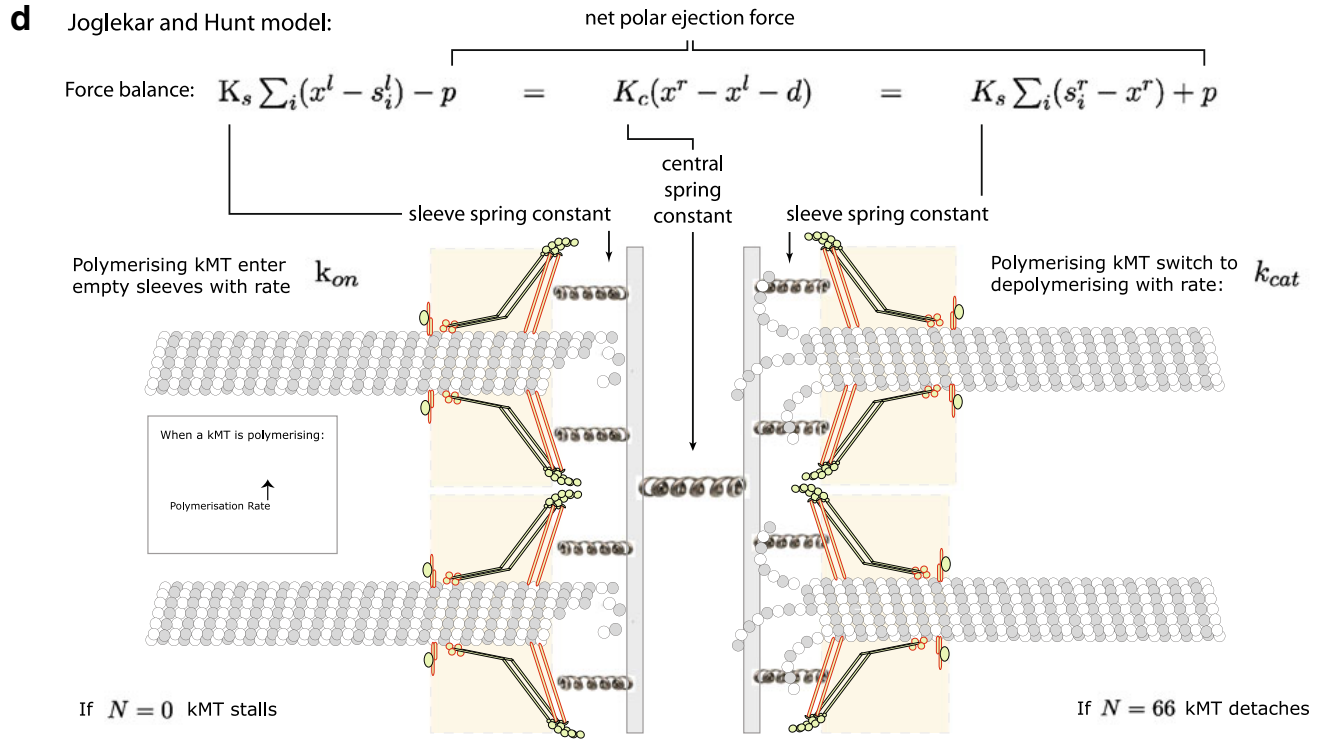
d Joglekar and Hunt model:
net polar ejection force
Force balance: $K_s \sum_i (x^l - s_i^l) - p = K_c(x^r - x^l - d) = K_s \sum_i (s_i^r - x^r) + p$
central spring constant
sleeve spring constant
sleeve spring constant
Polymerising kMT enter empty sleeves with rate $k_{on}$
Polymerising kMT switch to depolymerising with rate: $k_{cat}$
When a kMT is polymerising:
Polymerisation Rate
If $N = 0$ kMT stalls
If $N = 66$ kMT detaches

**Fig. 2** Hill sleeve and Joglekar and Hunt model. **a** A Hill sleeve balances its affinity for a MT (*green arrow*) against the restoring load (*red arrow*) pulling it back to the chromosome. **b** Contemporary view (*upper panel* from the side; *lower panel* is a 90° rotation showing end-on view) of a Hill sleeve. Binding sites inside the sleeve are shown as KMN networks and Ska complexes. These form multiple attachment sites for the MT as it penetrates into the sleeve, which is the outer plate of the kinetochore. The inward (*green arrow*) and outward (*red arrow*) movement rates of the MT are shown and depend on the position of the MT inside the sleeve and the restoring load on the sleeve. Position of kinetochore components within the kinetochore is based on super-resolution imaging and adapted from Wan et al. 2009. Subunit composition and organisation of complexes is based on Cheeseman et al. 2006; Maskell et al. 2010; Petrovic et al. 2010 and Wan et al. 2009. **c** A Monte Carlo simulation of the kMT tip position inside the sleeve gives the probability density distribution over position and load (based on rate equations from Joglekar and Hunt 2002). Higher loads on the sleeve increase the probability of MT tip shifting to positions further and further out of the sleeve. **d** The Joglekar and Hunt model is based on a force balance between the kinetochores, sleeves and polar ejection forces. The positions of the sleeves are determined by the kinetics of the sleeve-bound MT as determined by Hill's rate equations (Hill 1985). Polymerising MTs enter empty sleeves with a rate $k_{on}$ and switch to depolymerising with a rate $k_{cat}$. $N$ is the position of the MT tip inside the sleeve. When $N$=1 the MT is fully inserted, whereas the MT detaches from the sleeve when $N$=66

chromosome arms increased the average amplitude of oscillations indicating that the rate of directional reversals depends on the magnitude of PEF, specifically the load on the kinetochores, which is to be expected. The results lend support to the hypothesis that PEF is dependent on both the size of chromosome arms and microtubule density, and that kinetochores are responsive to external spindle forces, whilst providing experimental support for the J&H model. Ke et al. estimated the PEF distribution to increase sublinearly with the displacement $y$ from the spindle equator ($y^{0.57}$) suggesting that the PEF increases rapidly near the equator and flattens toward the poles These experimental data differ from the previously proposed inverse square law, and it remains to be tested how incorporation of such a PEF may affect the result of the simulation compared to experiment. Such a force profile could drive oscillations around the metaphase plate, but it is harder to see how this would provide a restoring force for a mono-orientated chromosome close to one spindle pole. Nevertheless, simulation of the J&H model using parameters estimated from Ptk1 and Newt lung cells is in good qualitative agreement with experimental data, reproducing key aspects of chromosome directional switching (Fig. 1b). Using an autocorrelation analysis (see box 2), these simulated oscillations are semi-regular with a half period of around 150 s (Fig. 1d)—a value that closely matches experimental measurements (Khodjakov and Rieder 1996). Importantly, the amplitude of the half and full period in the autocorrelation curve is very similar to that observed for sister kinetochore oscillations in human cells (Jaqaman et al. 2010 and compare with Fig. 1c). Thus, the J&H model is able to generate the key characteristics of this high-level emergent behaviour.

**Box 2:** Assessing oscillatory behaviour using the autocorrelation function

The autocorrelation function is commonly used to identify periodicity in a sequence of events by comparing the sequence to a time-lag version of itself (lag k). The lag k autocorrelation of discretely sampled data can be estimated by:

$$R(k) = \frac{1}{\sigma^2(n-k)} \sum_{t=1}^{n-k} (x_t - \mu)(x_{t+k} - \mu)$$

where $x_t$ is the value of observation at time t , μ is the mean and $\sigma^2$ the variance of the sample of observations. For example, a random process exhibits no periodic behaviour giving an autocorrelation that is zero up to stochastic noise.

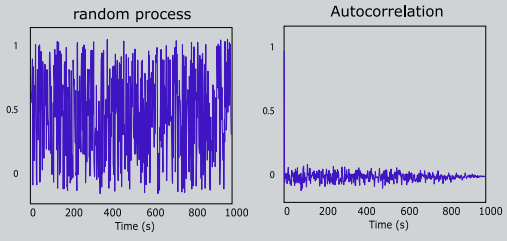


In contrast, the autocorrelation of a periodic signal, such as a sinusoidal wave, results in a plot where the first negative trough and the first positive peak represent the half and full period of the oscillation.

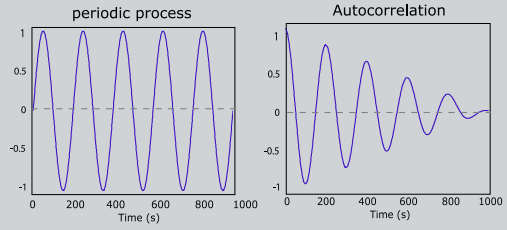


Autocorrelation is therefore a powerful statistical tool for analyzing and comparing oscillatory behaviors in biological systems (*e.g.* kinetochore trajectories) .

This agreement with experiment does not, however, mean that we now have a concrete mechanistic understanding of chromosomal directional instability. There are many missing behaviours and mechanisms that need to be incorporated. First, sister kinetochore pairs move in three dimensions (which can generate torque; Jaqaman et al. 2010), become stretched through forces generated by kMT dynamics (Maresca and Salmon 2009; Uchida et al. 2009) and are liable to effects from neighbouring chromosome (arms). Second, sister kinetochores undergo breathing that has a distinct period. Third, the catastrophe rate for kMTs is almost tenfold lower than that of non-kMTs in the spindle (Zhai et al. 1995) meaning that kinetochores must contain systems that slow kMT turnover. Indeed, inhibition of the aurora-B protein kinase causes a further reduction in the turnover rate (Cimini et al. 2006), whereas depletion of the CENP-A NAC/CAD kinetochore complex results in a kMT turnover rate indistinguishable from non-kMTs (Amaro et al. 2010). Moreover, the CENP-H and -I subunits of this complex are asymmetrically localised to the trailing (AP moving) kinetochore, and their depletion causes more frequent directional switches and irregular oscillations (Amaro et al. 2010). The integration of such a control system will be an important next step in developing models of chromosomal directional instability. Finally, the force generating effects of kinetochore-bound molecular motors and additional external spindle forces, such as poleward MT flux, need to be considered.

A model that incorporates molecular motors and includes the effects of poleward MT flux has been described (Civelekoglu-Scholey et al. 2006). At its conception, this model had the benefit of being composed of well-characterised components, and thus the model was more constrained than earlier models. The Civelekoglu-Scholey et al. model employs a force balance approach similar to the J&H model that is based on parameters and spindle organisation in *Drosophila* syncytial blastoderm embryos. It includes additional force terms, and separately considers force–balance for the kinetochores and for the kMT itself. For the case of the kinetochore, the force–balance equation includes terms for the viscous drag forces, the net force exerted by the antagonistic action of plus-end-directed (CENP-E) and minus-end-directed (dynein) motors stepping on the kMT lattice, the force of kMT polymerisation pushing on the kinetochore inner plate, the PEF (modelled as a quadratic function centred at the mitotic equator) and the inter-kinetochore tension (as in J&H). The presence of both minus- and plus-end-directed motors at a kinetochore generates a linkage to the kMT, one that has multiple binding sites and thus is similar to the Hill sleeve, although expends ATP when there is relative kMT motor movement. The well-characterised motor properties, i.e. load–velocity relationships, stall force and the maximum motor velocity essentially parametrise this ‘sleeve’ leaving only the number of motors per unit kMT length as free parameters. The above equation for the kinetochore is coupled to a force–balance equation for the kMT; this equation takes into account the net force generated at the plus end of the kMT engaged in the kinetochore i.e., the pulling force minus the pushing force and a balancing force due to poleward flux that is due to depolymerisation of minus-ends (at spindle poles) by depolymerisation motors. At the same time, kMT dynamic instability, i.e. stochastic switching between polymerising and depolymerising states, is incorporated. Importantly, the model includes a tension feedback in which the rates of rescue and catastrophe are modified by controlling the activity of the kinesin-13 depolymerase motor (KLP59C) through the tension acting on the kMT. This mechanism was successfully incorporated into the model of Odde and colleagues to explain chromosome congression in budding yeast (Gardner et al. 2005). Thus, when the kinetochore is under low tension, the catastrophe rate is high, driving poleward movement; when tension increases (due to PEF, cohesin stretching) then the depolymerase cannot act on the plus-end promoting switching to the polymerising state. In this way, kinetochores would “keep hold” of kMTs when under load. This aspect is consistent with the in vitro and in vivo work (described above) showing that kinetochore attachment improves with load (Akiyoshi et al. 2010; Nicklas 1988). At the mechanistic level, experimental work does support the idea that tension can regulate the activity of kinetochore components (for review see Lampson and Cheeseman 2010). However, to date, experiments show that tension may lead to the activation, rather than inactivation, of human kinesin-13 (MCAK). More work is needed to define these regulatory loops and relate the activity of MCAK and the related Kif2b to load variation. Kinesin-8 motors may also play a key role although it

is controversial as to whether human Kif18a is an MT depolymerase (Du et al. 2010; Mayr et al. 2007).

The above equations are solved numerically for varying numbers of kMT attachment sites. The model is able to reproduce both metaphase and anaphase (by simulating loss of cohesin) chromosome behaviour in *Drosophila* embryonic spindles, in which metaphase oscillations are barely detectable. The model can generate metaphase oscillations when the poleward flux rate is low and the kMT turnover rate is high enough (e.g. in budding yeast). The model cannot, however, account for oscillations in mammalian cells where the kMT turnover rate is slow. Moreover, the high dependence and role in the model on the CENP-E, dynein and MCAK molecular motors raises additional questions about the generality of the model. In human cells, depletion of CENP-E or MCAK has no effect on directional switching during metaphase (Jaqaman et al. 2010). In fact, data from human cells, instead, indicates that the depolymerising motors (MCAK and Kif18a) are required to set the speed of kinetochore movement (Jaqaman et al. 2010; Stumpff et al. 2008; Wordeman et al. 2007). Clearly, motors and sleeves must function together, and we need models to integrate these mechanisms of force generation with experimental data. Despite the modelling differences between J&H and Civelekoglu-Scholey et al., the kinetochore–kMT attachment models behave similarly, e.g. both give a load independent velocity suggesting that the fine detail is not crucial to emergent behaviour such as metaphase oscillations. Together with experimental work, these models support the idea that there are clearly different solutions to the "problem" of controlling chromosome motion in mitosis. Whilst the underlying mechanisms and components will be conserved, the functional dependency on them can (and does) vary between species. Both Civelekoglu-Scholey et al. and J&H provide important starting points for future efforts.

## Mechanochemical feedbacks

The last 5 years has seen limited advancement of these models, although there have been new efforts incorporating additional local mechanochemical feedbacks at the kinetochore (Liu et al. 2008; Shtylla and Keener 2010). These models are motivated by experiments that propose that kinetochores contain force sensitive components that are also involved in regulating kMT dynamics (Andrews et al. 2004). Liu et al. totally neglects the mechanical forces acting on the kinetochore and focuses solely on local chemical reactions within the kinetochore that respond, via a tension-sensitive protein, to control kMT dynamics; chromosome velocity is assumed linear in the activity of the tension sensor. However, the resulting oscillations around the metaphase plate are highly periodic and do not closely reflect experimental data. Shtylla and Keener used a similar tension-sensitive feedback, but integrated this with a mechanical force–balance model along the lines of J&H. The idea is that such regulatory feedbacks will be necessary to generate more robust oscillations and transitions between attachment states (see below). Interestingly, Civelekoglu-Scholey et al. have already included a tension-sensitive feedback to drive directional switches (Civelekoglu-Scholey et al. 2006). Overall, all these models need to be more closely linked to experiment, i.e. we do not know yet whether such negative feedback loops exist to control directional switching and the role of tension as a signal. Whether kinetochores can detect changes in tension is a matter of current debate (for review see Khodjakov and Pines 2010). However, this discussion is focused on whether kMT attachment, rather than tension, is sensed by the spindle checkpoint machinery. The in vitro work by Biggins and colleagues with purified kinetochore particles clearly shows that mechanical behaviour alters under varying load (Akiyoshi et al. 2010; see earlier discussion). Here, kinetochores are only bound to a single MT so these changes must be attributed to tension changes and not attachment. Understanding how such a tensionometer operates within the kinetochore is of major importance.

## Sisters are not always biorientated

The models discussed so far have all focused on the biorientated (also known as amphitelic) state and the emergence of oscillatory behaviours. Of course a kinetochore begins life unattached after nuclear envelope breakdown and can adopt different attachment states as time progresses: (1) lateral binding—kinetochore attached to the lattice of an MT, (2) monotelic—one sister bound to one pole, the other

sister unattached, (3) syntelic—both sisters bound to one pole, (4) amphitelic—each sister bound to opposite poles and (5) merotelic—one (or two) sister (s) bound to both poles. Through a poorly understood set of processes, sister kinetochores move between these attachment states, ending up in the (stabilised) biorientated state and finding their way to the spindle equator—a process termed congression (for review see Kops et al. 2010). We, therefore, need to understand these different attachment states in terms of their behaviour and mechanism. The holy grail is to develop and run simulations of the entire process from the initial unattached state to segregation of sisters in anaphase. Models do exist for a single mono-orientated kinetochore pair although these are in effect simplifications of the biorientated state (Campas and Sens 2006; Joglekar and Hunt 2002; Liu et al. 2007). No models exist for the syntelic or lateral state. It is worth noting that the mono-orientated chromosomes observed in live cell movies could be either monotelic or syntelic and that neither current data nor models distinguish between these two states. We clearly need more quantitative data and markers for these different attachment states in order to define their behaviour. A recent model by Tournier and colleagues (Courtheoux et al. 2009) made a first effort to model merotelic attachment, albeit during anaphase in fission yeast. This is a simplification of the Civelekoglu-Scholey et al. model and, as before, force–balance equations are established to describe the time evolution of the kinetochore position. The inter-chromatid tension is replaced by an outer–inner kinetochore plate tension to model merotely for a single kinetochore, whilst the chromosome drag forces are the same as before. The simplification comes in treating the force produced at the kinetochore (always directed poleward) as simple linear force–velocity relationships, with prescribed stall forces and maximum velocities, ignoring the intricacies of polymerisation, depolymerisation and motors. Furthermore, a stochastic process with constant frequencies of attachment and detachment controls the number of kMTs attached to the kinetochore. This minimal mechanical model can reproduce the dynamics of a merotelic fission yeast kinetochore in vivo. It makes the prediction that if three or more of the six kinetochores are merotelic then the spindle would collapse—future observations of live cells will be needed to test this hypothesis. However, the simplifications of the Courtheoux et al. model will need development if it is to drive our understanding of the merotelic state. Further work will also certainly be needed to understand the merotelic state in mammalian pre-anaphase and anaphase cells and whether we can be guided by these initial yeast-based models. Again, quantitative analysis of the dynamics of merotelic attached kinetochores is essential to inform the building of further models.

## New models, new experiments

Modelling of chromosome directional instability has demonstrated that there are key (structural) requirements for oscillatory behaviour, specifically a spatially dependent restoration force and a feedback mechanism, while a kinetochore–MT mechanism with a load-dependent variable number of bindings, as in the Hill sleeve, endows the oscillation with realistic constant velocity characteristics. A variety of biological processes can produce the latter, and thus testing out which factors are essential for a given system requires extensive experimentation. Oscillatory behaviour itself is not able to distinguish between mechanisms and asking which processes are essential for oscillations will only provide an entry point for further experiments. We know the minimal requirements for oscillations, but it is very unlikely that the system is minimal, and the key questions are what are the behavioural characteristics of the system and what processes provide that behaviour. The circadian clock field is an excellent exemplar; for decades the minimal requirements for an oscillatory clock have been known whilst only over the last decade has it become clear that behaviour such as tracking both dawn and dusk, and having a period that is tolerant to temperature variation are crucial aspects of the biological clock (Edwards et al. 2010; Gould et al. 2006), characteristics that emerge from a more complex clock network. A detailed analysis of kinetochore oscillatory trajectories and functional dependencies (of amplitude, shape and frequency) can thus determine underlying mechanisms, whilst defining the key behavioural characteristics will require a broader remit for experimentation and modelling, possibly incorporating error correction (merotelic and syntelic attachments), transitions between attachment states, robustness to noise, and

integration with spindle checkpoint processes. Crucial unresolved questions also remain to be answered: Is kMT dynamic instability the driving force for chromosome directional instability or is kMT (de) polymerization totally controlled through a chemical regulatory network? Which mechanisms and feedbacks are important for what aspects of the behaviour and in which species? Are there functional interactions between proximal chromosomes? How do kinetochores switch between attachment states? And then, the most important question of all—What are the oscillations actually for? We propose that they may reflect the underlying mechanochemistry of the kinetochore and function as a "self-test" on the system to check for the correct balance of forces/kMT engagement. This could be closely related to experimental work in *Drosophila* (and an associated mathematical model), which supports the idea that flux-dependent mechanisms could operate to equalise tension across kinetochores within the metaphase plate and that this is important for error-free anaphase (Matos et al. 2009). It will be exciting to see how oscillatory behaviour is coupled to spindle checkpoint activation/inactivation and/or downstream consequences for a chromosome in terms of anaphase fidelity. Other ideas are that the oscillations are crucial to avoid the chromosome arm entanglement that would otherwise be catastrophic for anaphase chromatid separation.

The major limitation to progress in this area is that we are data poor; there is an increasing need for large numbers of quantitative datasets that describe kinetochore trajectories and transitions between attachment states in three dimensions under multiple parameter variations (perturbations) and at varying temporal resolutions. Improvements in the application of fluorescent reporters in human cells, rapidly advancing microscope technology and the development of automated machine vision allows the collection of datasets consisting of hundreds of kinetochore trajectories (Jaqaman et al. 2010). The future should see the development of further live cell assays that can read out the multiple mechanical properties of the kinetochore-k-fibre-spindle pole system and/or report on the dynamics of kinetochore components, including Mad2 (checkpoint activation/inactivation), EB proteins (number of growing kMTs), CENP-H/I (control of kMT dynamics) during kinetochore directional switching. We then need to test models over a range of parameter variations, for example, those invoked by RNAi, somatic gene knockouts and targeted proteolysis methodologies that are workable in human cells (Elbashir et al. 2001; Berdougo et al. 2009; Nishimura et al. 2009). Such advances will open up a new area of data-driven modelling that will necessitate a computationally heavy statistical methodology to integrate models with experimental data. This will lead to an iterative cycle of mathematical modelling and empirical observation, which will be a powerful tool for providing new insight into the mechanisms of chromosome motion control.

**Acknowledgments** We thank Jonathan Armond, Catarina Samora, Patrick Meraldi, Jonathan Millar and Douglas Drummond for helpful discussions and comments on the manuscript. This work was funded by an EPSRC studentship (E.H.) and a programme grant from Marie Curie Cancer Care (A.M and E.V.).



## References

Akiyoshi B, Sarangapani KK, Powers AF, Nelson CR, Reichow SL, Arellano-Santoyo H, Gonen T, Ranish JA, Asbury CL, Biggins S (2010) Tension directly stabilizes reconstituted kinetochore–microtubule attachments. Nature 468:576–579

Alushin GM, Ramey VH, Pasqualato S, Ball DA, Grigorieff N, Musacchio A, Nogales E (2010) The Ndc80 kinetochore complex forms oligomeric arrays along microtubules. Nature 467:805–810

Amaro AC, Samora CP, Holtackers R, Wang E, Kingston IJ, Alonso M, Lampson M, McAinsh AD, Meraldi P (2010) Molecular control of kinetochore–microtubule dynamics and chromosome oscillations. Nat Cell Biol 12:319–329

Andrews PD, Ovechkina Y, Morrice N, Wagenbach M, Duncan K, Wordeman L, Swedlow JR (2004) Aurora B regulates MCAK at the mitotic centromere. Dev Cell 6:253–268

Berdougo E, Terret ME, Jallepalli PV (2009) Functional dissection of mitotic regulators through gene targetting in human somatic cells. Methods Mol Biol 545:21–37

Brinkley BR, Ouspenski I, Zinkowski RP (1992) Structure and molecular organization of the centromere-kinetochore complex. Trends Cell Biol 2:15–21

Campas O, Sens P (2006) Chromosome oscillations in mitosis. Phys Rev Lett 97:128102

Cheeseman IM, Chappie JS, Wilson-Kubalek EM, Desai A (2006) The conserved KMN network constitutes the core microtubule-binding site of the kinetochore. Cell 127:983–997

Cimini D, Wan XH, Hirel CB, Salmon ED (2006) Aurora kinase promotes turnover of kinetochore microtubules to reduce chromosome segregation errors. Curr Biol 16:1711–1718

Civelekoglu-Scholey G, Sharp DJ, Mogilner A, Scholey JM (2006) Model of chromosome motility in *Drosophila* embryos: adaptation of a general mechanism for rapid mitosis. Biophys J 90:3966–3982

Cleveland DW, Mao YH, Sullivan KF (2003) Centromeres and kinetochores: from epigenetics to mitotic checkpoint signaling. Cell 112:407–421

Courtheoux T, Gay G, Gachet Y, Tournier S (2009) Ase1/Prc1-dependent spindle elongation corrects merotely during anaphase in fission yeast. J Cell Biol 187:399–412

Cytrynbaum EN, Scholey JM, Mogilner A (2003) A force balance model of early spindle pole separation in *Drosophila* embryos. Biophys J 84:757–769

Du Y, English CA, Ohi R (2010) The kinesin-8 Kif18A dampens microtubule plus-end dynamics. Curr Biol 20:374–380

Dumont S, Mitchison TJ (2009) Force and length in the mitotic spindle. Curr Biol 19:R749–R761

Edwards KD, Akman OE, Knox K, Lumsden PJ, Thomson AW, Brown PE, Pokhilko A, Kozma-Bognar L, Nagy F, Rand DA, Millar AJ (2010) Quantitative analysis of regulatory flexibility under changing environmental conditions. Mol Syst Biol 6:424

Elbashir SM, Martinez J, Patkaniowska A, Lendeckel W, Tuschl T (2001) Functional anatomy of siRNAs for mediating efficient RNAi in *Drosophila melanogaster* embryo lysate. EMBO J 20:6877–6888

Gardner MK, Odde DJ (2006) Modeling of chromosome motility during mitosis. Curr Opin Cell Biol 18:639–647

Gardner MK, Pearson CG, Sprague BL, Zarzar TR, Bloom K, Salmon ED, Odde DJ (2005) Tension-dependent regulation of microtubule dynamics at kinetochores can explain metaphase congression in yeast. Mol Biol Cell 16:3764–3775

Gould PD, Locke JCW, Larue C, Southern MM, Davis SJ, Hanano S, Moyle R, Milich R, Putterill J, Millar AJ, Hall A (2006) The molecular basis of temperature compensation in the Arabidopsis circadian clock. Plant Cell 18:1177–1187

Hill TL (1985) Theoretical problems related to the attachment of microtubules to kinetochores. P Natl Acad Sci USA 82:4404–4408

Howard J (2005) Mechanics of motor proteins and the cytoskeleton. Sinauer Associates Inc., U.S

Hughes AF, Swann MM (1948) Anaphase movements in the living cell—a study with phase contrast and polarised light on chick tissue cultures. J Exp Biol 25:45–70

Jaqaman K, King EM, Amaro AC, Winter JR, Dorn JF, Elliott HL, Mchedlishvili N, McClelland SE, Porter IM, Posch M, Toso A, Danuser G, McAinsh AD, Meraldi P, Swedlow JR (2010) Kinetochore alignment within the metaphase plate is regulated by centromere stiffness and microtubule depolymerases. J Cell Biol 188:665–679

Joglekar AP, Hunt AJ (2002) A simple, mechanistic model for directional instability during mitotic chromosome movements. Biophys J 83:42–58

Joglekar AP, Bloom KS, Salmon ED (2010) Mechanisms of force generation by end-on kinetochore–microtubule attachments. Curr Opin Cell Biol 22:57–67

Johnston K, Joglekar A, Hori T, Suzuki A, Fukagawa T, Salmon ED (2010) Vertebrate kinetochore protein architecture: protein copy number. J Cell Biol 189:937–943

Kapoor TM, Compton DA (2002) Searching for the middle ground: mechanisms of chromosome alignment during mitosis. J Cell Biol 157:551–556

Ke K, Cheng J, Hunt AJ (2009) The distribution of polar ejection forces determines the amplitude of chromosome directional instability. Curr Biol 19:807–815

Khodjakov A, Pines J (2010) Centromere tension: a divisive issue. Nat Cell Biol 12:919–923

Khodjakov A, Rieder CL (1996) Kinetochores moving away from their associated pole do not exert a significant pushing force on the chromosome. J Cell Biol 135:315–327

Kops GJ, Saurin AT, Meraldi P (2010) Finding the middle ground: how kinetochores power chromosome congression. Cell Mol Life Sci 67:2145–2161

Lampson MA, Cheeseman IM (2010) Sensing centromere tension: Aurora B and the regulation of kinetochore function. Trends Cell Biol (in press)

Lewis WH (1939) Changes of viscocity and cell activity. Science 89:400

Liu J, Desai A, Onuchic JN, Hwa T (2007) A mechanobiochemical mechanism for monooriented chromosome oscillation in mitosis. P Natl Acad Sci USA 104:16104–16109

Liu J, Desai A, Onuchic JN, Hwa T (2008) An integrated mechanobiochemical feedback mechanism describes chromosome motility from prometaphase to anaphase in mitosis. P Natl Acad Sci USA 105:13752–13757

Loncarek J, Kisurina-Evgenieva O, Vinogradova T, Hergert P, La Terra S, Kapoor TM, Khodjakov A (2007) The centromere geometry essential for keeping mitosis error free is controlled by spindle forces. Nature 450:745–749

Maiato H, DeLuca J, Salmon ED, Earnshaw WC (2004) The dynamic kinetochore–microtubule interface. J Cell Sci 117:5461–5477

Maresca TJ, Salmon ED (2009) Intrakinetochore stretch is associated with changes in kinetochore phosphorylation and spindle assembly checkpoint activity. J Cell Biol 184:373–381

Maskell DP, Hu XW, Singleton MR (2010) Molecular architecture and assembly of the yeast kinetochore MIND complex. J Cell Biol 190:823–834

Matos I, Pereira AJ, Lince-Faria M, Cameron LA, Salmon ED, Maiato H (2009) Synchronizing chromosome segregation by flux-dependent force equalization at kinetochores. J Cell Biol 186:11–26

Mayr MI, Hummer S, Bormann J, Gruner T, Adio S, Woehlke G, Mayer TU (2007) The human kinesin Kif18A is a motile microtubule depolymerase essential for chromosome congression. Curr Biol 17:488–498

McAinsh AD, Tytell JD, Sorger PK (2003) Structure, function, and regulation of budding yeast kinetochores. Annu Rev Cell Dev Biol 19:519–539

Mogilner A, Oster G (2003) Force generation by actin polymerization II: the elastic ratchet and tethered filaments. Biophys J 84:1591–1605

Nicklas RB (1988) The forces that move chromosomes in mitosis. Annu Rev Biophys Biophys Chem 17:431–449

Nishimura K, Fukagawa T, Takisawa H, Kakimoto T, Kanemaki M (2009) An auxin-based degron system for the rapid depletion of proteins in nonplant cells. Nat Methods 6:917–922

Petrovic A, Pasqualato S, Dube P, Krenn V, Santaguida S, Cittaro D, Monzani S, Massimiliano L, Keller J, Tarricone A, Maiolica A, Stark H, Musacchio A (2010) The MIS12 complex is a protein interaction hub for outer kinetochore assembly. J Cell Biol 190:835–852

Powers AF, Franck AD, Gestaut DR, Cooper J, Gracyzk B, Wei RR, Wordeman L, Davis TN, Asbury CL (2009) The Ndc80 kinetochore complex forms load-bearing attachments to dynamic microtubule tips via biased diffusion. Cell 136:865–875

Santaguida S, Musacchio A (2009) The life and miracles of kinetochores. EMBO J 28:2511–2531

Sharp DJ, Rogers GC, Scholey JM (2000) Microtubule motors in mitosis. Nature 407:41–47

Shtylla B, Keener JP (2010) A mechanomolecular model for the movement of chromosomes during mitosis driven by a minimal kinetochore bicyclic cascade. J Theor Biol 263:455–470

Skibbens RV, Skeen VP, Salmon ED (1993) Directional instability of kinetochore motility during chromosome congression and segregation in mitotic newt lung-cells—a push–pull mechanism. J Cell Biol 122:859–875

Stumpff J, von Dassow G, Wagenbach M, Asbury C, Wordeman L (2008) The kinesin-8 motor Kif18A suppresses kinetochore movements to control mitotic chromosome alignment. Dev Cell 14:252–262

Toso A, Winter JR, Garrod AJ, Amaro AC, Meraldi P, McAinsh AD (2009) Kinetochore-generated pushing forces separate centrosomes during bipolar spindle assembly. J Cell Biol 184:365–372

Uchida KSK, Takagaki K, Kumada K, Hirayama Y, Noda T, Hirota T (2009) Kinetochore stretching inactivates the spindle assembly checkpoint. J Cell Biol 184:383–390

Wan X, O'Quinn RP, Pierce HL, Joglekar AP, Gall WE, DeLuca JG, Carroll CW, Liu ST, Yen TJ, McEwen BF, Stukenberg PT, Desai A, Salmon ED (2009) Protein architecture of the human kinetochore microtubule attachment site. Cell 137:672–684

Wei RR, Schnell JR, Larsen NA, Sorger PK, Chou JJ, Harrison SC (2006) Structure of a central component of the yeast kinetochore: the Spc24p/Spc25p globular domain. Structure 14:1003–1009

Welburn JPI, Grishchuk EL, Backer CB, Wilson-Kubalek EM, Yates JR, Cheeseman IM (2009) The human kinetochore Ska1 complex facilitates microtubule depolymerization-coupled motility. Dev Cell 16:374–385

Wordeman L, Wagenbach M, von Dassow G (2007) MCAK facilitates chromosome movement by promoting kinetochore microtubule turnover. J Cell Biol 179:869–879

Zhai Y, Kronebusch PJ, Borisy GG (1995) Kinetochore microtubule dynamics and the metaphase–anaphase transition. J Cell Biol 131:721–734

**Liam P Cheeseman et al. "Specific removal of TACC3-ch-TOG-clathrin at metaphase deregulates kinetochore fiber tension." In: *Journal of Cell Science* 126.Pt 9 (May 2013), pp. 2102–2113**

# Specific removal of TACC3–ch-TOG–clathrin at metaphase deregulates kinetochore fiber tension

**Liam P. Cheeseman[1], Edward F. Harry[2,3], Andrew D. McAinsh[2], Ian A. Prior[1] and Stephen J. Royle[1,2,*]**

[1]Department of Cellular and Molecular Physiology, Institute of Translational Medicine, University of Liverpool, Crown Street, Liverpool L69 3BX, UK
[2]Centre for Mechanochemical Cell Biology, Division of Biomedical Cell Biology, Warwick Medical School, University of Warwick, Gibbet Hill Road, Coventry CV4 7AL, UK
[3]Molecular Organization and Assembly in Cells Doctoral Training Centre, University of Warwick, Coventry CV4 7AL, UK
*Author for correspondence (s.j.royle@warwick.ac.uk)

*Accepted 1 February 2013*
*Journal of Cell Science 126, 2102–2113*

*doi: 10.1242/jcs.124834*

## Summary

Microtubule-associated proteins of the mitotic spindle are thought to be important for the initial assembly and the maintenance of spindle structure and function. However, distinguishing assembly and maintenance roles for a given protein is difficult. Most experimental methods for protein inactivation are slow and therefore affect both assembly and maintenance. Here, we have used 'knocksideways' to rapidly (~5 minutes) and specifically remove TACC3–ch-TOG–clathrin non-motor complexes from kinetochore fibers (K-fibers). This method allows the complex to be inactivated at defined stages of mitosis. Removal of TACC3–ch-TOG–clathrin after nuclear envelope breakdown caused severe delays in chromosome alignment. Inactivation at metaphase, following a normal prometaphase, significantly delayed progression to anaphase. In these cells, K-fiber tension was reduced and the spindle checkpoint was not satisfied. Surprisingly, there was no significant loss of K-fiber microtubules, even after prolonged removal. TACC3–ch-TOG–clathrin removal during metaphase also resulted in a decrease in spindle length and significant alteration in kinetochore dynamics. Our results indicate that TACC3–ch-TOG–clathrin complexes are important for the maintenance of spindle structure and function as well as for initial spindle assembly.

**Key words:** Checkpoint, Knocksideways, Microtubule, Mitotic spindle, Rapid inactivation

## Introduction

Accurate chromosome segregation by the mitotic spindle is essential for life. It must proceed error-free in order to prevent cell death, cancer or birth defects (Murray, 2011). The spindle apparatus is an ensemble of microtubules (MTs), motors and non-motor proteins (Peterman and Scholey, 2009). Non-motor spindle proteins are involved in the initial assembly of the spindle and the maintenance of spindle structure and function. However, distinguishing the role in assembly and maintenance for a given spindle protein is problematic.

Over the last decade, RNA interference (RNAi) has dominated cell biology and it is the method of choice for understanding the function of spindle proteins. However, interpreting depletion phenotypes at later stages of mitosis is problematic because any defects observed could be due to errors that occurred at earlier stages, e.g. assembly of a defective spindle. In this study, we have used the 'knocksideways' method to rapidly and inducibly reroute spindle proteins to nearby mitochondria (Robinson et al., 2010). This allowed us to examine the role of inter-MT bridges at specific stages of mitosis, and particularly, in mature K-fibers following normal assembly of the mitotic spindle. Briefly, the knocksideways (KS) method exploits the binding of mammalian target of rapamycin (mTOR) to a complex of rapamycin bound to FKBP12. Rapamycin binds via the FKBP domain of FKBP12 and this binds the FRB (FKBP and rapamycin-binding) domain of mTOR kinase. KS involves the depletion of the target protein by RNAi and the re-expression of a version of the target protein that is refractory to RNAi and is tagged with the FKBP domain from FKBP12. In the same cells, MitoTrap, a mitochondrially targeted FRB domain is also expressed. Addition of rapamycin induces the heterodimerization of FKBP and FRB domains. This results in the protein of interest being rerouted from one subcellular location to mitochondria on a timescale of seconds (Robinson et al., 2010). If this new localization is incompatible with function, then the protein is inactivated.

TACC3 is an essential non-motor protein that binds the MT polymerase ch-TOG and localizes it to spindle fibers (Gergely et al., 2003; Gergely et al., 2000a; Gergely et al., 2000b; Lee et al., 2001; Piekorz et al., 2002). It was originally proposed that TACC3–ch-TOG are important for promoting spindle assembly by stabilizing MT minus ends at the centrosome or by antagonizing the depolymerizing activity of MCAK (Barr and Gergely, 2008; Kinoshita et al., 2005; Peset and Vernos, 2008). Later, it was found that TACC3–ch-TOG are bound to clathrin (Booth et al., 2011; Fu et al., 2010; Hubner et al., 2010; Lin et al., 2010), and possibly GTSE1 (Borner et al., 2012; Hubner et al., 2010) on kinetochore fibers (K-fibers) of the spindle. Here, TACC3–ch-TOG–clathrin complexes are thought to crosslink MTs by forming inter-MT bridges, suggesting a possible role for this non-motor complex in maintenance of spindle structure (Booth et al., 2011; Cheeseman et al., 2011; Royle, 2012; Royle et al., 2005). A rapid method of inactivation is therefore required to distinguish the role of the TACC3–ch-TOG–clathrin complex in assembly and maintenance of spindle structure. Furthermore, clathrin has distinct functions in

Journal of Cell Science

membrane trafficking and centrosome maturation in interphase (Brodsky, 2012) and TACC3 has a role in mRNA translation (Peset and Vernos, 2008). Slow inactivation methods alter these processes, which may cause indirect effects on mitosis and further confuse the interpretation of mitotic phenotypes.

In this study we use KS to remove TACC3–ch-TOG–clathrin complexes from mitotic spindles following normal spindle assembly and chromosome alignment. We find that TACC3–ch-TOG–clathrin complexes are required for the maintenance of K-fiber tension. Our findings demonstrate the utility of KS versus RNAi alone and describe the importance of non-motor proteins in the maintenance of spindle structure and micromechanics beyond initial assembly.

## Results

### Knocksideways is effective in mitosis for rapid, inducible removal of TACC3 from the mitotic spindle

We began by determining if rapid removal of spindle proteins is feasible during mitosis using knocksideways (KS), and on what timescale it could occur. To do this, we co-transfected HeLa cells with a plasmid to express mCherry-MitoTrap and a pBrain vector that simultaneously depleted endogenous TACC3 via shRNA and re-expressed a shRNA-refractory version of TACC3 that was tagged with GFP and FKBP (Fig. 1A). Live cells at metaphase were identified and imaged, with addition of rapamycin (200 nM) after 3 minutes (supplementary material Movie 1; Fig. 1B). We observed the removal of GFP-FKBP-TACC3 from the metaphase spindle within ~5 minutes of rapamycin application, and its colocalization to the mitochondria surrounding the spindle (Fig. 1B,C). Rerouting of GFP-FKBP-TACC3 to mitochondria was slower than in interphase, where rerouting followed a double exponential decay (Fig. 1D). We suspect that this difference is due to absence of a spindle in interphase to which TACC3 binds. By comparison, GFP-FKBP was rerouted extremely rapidly to mitochondria in interphase and at metaphase (Fig. 1D).

In a typical KS experiment we used four conditions, three controls and one test condition (Fig. 2A). In vehicle-treated cells, GFP-FKBP-TACC3 remained unaltered; and in cells expressing GFP-TACC3 without the FKBP domain, localization was unaffected by vehicle or rapamycin addition (Fig. 2A; supplementary material Fig. S1).

We found that effective rerouting of TACC3 KS depended on co-transfection of both plasmids and good expression of MitoTrap, which must be present in excess. For the method to be useful, the levels of TACC3 prior to KS must be within the normal range and after KS, the levels must be comparable to RNAi or Aurora A inhibition with MLN8237 (Booth et al., 2011). We assessed the levels of TACC3 on the spindle and in the cytoplasm for all conditions (Fig. 2B). This analysis showed that our re-expression of shRNA-refractory TACC3 in cells depleted of endogenous TACC3 was equivalent to endogenous levels and was not overexpressed (Fig. 2B). In addition, TACC3 KS resulted in a lower level of TACC3 at the spindle compared to RNAi or Aurora A inhibition.

### TACC3 KS specifically removes the entire TACC3–ch-TOG–clathrin complex from the mitotic spindle

We next asked whether the rapid removal of TACC3 from the spindle affected other spindle proteins. To answer this question, we tested for rerouting of a number of other spindle proteins

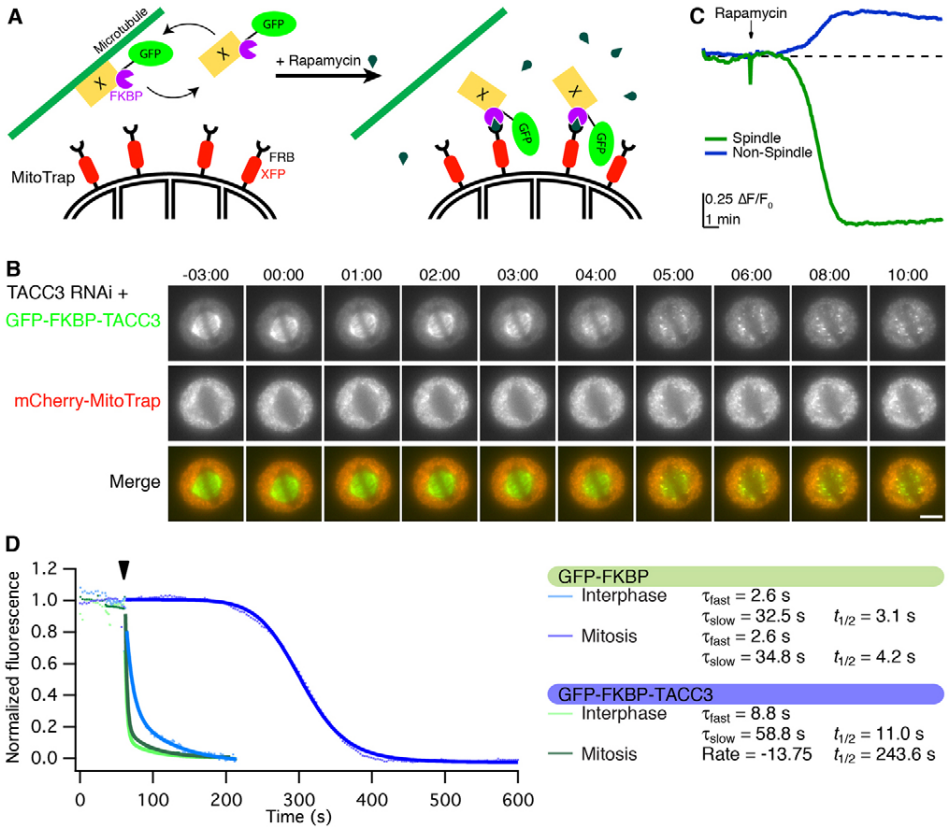


**Fig. 1. Rapid, induced removal of TACC3 by knocksideways.** (**A**) Diagram of knocksideways of a microtubule-associated protein. Protein X is depleted by RNAi and a shRNA-refractory version is re-expressed. Left: In the absence of rapamycin, the recombinant GFP- and FKBP-tagged protein X cycles on and off the microtubule. Right: Upon addition of rapamycin, the FKBP domain heterodimerizes with the FRB of XFP-MitoTrap (red) located on the mitochondria. (**B**) Video stills of TACC3 KS in a metaphase HeLa cell. Rapamycin (200 nM) was added at time zero (time is shown in minutes:seconds). GFP-FKBP-TACC3 is completely removed in ~5 minutes. Scale bar: 10 µm. (**C**) Quantification of GFP $\Delta F/F_0$ in the indicated areas over time during TACC3 KS. See supplementary material Movie 1. (**D**) Comparison of rerouting kinetics for GFP-FKBP-TACC3 or GFP-FKBP to mitochondria in interphase or mitosis, single cell examples. An overlay of curve fits to describe the rerouting are shown on the same time scale. Rapamycin application is denoted by the arrowhead. GFP-FKBP-TACC3 in mitosis was best fit by the Hill logistic function, all other data were best fit by a double exponential function.

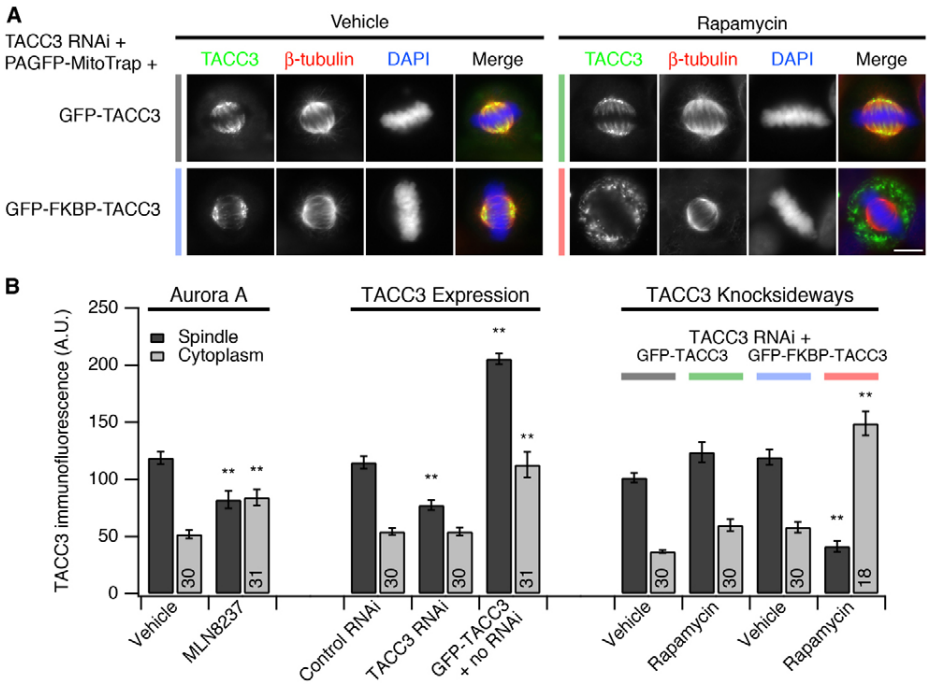


**Fig. 2. Removal of TACC3 from mitotic spindles by knocksideways.** (**A**) Representative micrographs of TACC3 KS. TACC3-depleted cells expressing PAGFP-MitoTrap (not visible) and the indicated TACC3 construct were treated for 30 minutes with 200 nM rapamycin or vehicle, fixed and stained for tubulin. Color coding for KS conditions is used throughout the paper. Full results are shown in supplementary material Fig. S1. Scale bar: 10 µm. (**B**) Bar chart to show quantification of TACC3 immunofluorescence in various experimental conditions. Total TACC3 was detected using anti-TACC3/A568 and analyzed by confocal microscopy. Aurora-A inhibition: using MLN8237 (1 µM) compared to vehicle. TACC3 expression: control RNAi + GFP, TACC3 RNAi + GFP and GFP-TACC3 expression (with no RNAi). TACC3 KS: TACC3 RNAi + PAGFP-MitoTrap + GFP-TACC3 or GFP-FKBP-TACC3; treated with vehicle or rapamycin (200 nM). Mean ± s.e.m. for spindle regions and cytoplasm. Number of cells was 18–31 as indicated, from two experiments. $^{**}P<0.001$ compared with vehicle (far left) values, one-way ANOVA with Tukey–Kramer post-hoc test.

following 10 minutes of rapamycin application (Fig. 3). Indirect immunofluorescence showed that TACC3 KS caused the removal of clathrin and ch-TOG from the spindle. In both cases, clathrin and ch-TOG were found colocalized with TACC3 at the mitochondria. Interestingly, GTSE1, a protein reported to be part of the TACC3–ch-TOG–clathrin complex (Hubner et al., 2010; Royle, 2012), was also lost from the spindle following TACC3 KS, although it was difficult to detect co-rerouting of GTSE1 at mitochondria (Fig. 3). Normal localizations of ch-TOG, clathrin and GTSE1 were observed in control cells, where GFP-FKBP-TACC3 was expressed and vehicle-treated (Fig. 3) or where GFP-TACC3 (without an FKBP domain) was expressed and cells treated with either rapamycin or vehicle (supplementary material Fig. S1). We also examined NuMA, Eg5 and HURP, as

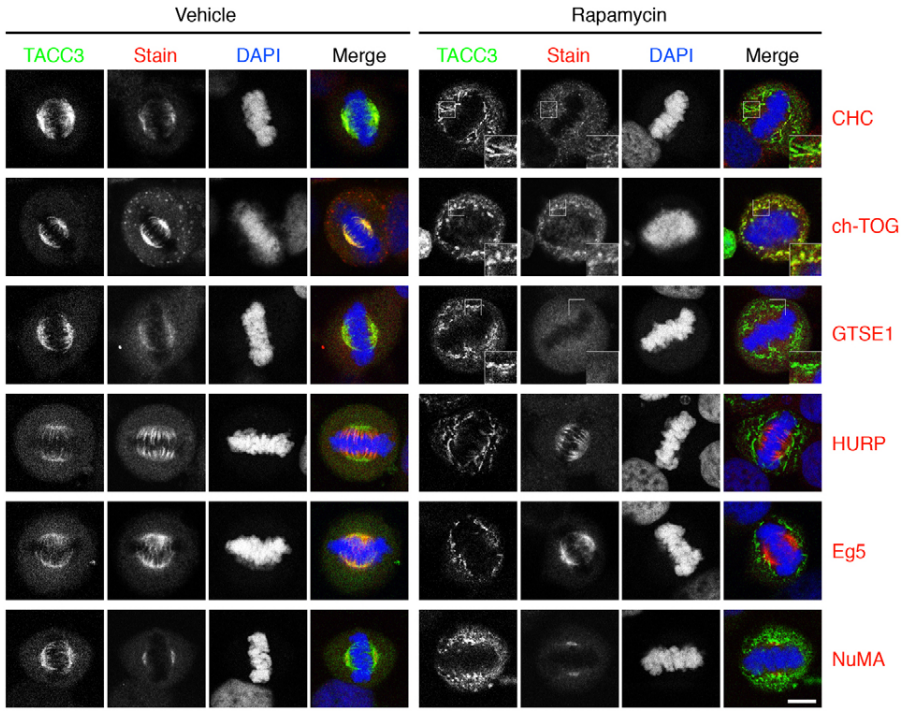


**Fig. 3. TACC3 KS removes ch-TOG, clathrin and GTSE1 from the spindle without affecting other spindle proteins.** Representative confocal micrographs of TACC3-depleted HeLa cells in metaphase expressing GFP-FKBP-TACC3 (green) and PAGFP-MitoTrap (not visible) that were treated with vehicle or rapamycin (200 nM) for 10 minutes, fixed and stained for the indicated proteins (red). TACC3 KS removed ch-TOG, clathrin heavy chain (CHC) and GTSE1 from the spindle. NuMA, HURP and Eg5 were unaffected by TACC3 KS. Zoomed areas show the colocalization of proteins at mitochondria following TACC3 KS. The results are typical of this experiment, repeated four times. See supplementary material Fig. S1 for full results. Scale bar: 10 µm.

these proteins localize to different areas of the spindle yet require phosphorylation by Aurora-A kinase for their activity, similarly to TACC3 (Giet et al., 1999; Kettenbach et al., 2011; Yu et al., 2005). The localization of all three proteins was unaltered by TACC3 KS (Fig. 3). We also tested whether TACC3 removal from the spindle would eventually cause deficiencies after prolonged drug application. The results of these experiments, with 30 minutes of drug application, were very similar to those with 10 minutes application (supplementary material Fig. S1). TACC3 KS is therefore a useful method to remove TACC3–ch-TOG–clathrin complexes specifically from spindles on a rapid timescale and that this will allow the molecular dissection of TACC3–ch-TOG–clathrin function at different stages of mitosis.

### Rerouting clathrin to mitochondria is equivalent to TACC3 KS

We also used a similar system to reroute clathrin from the spindle to mitochondria during mitosis (supplementary material Fig. S2). Removal occurred with similar kinetics to TACC3 KS (supplementary material Movie 2). Analysis of spindle protein localization showed that rerouting of clathrin also removed members of the TACC3–ch-TOG–clathrin complex including GTSE1, whereas Eg5, NuMA and HURP were unaffected (supplementary material Fig. S2). In cells with good rerouting of clathrin to mitochondria, TACC3 was completely colocalized with clathrin on the mitochondria (supplementary material Fig. S3). TACC3 was lost from spindle microtubules and centrosomes, even in early mitosis, arguing against the existence of a clathrin-independent pool of TACC3. However, due to the abundance of clathrin in the cell, we could not rule out the possibility that clathrin removal in some cells may be incomplete (supplementary material Fig. S2). Therefore TACC3 KS was used to remove TACC3–ch-TOG–clathrin in all subsequent experiments.

### TACC3 KS causes loss of a subpopulation of inter-MT bridges in K-fibers

K-fibers are bundles of parallel MTs that are crosslinked by inter-MT bridges (Hepler et al., 1970; McDonald et al., 1992; Nicklas et al., 1982). Previously, we showed that TACC3–ch-TOG–clathrin complexes form a subset of inter-MT bridges in K-fibers (Booth et al., 2011; Cheeseman et al., 2011; Royle, 2012; Royle et al., 2005). We next used correlative light-electron microscopy (CLEM) to verify if removal of TACC3–ch-TOG–clathrin complexes by KS resulted in a concomitant loss of inter-MT bridges. To do this, metaphase cells expressing GFP-FKBP-TACC3 and mCherry-MitoTrap were identified by fluorescence microscopy, and rapamycin (200 nM) or vehicle was applied for 10 minutes. TACC3 KS was visualized and the cells were then fixed and processed (Fig. 4A). The target cell was relocated in the resin and sectioned longitudinally relative to the spindle axis, and imaged by EM (Fig. 4A). Inter-MT bridges were quantified as previously described (Booth et al., 2011) (Fig. 4B). We found that there was a significant loss of inter-MT bridges in K-fibers after 10 minutes of TACC3 KS (Fig. 4C). This indicates that the removal of TACC3–ch-TOG–clathrin complexes from spindles by TACC3 KS results in removal of some inter-MT bridges. Many bridges clearly remain and these bridges must be composed of other proteins. With a method to inducibly and specifically remove TACC3–ch-TOG–clathrin bridges in hand we could investigate the role of these structures in K-fibers at different stages of mitosis.

### Removal of TACC3–ch-TOG–clathrin complexes at NEBD or after metaphase reveals two different aspects of crosslinking function

Our next aim was to use live-cell imaging and TACC3 KS to assess the role of TACC3–ch-TOG–clathrin inter-MT bridges at different stages in mitosis. For reference, TACC3 KS was compared with depletion of TACC3 by RNAi. Progression through mitosis of live HeLa cells expressing mCherry-H2B was visualized and the time from NEBD-to-metaphase and from metaphase-to-anaphase was measured (Fig. 5A). In agreement with previous studies, depletion of TACC3 by RNAi prolonged the time from NEBD to metaphase and the time from metaphase to anaphase, relative to untransfected cells (Gergely et al., 2003; Lin et al., 2010; Schneider et al., 2007) (Fig. 5B). These defects

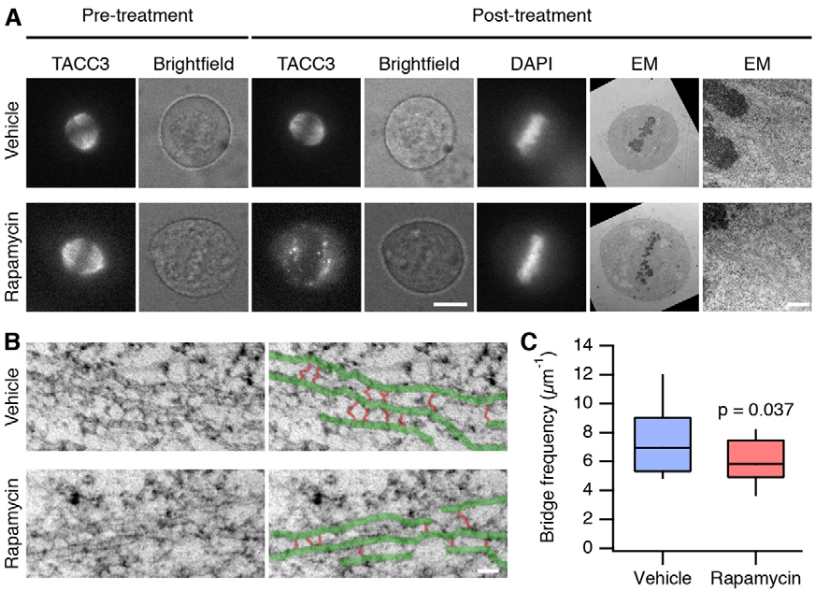


**Fig. 4. Loss of inter-microtubule bridges from K-fibers following TACC3 KS.** (**A**) TACC3-depleted HeLa cells at metaphase expressing GFP-FKBP-TACC3 and mCherry-MitoTrap were treated with rapamycin (200 nM) or vehicle for 10 minutes, fixed and processed for CLEM. The cell was located, 80-nm longitudinal sections taken (EM) and the bridge frequency in K-fibers quantified. Scale bars: 10 µm (left) and 500 nm (right). (**B**) Example micrographs to show visualization of inter-MT bridges for quantification. Annotated micrograph (right) shows MTs (green) and bridges (red). Scale bar: 50 nm. (**C**) Tukey box plot of inter-MT bridge frequency in K-fibers, expressed per micron of total MT length. In TACC3 KS cells, a significant loss of MT crosslinkers was observed: control $n=4$ cells (20 sections), TACC3 KS $n=5$ cells (25 sections); Student's $t$-test, $P=0.037$.

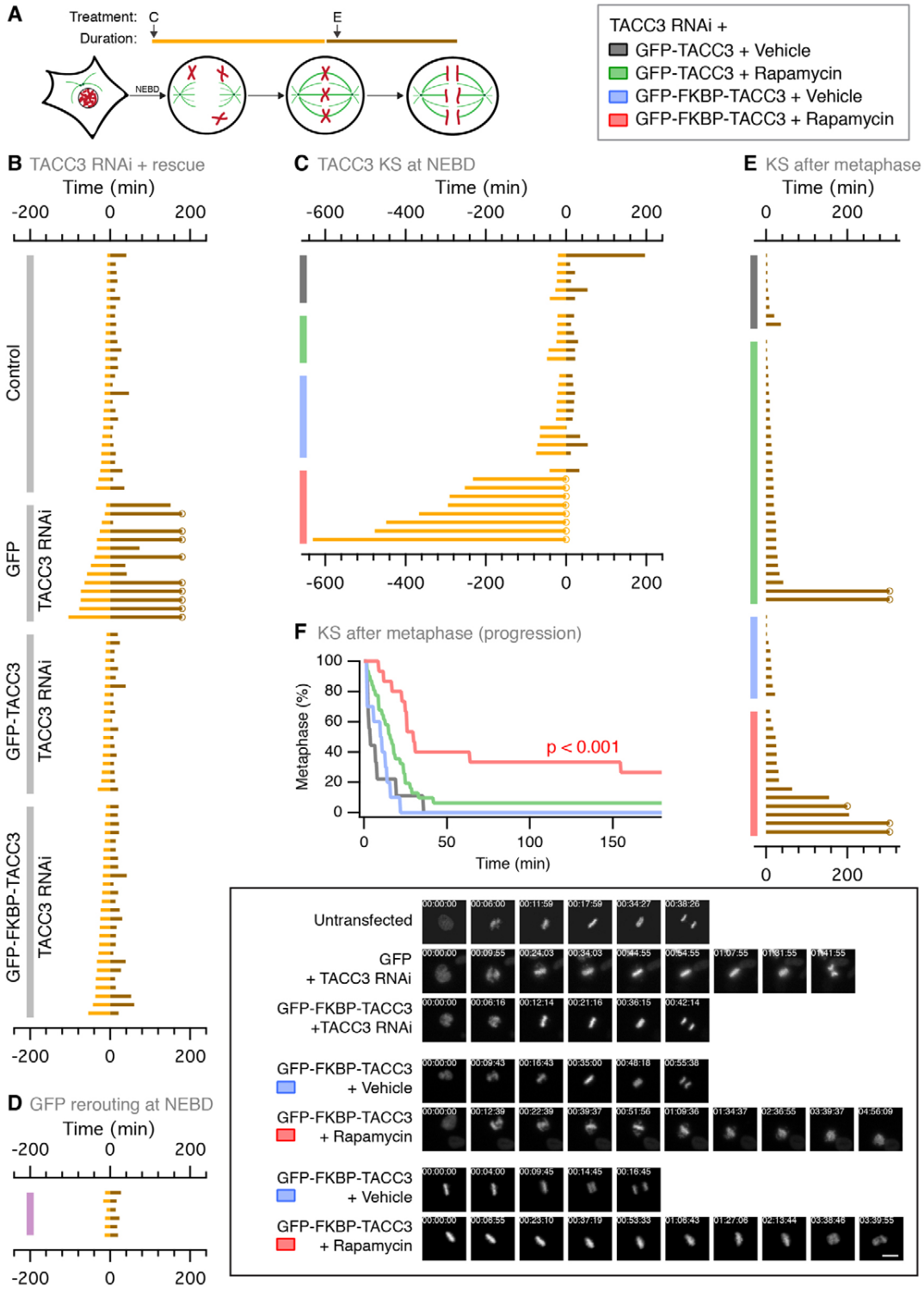


**Fig. 5. TACC3 KS at NEBD or after metaphase reveals two different aspects of crosslinking function.** (**A**) Diagram to show the timing of mitosis and experimental conditions. (**B**) Mitotic progression of control cells (no RNAi) and TACC3-depleted cells expressing GFP, GFP-TACC3 or GFP-FKBP-TACC3. TACC3 RNAi caused delay in chromosomal alignment in HeLa cells (NEBD-to-metaphase timing, gold) and also a delay in anaphase onset (metaphase-to-anaphase timing, brown). Cells that did not reach anaphase within the movie are marked with a circle. (**C**) Mitotic progression of TACC3-depleted HeLa cells expressing GFP-TACC3 or GFP-FKBP-TACC3; either vehicle or rapamycin (200 nM) was added at NEBD. (**D**) Normal mitotic progression of cells where GFP-FKBP was rerouted to mitochondria at NEBD. (**E**) Similar graph as in C except that TACC3 KS was performed after metaphase. All cells in the figure coexpressed H2B-mCherry for chromosome visualization and PAGFP-MitoTrap. (**F**) 'Survival curves' of the data shown in E. Example video stills from the indicated conditions are shown in the boxed area. Timings are indicated in hh:mm:ss. Scale bar: 20 µm.

were rescued by re-expression of shRNA-refractory GFP-TACC3 or GFP-FKBP-TACC3 (Fig. 5B), which indicates that the RNAi phenotype is specific to depletion of TACC3 and that our constructs are functional when expressed in cells depleted of TACC3. Delayed progression to anaphase in TACC3-depleted cells could be due to a role for MT crosslinking in K-fiber function at metaphase or simply a defect that is secondary to the prolonged prometaphase. These possibilities could now be distinguished using KS.

We next tested the effect of TACC3 KS at NEBD. To do this, live HeLa cells expressing PAGFP-MitoTrap, mCherry-H2B and TACC3 shRNA together with either GFP-TACC3 or GFP-FKBP-TACC3, were imaged with either vehicle or rapamycin added at NEBD. TACC3 KS at NEBD resulted in a severely prolonged prometaphase (Fig. 5C). The defects in chromosome alignment were so extreme that most TACC3 KS cells did not attain metaphase within several hours of imaging (Fig. 5C). The three control groups had normal prometaphase and subsequent metaphase-to-anaphase timings indicating that the effect of TACC3 KS was indeed due to removal of TACC3-containing complexes and not to application of rapamycin itself. This suggests that TACC3–ch-TOG–clathrin complexes are essential for an efficient and successful prometaphase, a time when the K-fiber matures.

TACC3 KS at NEBD produced a much stronger phenotype than TACC3 RNAi. To rule out the possibility that loading protein onto mitochondria delays mitosis non-specifically (‘neomorphic’ phenotype), we tested the effect of rerouting GFP-FKBP to mitochondria at NEBD. In six out of six cells, no delay was seen in NEBD–metaphase or in metaphase–anaphase timing (Fig. 5D). Furthermore, in TACC3 KS experiments, mitotic entry did not appear blocked in neighboring G2 cells. These observations indicate that the stronger phenotype upon rapid removal of TACC3 (compared to TACC3 RNAi), reflects a genuine difference between the methodologies.

To test the effect of TACC3–ch-TOG–clathrin complexes in mature spindles, we performed the same experiments but applied rapamycin after all chromosomes had aligned. These cells had therefore undergone a normal prometaphase and attained metaphase. Any changes caused by TACC3 KS would only be the result of TACC3–ch-TOG–clathrin loss from mature spindles and not from problems earlier in mitosis. TACC3 KS after metaphase caused a delay in anaphase onset (Fig. 5E), when compared with the three control groups (Fig. 5F). This indicates that removal of this complex from mature spindles at metaphase results in perturbed K-fiber function. Thus, TACC3–ch-TOG–clathrin inter-MT bridges are important for the function of mature K-fibers as well as having essential roles earlier in mitosis, e.g. in spindle assembly.

### TACC3 KS during metaphase reduces K-fiber tension and this is sensed by the spindle checkpoint

We next investigated the cause of the metaphase-to-anaphase delay that resulted from TACC3 KS at metaphase. First, we assessed the spindle checkpoint by quantifying Mad2-positive kinetochores in metaphase cells following rapamycin treatment (30 minutes). The number of Mad2 immunoreactive puncta per cell that colocalized with the anti-centromere antibody CREST was quantified (Fig. 6A,B). The proportion of cells containing no Mad2-positive kinetochores was decreased by 40% following

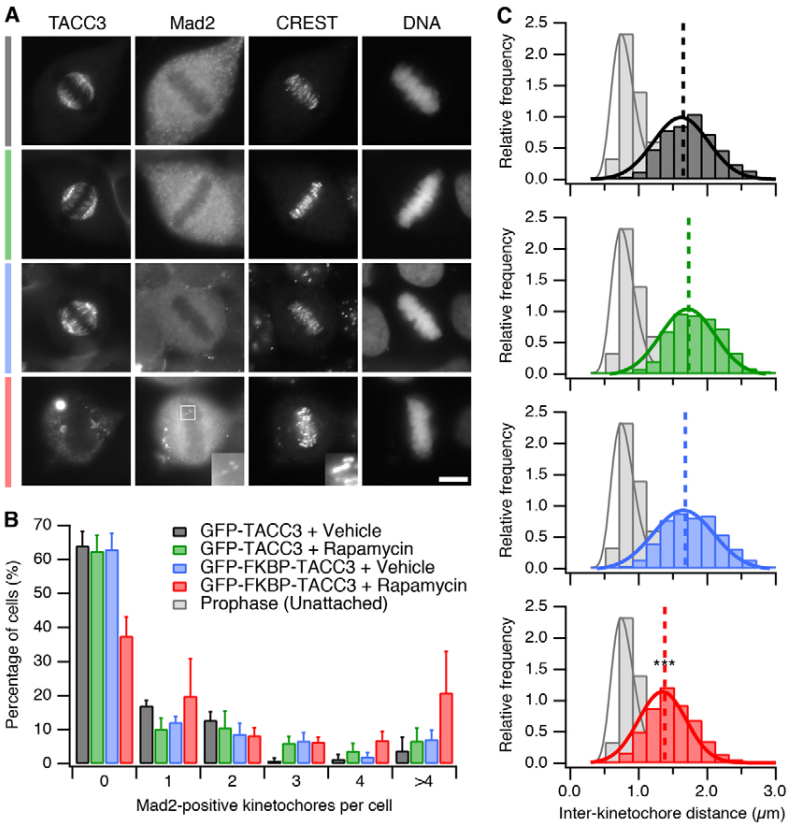


**Fig. 6. TACC3 KS at metaphase reduces K-fiber tension and cells are arrested by the spindle checkpoint.** (**A**) Representative confocal micrographs to show the recruitment of Mad2 to kinetochores following TACC3 KS. TACC3-depleted HeLa cells expressing GFP-TACC3 or GFP-FKBP-TACC3 were treated as indicated in the key in B. Inset shows three Mad2-positive kinetochores (2.5× zoom). Scale bar: 10 μm. (**B**) Proportion of cells with a satisfied or active spindle checkpoint, as revealed by Mad2 presence at kinetochores. Bars show mean ± s.e.m. of three experiments ($n$=90–93 cells). (**C**) Histograms of inter-kinetochore distances. Histograms (colored according to the key in B) are shown for GFP-TACC3 or GFP-FKBP-TACC3 treated with vehicle or rapamycin (200 nM) for 30 minutes, overlaid on a histogram of unattached inter-kinetochore distances from prophase/early prometaphase cells (light grey). The mean inter-kinetochore distance is shown by a dashed line. The unattached data were fitted with a log-normal function and all other data were fitted with a single Gaussian function. TACC3 KS cells (red, $n$=645 from 20 cells) displayed significantly reduced inter-kinetochore distance compared with controls (grey, $n$=654 from 22 cells; green, $n$=656 from 23 cells; blue, $n$=578 from 23 cells), but was not significantly different from unattached kinetochores ($n$=238 from 8 cells); ***$P$<0.001.

TACC3 KS compared to controls (Fig. 6B). In addition, the proportion displaying >4 Mad2-positive kinetochores was increased 3-fold following the removal of TACC3–ch-TOG–clathrin inter-MT bridges from K-fibers (Fig. 6B). Second, we assessed the effect of TACC3 KS on K-fiber tension by measuring inter-kinetochore distances. After rapamycin application (30 minutes), we observed a decrease in the mean ± s.d. inter-kinetochore distance from 1.68±0.06 μm (vehicle) to 1.38±0.04 μm (rapamycin). This suggested that the kinetochores were still attached but were under less tension because in prometaphase cells, unattached kinetochores had a mean inter-kinetochore distance of 0.83±0.06 μm (Fig. 6C). The distribution of inter-kinetochore distances showed an overall shift to lower values following TACC3 KS with no emergence of a second population around 0.6–1 μm suggesting no loss of attachment following TACC3 KS (Fig. 6C). Together, these results indicate that the slowed progression to anaphase following TACC3 KS was due to spindle checkpoint signaling. As the control cells had silenced the checkpoint satisfactorily and maintained tension, we interpret this to mean that the spindle checkpoint had been 're-activated' and that this re-activation was due to a loss of K-fiber tension.

### TACC3 KS from mature K-fibers causes minimal MT loss

In order to determine whether kinetochores had lost attachment to the spindle following TACC3 KS, we tested the number of kinetochores with cold-stable microtubule attachments in metaphase cells (Fig. 7A,B). In control or TACC3 KS cells, all kinetochores had cold-stable attachment to the spindle. Depletion of Nuf2 served as a positive control to show that we could detect kinetochores that lacked cold-stable attachments (Fig. 7B). TACC3 KS did not significantly alter the remaining tubulin signal in cold-treated cells relative to control cells, which suggested that MT occupancy is normal.

To investigate this further we used CLEM to analyze MT number in K-fibers sectioned orthogonally relative to the spindle axis (Fig. 7C). We found only a small decrease in MT number compared to controls after 10 minutes TACC3 KS, and this remained stable at 30 minutes (Fig. 7D), i.e. there was no progressive loss of MTs ($P>0.05$). Neither of these decreases was statistically significant compared to rapamycin-treated control K-fibers ($P>0.05$), although there was significant decrease when compared to vehicle-treated K-fibers ($P<0.001$). The cross-sectional area of K-fibers was estimated and the relation between K-fiber area and MT number plotted (Fig. 7E). These plots illustrate that after TACC3 KS, MT number per K-fiber is within the normal range, albeit at the lower end. The MT density within K-fibers was equivalent suggesting that any MT loss that occurred following TACC3 KS was limited to the periphery of the fiber. Nearest neighbor analysis and neighbor density analysis both failed to show any effect of TACC3 KS on MT spacing or distribution within K-fibers compared to control cells following 10 or 30 minutes rapamycin application (supplementary material Fig. S3). These results are in contrast to our previous analysis of K-fibers in clathrin RNAi cells, where MT loss occurred throughout the K-fiber (Booth et al., 2011). The difference is likely due to the fact that TACC3 KS was performed at metaphase after the K-fiber had accumulated the correct number of MTs and stabilized them; whereas clathrin-depleted cells may have been unable to accumulate MTs during prometaphase. Together, these results show that the number of attachments and the MT occupancy at kinetochores is normal following TACC3 KS. The mitotic delay and re-activated spindle checkpoint signaling following TACC3 KS indicates that the spindle checkpoint can sense reduced K-fiber tension that occurs without detectable loss of MT attachment.

### TACC3 KS from mature K-fibers causes changes in spindle shape and dynamicity

How does removal of TACC3–ch-TOG–clathrin inter-MT bridges result in reduced K-fiber tension? To address this question we examined mitotic spindle dynamics following removal of TACC3–ch-TOG–clathrin complexes, using 4D kinetochore and spindle pole tracking in live HeLa cells stably expressing GFP-CENP-A and centrin-GFP (Fig. 8). TACC3 KS was performed using mCherry-tagged TACC3 constructs at late prometaphase/metaphase. Cells were imaged and time-lapse datasets were analyzed as previously described (Jaqaman et al., 2010) and also with a new algorithm (see Materials and Methods), allowing kinetochore and spindle pole motions to be tracked in an automated manner (Fig. 8).

Removal of TACC3–ch-TOG–clathrin complexes by TACC3 KS resulted in a number of changes in kinetochore dynamics. First, kinetochore oscillations in typical trajectories from TACC3 KS cells were visibly dampened compared to controls (Fig. 8A–C). Second, inter-kinetochore distance was reduced by ~10% (Fig. 8D,E) confirming in live cells our earlier observations in fixed cells that K-fiber tension was decreased despite normal MT occupancy. Third, the metaphase plate was thicker following TACC3 KS, as the distance of sister kinetochore centers was more variable than in cells without TACC3 removal (Fig. 8E; Bartlett's statistic, 87.799, $P<0.001$). Note, that this variability is likely much larger as the analysis rejects kinetochores where $x>2.5\sigma$. Fourth, auto-correlation analysis of sister center displacement ($\Delta x$) showed that kinetochore oscillations had a reduced periodicity following TACC3 KS (Fig. 8F), whereas sister displacement cross-correlation analysis showed no alteration of kinetochore 'breathing' by TACC3 KS. Fifth, mean squared displacement analysis for kinetochore pairs showed that movement of kinetochores following TACC3 KS was less constrained compared to controls (Fig. 8G). In other words, for a given duration, kinetochores have moved further following TACC3 KS than in cells with normal levels of TACC3 on the spindle. This observation is in agreement with the increased variability in $x$ (Fig. 8E). All of these changes in kinetochore dynamics following TACC3 KS during metaphase are consistent with a decrease in K-fiber tension.

We also analyzed the motions of spindle poles in the same cells using automated tracking (Fig. 8H). This analysis revealed that the pole-to-pole distance of spindles was reduced by ~12% following TACC3 KS (Fig. 8I). This decrease in spindle length ($S$), which was noted previously (Fig. 2A), was the only detectable change in spindle pole dynamics. The movement of spindle poles is random, i.e. they do not undergo oscillations over time; and there was no alteration in the mean squared displacement (m.s.d.) of spindle poles following TACC3 KS. The average inter-kinetochore distance ($d$) was plotted as a function of the average pole-to-pole distance ($S$) for each cell analyzed across four experiments (Fig. 8J). This showed that the $d$ and $S$ did not scale with one another and argues that the decrease in $d$ is not caused by the reduction in $S$. These results indicate that removal of TACC3–ch-TOG–clathrin complexes

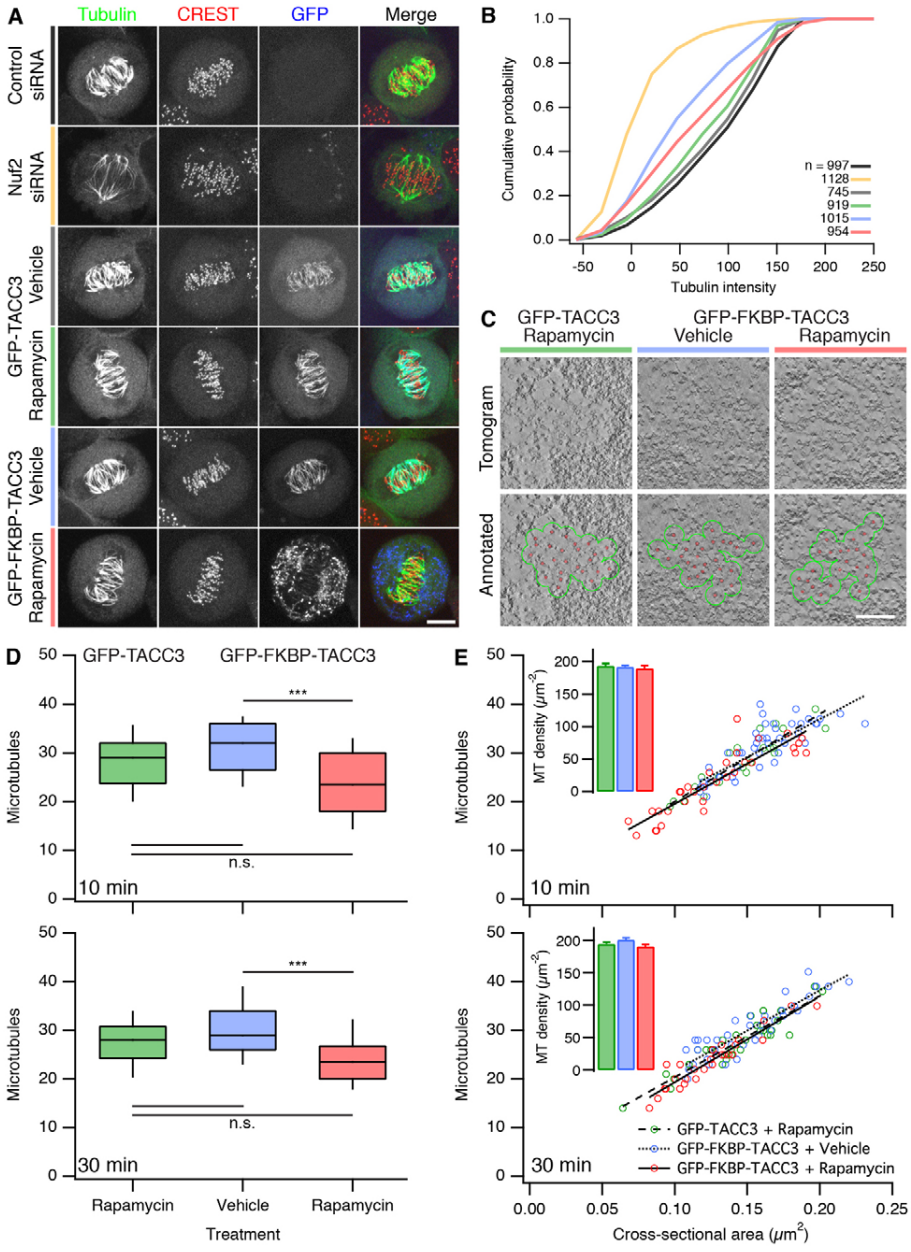


**Fig. 7. TACC3 KS at metaphase does not significantly alter kinetochore–microtubule attachments.** (**A**,**B**) Cold-stable kinetochore–microtubule attachments. (A) Representative pictures of each condition analyzed are shown as maximum intensity projections of confocal Z-series micrographs. Metaphase cells were cold-treated, fixed and stained with anti-tubulin (green) and CREST (red); GFP channel (blue) shows TACC3 KS. Scale bar: 10 µm. (B) Analysis of confocal z-series micrographs to detect cold-stable kinetochore–microtubule attachments. Cumulative frequency plot to show the average tubulin signal adjacent to kinetochores. $N_{cell}$=9–12 from two experiments. $N_{kinetochore}$ is shown in the legend. (**C**) Representative views of electron tomograms of orthogonal sections of K-fibers in metaphase HeLa cells expressing mCherry-MitoTrap and GFP-TACC3 or GFP-FKBP-TACC3 treated as indicated. Overlaid are microtubules (red) and the calculated K-fiber perimeter (green). Scale bar: 100 nm. (**D**) Tukey box plots of K-fiber MT number in TACC3-depleted HeLa cells expressing mCherry-MitoTrap and GFP-TACC3 or GFP-FKBP-TACC3, treated with vehicle or rapamycin (200 nM) for 10 minutes (top) or 30 minutes (bottom). TACC3 KS (red) causes a slight reduction in MTs of K-fibers after both 10 minutes and 30 minutes of rapamycin application. The reduction was significantly lower than for vehicle-treated cells (ANOVA with Tukey–Kramer post-hoc test, ***$P<0.01$), but not when compared with rapamycin-treated GFP-TACC3-expressing cells (n.s. indicates $P>0.05$). (**E**) Plots of MT number versus K-fiber cross-sectional area after 10 minutes and 30 minutes of treatment. Lines of best fit show the similar MT density in all conditions. Insets show mean ± s.e.m. K-fiber MT density in control (green, blue) or TACC3 KS cells (red) (10-minute data: green, $n$=22 K-fibers; blue, $n$=54; red, $n$=32. 30-minutes data: green, $n$=32; blue, $n$=38; red, $n$=28). See supplementary material Fig. S4 for spatial analysis of K-fibers.

from mitotic spindles that had completed a normal prometaphase caused the following changes: reduced spindle length, reduced K-fiber tension and decreased micromechanics of the spindle.

## Discussion

We investigated the requirement for one class of non-motor MT crosslinker (TACC3–ch-TOG–clathrin) for the function of mature K-fibers. Such an investigation was made possible by the knocksideways technique which allowed the inducible, rapid removal of certain inter-MT bridges from K-fibers at different stages of mitosis. Our findings demonstrated the utility of KS versus RNAi and a role for TACC3–ch-TOG–clathrin complexes in the shape and micromechanics of mature spindles.

The advantages of KS over RNAi are clear, given that protein depletion via RNAi is slow (24–72 hours) compared to the timescale of mitosis (1–2 hours). Using RNAi, attempts to determine the function of a spindle protein are complicated because the cell may have undergone several cell cycles with gradually declining levels of the protein. In this time, the cell may upregulate alternative pathways to compensate for the reduced protein, potentially masking the true phenotype. For spindle proteins with distinct interphase functions the picture is further complicated (Royle, 2011). In addition, trying to understand RNAi phenotypes at later stages of mitosis are potentially confounded by earlier defects. In other words, is the phenotype caused by a true requirement for the depleted protein at that later stage or is it because the earlier absence of the protein produced a defective spindle? It is now possible to dissect these differences using KS. Rapid inactivation methods are particularly crucial for mitosis, which is a succession of steps, each lasting less than 30 minutes.

The effectiveness of KS on a timescale of ~5 minutes makes it better suited than methods for inducible protein degradation, which work on the timescale of 30 minutes (Nishimura et al., 2009). Besides the use of KS as a tool for protein inactivation (Hirst et al., 2012; Robinson et al., 2010), we showed indirectly two additional uses for the method. First, the lifetime of proteins on the spindle could be inferred by comparing the kinetics of rerouting in mitotic and interphase cells. Second, testing which proteins are co-rerouted to mitochondria upon KS is a useful way to determine which proteins bind one another in cells.

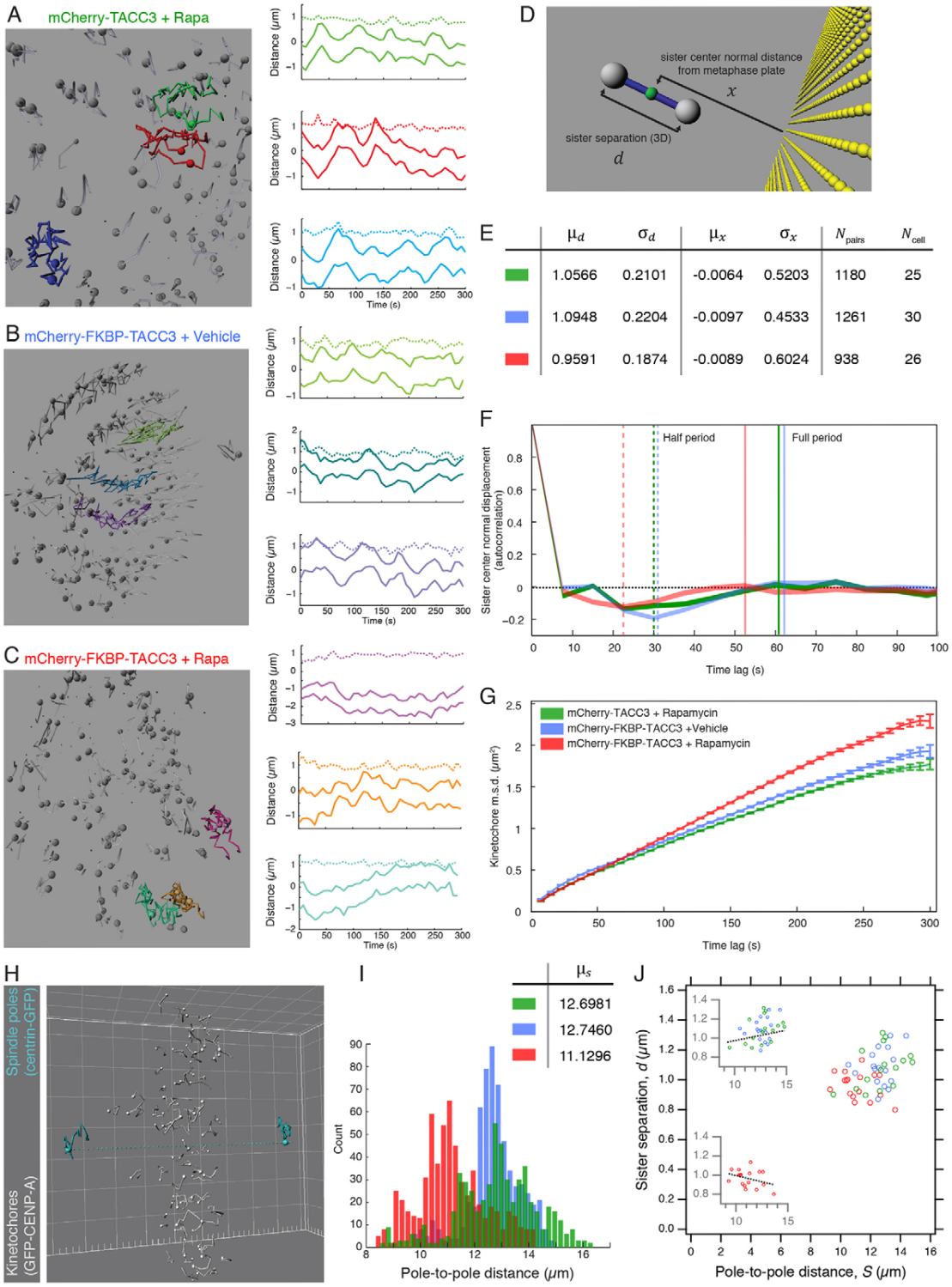


**Fig. 8.** See next page for legend.

TACC3 KS caused the specific rerouting of ch-TOG and clathrin from the spindle to mitochondria. Importantly, these partners were co-rerouted with TACC3 to the mitochondria, rather than being simply lost from the spindle, unable to bind in the absence of TACC3. This observation indicates that TACC3 KS reroutes the intact TACC3–ch-TOG–clathrin complex. Moreover, the co-rerouting suggests that interactions within the complex, for example between clathrin and TACC3, are of higher affinity than clathrin–adaptor interactions, as it was shown previously that AP-2 KS did not co-reroute clathrin to mitochondria (Robinson et al., 2010). We note that a pool of ch-TOG was retained at the spindle pole after TACC3 KS (supplementary material Fig. S1), which presumably corresponds to a functionally separate ch-TOG population, as previously described (Booth et al., 2011; Cassimeris et al., 2009; Gergely et al., 2003). Since the discovery of clathrin as a binding partner of TACC3–ch-TOG, it has been debated whether TACC3–ch-TOG can operate independently of this complex (Booth et al., 2011; Fu et al., 2011; Fu et al., 2010; Hubner et al., 2010; Lin et al., 2010; Royle, 2012). Co-rerouting of TACC3 and clathrin was complete, indicating that these proteins do not exist as functionally separate entities at the spindle and are probably interdependent for their recruitment to the spindle (Royle, 2012).

TACC3 KS caused the loss of some inter-MT bridges. However, we found that the extent of loss following TACC3 KS was less than that observed after RNAi of TACC3 or clathrin (Booth et al., 2011) or after inhibition of Aurora-A kinase using MLN8237–Alisertib (Cheeseman et al., 2011). As KS is a more rapid and specific method for protein inactivation, we interpret this to mean that our previous analyses overestimated the size of this population of inter-MT bridge. If correct, this points to secondary effects of RNAi or Alisertib beyond the simple removal of TACC3–ch-TOG–clathrin complexes. For example, clathrin-depleted K-fibers had fewer MTs than control RNAi and this could have confounded the quantification of bridge frequency (Booth et al., 2011). As noted previously, many crosslinkers remain in the K-fiber following TACC3 KS and this underscores that other inter-MT bridges exist in K-fibers that are not composed of TACC3–ch-TOG–clathrin.

Using TACC3 KS to remove TACC3–ch-TOG–clathrin inter-MT bridges at metaphase, following a normal prometaphase, we observed delays in the progression to anaphase. We found a net decrease in K-fiber tension despite normal MT attachment and that this state was detected by the spindle checkpoint. These observations could be taken as evidence that the spindle checkpoint can sense K-fiber tension, distinctly from MT attachment (Khodjakov and Pines, 2010). However, the number of Mad2-positive kinetochores was only a small fraction of the total kinetochores despite an overall shift to lower tension at all kinetochores. This result is similar to delayed progression to anaphase in taxol-treated PtK1 cells, where tension is reduced, MT attachment is normal, but Mad2 is only recruited to a subset of kinetochores (McEwen et al., 1997; Waters et al., 1998). The range of MTs/fiber had a tendency to be lower after TACC3 KS and so it is difficult to exclude the possibility that Mad2 is recruited to those kinetochores with fewest MTs.

The decrease in inter-kinetochore distance following TACC3 KS was 10%, while the decrease in pole–pole distance was ~12%. Although these changes are equivalent, several observations suggest that the decreases in inter-kinetochore distance are due to loss of K-fiber tension rather than being simply scaled with spindle size. First, experimental manipulation of pole–pole distance and the resultant change of spindle size have little effect on kinetochore separation (Dumont and Mitchison, 2009). Second, MT crosslinkers increase the tensile strength of MT bundles *in vitro* (Charlebois et al., 2011) and so the removal of a crosslinker is consistent with decreased K-fiber tension. Third, we saw changes in the dynamicity of the spindle and behavior of kinetochores, which argues that TACC3 KS affects the micromechanical properties of the K-fibers in addition to spindle size. Finally, plots of the average inter-kinetochore distance versus pole-to-pole distance showed that these two measures were independent.

One further surprising finding was the magnitude of mitotic delay induced by TACC3 KS at NEBD. This manipulation was predicted to be equivalent to TACC3 RNAi, but was far more severe. Using RNAi, TACC3-depleted cells had a delayed prometaphase but did eventually align their chromosomes. By contrast, cells with TACC3 KS at NEBD were unable to align the chromosomes at all. Four possibilities to explain this difference are: (i) TACC3-depleted cells may have time to compensate for the loss of TACC3 during the depletion period; (ii) removal of TACC3 from spindles by KS may be more extensive than RNAi, due to dimerization of GFP-FKBP-TACC3 with residual TACC3; (iii) rerouting of the whole TACC3–ch-TOG–clathrin complex may result in a significant fraction of ch-TOG and clathrin being trapped on mitochondria and thus unavailable for potential functions that are independent of the complex; (iv) a ‘neomorphic’ phenotype, where loading mitochondria with heterologous proteins delays mitosis non-specifically. This latter possibility was ruled out by the normal NEBD–anaphase times for cells with rerouting of GFP-FKBP and the observation that TACC3 KS does not impede mitotic entry. Quantification of TACC3 levels on spindle MTs following KS versus TACC3 RNAi suggest that the levels are indeed lower, arguing for the second possibility. Whatever the reason, we think that it is possible that RNAi phenotypes of other spindle proteins may

**Fig. 8. TACC3 KS at metaphase alters kinetochore dynamics and decreases spindle length.** Analysis of kinetochore motions in live HeLa cells stably expressing CENP-A-GFP and Centrin-GFP. Cells were depleted of endogenous TACC3 and were coexpressing PAGFP-MitoTrap and either mCherry-TACC3 or mCherry-FKBP-TACC3 and were treated with DMSO (vehicle) or rapamycin (200 nM). (**A–C**) Three example kinetochore trajectories from typical cells are shown. Left: Images of automated kinetochore tracking. Right: Plots of kinetochore distances relative to the metaphase plate as a function of time. Tracks of two sisters are shown for each pair; difference plot is shown (dotted line). (**D**) Diagram to show the measurement of $d$ and $x$. (**E**) Population data for sister separation ($d$, inter-kinetochore distance) and sister center normal position ($x$). (**F**) Sister center normal displacement ($\Delta x$ auto-correlation). Line thickness represents 95% confidence interval. Peaks of negative and positive lobes (half- and full-period) are shown by dashed and full vertical lines, respectively. (**G**) Mean squared displacement analysis for kinetochore pairs. Error bars show s.e.m. (**H**) Image to show the automated 4D tracking of spindle poles (centrin-GFP) in addition to kinetochores (see Materials and Methods). See supplementary material Movie 3. (**I**) Euclidian interpolar distances ($S$) for each condition. Color coding is the same as in previous figures. (**J**) Scatter plots to show that the average inter-kinetochore distance ($d$) does not vary as a function of spindle length ($S$). Insets show control data (above) and TACC3 KS data (below) for reference; a line of best fit is shown ($r^2=0.08$ and 0.11, respectively). Analysis in all figure panels is from four independent experiments.

have been similarly underestimated. Revisiting some of these proteins using KS in the future may give a more accurate picture of their mitotic function(s).

## Materials and Methods

### Molecular biology

To make pBrain-GFP-FKBP-TACC3KDP-shTACC3, an FKBP fragment was amplified from gamma-FKBP by PCR and inserted into pBrain-GFP-TACC3KDP-shTACC3 via Acc65I/BsrGI and Acc65I. To make mCherry- or PAGFP-MitoTrap, YFP in YFP-MitoTrap (pMito-YFP-FRB) was replaced with either mCherry or photo-activatable-GFP (PAGFP) via AgeI and BsrGI. PAGFP-MitoTrap was used as an 'invisible' MitoTrap to make other channels available for experiments (Willox and Royle, 2012). Gamma-FKBP and YFP-MitoTrap were kind gifts from Prof. M. S. Robinson (Cambridge Institute for Medical Research, UK).

For clathrin rerouting experiments, GFP-FKBP-LCa was used with no RNAi. GFP-FKBP-LCa was made by inserting a PCR-amplified FKBP fragment between GFP and LCa via BsrGI/Acc65I. GFP was exchanged with mCherry to make mCherry-H2B using AgeI/NotI from GFP-H2B. GFP-H2B, GFP-LCa and pBrain-GFP-TACC3KDP-shTACC3 were available from previous work (Booth et al., 2011; Royle et al., 2005).

### Cell culture, reagents and antibodies

HeLa cells were cultured in Dulbecco's Modified Eagle Medium (Invitrogen) supplemented with 10% fetal bovine serum (FBS) and 100 U/ml penicillin/streptomycin at 37℃ and 5% $CO_2$. Cells were transfected using GeneJuice (Novagen). Rapamycin (SigmaAldrich) was used at 200 nM, vehicle was ethanol (0.1%). MLN8237 (Selleck) was used at 1 µM, vehicle was DMSO (0.01%).

For indirect immunofluorescence, HeLa on coverslips were fixed with PTEMF (50 mM PIPES [1,4-Piperazinediethanesulfonic acid], pH 7.2, 10 mM EGTA, 1 mM $MgCl_2$, 0.2% Triton X-100, 4% paraformaldehyde) at room temperature, or methanol at −20℃ for ch-TOG staining. Cells were then permeabilized (PBS with 0.5% Triton X-100) and blocked (PBS with 5% BSA and 5% goat serum). The following antibodies were used: (1) mouse monoclonals: clathrin heavy chain (X22, CRL-2228 ATCC), TACC3 (ab56595, Abcam), and Eg5 (611186, BD Biosciences) (2) mouse polyclonal: GTSE1 (H00051512-B01P, Abnova), (3) rabbit polyclonals: ch-TOG (34032, Autogen Bioclear) and β-tubulin (ab6046, Abcam), NuMA (3888s, Cell Signaling), HURP (kind gift from Prof. E. A. Nigg, University of Basel, Switzerland), Mad2 (Covance), (4) human polyclonal: Crest (CS1058, Europa Bioproducts). Fluorescently-conjugated secondary antibodies were Alexa488, Alexa568 or Alexa633 (Molecular Probes). Coverslips were mounted using Mowiol containing 4′,6-diamidino-2-phenylindole (DAPI).

### Light microscopy

Live-cell imaging of KS kinetics was performed on an Olympus IX71 in glass-bottom dishes heated to 37℃ (Bioptechs Delta T5 µ-environmental culture dish controller) in $CO_2$-independent medium (Invitrogen) supplemented with 10% FBS and 100 U/ml penicillin/streptomycin, using Cell-R acquisition software and a Hamamatsu ORCA-ER C4742-80 camera with a 60× oil-immersion objective (1.42 NA). Quantification of GFP intensity during KS was performed using ImageJ, with an ROI that defined the spindle and one that excluded it, and plotted as $\Delta F/F_0$.

Live-cell imaging of mitotic progression following RNAi or KS was performed on a Nikon Eclipse Ti with a heated Perspex chamber (OKOlab) using standard filter sets for visualization of GFP and mCherry, NIS acquisition software, a CoolSNAP HQ2 camera and a 20× air objective (0.45 NA). Cells were kept at 37℃, in supplemented $CO_2$-independent medium. Light intensity was kept to a minimum to avoid light-induced cell damage. Chromosomes were visualized with mCherry-H2B (imaged once per minute), and GFP monitored every 5 minutes. Rapamycin was added to 200 nM by adding a concentrated media solution at 37℃ to the cell culture medium. Note that, for rerouting at metaphase, KS was induced at a variable time after the last chromosome aligned. It is likely therefore that we have underestimated the metaphase delay.

Confocal imaging was performed using a Leica confocal microscope SP2 with a 63× (1.4 NA) oil-immersion objective as described previously (Booth et al., 2011). For inter-kinetochore distance measurements, Z-stacks of CREST-immunostained cells were taken, assembled in ImageJ and distances between unambiguous CREST-positive kinetochore pairs in the stack were measured. For measurement of TACC3 levels, fixed, stained cells were imaged using identical acquisition parameters for all conditions. Mean pixel intensity for TACC3 was measured in a 20×20 pixel ROI using ImageJ software and the background subtracted.

Epifluorescence images of fixed cells were taken using a Nikon Eclipse Ti-U microscope with standard filter sets for visualization of DAPI, GFP, Alexa Fluor 568 and Alexa Fluor 633, a Nikon Digital Sight DS-Qi1Mc camera, a 60× (1.40 NA) oil-immersion objective and NIS acquisition software. To quantify Mad2 recruitment to the kinetochore, cells immunostained for Mad2 and CREST were imaged throughout the full Z dimension of the metaphase plate, and Mad2 puncta which colocalized with CREST were counted.

Cold-stable MT assay and analysis was performed as described previously (Toso et al., 2009). Briefly, cells treated with RNAi (48 hours) or KS (30 minutes), were placed in ice-cold medium, and incubated on ice for 10 minutes. The cells were then fixed with PTEMF and stained for tubulin and CREST. Confocal Z stacks were taken of metaphase cells and analyzed using Imaris as described.

### 4D kinetochore and spindle pole tracking

Cells were seeded in 35-mm Fluorodishes (WPI) in DMEM with 10% FBS and imaged on a widefield imaging system (Personal DeltaVision; Applied Precision) fitted with an environmental chamber maintained at 37℃ and 10% $CO_2$ atmospheric concentration. Images were acquired with a 100× 1.35 NA objective (Olympus) and a CDC (CoolSnap HQ2; Photometrics). Image acquisition was controlled by the softWoRx software suite (Applied Precision), 15 image stacks spaced 0.5 µm apart were collected every 7.5 seconds for 5 minutes (41 time-points). Pixels were set to 1×1 binning (65 nm effective pixel size).

Movies were deconvolved in softWoRx before tracking analysis. Automatic kinetochore tracking was performed as described (Jaqaman et al., 2010). All analysis was performed in MATLAB R2012a (MathWorks) with core algorithms written in C (compiled with the MATLAB MEX compiler). Only inlier kinetochores were used for analysis (spots that were $<2.5\sigma$ from metaphase plate).

Spindle pole tracks were identified by assigning a cost to each pair of tracks. The cost was defined as $c=|d-s| * a$ where $d$ was the average distance between the tracks, $s$ was the expected average spindle length, set to 11 µm and $a$ was the average angle between the tracks and the metaphase plate. Tracks were only considered if $d > 5$ µm and $a < 30^{\circ}$, and if both tracks were unaligned throughout both their lifetimes. The pair of tracks with the lowest cost was chosen. Since both centrioles in each pole were tagged, the second centriole track for each pole was found by assigning a cost: $c=g^{-1}$ where $g$ was the cross-correlation between the pole track and the candidate track. Tracks were only considered if $g > 0.9$ and if the average distance between the tracks was less than 1 µm. The track with the lowest cost was chosen for each pole as its respective second centriole.

For pole tracks where two centrioles were found, the pole position was defined as the center point between the two, otherwise the position of a single centriole was used. Spindle length was taken as the 3D distance between the two poles.

### Correlative light-electron microscopy

Correlative light-electron microscopy was performed as previously (Booth et al., 2011). HeLa cells were transfected with mCherry-MitoTrap and either pBrain-GFP-FKBP-TACC3KDP-shTACC3 or pBrain-GFP-TACC3KDP-shTACC3. Tomograms were assembled from tilt image series using eTOMO software (Boulder Laboratory for 3D Electron Microscopy). Quantification of EM images was carried out by an experimenter blind to the conditions of the experiment. All methods were as described previously (Booth et al., 2011), with the following exceptions. MT positions and cross-sectional area were plotted and calculated in tomograms. For measurement of K-fiber cross-sectional area, a 40 nm perimeter was computed around clusters of annotated MTs and measured using ImageJ. MTs within this boundary were counted as part of the K-fiber. To measure inter-MT distances, a map of MTs was created using IMOD Software (Boulder Laboratory for 3D Electron Microscopy), the coordinates were exported using model2point. The distance between each point was calculated in Microsoft Excel, from here the distance for each MT and its nearest neighboring MT was selected. To give the edge-to-edge distance, 20 nm was subtracted from these measurements. Neighbor density analysis was performed using nda in IMOD. MTs were annotated as circles of ~25 nm diameter throughout the Z slices, and flattened to a single Z plane. MTs within 80 nm of each other were padded by 50 nm using a convex polygon boundary.

### Data analysis

Statistical testing was performed with InStat or SPSS. Normally distributed data were compared using one-way ANOVA followed by a Tukey–Kramer *post hoc* test. Student's unpaired *t*-test was used to compare two data sets. Non-parametric data were compared using Kruskal–Wallis' ANOVA test. The Kolmogorov–Smirnov test was used to determine if the data followed a Gaussian distribution. Cox regression analysis was used to test for significance of mitotic delays. Tukey box plots show the median, interquartile range and the 10th and 90th percentile. Figures were assembled using IgorPro 6.22A (Wavemetrics), Matlab (R2012), Adobe Photoshop and Adobe Illustrator.

## Acknowledgements

We thank members of the Royle laboratory for useful comments and Sylvie Urbé for generous access to her live-cell imaging system. We are grateful to Scottie Robinson and Erich Nigg for essential reagents and David Mastronarde for advice and help with nda/IMOD. The authors declare that they have no conflict of interest.

## Author contributions

L.P.C. designed, carried out and analyzed the experiments, E.F.H. and A.D.M. helped with tracking experiments and analysis, I.A.P. helped with the design and implementation of electron microscopy, S.J.R. designed the experiments, analyzed data, coordinated the work and wrote the manuscript with input from all authors.

## Funding

L.P.C. is the recipient of a Wellcome Trust Prize Studentship. This work was supported by a Career Establishment Award from Cancer Research UK [grant number C25425/A8722 to S.J.R.]. S.J.R. is a Senior Cancer Research Fellow for Cancer Research UK. A.D.M. was supported by a Biotechnology and Biological Sciences Research Council (BBSRC) project grant [grant number BB/I021353/1]. E.F.H. was supported by the Engineering and Physical Sciences Research Council (EPSRC) [grant number EP/F500378/1] via the MOAC doctoral training centre. Deposited in PMC for release after 6 months.

Supplementary material available online at
http://jcs.biologists.org/lookup/suppl/doi:10.1242/jcs.124834/-/DC1

## References

**Barr, A. R. and Gergely, F.** (2008). MCAK-independent functions of ch-Tog/XMAP215 in microtubule plus-end dynamics. *Mol. Cell. Biol.* **28**, 7199-7211.

**Booth, D. G., Hood, F. E., Prior, I. A. and Royle, S. J.** (2011). A TACC3/ch-TOG/clathrin complex stabilises kinetochore fibres by inter-microtubule bridging. *EMBO J.* **30**, 906-919.

**Borner, G. H., Antrobus, R., Hirst, J., Bhumbra, G. S., Kozik, P., Jackson, L. P., Sahlender, D. A. and Robinson, M. S.** (2012). Multivariate proteomic profiling identifies novel accessory proteins of coated vesicles. *J. Cell Biol.* **197**, 141-160.

**Brodsky, F. M.** (2012). Diversity of clathrin function: new tricks for an old protein. *Annu. Rev. Cell Dev. Biol.* **28**, 309-336.

**Cassimeris, L., Becker, B. and Carney, B.** (2009). TOGp regulates microtubule assembly and density during mitosis and contributes to chromosome directional instability. *Cell Motil. Cytoskeleton* **66**, 535-545.

**Charlebois, B. D., Kollu, S., Schek, H. T., Compton, D. A. and Hunt, A. J.** (2011). Spindle pole mechanics studied in mitotic asters: dynamic distribution of spindle forces through compliant linkages. *Biophys. J.* **100**, 1756-1764.

**Cheeseman, L. P., Booth, D. G., Hood, F. E., Prior, I. A. and Royle, S. J.** (2011). Aurora A kinase activity is required for localization of TACC3/ch-TOG/clathrin inter-microtubule bridges. *Commun. Integr. Biol.* **4**, 409-412.

**Dumont, S. and Mitchison, T. J.** (2009). Compression regulates mitotic spindle length by a mechanochemical switch at the poles. *Curr. Biol.* **19**, 1086-1095.

**Fu, W., Tao, W., Zheng, P., Fu, J., Bian, M., Jiang, Q., Clarke, P. R. and Zhang, C.** (2010). Clathrin recruits phosphorylated TACC3 to spindle poles for bipolar spindle assembly and chromosome alignment. *J. Cell Sci.* **123**, 3645-3651.

**Fu, W., Jiang, Q. and Zhang, C.** (2011). Novel functions of endocytic player clathrin in mitosis. *Cell Res.* **21**, 1655-1661.

**Gergely, F., Karlsson, C., Still, I., Cowell, J., Kilmartin, J. and Raff, J. W.** (2000a). The TACC domain identifies a family of centrosomal proteins that can interact with microtubules. *Proc. Natl. Acad. Sci. USA* **97**, 14352-14357.

**Gergely, F., Kidd, D., Jeffers, K., Wakefield, J. G. and Raff, J. W.** (2000b). D-TACC: a novel centrosomal protein required for normal spindle function in the early Drosophila embryo. *EMBO J.* **19**, 241-252.

**Gergely, F., Draviam, V. M. and Raff, J. W.** (2003). The ch-TOG/XMAP215 protein is essential for spindle pole organization in human somatic cells. *Genes Dev.* **17**, 336-341.

**Giet, R., Uzbekov, R., Cubizolles, F., Le Guellec, K. and Prigent, C.** (1999). The Xenopus laevis aurora-related protein kinase pEg2 associates with and phosphorylates the kinesin-related protein XlEg5. *J. Biol. Chem.* **274**, 15005-15013.

**Hepler, P. K., McIntosh, J. R. and Cleland, S.** (1970). Intermicrotubule bridges in mitotic spindle apparatus. *J. Cell Biol.* **45**, 438-444.

**Hirst, J., Borner, G. H., Antrobus, R., Peden, A. A., Hodson, N. A., Sahlender, D. A. and Robinson, M. S.** (2012). Distinct and overlapping roles for AP-1 and GGAs revealed by the 'knocksideways' system. *Curr. Biol.* **22**, 1711-1716.

**Hubner, N. C., Bird, A. W., Cox, J., Splettstoesser, B., Bandilla, P., Poser, I., Hyman, A. and Mann, M.** (2010). Quantitative proteomics combined with BAC TransgeneOmics reveals in vivo protein interactions. *J. Cell Biol.* **189**, 739-754.

**Jaqaman, K., King, E. M., Amaro, A. C., Winter, J. R., Dorn, J. F., Elliott, H. L., McHedlishvili, N., McClelland, S. E., Porter, I. M., Posch, M. et al.** (2010). Kinetochore alignment within the metaphase plate is regulated by centromere stiffness and microtubule depolymerases. *J. Cell Biol.* **188**, 665-679.

**Kettenbach, A. N., Schweppe, D. K., Faherty, B. K., Pechenick, D., Pletnev, A. A. and Gerber, S. A.** (2011). Quantitative phosphoproteomics identifies substrates and functional modules of Aurora and Polo-like kinase activities in mitotic cells. *Sci. Signal.* **4**, rs5.

**Khodjakov, A. and Pines, J.** (2010). Centromere tension: a divisive issue. *Nat. Cell Biol.* **12**, 919-923.

**Kinoshita, K., Noetzel, T. L., Pelletier, L., Mechtler, K., Drechsel, D. N., Schwager, A., Lee, M., Raff, J. W. and Hyman, A. A.** (2005). Aurora A phosphorylation of TACC3/maskin is required for centrosome-dependent microtubule assembly in mitosis. *J. Cell Biol.* **170**, 1047-1055.

**Lee, M. J., Gergely, F., Jeffers, K., Peak-Chew, S. Y. and Raff, J. W.** (2001). Msps/XMAP215 interacts with the centrosomal protein D-TACC to regulate microtubule behaviour. *Nat. Cell Biol.* **3**, 643-649.

**Lin, C. H., Hu, C. K. and Shih, H. M.** (2010). Clathrin heavy chain mediates TACC3 targeting to mitotic spindles to ensure spindle stability. *J. Cell Biol.* **189**, 1097-1105.

**McDonald, K. L., O'Toole, E. T., Mastronarde, D. N. and McIntosh, J. R.** (1992). Kinetochore microtubules in PTK cells. *J. Cell Biol.* **118**, 369-383.

**McEwen, B. F., Heagle, A. B., Cassels, G. O., Buttle, K. F. and Rieder, C. L.** (1997). Kinetochore fiber maturation in PtK1 cells and its implications for the mechanisms of chromosome congression and anaphase onset. *J. Cell Biol.* **137**, 1567-1580.

**Murray, A. W.** (2011). A brief history of error. *Nat. Cell Biol.* **13**, 1178-1182.

**Nicklas, R. B., Kubai, D. F. and Hays, T. S.** (1982). Spindle microtubules and their mechanical associations after micromanipulation in anaphase. *J. Cell Biol.* **95**, 91-104.

**Nishimura, K., Fukagawa, T., Takisawa, H., Kakimoto, T. and Kanemaki, M.** (2009). An auxin-based degron system for the rapid depletion of proteins in nonplant cells. *Nat. Methods* **6**, 917-922.

**Peset, I. and Vernos, I.** (2008). The TACC proteins: TACC-ling microtubule dynamics and centrosome function. *Trends Cell Biol.* **18**, 379-388.

**Peterman, E. J. and Scholey, J. M.** (2009). Mitotic microtubule crosslinkers: insights from mechanistic studies. *Curr. Biol.* **19**, R1089-R1094.

**Piekorz, R. P., Hoffmeyer, A., Duntsch, C. D., McKay, C., Nakajima, H., Sexl, V., Snyder, L., Rehg, J. and Ihle, J. N.** (2002). The centrosomal protein TACC3 is essential for hematopoietic stem cell function and genetically interfaces with p53-regulated apoptosis. *EMBO J.* **21**, 653-664.

**Robinson, M. S., Sahlender, D. A. and Foster, S. D.** (2010). Rapid inactivation of proteins by rapamycin-induced rerouting to mitochondria. *Dev. Cell* **18**, 324-331.

**Royle, S. J.** (2011). Mitotic moonlighting functions for membrane trafficking proteins. *Traffic* **12**, 791-798.

**Royle, S. J.** (2012). The role of clathrin in mitotic spindle organisation. *J. Cell Sci.* **125**, 19-28.

**Royle, S. J., Bright, N. A. and Lagnado, L.** (2005). Clathrin is required for the function of the mitotic spindle. *Nature* **434**, 1152-1157.

**Schneider, L., Essmann, F., Kletke, A., Rio, P., Hanenberg, H., Wetzel, W., Schulze-Osthoff, K., Nürnberg, B. and Piekorz, R. P.** (2007). The transforming acidic coiled coil 3 protein is essential for spindle-dependent chromosome alignment and mitotic survival. *J. Biol. Chem.* **282**, 29273-29283.

**Toso, A., Winter, J. R., Garrod, A. J., Amaro, A. C., Meraldi, P. and McAinsh, A. D.** (2009). Kinetochore-generated pushing forces separate centrosomes during bipolar spindle assembly. *J. Cell Biol.* **184**, 365-372.

**Waters, J. C., Chen, R. H., Murray, A. W. and Salmon, E. D.** (1998). Localization of Mad2 to kinetochores depends on microtubule attachment, not tension. *J. Cell Biol.* **141**, 1181-1191.

**Willox, A. K. and Royle, S. J.** (2012). Stonin 2 is a major adaptor protein for clathrin-mediated synaptic vesicle retrieval. *Curr. Biol.* **22**, 1435-1439.

**Yu, C. T., Hsu, J. M., Lee, Y. C., Tsou, A. P., Chou, C. K. and Huang, C. Y.** (2005). Phosphorylation and stabilization of HURP by Aurora-A: implication of HURP as a transforming target of Aurora-A. *Mol. Cell. Biol.* **25**, 5789-5800.